

# Searching for warm dark matter down on Earth and among the stars

Dissertation submitted for the award of the title  
“Doctor of Natural Sciences”  
to the faculty of Physics, Mathematics and Computer science of  
Johannes Gutenberg-Universität in Mainz

Sven Baumholzer  
born in Worms

Mainz, November 29th, 2021



First examiner: Prof. Dr. Pedro Schwaller  
Date of submission: 29.11.2021  
Date of defense: 18.03.2022

# Abstract

---

There are experimental and observational hints calling for new physics beyond the standard model (SM), among them the intriguing question of the nature of dark matter (DM). In this thesis we study the phenomenology of models featuring warm DM.

First, we consider the scotogenic model, which features a radiative generation of neutrino masses, and explore its light dark matter phenomenology. In particular, we focus on keV-scale DM which can be produced either via a freeze-in mechanism through the decays of newly introduced scalars or the decays of the next-to-lightest fermionic particle in the spectrum. The latter possibility is required to be suppressed as it typically produces a hot DM component. Constraints from big bang nucleosynthesis (BBN) and the number of non-photon relativistic particle species,  $N_{\text{eff}}$ , are also considered, and in combination with couplings needed to produce enough DM, the DM candidate is required to be light. To estimate the discovery potential for this scenario we consider collider analyses at the high luminosity upgrade of the Large Hadron Collider (HL-LHC) and proposed future hadron and lepton colliders, namely FCC-hh and CLIC, focusing on final states with two leptons and missing transverse energy. Taking into account the cosmological bounds, we show that they already probe parts of the HL-LHC discovery region for this scenario, while future colliders access an even larger region of parameter space.

Second, we derive structure formation limits on DM composed of keV-scale axion-like particles (ALPs), produced via freeze-in through their interaction with photons and SM fermions. We employ results from Lyman- $\alpha$  forest data sets as well as the observed number of Milky Way (MW) subhalos. We compare the momentum distribution function obtained using Maxwell-Boltzmann and quantum statistics for describing the SM thermal bath. It should be emphasized that the presence of logarithmic divergences complicates the calculation of the production rate.

The results obtained in this way, in combination with gamma-ray bounds, exclude the possibility for a photophilic “frozen-in” ALP DM with mass below  $\sim 19$  keV. For the photophobic ALP scenario, in which DM couples primarily to SM fermions, the ALP DM distribution function is peaked at lower momentum and hence results in weaker limits on the DM mass. Future facilities, such as the upcoming Vera C. Rubin observatory, will significantly improve the current bounds up to  $\sim 80$  keV.

Lastly, we generalize DM production via multiple mechanisms by introducing a model-independent framework and assess whether its consistency with structure formation observations. We simulate the matter power spectrum for DM scenarios characterized by at least two temperatures stemming from the different production mechanisms, and derive the suppression of structures at small scales and the expected number of MW subhalos. This allows us to obtain constraints on the parameter space of non-thermally produced DM. We propose a simple parameterization for non-thermal DM momentum distributions, present a fitting procedure that can be used to adapt our results to other models, and demonstrate via some toy models how our results can be applied to other non-thermal DM models.

*Ewig leuchten die Sterne  
Und unaufhörlich fällt der Schnee...*

*Der Blick nach oben eröffnet mir  
Die Klarheit, Einfachheit und zugleich unendliche Komplexität des Seins*

*Und ewig leuchten die Sterne...*

**Ewig leuchten die Sterne - Paysage d'Hiver, Das Tor**

*Then Varda went forth from the council, and she looked out from the height of Taniquetil, and beheld the darkness of Middle-earth beneath the innumerable stars, faint and far. Then she began a great labour, greatest of all the works of the Valar since their coming into Arda. She took the silver dews from the vats of Telperion, and therewith she made new stars and brighter against the coming of the Firstborn; (..)*

**John Ronald Reuel Tolkien, Christopher Tolkien (ed.), The Silmarillion, 1977**

# List of publications

---

This thesis is based on the following publications and research work. We highlight the author contribution to each of them.

- S. Baumholzer, V. Brdar, P. Schwaller and A. Segner, *Shining Light on the Scotogenic Model: Interplay of Colliders and Cosmology*, *JHEP* **09** (2020) 136, [[1912.08215](#)], [[1](#)]: The foundation of this work was laid in Ref. [[2](#)] and thus the introduction into Chapter [III](#) is influenced by chapter V of this reference. All co-authors of [[1](#)] contributed to the text of the manuscript, while the author particularly contributed the Monte Carlo simulations for the HL-LHC projections and all calculations for the combined DM and cosmology part of the project. Results for the future collider studies were derived by Alexander Segner and cross checked by the author. All plots have been derived by the author, while the exclusion plots based on CLIC and FCC are based on data from Alexander Segner. The publication is the basis for Chapters [III](#) and [IV](#).
- S. Baumholzer, V. Brdar and E. Morgante, *Structure Formation Limits on Axion-Like Dark Matter* *JCAP* **05** (2021) 004, [[2012.09181](#)], [[3](#)]: The author performed all numerical simulations regarding structure formation probes of the model and the corresponding plots are either made by himself or based on his data. The derivation of the momentum distribution function for the ALP DM was done in joint collaboration with Dr. Enrico Morgante and the author crosschecked the results. All co-authors contributed to the text of the manuscript. Figures not made by the author are marked as such. Chapter [V](#) of this thesis is based on this publication.
- S. Baumholzer and P. Schwaller, *Probing non-thermal light DM with structure formation and  $N_{\text{eff}}$* : All calculations, parameter scans, numerical studies, the corresponding plots and the text were done by the author with advice and corrections from Prof. Dr. Pedro Schwaller. It is the basis for Chapter [VI](#). The project is in final preparation for publication.

If not mentioned otherwise, all figures shown in this thesis are done by the author. Figures produced from co-authors are indicated as such and some of them are modified by the author.

# Contents

---

<b>Abstract</b>	<b>i</b>
<b>List of publications</b>	<b>iii</b>
<b>Prelude</b>	<b>1</b>
<b>I Introduction</b>	<b>3</b>
<b>II Theoretical background</b>	<b>7</b>
II.1 The standard model and beyond . . . . .	7
II.1.1 What we know: the standard model . . . . .	7
II.1.2 Neutrino masses and mixings . . . . .	9
II.1.3 What we don't know: dark matter . . . . .	11
II.2 Cosmology and structure formation . . . . .	18
II.2.1 A brief thermal history of the Universe . . . . .	18
II.2.2 Particles in equilibrium . . . . .	19
II.2.3 Out of equilibrium thermodynamics . . . . .	20
II.2.4 Cosmological linear perturbation theory . . . . .	21
II.2.5 The matter power spectrum . . . . .	22
II.2.6 Impact of warm dark matter on structure formation . . . . .	23
II.2.6.1 Half-mode analysis . . . . .	25
II.2.6.2 Constraints from the Lyman- $\alpha$ forest . . . . .	26
II.2.6.3 Counting the number of Milky Way satellites . . . . .	27
II.3 Prelude . . . . .	29
<b>Main part I: dark matter at current and future colliders</b>	<b>31</b>
<b>III Collider studies of the scotogenic model</b>	<b>33</b>
III.1 Introduction . . . . .	33
III.2 Motivation . . . . .	34
III.3 The model and neutrino mass generation . . . . .	36
III.4 Projections for the HL-LHC . . . . .	38
III.4.1 Di-tau+ $\cancel{E}_T$ signature . . . . .	39
III.4.2 Di-lepton + $\cancel{E}_T$ signature . . . . .	42
III.5 Projections for future colliders . . . . .	44

III.5.1 FCC-hh . . . . .	44
III.5.2 CLIC . . . . .	45
III.6 Summary of Chapter III . . . . .	49
<b>Main part II: warm dark matter in cosmology: from models to a full picture</b>	<b>51</b>
<b>IV The scotogenic model and cosmology</b>	<b>53</b>
IV.1 Introduction . . . . .	53
IV.2 Light dark matter in the scotogenic model . . . . .	53
IV.2.1 Dark matter production mechanisms . . . . .	54
IV.3 Cosmological constraints . . . . .	56
IV.3.1 Constraints from structure formation . . . . .	56
IV.3.2 Constraints from additional radiation contribution . . . . .	60
IV.3.3 Constrains from big bang nucleosynthesis . . . . .	63
IV.4 Combining collider and cosmological limits . . . . .	64
IV.5 Summary of Chapter IV . . . . .	67
<b>V The cosmology of frozen-in axion-like particle dark matter</b>	<b>69</b>
V.1 Motivation . . . . .	69
V.2 The model setup . . . . .	70
V.2.1 Calculation of the momentum distribution function . . . . .	71
V.2.2 Axion-like particle properties and production . . . . .	76
V.3 Structure formation probes: Lyman- $\alpha$ forests and Milky Way satellites . . . . .	78
V.4 Suppressing production from misalignment and topological defects . . . . .	81
V.5 Structure formation limits on the model parameter space . . . . .	83
V.5.1 Results for the photophilic scenario . . . . .	83
V.5.2 Results for the photophobic scenario . . . . .	85
V.6 Summary of Chapter V . . . . .	90
V.7 Appendix of Chapter V . . . . .	91
V.7.1 Amplitudes for dark matter production channels . . . . .	91
V.7.1.1 Process A: $f\gamma \rightarrow fa$ . . . . .	91
V.7.1.2 Process B: $f\bar{f} \rightarrow \gamma a$ . . . . .	92
V.7.2 Calculating the cross section . . . . .	93
V.7.2.1 Cross section for process A . . . . .	95
V.7.2.2 Cross section for process B . . . . .	95
V.7.3 Impact of $N_{\text{sub}}$ on the mass limits . . . . .	96
<b>VI Two temperature dark matter: a general picture</b>	<b>99</b>
VI.1 Motivation . . . . .	99
VI.2 Setup of the framework . . . . .	100
VI.2.1 Decay parametrization . . . . .	101
VI.2.2 Decay modeling . . . . .	101

VI.3	Constraints on the model parameter space . . . . .	104
VI.3.1	Limits from additional radiation . . . . .	104
VI.3.2	Limits from structure formation . . . . .	105
VI.3.2.1	Lyman- $\alpha$ forest data . . . . .	107
VI.3.2.2	Number of Milky Way satellites . . . . .	108
VI.4	Detailed study of the parametrization . . . . .	108
VI.4.1	Non-thermalized parent particles . . . . .	109
VI.4.2	Impact of a variation in $g_*^s(T)$ during dark matter production . . . . .	110
VI.4.3	Three-body decays . . . . .	112
VI.5	Analytical fitting of the exclusion limits . . . . .	113
VI.6	Application to sample models . . . . .	115
VI.6.1	Model I: thermalized + out of equilibrium parents, constant $g_*^s(T)$ . . . . .	115
VI.6.2	Model II: thermalized + out of equilibrium parents . . . . .	115
VI.6.3	Model III: thermalized + frozen-in parents . . . . .	119
VI.6.4	Exploring the cold limit of the model parametrization . . . . .	120
VI.7	Summary of Chapter VI . . . . .	122
VI.8	Appendix of Chapter VI . . . . .	123
VI.8.1	Momentum distribution function of out of equilibrium parents . . . . .	123
VI.8.2	Momentum distribution function of never thermalized parents . . . . .	123
VI.8.3	Change in $\langle x \rangle$ due to $g_*^s(T)$ . . . . .	123
VI.8.4	Details on fitting procedure . . . . .	123
VI.8.5	Impact of $N_{\text{sub}}$ on the parameter limits . . . . .	125
	<b>Aftermath</b> . . . . .	<b>127</b>
	<b>VII Summary and conclusion</b> . . . . .	<b>129</b>
	<b>List of figures</b> . . . . .	<b>140</b>
	<b>List of tables</b> . . . . .	<b>142</b>
	<b>List of abbreviations</b> . . . . .	<b>143</b>
	<b>List of experiments and surveys</b> . . . . .	<b>144</b>
	<b>References</b> . . . . .	<b>165</b>





# Prelude





# Introduction

The standard model (SM) of particle physics is one of the most successful theories ever developed in the field of physics and is the framework for a wide variety of phenomena. It was developed and established in the 1960s [4–7] and contains all known particles and their interactions via the strong, weak and electromagnetic force. One crucial cornerstone is the Higgs boson [8–12]; a massive neutral scalar responsible for the generation of particle masses via its spontaneous symmetry breaking. It was a longstanding prediction of the SM and its final discovery at the ATLAS and CMS experiments at the LHC in 2012 [13, 14] marks a triumph of the predictive power of the SM. Besides this, the SM was further successfully tested in a wide variety of processes at the LHC and other colliders.

On the contrary, despite the confirmation of many predictions of the SM, there are several pressing open questions whose answers require physics beyond the existing framework, known as beyond the SM (BSM) physics. On the one hand, these problems arise from theoretical viewpoints and considerations, such as the hierarchy or naturalness problem of the different scales within the SM or the question why the strong interaction violates CP only minimally. On the other hand, there are experimental anomalies and observations that are not in agreement with the predictions of the SM. Examples include the observation of neutrino oscillations due to non-vanishing mass squared differences, the existence of an asymmetry between matter and antimatter, evidence for the existence of new physics through differences in decays of  $b$ -quarks (commonly referred to as  $b$ -anomalies), and last but not least, very strong cosmological evidence for the existence of dark matter (DM), which is one of the most pressing open questions in physics today.

So far, a wide range of different models has been proposed to extend the SM and address one or several of these open questions. The discussion ranges from simple SM extensions with gauge singlet particles to the introduction of entire new sectors with their own particles and interactions. A popular example for the latter case are supersymmetric extensions (SUSY) of the SM. In this thesis we explore the phenomenology of BSM models using the scotogenic model (ScM) and an axion-like particle (ALP) extension of the SM. In particular, we investigate the nature of the associated DM candidates. In Chapters III to V, we focus on these specific SM extensions, while in Chapter VI we present a model-independent parametrization to study non-thermally produced DM in a more general context.

We will use two complementary probes to test and constrain these BSM models. In the first direction, collider experiments for both  $pp$  and  $e^+e^-$  facilities will be used to search for signatures of the ScM in final states with missing transverse energy. The second approach, on the other hand, uses cosmological observations to study the influence of DM on the evolution of the early Universe and formation of structures.

Following the first avenue, particle colliders are a powerful tool to explore phenomenon in elementary particle physics at high energies. Colliding highly energetic particles essen-

tially creates a small “Big Bang” and the observation of the collision remnants allows us to unravel the physics at high energy scales which are otherwise difficult to access. These facilities, including the LHC, allow the SM to be measured very accurately and precisely and thus contribute significantly to our current understanding of particle physics by revealing numerous particles. Finally, these colliders open a window to the potential discovery of new physics, because collisions of highly energetic particles allow for a substantial production of new heavy states. Due to their large masses these new particles are in general only short-lived, i.e. they decay promptly into SM particles after their production. Either the decay products such as leptons or quarks are directly traceable, or can be only seen indirectly, if they are neutrinos or DM candidates. In addition, there are other possible decay topologies, for example new particles may travel a macroscopic distance from the interaction point before they decay.

However, this assumes that a BSM model couples sufficiently strong to the SM and its particle masses are at least couples of GeV in order to be detectable. If DM is light and/or only weakly coupled to the SM, or even worse, interacts only gravitationally, it cannot be discovered at colliders. In fact, despite their great potential, colliders have not reported any clear observation of new physics and complementary probes are needed to explore the phenomenology of BSM models. Instead of colliding highly-energetic particles, we can simply look at the stars instead: cosmological and astrophysical observations allow us to test DM scenarios which are not accessible at colliders. According to our current understanding, after its creation, the Universe underwent a phase of exponential expansion during which it increased dramatically in size. This phase of inflation left a nearly homogenous and flat Universe which was reheated after inflation ended. Afterwards, it kept expanding and its temperature decreased while it evolved in time. During its cooling, the Universe went through several important stages. In its early stage, these are the electroweak symmetry breaking and the quantum chromodynamics (QCD) phase transitions, as well as the formation of light nuclei. Later, the age of recombination follows, at the end of which the Universe becomes translucent; even today, we can perceive this afterglow in the form of the cosmic microwave background (CMB). Finally, the age of structure formation of galaxies and clusters follows.

Light DM present during some of these formative stages can leave an imprint which is observable today. For instance, the formation of light nuclei limits the number of relativistic particle species, as does the CMB which furthermore measures the total amount of DM. Surveys dedicated to unraveling the distribution of matter can be used to place constraints on the suppression of structure formation. This includes, for instance, the number of accompanying Milky Way (MW) dwarf galaxies.

In summary, there is an intriguing interplay between laboratory and cosmological probes of BSM models, as they offer complementary ways to probe the parameter space of new physics. Experiments at collider and accelerators can detect new particles either directly via resonances or indirectly via their effect on observables. Cosmology, on the other hand, constrains model features in a more general way, such as the mass of a new light DM candidate or the associated averaged momentum of its production mechanism.

This thesis is organized as follows. We start by briefly reviewing the SM and its open problems and present an introduction to the standard model of cosmology, the  $\Lambda$ CDM, and galactic structure formation in Chapter II. Then, in the first part of the thesis, we present dedicated collider searches. Focusing on two leptons ( $e$ ,  $\mu$  or  $\tau$ ) and missing transverse energy in the final state, we derive limits on the ScM in Chapter III. Afterwards, we turn towards the cosmological impact of light DM. Again, we consider the ScM, but derive cosmological limits based on the effective number of relativistic particle species, lifetime

---

bounds stemming from the abundance of light nuclei and suppression of small scale structures. We overlap them with the collider analysis results in Chapter IV. Chapter V is dedicated to warm axion-like particle DM produced in  $2 \rightarrow 2$  scattering and annihilation processes. We derive two complementary structure formation bounds for the case where the ALP couples either to photons or fermions only. We generalize our findings in Chapter VI where we develop a model-independent parametrization to consider the impact of DM produced at different times on the formation of galactic structures. This allows to easily adapt our approach for more specific models of light and “warm” DM. We summarize and conclude our results in Chapter VII.



# Theoretical background

## II.1 The standard model and beyond

Our journey begins with a brief review of the standard model of particle physics (SM). For a more comprehensive study we would like to point the reader to existing literature [15–18] and references therein. Following this chapter, we present another short review on the cosmological standard model and proceed with discussing open questions beyond the standard model (BSM), which are the main motivation behind this thesis.

### II.1.1 What we know: the standard model

The *standard model of particle physics*, or in short *standard model*<sup>1</sup>, emerged in the 70s after a stormy decade full of discoveries and newly found particles. It was established by the groundbreaking work of many people in the physics community [4–7] in order to structure and organize the “zoo of particles” which puzzled particle physicists for decades. Following its first formulation nearly all of its forecasts have been confirmed so far in a wide range of experiments and observations. The end of this road is marked by the important discovery of the so-called Higgs particle, the last cornerstone of the SM, by the two experimental collaborations ATLAS [13] and CMS [14] at the LHC in CERN.

The SM is a renormalizable quantum field theory which describes all known particle species and the three fundamental interactions among them: strong, weak and electromagnetic force, while gravity is not included in this framework. The backbone of the SM is the gauge group  $SU(3)_C \times SU(2)_L \times U(1)_Y$ , which contains a  $SU(3)_C$  color group of quantum chromodynamics (QCD) and the unification of the electroweak force in terms of a  $SU(2)_L$  subgroup for the weak isospin and a hypercharge  $U(1)_Y$  subgroup. The fermionic particle content of the SM is given by the following gauge group representations and charges:

	$SU(3)_C$	$SU(2)_L$	$U(1)_Y$
LH quarks $Q_L^i$	<b>3</b>	<b>2</b>	$\frac{1}{6}$
RH up-type quarks $u_R^i$	<b>3</b>	<b>1</b>	$\frac{2}{3}$
RH up-type quarks $d_R^i$	<b>3</b>	<b>1</b>	$-\frac{1}{3}$
LH leptons $\ell_L^i$	<b>1</b>	<b>2</b>	$-\frac{1}{2}$
RH charged leptons $e_R^i$	<b>1</b>	<b>1</b>	$-1$

Here,  $i = 1, 2, 3$  labels the three copies of each representation. The SM is a chiral gauge theory because left- and right-handed fermions are living in different gauge representations

<sup>1</sup> Not to be confused with the *cosmological standard model* which will be explained in the next section.

of the  $SU(2)_L \times U(1)_Y$  group. The right-handed (RH) fermions are singlets, while the left-handed (LH) particles are grouped in doublets,  $Q_L = (u_L^i, d_L^i)^T$  and  $\ell_L = (\nu_L^i, e_L^i)^T$ . Besides the fermions, the SM contains four additional bosons which acts as the interaction mediators. The strong force is mediated by eight color carrying gluons, while the electroweak force is carried by a charged  $W^\pm$  boson and 2 neutral bosons, the  $Z$  boson and the photon  $\gamma$ .

Finally, the SM contains a  $SU(2)_L$  doublet scalar field  $H$ , which transforms as  $(\mathbf{1}, \mathbf{2}, 1/2)$  under the SM gauge group and is commonly called the Higgs doublet. Its existence makes life much more interesting, because it acquires a vacuum expectation value (VEV) and spontaneously breaks the group  $SU(2)_L \times U(1)_Y$  down to electromagnetism (EM)  $U(1)_{\text{EM}}$ . This mechanism is the so-called Higgs mechanism which is crucial for the generation of mass terms for the otherwise massless SM particles [8–12]. The Higgs boson acts as an ultraviolet (UV)-completion of the electroweak theory, because it guarantees renormalizability at energies  $E \gtrsim 1$  TeV. The complex Higgs doublet can be decomposed as following,

$$H = \left( \begin{array}{c} G^+ \\ \frac{1}{\sqrt{2}}(h + v + iG_0) \end{array} \right), \quad (\text{II.1})$$

where  $v \approx 246$  GeV is the VEV of the Higgs,  $h$  the physical real Higgs scalar and  $G^+$ ,  $G_0$  are massless Goldstone bosons which become the longitudinal modes of the gauge bosons  $W^\pm$  and  $Z$  after electroweak symmetry breaking (EWSB). They acquire a mass term induced by their derivative coupling to the Higgs boson after EWSB, while the photon is the only remaining massless boson.

Additionally, the introduction of the Higgs doublet allows us to write down gauge invariant Yukawa interactions between LH and RH fermions,

$$\mathcal{L}_{\text{Yuk}} = -(y_e)_{ij} \bar{\ell}_L^i H e_R^j - (y_u)_{ij} \bar{Q}_L^i \tilde{H} u_R^j - (y_d)_{ij} \bar{Q}_L^i H d_R^j + h.c., \quad (\text{II.2})$$

where the  $(y_k)_{ij}$  are in general complex  $3 \times 3$  Yukawa matrices. For the up-type quark mass term, the quantity  $\tilde{H} \equiv i\sigma_2 H^*$ , where  $\sigma_2$  is the second Pauli matrix has to be used due to project out the correct component of the  $Q_L^i$  doublet for up-type quarks. After the Higgs gains a VEV, fermions acquire a mass via above Yukawa interactions. Substituting the  $SU(2)_L$  doublets, the following mass terms can be derived:

$$\mathcal{L}_{\text{Yuk}} \supset -(M_e)_{ij} \bar{e}_L^i e_R^j - (M_u)_{ij} \bar{u}_L^i u_R^j - (M_d)_{ij} \bar{d}_L^i d_R^j + h.c., \quad (\text{II.3})$$

where mass matrices  $M_f = y_f v / \sqrt{2}$ , ( $f = u, d, e$ ) are introduced. They can be diagonalized using a singular value decomposition by independently rotating the LH and RH fields by unitary  $3 \times 3$  matrices and one is left with nine real mass eigenstates (six quarks and three charged leptons) whereas the three neutrinos, or neutral leptons, stay massless in the SM. In the quark sector, the mass matrices can be diagonalized by transforming to the basis  $(u_L^i, d_L^i)$ ,

$$u_L^i = U_u^{ij} u_L^j, \quad d_L^i = U_d^{ij} d_L^j. \quad (\text{II.4})$$

In this basis, all SM quark currents except the  $W^\pm$  boson current,  $J_W^\mu$ , remain unchanged: it transforms to

$$J_W^\mu = \frac{1}{\sqrt{2}} \bar{u}_L^i \gamma^\mu d_L^i \quad \Rightarrow \quad \frac{1}{\sqrt{2}} \bar{u}_L^i \gamma^\mu (U_u^\dagger U_d) d_L^i \equiv \frac{1}{\sqrt{2}} \bar{u}_L^i \gamma^\mu V_{ij} d_L^i, \quad (\text{II.5})$$

where the unitary mixing matrix  $V_{ij}$  has been introduced, it is the *Cabibbo-Kobayashi-Maskawa* (CKM) matrix [19, 20]. Its off-diagonal entries are responsible for transitions between different quark families mediated by charged  $W$  bosons.



As a unitary matrix,  $V$  has  $3^2 = 9$  real parameters: six phases and three rotation angles. However, of these five phases can be absorbed by rotating the quark fields by global phases and only one CP violating phase is left.

On the contrary, the lepton sector does not contain such a mixing matrix, because there is no mass term for the neutrinos  $\nu_L^i$  and this additional freedom allows us to transform the LH neutrinos in the same way as  $e_L^i$  and so the would-be mixing matrix simply gives an identity matrix. Only after the  $\nu_L^i$  acquire a mass term via some mechanism beyond the SM is a leptonic mixing matrix, the so-called Pontecorvo-Maki-Nakagawa-Sakata matrix (PMNS) generated [21–23]. We will discuss ways to achieve a mass term for the neutrinos in Section II.1.2.

### II.1.2 Neutrino masses and mixings

As pointed out in the previous section, there is no way to generate a gauge invariant mass term for the neutrinos in the SM at renormalizable level and they are considered to be massless particles. However, measurements of the electron neutrino flux from the sun already done in the late 1960’s observed a flux deficit compared to the SM prediction [24]. This observation was later attributed to oscillations among the three neutrino states and confirmed by an independent measurement of atmospheric neutrinos [25]. While these experiments established that there are tiny, but non-zero, mass differences between the individual neutrino states, the absolute mass scale is still unknown and only an upper mass limit exists. Recent measurements of the end point of the energy spectrum of  $\beta$ -decay electrons by KATRIN using kinematic methods have brought the limit down to  $m_\nu < 1.1$  eV (90% CL) [26]. Further, observations of the cosmic microwave background (CMB) power spectrum and baryonic acoustic oscillations by the Planck collaboration point to even lower values on the sum of neutrino masses,<sup>2</sup>  $\sum m_\nu < 0.12$  eV (95% CL) [27]. Another experimental method is to search for neutrinoless double-beta decays, which places a limit on the effective mass down to  $m_{\beta\beta} \equiv |U_{ei}^2 m_\nu^i| < 0.11$  eV (see Ref. [28] for an overview), where  $U$  is the PMNS matrix.

Another open question is the ordering of neutrino masses. Since only the absolute size of two mass differences are known at the moment, there are two ways to arrange them. One is called the *normal* ordering where the two lighter neutrinos are close in mass and the heavy neutrino is separate. Flipping the mass spectrum such that the two heavier states are nearly mass degenerate is referred to as *inverted* ordering. At the moment, there is only a mild preference for the normal ordering scenario [29], but the exact nature is still under debate, and future experiments as the long baseline experiment DUNE are expected to settle the ordering discussion [30].

Neutrinos do not carry a charge under the SM gauge group and hence they are the only known particles which could have in principle a Majorana nature and this would allow for a Majorana mass term of the form (dropping flavor indices):

$$\mathcal{L}_m^M \supset -\frac{1}{2} m_L \bar{\nu}_L \nu_L^c, \quad (\text{II.6})$$

where the charge conjugation matrix  $C = i\gamma^2$  has been used and  $\nu_L^c \equiv C\nu_L^T$ . However, such an expression would break the global total lepton number of the SM by two units. There are ongoing efforts to look for neutrinoless double beta decays to look into the nature of neutrinos (see Ref. [31] for an overview).

Although there is no renormalizable expression to generate neutrino masses within the SM,

<sup>2</sup> Although this mass limit is one order of magnitude stronger than the KATRIN limit, it is not completely model independent but relies on assumptions about the cosmological history. In that sense the kinematically derived mass limit is more robust.

they can be created by a unique non-renormalizable dimension five operator, the *Weinberg operator* [32], by combining two bilinears  $\ell H$  in a gauge invariant way,  $\Lambda^{-1}(\bar{\ell}_L^c \tilde{H}^*)(\tilde{H}^\dagger \ell_L)$ . The scale  $\Lambda$  corresponds to a scale where new physical degrees of freedom have to be incorporated in the theory as well.<sup>3</sup> A simple way to explicitly realize the Weinberg operator at tree-level is the introduction of SM gauge singlets or RH neutrinos  $N_R^\alpha$ ,  $\alpha = (1, \dots, n)$ . This allows mass terms analogous to the Higgs mechanism by coupling the SM neutrinos with these new states by a new Yukawa coupling  $y_\nu$ ,

$$\mathcal{L}_{\text{BSM}} \supset -(y_\nu)_{i\alpha} \bar{\ell}_L^i \tilde{H} N_R^\alpha. \quad (\text{II.7})$$

Similar to charged leptons, after electroweak symmetry breaking, this term gives rise to a Dirac mass  $(m_D)_{i\alpha} \equiv (y_\nu)_{i\alpha} v / \sqrt{2}$  for the  $\nu_L^i$ , but the smallness of the neutrino masses of  $\mathcal{O}(1 \text{ eV})$  requires puzzlingly small couplings  $(y_\nu)_{i\alpha} \approx 10^{-11}$ , way smaller than the electron Yukawa couplings.

Including Majorana mass terms for the RH neutrino states paves the way to explain the tiny neutrino masses via the so-called (type-I) seesaw mechanism [33–35]. In this scenario, the SM Lagrangian is extended by the following terms

$$\mathcal{L}_{\text{BSM}} \supset -(Y_\nu)_{i\alpha} \bar{\ell}_L^i \tilde{H} N_R^\alpha - \frac{1}{2} (M_R)_{\alpha\beta} \bar{N}_R^\alpha (N_R^\beta)^c + h.c., \quad (\text{II.8})$$

where  $M_R$  is a  $n \times n$  Majorana mass matrix for the  $N_R^\alpha$ . In a basis  $(\nu_L^c, N_R)^T$  the mass terms can be rewritten in a compact form as

$$\mathcal{L}_m \supset -\frac{1}{2} (\bar{\nu}_L \quad \bar{N}_R^c) \begin{pmatrix} 0 & m_D \\ m_D^T & M_R \end{pmatrix} \begin{pmatrix} \nu_L^c \\ N_R \end{pmatrix} \equiv -\frac{1}{2} (\bar{\nu}_L \quad \bar{N}_R^c) \mathcal{M} \begin{pmatrix} \nu_L^c \\ N_R \end{pmatrix} + h.c.. \quad (\text{II.9})$$

For the sake of simplification flavor indices have been omitted. Diagonalizing this mass matrix gives rise to  $3+n$  Majorana neutrinos and its off-diagonal element  $m_D$  introduces a mixing among them. Now, the smallness of the  $\nu_L$  can be explained by “seesawing” them with a large right-handed neutrino mass  $M_R$ . In fact, in the seesaw limit, if one sets  $m_D$  to be at the weak scale while  $M_R$  is much larger, there are 3 light neutrinos with masses  $m_\nu \simeq -m_D M_R^{-1} m_D^T$  and  $n$  heavy neutrinos with masses  $\sim M_R$ , while the mixing among the light and heavy states are governed by a mixing angle  $\theta \simeq m_D M_R^{-1} \ll 1$ . In order to reproduce the experimental observed neutrino mass squared differences, at least two right-handed neutrinos are needed with masses of  $M_R^\alpha \sim 10^{14} \text{ GeV}$ , but apart from that there is no upper limit on their quantity  $n$ . Another attractive feature is the possibility to explain further problems of the SM within this framework. For example, the heavy right-handed neutrinos can be used to explain the observed matter-antimatter asymmetry in the Universe by the so-called *leptogenesis* mechanism [36, 37], a topic to which we will return briefly in Chapter III.

Besides the type-I seesaw, there are other possibilities to realize the Weinberg operator. For instance, in a similar spirit as the type-I, one can add a scalar  $SU(2)_L$  triplet instead of SM gauge singlets to generate neutrino masses as in the type-II seesaw [34, 38, 39] or employ a type-III seesaw scenario which comes with new fermion  $SU(2)_L$  triplets [40, 41]. Usually these tree-level realizations require heavy new states and/or small couplings to the SM, a fact which makes it hard to look for these new particles in experiments. An interesting alternative is to add new particles and interactions such that neutrino masses are generated radiatively at one-loop or even higher (see Ref. [42] for an overview). Because of additional loop suppression the new particle masses do not have to be extremely large and hence one can exploit already existing experiments to test this class of neutrino mass models. As an example we will discuss the so-called *scotogenic model* in Section V.2.

<sup>3</sup> In a similar way, the  $\beta$ -decay can be described by an effective four-fermion operator at low scales by integrating out the weak scale particles.

### II.1.3 What we don't know: dark matter

Another important, if not the most important, question unanswered in the SM is the existence of dark matter (DM), and answering this puzzle is one of the cornerstones of this thesis.

The nature of DM is a long standing open question with a long history spanning nearly a century (for a review on this topic we refer to Ref. [43]). Hints or indications of DM could be found on a wide range of length scales [44]. There are ideas that the observed phenomena can be explained by a modification of general relativity (GR). The most famous of these theories is the *Modified Newtonian Dynamics* model (MOND): it is an alteration of standard GR at large scales, such that the observed galactic rotation curves can be explained without the existence of DM. Currently, this theory is still lacking a conclusive general picture<sup>4</sup> and it is not easy to generalize this theory to incorporate relativistic effects.

Therefore, it is established that DM is a non-luminous type of matter which interacts at least gravitationally. Furthermore, it cannot be of baryonic origin, as gravitational microlensing searches for faint massive compact halo objects (MACHOs)<sup>5</sup> composed of ordinary matter found that only a small part of the observed DM amount could be in form of MACHOs [45, 46]. Another possible DM candidate are primordial black holes (PBH), which could explain the observed DM abundance, only if they are very light or very massive (see Ref. [47] for a recent overview). We know that DM make up 27% of today's energy budget of the Universe, whereas only 5% is visible matter and the rest is composed of “dark energy”, an even more mysterious component responsible for the accelerated expansion of the Universe. Taken together, dark energy expressed in terms of a cosmological constant  $\Lambda$ , cold dark matter (CDM), ordinary matter and radiation form the building blocks of the *cosmological standard model*, the  $\Lambda$ CDM.

First evidence for DM had been found by Zwicky in 1933 when he measured the velocity dispersion of the Coma cluster and found higher values than expected from luminous matter only [48]. On smaller galactic scales, the indication for DM was found in 1970 by Rubin and Ford who measured the circular velocity profile of stars and gas clouds, or rotation curve, of the Andromeda galaxy [49]. They observed an unexpected behavior of galactic rotation curves at large radii: instead of the expected  $1/\sqrt{r}$ , the curves tend to stay flat for a wide range of radii, indicating more matter than visible in the outer parts of galaxies. Further evidence was gathered in observations of the Bullet cluster which consists of two colliding galaxies [50, 51]. While the luminous parts of both galaxies were heavily affected and slowed down by the collision, gravitational lensing indicated that the bulk mass remained unaffected. Lastly, DM leaves an imprint on the largest scales as well, as can be inferred from anisotropies in the power spectrum of the cosmological microwave background (CMB). A study of these anisotropies allows to determine the total amount of cold dark matter in the Universe,  $\Omega_{\text{DM}}h^2 = 0.120 \pm 0.001$  [52]. Here “cold” means that the DM becomes non-relativistic before the epoch of structure formation, hence allowing for a fast collapse of DM clumps and birthing seeds for the latter formation of baryonic structures. If the DM stays relativistic at the beginning or during the early formation of structures, it will have finite free-streaming length below which small scale formation is delayed or completely erased. Such DM candidates are called “warm” or even “hot” DM and structure formation observables can place constraints on the “warmness” of DM as we will discuss in Section II.2.6. For example SM neutrinos can be considered as “hot” DM, but it turned out there are

<sup>4</sup> Fitting a variety of different rotation curves does not give one universal parameter, but rather one unique parameter for each galaxy observed.

<sup>5</sup> Examples include black holes, brown dwarfs, neutron stars and old white dwarfs.

too few of them to explain  $\Omega_{\text{DM}}h^2$  and furthermore it is not even possible to have neutrinos as DM, because this scenario would radically alter the formation of structures of small scales and hence light SM neutrinos can only constitute a subfraction of DM.

Although we have surprisingly exact knowledge about *how much* DM there is, we do not know *what* it is. We only know that DM has a gravitational interaction, is stable or has a lifetime larger than the age of the Universe, and is electrically neutral or at most, it could only carry a small fraction of the electric charge. There exists a large plethora of different DM models, each with its own set of DM candidate(s) and production mechanisms to reproduce the observed DM abundance and match the cosmological and astrophysical observations. In fact, the mass range of potential DM candidates spans several orders of magnitude. An upper bound of  $m_{\text{DM}} < 10^{18} M_{\odot}$  [47], where  $M_{\odot} \approx 2 \times 10^{30}$  kg denotes a solar mass, can be applied for DM in form of PBHs. From a particle physics point of view the upper mass bound for a DM particle is the Planck scale  $\sim 10^{19}$  GeV. On the other hand, lower mass bounds depend on the type of particles. Bosonic DM can be ultralight as long as the corresponding De Broglie wavelength  $\lambda \sim 1/m_{\text{DM}}$  is smaller than the size of dwarf galaxies. Observations of structure formation and the Lyman- $\alpha$  forest indicate a bound of  $m_{\text{DM}} \geq 10^{-21}$  eV [53]. On the other hand, the mass of fermionic DM is more severely constrained due to the Pauli exclusion principle blocking phase space occupation numbers for fermions, the so-called *Tremaine-Gunn* bound limit [54]. Analysis using Lyman- $\alpha$  data from dwarf galaxies yields  $m_{\text{DM}} \geq 70$  eV [55]. Even stronger mass limits, based on Lyman- $\alpha$  observations, can be derived for thermal DM whose mass must not fall below  $m_{\text{DM}} \geq 5.3$  keV [56], otherwise the structure formation on small scales will be too strongly affected. We will explain in particular this last mass limit in Section VI.3.2 in more detail.

In the following we briefly present a selection of possible DM candidates which are of importance for the considered mechanisms and models in this thesis.

- **WIMPs**

One simple model to answer the DM puzzle introduces a weakly interacting massive particle (WIMP) as a DM candidate which couples to some SM particles. Within this framework, DM thermalizes in the early Universe, because its coupling with SM particles keeps DM number density changing processes in equilibrium with each other. At some later point these processes become inefficient when their respective interaction rates are becoming smaller than the expansion rate of the Universe, characterized by the Hubble rate. Finally, the DM decouples chemically from the thermal plasma and its comoving number density stays constant until today. This DM production mechanism is called *thermal freeze-out* and it will play a role for DM production in Chapters IV and VI. Boltzmann equations are used to track the time evolution of the corresponding DM number density [57] which evaluates approximately to [58, 59]

$$\Omega_{\text{DM}}h^2 \simeq 0.12 \left( \frac{6 \times 10^{-28} \text{ cm}^3 \text{ s}^{-1}}{\langle \sigma v \rangle} \right) x_f, \quad (\text{II.10})$$

where  $\langle \sigma v \rangle$  denotes the corresponding thermally averaged cross section of the number density changing processes and  $x_f = m_{\chi}/T_f$  is the time at which DM drops out of equilibrium, or “freeze-out”; for WIMPs it evaluates to  $x_f \simeq 20$ . This numerical result for the DM abundance is the origin of the so-called “WIMP miracle”: WIMPs with masses between 10 GeV and a few TeV and approximately weak scale cross sections reproduce the observed DM abundance and are ideal candidates for CDM. For example, in supersymmetry (SUSY) models the lightest supersymmetric particle can constitute a WIMP DM candidate if it does not carry an EM charge.

In terms of experimental evidence, WIMPs have the pleasant property that there is a close relationship between the process responsible for thermal freeze-out and other open avenues to detect these kind of particles in experimental setups or observational surveys, and in the last few decades there had been tremendous experimental progress to search for WIMPs. The three different ways to detect WIMP DM are sketched in Fig. II.1 and they can be formulated flatly as “shake it, make it or break it”. The first process refers to direct detection by elastic or inelastic DM scattering off heavy atomic nuclei or electrons inside detector materials (see Ref. [60] for an overview). The recoiling scattering partners would then leave a trace inside the detector which can be observed [61]. At the moment, leading limits are set by the XENON1T experiment which uses liquid Xenon as their target medium. It can probe WIMP DM with masses between a few GeV up to 1 TeV and excludes spin independent nucleon cross sections down to  $\sigma_{SI} \gtrsim 4 \times 10^{-47} \text{ cm}^2$  [62]. Probing WIMP DM at smaller masses require different experimental setups and analysis techniques. For example, doing a *S2 only* analysis,<sup>6</sup> masses down to 60 MeV can be probed by XENON1T measuring electronic recoils [63]. Even lower masses can be reached by searches for electron recoils in cryogenic solid-state detectors and experiments like CRESST-III [64] and SuperCDMS [65] may reach masses down to  $m_{DM} \simeq 1 \text{ MeV}$ . Finally, the sub-MeV mass range can be explored by experiments like SENSEI, which uses a skipper-charged-coupled-device to search for low energy electron recoils [66].

Indirect detection of DM searches for SM remnants, like photons, neutrinos,  $e^\pm$  or protons and antiprotons, produced in regions with a high DM concentration by the same annihilation processes that also fix the DM relic density. These annihilation channels could produce distinctive signatures such as highly energetic neutrinos produced in the sun, or gamma-rays from the center of the Milky Way (MW). For instance, IceCube searched for high energy neutrinos coming from DM annihilation processes in the sun [67] or the galactic core [68]. Dedicated DM annihilation gamma-ray searches were performed by Fermi-LAT, H.E.S.S. and MAGIC, observing dwarf spheroidal galaxies of the MW [69, 70] or its galactic center [71].

Lastly, inverting the annihilation process, DM can be pair-produced by accelerating and colliding highly energetic SM particles. After their production, the DM particles escape the detectors without any visible trace, leaving a missing energy signature which can be measured. Hence, dedicated DM searches at colliders exploit recoiling SM particles such as photons [72, 73] or jets [74, 75].

However, despite all the experimental efforts so far, no conclusive positive WIMP DM

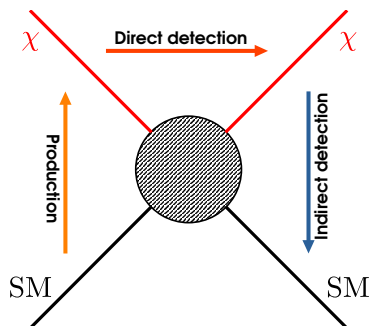


Figure II.1: The trinity of DM detection: production of DM with highly energetic beams at colliders, direct detection of DM scattering events inside detectors and searches for decay products from DM annihilation processes. The circle in the middle represents an unspecified effective coupling between two DM particles  $\chi$  and SM particles.

<sup>6</sup> Here, S2 refers to a secondary scintillation signal, in contrast to the prompt signal S1. Most analysis use both signals for a better discrimination between DM candidates and background events.

signals had been found and there exist strong exclusion limits on the masses and interactions of this DM candidate. Although it does not mean that WIMP DM can be considered “dead” or ruled out, it is definitely challenging the WIMP paradigm and new DM models and production mechanisms are studied going beyond the thermal freeze-out scenario. Interesting alternatives include for example a non-thermal DM production by decays or scatterings of thermal bath particles [76], production by decaying topological effects [77] or the introduction of entire dark sectors with new number-changing processes [78, 79]. Some of these beyond-WIMP avenues will be explored in this thesis.

- **Sterile neutrinos**

As already pointed out in Section II.1.2, right-handed neutrinos are a well-motivated extension of the SM. They are gauge singlets and therefore do not weakly interact, hence they are often called “sterile” neutrinos in contrast to the “active” LH SM neutrinos. In addition to their role in neutrino mass generation, they may also serve as an interesting DM candidate, an idea which was already put forward over two decades ago [80] (see Refs. [81, 82] for an overview).

A simple sterile neutrino production is the so-called *Dodelson-Widrow* mechanism [80]. It is a freeze-in mechanism, i.e. compared to the previously discussed WIMP production, this DM candidate is only weakly coupled and does not thermalize with the SM plasma in the early Universe. Its abundance is not determined by a decoupling from the plasma but is instead produced via a small mixing  $\vartheta$  between the sterile and the active neutrino states. Thus larger couplings yields larger DM abundances, as opposed to a freeze-out, where stronger couplings keeps DM longer in thermal equilibrium and deplete the abundance. If a SM neutrino flavor eigenstate is produced in the early Universe, it will contain an admixture of a sterile state proportional to  $\vartheta$ . As it travels, it can scatter coherently with weakly charged particles and by doing so it acquires an effective mass and thus an effective mixing angle based on the vacuum angle  $\vartheta$  arises [83],

$$\sin^2(2\vartheta_m) = \frac{\Delta^2(p) \sin^2(2\vartheta)}{\Delta^2(p) \sin^2(2\vartheta) + (\Delta(p) \cos(2\vartheta) - V^D - V^T(p))^2}. \quad (\text{II.11})$$

Here,  $\Delta(p) = \Delta m^2/(2p)$  is set by the vacuum mass splitting between neutrino mass eigenstates, and matter effects are separated into finite density and temperature potentials,  $V^D$  and  $V^T$ . If the SM neutrino experiences a energy or momentum changing scattering, i.e. a measurement, the sterile neutrino eigenstate will be projected out with a probability  $\propto \sin^2(2\vartheta_m)$ . If there is no resonant enhancement, the resulting sterile neutrino abundance will be set by the relation [83]

$$\Omega_{\text{DM}} h^2 \approx 0.3 \left( \frac{\sin^2(2\vartheta_m)}{10^{-10}} \right) \left( \frac{m_s}{100 \text{ keV}} \right)^2. \quad (\text{II.12})$$

In order to explain the relic density with not too large mixing angles, sterile neutrinos need a mass of at least  $\mathcal{O}(\text{keV})$  which is also required by the aforementioned Tremaine-Gunn bound.<sup>7</sup> The same mixing angles also controls back-reactions of sterile neutrinos. Precisely, they decay mainly into three neutrinos at tree level,  $\nu_s \rightarrow \nu\nu\nu$ , and their lifetime  $\tau$  is given by [82]

$$\tau = \Gamma(\nu_s \rightarrow 3\nu)^{-1} = 1.5 \times 10^{14} \text{ s} \left( \frac{10 \text{ keV}}{m_s} \right)^5 \frac{1}{\vartheta^2}, \quad (\text{II.13})$$

<sup>7</sup> An anomalous neutrino flux excess in short baseline experiments may hint to an additional sterile neutrino state with mass  $\mathcal{O}(\text{eV})$  [84]. Although these might be a potential sign for new physics, the best fit parameters for this sterile neutrino are in conflict with cosmological observations, i.e. they give a too large mixing angle. New measurement results published by the MicroBooNE experiment, however, could not verify this anomalous excess [85].

where  $\bar{\vartheta}^2 \equiv \sum_{\alpha} |\vartheta_{\alpha}|^2$ . Requiring it to be larger than the lifetime of the Universe,  $\tau_U \approx 4.3 \times 10^{17}$  s, places an upper bound on the mixing angle. Stronger constraints can be derived from sub-dominant radiative decays,  $\nu_s \rightarrow \nu \gamma$ , whose decay rates are given by [86–88]

$$\Gamma(\nu_s \rightarrow \gamma \nu) = 1.38 \times 10^{-29} \text{ s}^{-1} \left( \frac{\sin^2(2\vartheta)}{10^{-10}} \right) \left( \frac{m_s}{\text{keV}} \right)^5. \quad (\text{II.14})$$

It would leave a potentially visible peak in the gamma-ray spectrum at energies half the DM mass [89]. Dedicated surveys have been done to look for signals in the energy range between keV and MeV, such as XMM-Newton [90], Suzaku [91], Fermi-LAT [92] and NuStar [88]. Interestingly, several experiments have found an unidentified line feature at an energy of  $\sim 3.55$  keV in the gamma-ray spectra of galaxy clusters [93], the Andromeda [94] and the MW galaxy [95] with a formal statistical significance above  $5\sigma$  [94]. This sparked some interest in keV-scale neutrino DM, because it can be attributed to decays of sterile neutrinos with mass 7.1 keV and an accordingly chosen mixing angle. However, this line could not be found in all surveys looking at DM-dominated regions of space and up to date there is no conclusive interpretation, since this gamma-ray line could origin from atomic transitions in gas clouds instead (for a detailed discussion see Ref. [96] and Refs. [97, 98]). The next generation of gamma-ray experiments will definitely shed more light onto this question.

Nevertheless, ongoing and past gamma-ray surveys together with bounds from structure formation have placed strong constraints on the mass-mixing angle plane and the simple Dodelson-Widrow mechanism is now completely ruled out in the favored mass range [88, 99]. One way to circumvent this gamma-ray bounds is to introduce an effective background caused by a lepton asymmetry to allow for a resonantly enhanced production rate even with small mixing angles [100], similarly to the *Mikheyev-Smirnov-Wolfenstein* (MSW) [101, 102] seen in neutrino oscillations inside matter. If sterile neutrinos are added with an entire dark sector, there is the possibility to protect them from decaying into visible gamma-rays by charging them and the other dark sector particles under a discrete symmetry, for instance a  $\mathbf{Z}_2$  [2, 103]. An interesting model is the *neutrino minimal standard model* ( $\nu$ MSSM) [104, 105]. It extends the SM by three additional RH neutrinos and two of them explain the observed mass squared differences of the active neutrinos and provide an explanation for a non-vanishing lepton asymmetry, while the third one serves as a keV-scale DM candidate.

A non-thermal production of sterile neutrino DM is also possible via decays of parent particle, either while they are in thermal equilibrium or at later times and already frozen-out. Compared to the production via active-sterile mixing, a decay production allows for larger sterile neutrinos masses even above the electroweak scale. For instance they are produced by decays of SM particles, such as pions [106], the Higgs boson [107] or vector bosons [108], but these production modes are subdominant compared to the freeze-in via aforementioned mixing angle. Enhancing this idea further, new models with particles coupled to sterile neutrinos have been proposed in order to achieve a sizeable production via decays. Examples include a scalar singlet coupled via a Yukawa interaction to  $\nu_s$  [109–111] or an additional Higgs doublet [112, 113]. We will explore and discuss an example for the latter possibility in more details in Chapter III.

If DM is made up by keV-scale sterile neutrinos, this would indicate a deviation from  $\Lambda$ CDM, because the DM is not necessarily cold anymore and would be called “warm” DM (WDM) (see for example [80, 100, 114]). In contrast to CDM, WDM is relativistic when it is produced, for instance by decays of thermal bath particles, but becomes non-relativistic before matter-radiation equality. This property changes the formation of structures in the early Universe, as relativistic WDM do not clump together at these early times as compared to non-relativistic CDM and hence structures are washed out below a non-vanishing

free-streaming length [58, 115],

$$\lambda_{\text{FS}} = \int_{t_i}^t dt' \frac{v(t')}{a(t')} \approx 1 \text{ Mpc} \left( \frac{1 \text{ keV}}{m_s} \right) \frac{T_{\text{DM}}}{T}, \quad (\text{II.15})$$

where  $T_{\text{DM}}$  is the corresponding WDM temperature.<sup>8</sup> There are several options to search for the impact of WDM on the formation of structures: first, a measurement of the matter power spectrum at different scales, for instance using the so-called Lyman- $\alpha$  forest or the 21 cm absorption line spectroscopy, counting the number of observed collapsed structures such as dwarf galaxies (or quasars) and compare them against WDM predictions. Last but not least, one can use the matter distribution inside DM dominated objects to place constraints. We will elaborate further on these techniques in Section II.2.

- **Axions and axion-like particles**

Another way to realize DM is via axion-like particles (ALP). Since they are neutral scalars or pseudo-scalars, the Tremaine-Gunn bound does not apply for them and they can explain the DM relic density with even lighter masses compared to sterile neutrinos. They can be associated to a spontaneous breaking of a global  $U(1)$  symmetry. It gives rise to massless Nambu-Goldstone bosons (NGB) and if there is a small explicit symmetry breaking, they acquire a mass and are called pseudo-NGBs. Their coupling to the SM is inversely proportional to a decay constant  $f$  which in turn is linked to the scale of symmetry breaking. Usually the symmetry breaking takes place at very high scales and therefore these light states couple only weakly to the SM. Usually, the expression “axion” is used for the pseudo-NGB associated to the spontaneously broken Peccei-Quinn  $U(1)_{\text{PQ}}$  symmetry which is a possible solution to the strong CP problem in QCD. This problem is a matter of naturalness: the QCD Lagrangian allows to define a CP violating term, the so-called  $\theta$  term, of the following form,

$$\mathcal{L}_\theta = \theta \frac{g_s^2}{32\pi^2} G_{\mu\nu,a} \tilde{G}^{\mu\nu,a}, \quad (\text{II.16})$$

where  $G^{\mu\nu}/\tilde{G}^{\mu\nu}$  is the field strength tensor and its dual. Although the term can be written as a total derivative, it has to be kept in the Lagrangian, because it is related to the QCD vacuum structure and corresponding instanton effects. Due to the chiral anomaly, the quark fields can be rotated  $q \rightarrow e^{i\alpha\gamma_5} q$  and this changes the  $\theta$  value into  $\bar{\theta} = \theta + \arg \det(M_q)$ ; a quantity which can be physically measured in the electric dipole moment (EDM) of the neutron [116, 117]. A recent measurement of the EDM indicates that  $\bar{\theta} < 5 \times 10^{-12}$  (90% CL) [118], a puzzingly small number compared to the technical natural choice  $\theta \approx \mathcal{O}(1)$ . A solution is to introduce the axion, a dynamical pseudo-scalar field  $\phi_a$  characterized by its decay constant  $f_a$ . It features an additional coupling to  $G\tilde{G}$  such that Eq. (II.16) is modified to

$$\mathcal{L}_\theta = \frac{g_s^2}{32\pi^2} \left( \bar{\theta} + \frac{\phi_a}{f_a} \right) G_{\mu\nu,a} \tilde{G}^{\mu\nu,a}. \quad (\text{II.17})$$

The axion field  $\phi_a$  is the NGB of a broken  $U(1)_{\text{PQ}}$  symmetry [119, 120]. Including the effects of the QCD anomaly, there is an effective potential for the axion field given by  $V_{\text{eff}} \sim \cos \left( \bar{\theta} + \frac{\langle \phi_a \rangle}{f_a} \right)$  [121], that means the effective potential is minimized if the axion

<sup>8</sup>In principle, for scenarios with only a single DM production mechanism, the free-streaming length can be used to quantify the “warmness” of the DM candidate. For example, DM with  $\lambda_{\text{FS}} < 0.01$  Mpc can be designated as “hot” and with lengths above as “warm”. In the following, however, we will not make use of such a definition because the models we will study feature multiple DM production mechanisms.



acquires a VEV that cancels the  $\bar{\theta}$  exactly. This explains the observed smallness of the CP violation in the strong sector.

The corresponding axion mass,  $m_a$ , calculated in chiral perturbation theory is given by [122, 123]

$$m_a \approx 6 \text{ meV} \left( \frac{10^9 \text{ GeV}}{f_a/C} \right), \quad (\text{II.18})$$

where the integer valued  $C$  is the color anomaly of the PQ symmetry. The decay constant and mass of a QCD axion are related to each other and fixed by Eq. (II.18). On the contrary, generalized ALPs do not have to fulfill this relation and they have a larger available parameter space for  $f_a$  and  $m_a$  which can be tested and constrained by a plethora of various laboratory, astrophysical and cosmological probes (see Ref. [124] for an overview) by exploiting that ALPs couple to SM particles via the following Lagrangian

$$\mathcal{L}_a = -\frac{c_{aXX}}{4f_a} X_{\mu\nu} \tilde{X}^{\mu\nu} \phi_a + \frac{c_{aff}}{f_a} \partial_\mu \phi_a \bar{f} \gamma^\mu \gamma_5 f, \quad (\text{II.19})$$

where  $f$  denotes a SM fermion and  $X^{\mu\nu}$  is an arbitrary field strength tensor. For example, there are dedicated collider analysis searching for heavy ALPs decaying into a pair of SM particles or missing energy signatures due to ALPs in the final state [125]. “Light shining through a wall” experiments such as the Any Light Particle Search (ALPS) [126] use strong magnetic fields to convert photons into axions which then travel freely through a wall and are converted back into photons. Another set of tools are helioscopes such as CAST [127]. They rely on axion production inside the sun and converting them into a photon in a magnetic field at the earth. Recently, low-energy electronic recoil data released by XENON1T has shown an excess of recoil events at energies between 2 – 3 keV [128]. One explanation are solar axions produced in the sun, traveling to the detector and recoiling against electrons inside it [128, 129], but the best fit parameters for this models are severely in tension with stellar constraints [130] and the excess may be caused by a contamination of the target material with unaccounted radioactive sources. Other astrophysical bounds stem from the ratio of horizontal branch (HB) stars to red giants in galactic globular clusters [131]. Axion conversion inside star cores would lead to an energy loss and an observable lifetime of HB stars. All these examples do not rely on the assumption that all of DM consists of ALPs. If DM consists of an ALP, there will be more experimental constraints on the parameter space, for example from haloscope searches [132]. They use a cavity to resonantly enhance the conversion rate of an axion into a photon which can then be detected. Similarly to sterile neutrinos, ALP DM can leave a detectable signal in gamma-ray spectra from decays  $\phi_a \rightarrow \gamma\gamma$ . Finally, analyzing the acoustic peaks and anisotropies of the CMB matter power spectrum constrain ALPs at really low masses,  $m_a \lesssim 10^{-25}$  eV [133, 134].

The details of ALP DM production, for instance if it is produced during or after inflation, depends on the specific model, but a convenient way to produce ALP DM non-thermally is via the misalignment mechanism [135]. In the early Universe, the axion field is elongated at some initial value  $\phi_a^i$  and frozen due to strong Hubble friction. Once the Hubble rate become comparable to the axion mass, it starts to roll down its potential and oscillates around its minimum. This oscillations give the same behavior as non-relativistic matter and hence, despite its low mass, this axion DM can be considered CDM. If the PQ symmetry is broken before the end of inflation, the axion abundance is given by [136]

$$\Omega_a h^2 \approx 0.12 \left( \frac{m_a}{54 \text{ eV}} \right)^{1/2} \left( \frac{f_a \phi_a^i}{10^{11} \text{ GeV}} \right) \mathcal{F}(T_1), \quad (\text{II.20})$$

where  $\mathcal{F}(T_1)$  is a smooth function of  $\mathcal{O}(1)$  evaluated at temperature  $T_1$  set by the criterion  $3H(T_1) \equiv m_a$ . Other non-thermal mechanisms to produce ALP DM will be discussed in Chapter V.

## II.2 Cosmology and structure formation

Over the past decades there had been a tremendous progress in understanding the evolution of our Universe from its hot epoch shortly after the big bang until its much cooler state today. All this information is condensed in one single model, which can explain several key observations such as the existence of the cosmological microwave background (CMB), the formation and abundance of light nuclei (like deuterium, Helium and Lithium), the observed large scale galactic structure or distribution of matter and the accelerated expansion of the Universe. This model is the  $\Lambda$ CDM model, and it is the simplest model to account for these observations. This model describes the Universe as almost flat, homogeneous and expanding by a *Friedmann-Robertson-Walker* (FRW) metric. Today, it consists mainly of collisionless cold dark matter, a small amount of baryonic matter and an even smaller radiation contribution. Besides that it also contains dark energy which is thought to be responsible for a non-vanishing cosmological constant  $\Lambda$ .

In the following we assume that the reader is at least familiar with the basic principles of cosmology and we only very briefly repeat some details. Instead we focus on an introduction into the topic of formation of structures within linear perturbation theory, because this paves the road for some methods used in Chapter III. We refer the interested reader to [58, 59, 137] for an introduction into cosmology and the formation of structures.

### II.2.1 A brief thermal history of the Universe

The origin of our Universe we live in is still one of (if not *the*) biggest mysteries of physics. It is believed it had been formed in a big bang out of a single singularity. Although our current picture does not offer an explanation for its starting point, extrapolating our knowledge back allows for a surprisingly accurate understanding of the early epoch directly after the big bang. At these times the Universe was totally different compared to today: it consisted of a hot and dense thermal plasma of rapidly interacting particles without any visible structures at all. Very simplistic the Universe can be understood as an expanding fluid which cools down over time.

Its composition in terms of energy densities is expressed in the first Friedmann equation:

$$\frac{H^2(R)}{h^2} = \Omega_r R^{-4} + \Omega_m R^{-3} + \Omega_k R^{-2} + \Omega_\Lambda, \quad \text{where } \Omega_X \equiv \frac{\rho_X}{\rho_{\text{crit}}}. \quad (\text{II.21})$$

Here,  $R$  is the scale factor, a quantity which can be used to track the time evolution of the Universe,<sup>9</sup>  $H(R)$  is the Hubble factor  $H(R) \equiv \dot{R}/R$  and  $h$  is the Hubble constant. Moreover, we introduced dimensionless density parameters  $\Omega_i$  with respect to the critical energy density  $\rho_c$  for radiation, matter, curvature<sup>10</sup> and dark energy. Since each of the individual components scale differently with  $R$ , there are times in the Universe where only one of the components dominates. In the early epoch, radiation is dominating, but since it falls off quicker compared to the other ingredients, matter starts to take over after a certain time (often called *matter-radiation equality*). Finally, the dark energy contribution will dominate over matter in the latter stage of the Universe until today.<sup>11</sup>

<sup>9</sup> Another convenient time variable is the redshift  $z$ . It stems from observations of distant objects and acts as a distance measure in that sense. It is related to  $a$  by  $1 + z = 1/R$ .

<sup>10</sup> We included this expression for the sake of completeness only. In the following we assume that  $\Omega_k = 0$ .

<sup>11</sup> At the moment it is not clear, whether  $\Omega_\Lambda$  will stay constant forever, or may show a slow dynamics. Its behavior will govern the future evolution of our Universe

## II.2.2 Particles in equilibrium

The early Universe is characterized by high temperatures and densities, and all SM particle species are in thermal, i.e. chemical and kinetic, equilibrium with each other. Together they form a thermal plasma. Any new BSM particle will be part of it if its interaction with the plasma, specified by an interaction rate  $\Gamma$ , is large enough.

If  $\Gamma$  is larger than  $H$ , particles will interact very rapidly compared to the expansion time scale and thus are kept in thermal equilibrium. As the Universe expands throughout time, it cools down and  $\Gamma$  decrease faster than  $H$ . At the point where  $\Gamma \sim H$  the interaction rates are not fast enough anymore to keep these particle species in equilibrium and they decouple from the thermal plasma. In general, all particle species decouple at different times, characterized by the size of  $\Gamma$ , and weakly coupled particles will decouple earlier.

To describe the macroscopic behavior of microscopic particles in the early Universe, methods and techniques of statistical mechanics are used. A dilute, weakly interacting gas of particles is characterized by its number density  $n$ , energy density  $\rho$  and pressure  $P$ . These quantities depend on the distribution of particles in momentum space, as encoded in the corresponding momentum (or phase space) distribution function  $f(|\mathbf{p}|, t)$ .<sup>12</sup> For a given particle distribution function,  $f(p, t)$ , its properties are given by:

$$n(t) = \frac{g}{(2\pi)^3} \int d^3p f(p, t), \quad (\text{II.22})$$

$$\rho(t) = \frac{g}{(2\pi)^3} \int d^3p E(p) f(p, t), \quad (\text{II.23})$$

$$P(t) = \frac{g}{(2\pi)^3} \int d^3p \frac{|\mathbf{p}|^2}{3E(p)} f(p, t), \quad (\text{II.24})$$

where  $g$  denotes the internal degrees of freedom (DOF) of the particle in question. If particles exchange energy and momentum effectively via scattering off the thermal plasma, they will be in kinetic equilibrium and in that case  $f(p, t)$  will be given by

$$f(p, t) = \frac{1}{\exp[(E(p) - \mu)/T] \pm 1} \stackrel{\text{low } T}{\Rightarrow} f(p, t) \approx e^{-(E(p) - \mu)/T}, \quad (\text{II.25})$$

with a Fermi-Dirac (upper sign) for fermions or a Bose-Einstein distribution (lower sign) for bosons. Here,  $\mu$  is the chemical potential of the particle species. If particles are in chemical equilibrium, i.e. they equally react back and forth, their chemical potentials will be related to each other. However, at early times they are negligible compared to  $E$ ,  $\mu \ll T$ . If particles are in thermal equilibrium, they will share a common temperature, usually called ‘‘temperature of the Universe’’.<sup>13</sup>

Considering the total energy density of the Universe, it is a good approximation to include relativistic particles only, because  $\rho$  is exponentially suppressed for non-relativistic particles. In that case, the sum over all relativistic species yields

$$\rho_r = \sum_i \rho_i \equiv \frac{\pi^2}{30} g_*(T) T^4, \quad (\text{II.26})$$

where  $T$  is the photon temperature and  $g_*(T)$  is the effective number of relativistic DOF, defined as

$$g_*(T) = \sum_{\text{bosons}} g_i \left( \frac{T_i}{T} \right)^4 + \frac{7}{8} \sum_{\text{fermions}} g_i \left( \frac{T_i}{T} \right)^4. \quad (\text{II.27})$$

<sup>12</sup> Since the Universe is isotropic and spatially homogenous, it only depends on the absolute value of the momentum,  $|\mathbf{p}| = p$ .

<sup>13</sup> Often, this is called photon temperature instead, since photons are the only relativistic thermal bath particles left in Universe today, whereas all other particles have become non-relativistic way earlier.

$T_i$  is the temperature for each species which can be different from the photon temperature if the species is not coupled anymore to the thermal bath. We will discuss examples for this in Chapter VI. At high temperatures all SM particles are in thermal equilibrium and  $g_*(T) = 106.75$ . As temperature drops, various particle species become non-relativistic and  $g_*(T)$  decreases.

In a radiation dominated Universe, Eq. (II.26) allows to relate temperature and time via the Friedmann equation for  $H(t)$ ,

$$H(t) = \frac{1}{2t} = \sqrt{\frac{8\pi}{3M_{\text{Pl}}^2} \rho_r} \simeq 1.66 \sqrt{g_*(T)} \frac{T^2}{M_{\text{Pl}}}, \quad (\text{II.28})$$

where  $M_{\text{Pl}} \simeq 1.22 \times 10^{19}$  GeV is the Planck mass. Another important quantity is the entropy of the Universe. Since the Universe expands approximately adiabatic, the entropy stays constant and one can define an entropy density  $s$  by

$$s = \sum_i \frac{\rho_i + p_i}{T_i} \equiv \frac{2\pi^2}{45} g_*^s(T) T^3, \quad (\text{II.29})$$

where  $g_*^s(T)$  is the effective number of entropic DOF. In our subsequent analysis in Chapters IV to VI we will use an analytical expression for the DOF (see Appendix of Ref. [135]):

$$g_*^s \left( \frac{T}{\text{GeV}} \right) = \exp \left[ c_0 + \sum_{i=1}^5 c_1^i \left( 1 + \tanh \frac{T - c_2^i}{c_3^i} \right) \right], \quad (\text{II.30})$$

$$c_0 = 1.36,$$

$$c_1 = (0.498, 0.327, 0.579, 0.140, 0.109),$$

$$c_2 = (-8.74, -2.89, 1.79, -0.102, 3.82),$$

$$c_3 = (0.693, 1.01, 0.155, 0.963, 0.907).$$

Entropy conservation implies  $s R^3 \propto g_*^s(T) T^3 R^3 = \text{const}$ . That means, away from particle thresholds, the thermal plasma cools down as  $T \propto R^{-1}$ . On the contrary, if particles drop out of thermal equilibrium, conservation of entropy implies a reheating of the remaining bath, due to a decrease in  $g_*^s(T)$ . For example, SM neutrinos have a slightly colder temperature compared to the photon bath, because they had decoupled before the entropy in electron-positron pairs has been transferred to the remaining photons.

In the latter chapters, it will be convenient to calculate the DM abundance  $\Omega_{\text{DM}} h^2$  by integrating the corresponding momentum distribution function  $f(p, t)$  over all momenta and normalize it by the entropy density [58],

$$\Omega_{\text{DM}} h^2 = \frac{s_0 m_{\text{DM}}}{\rho_c / h^2} \left( \frac{45}{4\pi^4 T^3 g_*(T_{\text{prod}})} \int_0^\infty dp p^2 f(p, t_0) \right), \quad (\text{II.31})$$

where  $f(p, t_0)$  is evaluated today; the entropy density is  $s_0 = 2891.2 \text{ cm}^{-3}$  [138] and the critical density is given by  $\rho_c = 1.054 \times 10^{-2} \text{ MeV cm}^{-3} h^2$  [138].

### II.2.3 Out of equilibrium thermodynamics

If the Universe had been in thermal equilibrium from its beginning until present days, it essentially would have been an empty place, since there would have been no formation of structures. Deviations from equilibrium, i.e. decouplings from thermal plasma indicated by  $H \ll \Gamma$ , are thus a necessity.

In order to track the evolution of a particle's momentum distribution function  $f(E, t)$  a Boltzmann equation has to be defined. In its most general form it is given by

$$\hat{\mathbf{L}}[f] = \hat{\mathbf{C}}[f]. \quad (\text{II.32})$$

$\hat{\mathbf{L}}[f]$  is the Liouville operator, describing the evolution of  $f$  due to gravitational forces and the collision operator  $\hat{\mathbf{C}}[f]$  inhibits particle number changing processes. For a FRW metric, it can be rewritten in terms of the number density as

$$\dot{n} + 3Hn = \frac{g}{(2\pi)^3} \int \frac{d^3p}{E} \hat{\mathbf{C}}[f]. \quad (\text{II.33})$$

In case of no number-changing collision processes the r.h.s is zero and  $n$  is simply proportional to  $R^{-3}$  as the Universe expands.

The exact form of the collision operator is determined by the particle physics model and depending on the size of the interactions; there are a lot of different possibilities how  $n(t)$  evolves throughout time. For example, as explained in Section II.1.3, WIMPs are coupled to the thermal plasma in the early Universe but freeze-out at a later time. On the other hand, we will see other possibilities in Chapters IV to VI, where particles are never in thermal equilibrium and their abundance will *freeze-in* instead [76].

## II.2.4 Cosmological linear perturbation theory

The CMB is remarkably isotropic and only small anisotropies have been observed, i.e. the Universe had been nearly smooth at these times. Today this is still true at scales larger than galactic clusters, i.e. above 100 Mpc, but at the scale below this is certainly not true anymore as there are large differences in the observed energy densities. The question is how this density fluctuations arose between the CMB epoch and today.

It can be explained by the phenomenon of gravitational instability: as matter is attracted by regions of high-density it starts to collapse and increase the density of these regions even further. To illustrate this effect in the following, we restrict our discussion on Newtonian dynamics to highlight some of the key features of the growth of structures.

A perfect fluid is described by seven characteristics: energy density  $\rho$ , pressure  $P$ , entropy  $S$ , gravitational potential  $\Phi$  and the three-dimensional local fluid velocity  $\mathbf{v}$ . Considering only slight and adiabatic, i.e. spatially constant, perturbations of these quantities, a linear expansion in these disturbances can be done. It is convenient to define a fractional density fluctuation with respect to an averaged density  $\bar{\rho}$  as

$$\delta(\mathbf{x}) \equiv \frac{\delta\rho(\mathbf{x})}{\bar{\rho}} = \frac{\rho(\mathbf{x}) - \bar{\rho}}{\bar{\rho}}, \quad \text{where } \delta(\mathbf{x}) \ll \bar{\rho}. \quad (\text{II.34})$$

A Fourier expansion of the averaged density yields in the continuum limit

$$\delta(\mathbf{x}) = \frac{V}{(2\pi)^3} \int_V d^3k \delta_k e^{-i\mathbf{x}\cdot\mathbf{k}}, \quad (\text{II.35})$$

$$\delta_k = \frac{1}{V} \int_V d^3x \delta(\mathbf{x}) e^{i\mathbf{x}\cdot\mathbf{k}}. \quad (\text{II.36})$$

For the time-dependent Fourier modes  $\delta_k \equiv \delta_k(t)$  the following set of independent equations can be derived:

$$\ddot{\delta}_k + 2H\dot{\delta}_k + \left( \frac{c_s^2 k^2}{R^2} - 4\pi G\bar{\rho} \right) \delta_k = 0, \quad (\text{II.37})$$

where  $c_s$  is the speed of sound in the thermal plasma. This set of equation describes the time evolution of density fluctuations in an expanding Universe whose characteristics are determined by their wavenumber  $k$  (and their corresponding length scale  $\lambda \propto k^{-1}$ ). There is an associated critical wavenumber, the *Jeans wavenumber*  $k_J$  defined by the relation

$$k_J = \frac{R}{c_s} \sqrt{4\pi G \bar{\rho}}. \quad (\text{II.38})$$

If the wavenumber is small, i.e.  $k < k_J$ , the density fluctuations will be sound waves traveling through the plasma. On the other hand, if the wavenumber is larger than the Jeans wavenumber, there will be a power-law growth of these density fluctuations. The scaling is governed by the dominating energy contribution during the time of growth: during the radiation-dominated era, the density fluctuations evolve like  $\delta \propto C_1 + C_2 \ln R$ .<sup>14</sup> On the other hand, for a matter-dominated epoch,  $\delta_k \propto C_1 R^{-3/2} + C_2 a$  and finally  $\delta_k \propto C_1 + C_2 R^{-2}$ , for a  $\Lambda$ -dominated Universe. It is worth noting, that the growth of  $\delta_k$  is only efficient during matter-domination. If radiation is dominating, fluctuations will only grow slowly, i.e. formation of structures are effectively taking place only after matter-radiation equality. In the last stage, when dark energy is dominating, it counter-balances gravitational effects and hence the fluctuations stop growing. In summary, since density fluctuations only grows substantially during matter-domination, the initial density perturbations have to be large enough and the CDM contribution has to take over radiation early enough such that the observed structures in the Universe can form.

However, the Newtonian limit only holds for subhorizon modes, i.e.  $k < H$ . The treatment of modes which are larger than the Hubble horizon at a given time needs a fully general-relativistic treatment, as does the inclusion of relativistic fluids. In the relativistic treatment, one solves for the gravitational potential which in turns determine the evolution of density fluctuations. At subhorizon scales this treatment shows the same behavior as the Newtonian limit: during radiation domination the density fluctuations only grow slow and the gravitational potential decays due to radiation pressure, while a stronger growing shows up in matter-dominated phase. On the other hand, at superhorizon scales, the fluctuations are frozen as the potential stays constant.

### II.2.5 The matter power spectrum

The degree of clustering, i.e. the excess probability, can be analyzed by using the two-point correlation (or auto-correlation) function  $\xi(r)$  of density fluctuations  $\delta(\mathbf{x})$ ,

$$\xi(r) = \langle \delta(\mathbf{x}) \delta(\mathbf{x} - \mathbf{r}) \rangle, \quad (\text{II.39})$$

where  $\langle \dots \rangle$  denotes an ensemble averaging. In Fourier space, it can be expressed by the matter power spectrum  $P(k)$  defined by

$$P(k) = \langle |\delta(k)|^2 \rangle. \quad (\text{II.40})$$

Isotropy demands that it only depends on  $k = |\mathbf{k}|$ . Consequently,  $P(k)$  and  $\xi(r)$  are related by

$$\xi(r) = \int dk P(k) k^2 \frac{\sin(kr)}{kr}. \quad (\text{II.41})$$

Because the growth rate of fluctuation modes is time- and scale-dependent, the power spectrum at late times<sup>15</sup> can be decomposed in the following form:

$$P(k, R) \propto \mathcal{T}^2(k) D^2(R) k^{n_s}. \quad (\text{II.42})$$

<sup>14</sup> Here and in the following,  $C_{1,2}$  denotes some arbitrary coefficients.

<sup>15</sup> This assumption is valid, because observations of the power spectrum take place at  $z \rightarrow 0$ .

Here,  $\mathcal{T}(k)$  is a transfer function which describes the growth of modes at horizon crossing and the transition from radiation to matter-domination (characterized by  $R_{\text{EQ}}$ ). The growth factor  $D(R)$  encapsulates the growing of modes in time, as explained in the previous section. Finally, a convenient choice is to set the spectral index of  $P(k)$  to  $n_s = 1$  [139, 140].

This allows us to describe the asymptotic behavior of the matter power spectrum. It can be qualitatively understood from the different growing behavior of modes which enter the horizon at different times. Modes with large  $k$  enter the horizon well before matter-radiation equality  $R_{\text{EQ}}$  and thus the associated gravitational potential decays, leading to a decrease of  $\mathcal{T}(k)$  which is proportional to  $k^{-2}$ . On the other hand, small  $k$  modes enter the horizon after  $R_{\text{EQ}}$  and experience no suppression, i.e.  $\mathcal{T}(k) \propto 1$  for these modes. For these reasons, the power spectrum scales as:

$$P(k) \propto \begin{cases} k, & k < k_{\text{EQ}}, \\ k^{-3}, & k > k_{\text{EQ}}. \end{cases} \quad (\text{II.43})$$

The wavenumber  $k_{\text{EQ}}$  reenters the horizon at matter-radiation equality; it further determines the turnover in  $P(k)$  as it transits from small to large  $k$ . An example for the matter power spectrum at  $z = 0$  is shown in Fig. II.2. It clearly features a peak at  $k_{\text{EQ}} \sim 10^{-2} h/\text{Mpc}$ . Qualitatively, the mode at this wavenumber is the largest in the spectrum, because it is not suppressed due to radiation and has the longest time to grow. Smaller wavenumbers show a smaller grow due to reentering the horizon in radiation domination, while larger wavenumbers have less time to grow.

The small bumps at wavenumbers  $k \simeq 0.1 h/\text{Mpc}$  shown in Fig. II.2 stem from baryonic acoustic oscillations (BAO): in contrast to CDM, baryons are electromagnetically coupled to photons. After recombination the photon mean free path dramatically increases and this creates a baryon drag out of gravitational wells formed by CDM. After some time they bounce back into these regions and this leads to the BAO. The horizontal lines refers to  $k$ -ranges which can be probed by different observations and surveys. The red line refers to precise measurements of different CMB modes [27], the blue line are galaxy count surveys [141], the orange one indicates observations of the Lyman- $\alpha$  forest [142] and lastly, the cyan line is weak lensing data due to cosmic shear effects of underlying matter on far-traveling photons [143, 144]. All of them allow to probe the matter power spectrum across a broad range of scales.

### II.2.6 Impact of warm dark matter on structure formation

The  $\Lambda$ CDM explains the observed behavior of our Universe to a very good degree, incorporating DM which became non-relativistic at pretty early times, therefore called “cold” DM and whose density fluctuations acts as gravitational wells for the baryonic matter, hence it is crucial for the formation of structures over a broad range of scales. However, as already pointed out in Section II.1.3, there is the intriguing idea to deviate from this picture and allow for DM candidates which stay relativistic for longer times. Such particles are referred to as “warm” DM and they influence the formation of structures in the Universe, because they come with a non-vanishing free-streaming length. This length is associated to the time period where the DM was relativistic, i.e. particles which become non-relativistic at later times thus have a larger free-streaming length. An example are SM neutrinos: in principle they are a good DM candidate, because they carry no electric charge and interact only very weakly with matter. However, as we have seen in Section II.1.2 neutrinos are extremely light and are relativistic until late times. If neutrinos constituted all of DM, we would face the following problem: they are simple moving too fast to allow for clumping of baryonic matter, because there would be no gravitational

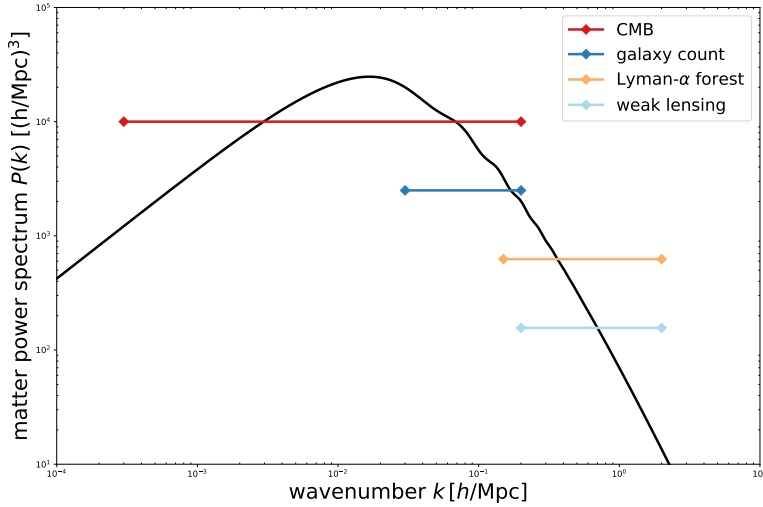


Figure II.2: The matter power spectrum  $P(k)$  derived using CLASS [145, 146] and for cosmological parameters specified in Ref. [27]. At small wavenumbers it is increasing  $\propto k$ , whereas it drops  $\propto k^{-3}$  after it reaches a peak at  $k \approx 10^{-2} h/\text{Mpc}$ . The different colored horizontal lines indicate ranges of the spectrum which can be experimentally verified by observations and which are explained in more detail in the text. This figure is inspired by Fig. 1 in Ref. [147].

wells as neutrinos would exit such high density regions of space with the speed of light. In conclusion, neutrinos as DM were already excluded decades ago as they are essentially too “hot”.

Now one may ask, whether there is a DM species with non-vanishing free-streaming length but smaller than that for neutrinos. In that case, a similar but weaker effect would take place. The escape of this DM would erase gravitational sinks below a certain scale and hinder the formation of structures smaller than this given size. Such a candidate would leave us with some fingerprints in the matter power spectrum, as shown in Fig. II.3. We assumed a warm DM with a Fermi-Dirac distribution similar to neutrinos, but with masses  $\mathcal{O}(\text{keV})$ . It is clearly visible, that WDM with smaller masses give rise to a matter power spectrum which deviates from  $\Lambda\text{CDM}$  at smaller wavenumbers, or inversely, on larger scales.

The deviation for a given WDM model can be quantified by the ratio of the corresponding power spectra, called linear squared transfer function  $T(k)$ :

$$T^2(k) \equiv \frac{P_{\text{WDM}}(k)}{P_{\text{CDM}}(k)}. \quad (\text{II.44})$$

The transfer function for a WDM model can be expressed via the following analytical expression [148]:

$$T(k) = \left(1 + (\alpha k)^{2\beta}\right)^{-5/\beta}, \quad (\text{II.45})$$

$$\text{where } \beta = 1.12, \alpha = 0.049 \left(\frac{m_{\text{WDM}}}{1 \text{ keV}}\right)^{-1.11} \left(\frac{\Omega_{\text{WDM}}}{0.25}\right)^{0.11} \left(\frac{h}{0.7}\right)^{1.22} h^{-1} \text{ Mpc}. \quad (\text{II.46})$$

As shown in Fig. II.2 there are surveys and observational techniques which can probe  $P(k)$  at these scales and search for deviations from  $\Lambda\text{CDM}$ . These allow us to place constraints



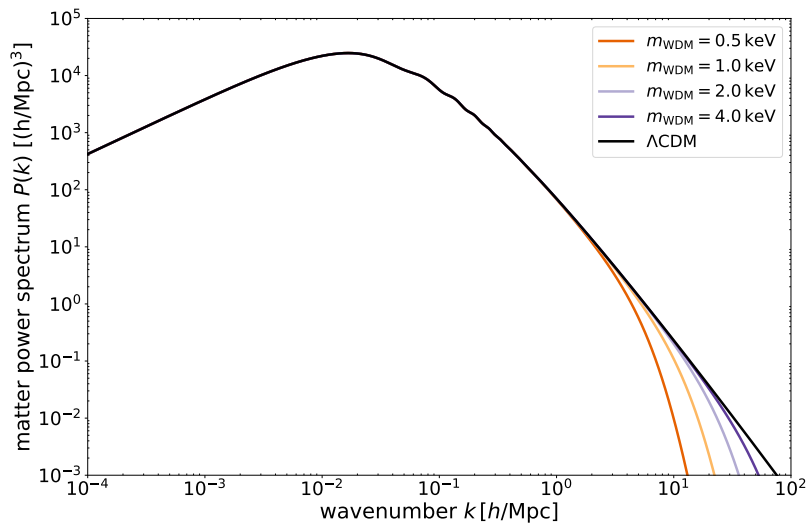


Figure II.3: The corresponding matter power spectrum for a WDM with mass in range  $m_{\text{WDM}} = 0.5\text{ keV} - 4\text{ keV}$ . In general, a suppression of the power spectrum compared to  $\Lambda\text{CDM}$  can be observed and the scale at which it starts to deviate is related to the mass of the WDM candidate.

on the parameters of a WDM model. Usually, one has to rely on extensive hydrodynamical  $N$ -body simulations for a given WDM model and compare their predictions against observations. However, there are shortcuts to this procedure and we will explain in the following how to probe the matter spectrum using three different approaches which were used to constrain our model setups given in Refs. [1, 3].

### II.2.6.1 Half-mode analysis

Conventionally, structure formation analyses quote their limits on WDM in terms of a thermal relic WDM candidate with mass  $m_{\text{TR}}$  as a reference. It is assumed that it was thermalized early in the Universe and thus maintained a Fermi-Dirac distribution before it decoupled at some point at temperature  $T_D$ . It allows for an adaption of structure formation limits for other similar models, although it is not a “physical” model, because it would require too much entropy dilution to reproduce the observed DM relic abundance,  $\Omega_{\text{DM}}h^2$ , with  $\mathcal{O}(\text{keV})$  DM masses [149],

$$\Omega_{\text{DM}} \approx 10 \left( \frac{g_*^s(T_\nu)}{g_*^s(T_D)} \right) \left( \frac{m_{\text{TR}}}{\text{keV}} \right), \quad (\text{II.47})$$

where  $T_\nu$  is the temperature of neutrino decoupling. Consequently,  $g_*^s(T_D) \approx 900$  would be required to satisfy  $\Omega_{\text{DM}}h^2 = 0.12$ .

For  $\Lambda\text{CDM}$ ,  $T^2(k) = 1 \forall k$ , whereas for a given WDM setup, it is clear that  $\lim_{k \rightarrow 0} T^2(k) = 1$  because at large scales it is indistinguishable from  $\Lambda\text{CDM}$ . On the other hand, at small scales,  $\lim_{k \rightarrow \infty} T^2(k) < 1$ , because of the suppression of structures due to WDM. The simplest approach is to calculate  $T^2(k)$  for a WDM model and compare it against a reference model by inserting a specific limit on the TR mass as  $m_{\text{WDM}}$  in Eq. (II.46), this defines a reference transfer function  $T_{\text{lim}}^2(k)$ . If  $T^2(k) \leq T_{\text{lim}}^2(k) \forall k$ , the WDM will not be in conflict with observations, because its suppression is less than observed. However, the WDM momentum distribution does not necessarily have to be of thermal origin as it is

the case for the reference model. In general, the corresponding transfer function can have a different slope compared to  $T_{\text{lim}}^2(k)$  and both might intersect each other. Therefore, it is convenient to define the half-mode  $k_{\text{half}}$  by demanding that [111]

$$T^2(k_{\text{half}}) \stackrel{!}{=} \frac{1}{2}. \quad (\text{II.48})$$

Based on this wavenumber, we can use the following criteria whether a given WDM model is allowed if and only if the following criterion is fulfilled:

$$T^2(k) \leq T_{\text{lim}}^2(k) \quad \forall k < k_{\text{half}}. \quad (\text{II.49})$$

This analysis technique will be used to constrain freeze-in ALP DM in Chapter V and an adapted version will be used in Chapter IV to place limits on light DM in the context of the scotogenic model.

### II.2.6.2 Constraints from the Lyman- $\alpha$ forest

Another way to constrain WDM models uses the so-called *Lyman- $\alpha$  forest*. As shown in Fig. II.2, it can be used to probe the smallest scales of the matter power spectrum and to measure potential deviations from  $\Lambda$ CDM stemming from WDM<sup>16</sup>. The Lyman- $\alpha$  forest method examines the intergalactic medium (IGM) by looking at absorption lines from neutral hydrogen along the line-of-sight of highly redshifted quasars. The most prominent one of these absorption lines is the Lyman- $\alpha$ , hence the obvious name for this observation method. Each point along one line-of-sight corresponds to different redshifts and thus the respective absorption lines are observed at different wavelengths. A combination of various line-of-sight measurements allow to estimate the hydrogen density, which in turns acts as a tracer for the underlying DM density.

The Lyman- $\alpha$  forest surveys probe the absorption line spectra of quasars at redshifts  $3.5 < z < 5$  and the flux power spectrum,  $P_F(z, k_\nu)$ , at these redshifts is derived for different wavenumbers in velocity-space,  $k_\nu$ . In order to derive constraints for a specific WDM model, the one-dimensional power spectrum  $P_{1D}(k)$  (see for instance Refs. [99, 150, 151]) is derived by integrating the matter power spectrum along the observed  $k$ -range. The one-dimensional spectrum is related to the measured flux spectrum by a bias function,  $b^2(k) \equiv P_F(k_\nu, z)/P^{1D}(k)$ , which allows us to translate bounds from surveys into a quantity which can be accessed easily for a given WDM model by computing its matter power spectrum. The conversion factor between velocity-space wavenumbers and inverse comoving length scales used in the power spectrum is given by  $k = \frac{H(z)}{1+z} k_\nu$ . The one-dimensional power spectrum is an integral of the  $P(k)$  evaluated at  $z = 0$  and given by

$$P^{1D}(k) = \frac{1}{2\pi} \int_k^\infty dk' k' P(k'). \quad (\text{II.50})$$

A suppression of this spectrum can be quantified by defining a one-dimensional transfer function  $\phi(k)$  in a similar way as  $T(k)$ ,

$$\phi(k) = \frac{P_{\text{WDM}}^{1D}(k)}{P_{\Lambda\text{CDM}}^{1D}(k)}, \quad (\text{II.51})$$

<sup>16</sup> Strictly speaking, possible deviations do not necessarily have to be caused by DM; they can also be indications of unknown processes in structure formation at these scales. This is one of the reasons why there are sometimes significant differences in the limits for  $m_{\text{TR}}$  quoted in the literature.

where  $P_{\Lambda\text{CDM}}^{1D}(k)$  is the one-dimensional power spectrum of  $\Lambda\text{CDM}$ . The next step is to quantify how much a given WDM model differs from a  $\Lambda\text{CDM}$  scenario. We integrate Eq. (II.51) over all scales typically probed by Lyman- $\alpha$  observations given in the range  $(k_{\min}, k_{\max})$ :

$$A = \int_{k_{\min}}^{k_{\max}} dk \phi(k), \quad (\text{II.52})$$

and this integral can be used to approximate the amount of suppression for a given WDM model by defining the estimator

$$\delta A \equiv \frac{A_{\Lambda\text{CDM}} - A}{A_{\Lambda\text{CDM}}}, \quad (\text{II.53})$$

where  $A_{\Lambda\text{CDM}} = k_{\max} - k_{\min}$ , whose value is set by the respective observational data set of Lyman- $\alpha$  surveys.

In the final step, we have to calculate a reference value  $\delta A_{\text{ref}}$  first, using a thermal relic with mass  $m_{\text{TR}}$ , where  $m_{\text{TR}}$  is an observational limit from Lyman- $\alpha$  surveys. Now, WDM models which give rise to  $\delta A > \delta A_{\text{ref}}$  are excluded because their small scale suppression is too large.

### II.2.6.3 Counting the number of Milky Way satellites

An additional way to search for deviations from  $\Lambda\text{CDM}$  at galactic scales is to estimate the number of accompanying satellites of the Milky Way (MW). Generally, WDM models predict fewer satellites for MW-like galaxies compared to vanilla  $\Lambda\text{CDM}$ , because they tend to suppress the mass distribution function of the subhalos [148, 149, 152–154]. This can be understood by defining an effective *Jeans mass*  $M_J(t)$  based on Eq. (II.38) which is given by [155]

$$M_J(t) = \frac{4\pi}{3} \rho_m(t) \left( \frac{\pi}{k_J} \right)^3, \quad (\text{II.54})$$

and perturbations are damped for  $M < M_J$ . Using observational data to count the accompanying satellites of the MW, we can place limits on WDM models by calculating their predicted number of subhalos.<sup>17</sup>

The starting point to estimate the number of subhalos accompanying the MW is to use an extension of the *Press-Schechter* formalism [162] to determine the number density of halos. Using linear perturbation theory for the density fluctuations, the probability for the collapse of a fluctuation is related to the mass of the respective halo. Based on this, we define a conditional mass function which takes the merging history of halos into account [154, 163],

$$\frac{dn(M|M_0)}{d \log(M)} = -\frac{M_0}{M} f(\delta_c, S|\delta_{c,0}, S_0) \frac{dS}{d \log(M)}. \quad (\text{II.55})$$

Here,  $\delta_c$  is the critical density below which fluctuations collapse and form compact structures; it is a time dependent quantity and can be seen as a time variable.  $S$  is the variance of the matter power spectrum smoothed by a *sharp-k* window function  $W(k, R)$ ,

$$S(R) = \int \frac{dk k^2}{2\pi^2} P(k) W^2(k, R), \quad W(k, R) = \theta(1 - kR), \quad (\text{II.56})$$

<sup>17</sup> Associated to this is the “missing satellite” debate: simulations of galaxy formation using only  $\Lambda\text{CDM}$  predicted too many accompanying dwarf galaxies compared to the observed number of satellites of the MW [156–158] which sparked particular interest in WDM models. However, recent detections of ultra faint dwarfs [159, 160] and more detailed investigations of the halo profile [161] indicate that this problem can also be solved within the  $\Lambda\text{CDM}$  paradigm.

where the filter scale  $R$  is related to an enclosed mass  $M$  by  $M = \frac{4\pi}{3}\Omega_m\rho_c(cR)^3$ , where  $c = 2.5$  stems from a matching to simulations [99], and the matter density is given by  $\Omega_m = 0.315$ . Finally,  $f(\delta_c, S|\delta_{c,0}, S_0)$  is a probability distribution which encodes the merging history of a halo forming at  $\delta_c$  with variance  $S$  up to present time  $\delta_{c,0}$  with  $S_0(R_0)$ , where  $R_0$  is the filter scale associated to the host galaxy with mass  $M_h$ . Assuming a spherical collapse, it is given by [163]

$$f(\delta_c, S|\delta_{c,0}, S_0) = \frac{\delta_c - \delta_{c,0}}{\sqrt{2\pi(S(R) - S_0(R_0))^3}} \exp\left[-\frac{(\delta_c - \delta_{c,0})^2}{2(S(R) - S_0(R_0))}\right]. \quad (\text{II.57})$$

Integrating Eq. (II.55) over time gives the number of subhalos  $N_{\text{sub}}$ :

$$\frac{dN_{\text{sub}}}{d\log(M)} = \frac{1}{C} \int_{\delta_{c,0}}^{\infty} d\delta_c \frac{dn(M|M_h)}{d\log(M)} = \frac{1}{C} \frac{1}{6\pi^2} \frac{M_h}{M} \frac{P(1/R)}{R^3 \sqrt{2\pi(S - S_0)}}, \quad (\text{II.58})$$

where  $C$  is a normalization constant used to match with  $N$ -body simulations and depends on the definition of the host halo. In our case, the boundary of the host halo is set by the criterion that its density is 200 times the critical density  $\rho_c$  of the Universe and hence we use  $C = 34$  [99] in the following.

Finally, Eq. (II.58) gives an estimate for the numbers of subhalos with mass  $M$  around the host galaxy, thus integrating Eq. (II.58) from  $M_{\text{min}} = 10^8 h^{-1} M_{\odot}$  to  $M_h$  yields the total amount of subhalos

$$N_{\text{sub}} = \int_{M_{\text{min}}}^{M_h} dM \frac{dN_{\text{sub}}}{d\log(M)}. \quad (\text{II.59})$$

There are two uncertain numbers in the following discussion: first, the observed number of MW subhalos and second the mass of the host galaxy, i.e. the MW in our case.

Addressing the counting of subhalos we follow the approach outlined in Refs. [99, 151]: there exist 11 ‘‘classical’’ satellites which are combined with 15 ultra-faint satellites found by the Sloan Digital Sky Survey (SDSS) (taken from the seventh data release, see Refs. [164, 165] for more details). Assuming that the satellites found by SDSS are distributed isotropically over the sky, the latter number can be multiplied by a factor of 7/2 because SDSS has a sky coverage of only 28.3%; this yields in total  $N_{\text{sub}} = 64$ .<sup>18</sup> However, as pointed out in Ref. [99] we should decrease this number by  $\sim 10\%$  to take the history of halo formation into account. Further, the assumption that the satellites found by SDSS are isotropically distributed might lead to an overestimation of  $N_{\text{sub}}$ , for example, the classical satellites are arranged in a plane rather than isotropically [166].

On the other hand, in addition to SDSS, several more ultra-faint satellites or candidates have been reported by other surveys (see for instance Ref. [167]) and future searches could reveal even more satellites, so we regard  $N_{\text{sub}} = 64$  as a conservative estimate for the number of MW companions. In fact, simulations predict  $\mathcal{O}(100)$  subhalos [168, 169] which could be detected with future observations and therefore open new possibilities to test WDM models even further.

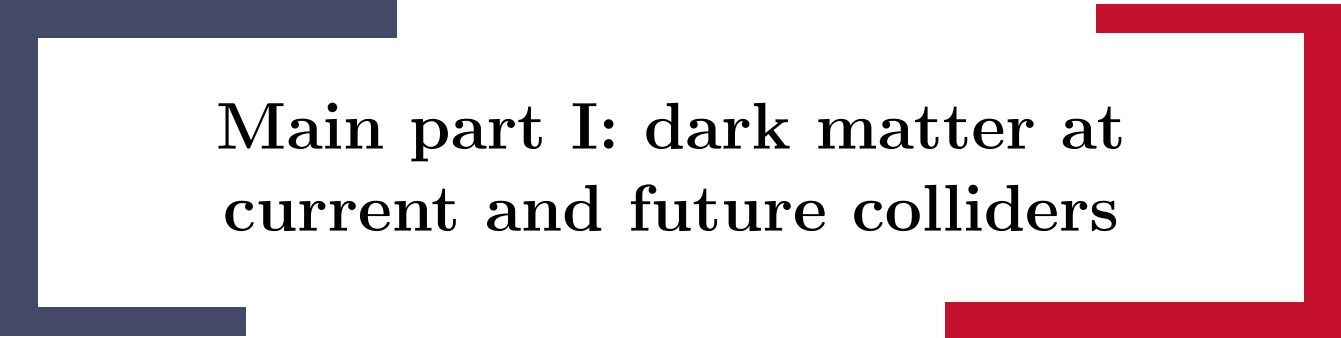
Since we make different assumptions for the MW mass in our subsequent analysis, we refer the reader to Chapters V and VI for further discussion, where we use  $N_{\text{sub}}$  to constrain warm ALP DM and a more general WDM framework respectively.

<sup>18</sup> Assuming Poisson statistics, the error of this number is  $\approx 13$ . Nonetheless, we will mostly refer to the mean value of  $N_{\text{sub}}$ , but comment on the dependency in the respective chapters.

## **II.3 Prelude**

During this research, programs, libraries and other tools were used in addition to those explicitly mentioned in the relevant chapters. For example `Mathematica 11+12` [170] was used for numerical calculations. Furthermore, `Python 2.7` [171] and `Python 3.6` [172] was used in combination with the libraries `NumPy` [173], `Matplotlib` [174], `SymPy` [175], `SciPy` [176] and the `IPython` [177] environment. All Feynman diagrams were created with the `TikZ-Feynman` package [178]. The `Pandas` [179] package was used for parts of data manipulation.





**Main part I: dark matter at  
current and future colliders**

The first part of this thesis is dedicated to collider probes of extensions of the standard model. In the following, we are going to consider the well motivated scotogenic model (ScM) as an exemplary extension.

The current energy frontier is set by the largest collider experiment, the Large Hadron Collider (LHC) located at CERN. It delivers and collides protons or heavy ions with center-of-mass energies up to  $\sqrt{s} = 13$  TeV for four different experiments: ATLAS, CMS, LHCb and ALICE. For our analysis the first two will be the most relevant, since they allow for a dedicated search for new particles produced in collisions and decaying promptly, leaving recognizable signatures in the outward detector layers.

Data collection started in 2011/2012 at  $\sqrt{s} = 7$ –8 TeV respectively and an integrated luminosity of roughly  $20$ – $25$  fb $^{-1}$  was reached. During the second run, in which data was taken at  $\sqrt{s} = 13$  TeV from 2015 until the end of 2018, the LHC delivered additionally  $\sim 150$  fb $^{-1}$  to both, ATLAS and CMS. After a long shutdown, the experiment is planned to resume in 2022 with Run-3 at an increased energy of  $\sqrt{s} = 14$  TeV and collecting at least  $\sim 300$  fb $^{-1}$  of  $pp$  collision data until the end of 2024.

After this run, it is foreseen to upgrade the existing LHC collider into the high-luminosity LHC (HL-LHC) and increase the number of  $pp$  collisions dramatically. This will allow to reach an integrated luminosity up to  $4000$  fb $^{-1}$  at  $\sqrt{s} = 14$  TeV in a decade starting from 2027.

At the moment, possible experiments for the post-LHC era are being discussed and their potential to measure the SM at high precision and search for new physics is being evaluated. One idea is to reuse the LHC infrastructure and upgrade the machine such that it can deliver  $pp$  collisions at  $\sqrt{s} = 27$  TeV, the high-energy LHC (HE-LHC). Going even beyond, options for a circular proton collider at  $\sqrt{s} = 100$  TeV denoted by Future Circular Collider (FCC-hh) have been considered.

On the other hand, new electron-positron colliders are discussed as well. This includes circular colliders similar to proton colliders such as the Circular Electron Positron Collider (CEPC) in China or the FCC-ee at CERN, both running at energy setups  $\sqrt{s} \sim 100$ – $350$  GeV. Since  $e^+e^-$  collisions offer a cleaner experimental condition compared to  $pp$  collisions, these machines would allow for precise measurements of observables. However, energy losses due to Bremsstrahlung limit the acceleration of electrons inside circular colliders and thus linear colliders have been proposed as well. Future facilities like the International Linear Collider (ILC) or the Compact Linear Collider (CLIC) would deliver energies up to  $\sqrt{s} = 1$  TeV and  $\sqrt{s} = 3$  TeV, respectively, together with high luminosities.

Current and future colliders allow to probe new physics beyond the SM (BSM) in different ways: there are direct searches looking for distinctive signatures caused by new particles, such as corresponding large missing-energy signatures. A plethora of studies have been conducted by ATLAS and CMS and results are often quoted in a specific supersymmetric model (SUSY) framework. Limits on BSM models are extracted from these studies by recasting and adapting these searches using Monte Carlo simulations. Alternatively, BSM models can have an indirect effect on SM processes. For instance electroweak precision measurements allow to place bounds on new physics extensions.

In the following chapter, we will present an example for the first approach. We recast existing searches for pair production of the electroweak SUSY partners to limit the ScM parameter space in Chapter III. Further we present search strategies to test this model at future colliders as well.



# Collider studies of the scotogenic model

## III.1 Introduction

While more than two decades have passed since the groundbreaking discovery of neutrino oscillations, which unambiguously established that the most elusive standard model (SM) particles are massive, the origin of neutrino mass still remains unknown. In spite of the viable scenario in which, by supplementing SM left-handed neutrino fields with right-handed (RH) components, neutrino masses are generated in the same way as for all the other fermions, the smallness of Yukawa couplings required for generating eV-scale masses has led to a much greater interest in Majorana mass models. The most famous realization of the latter possibility is the type-I seesaw model [33, 35, 180, 181] in which neutrino masses are generated at tree-level in the presence of at least two generations of heavy neutral leptons. For “natural”  $\mathcal{O}(1)$  Yukawa couplings, this model implies that the heavy lepton mass scale is  $\simeq 10^{13}$  GeV, unreachable at any terrestrial experiment. In contrast, radiative neutrino mass models can lower the scale of new physics by several orders of magnitude.

Among radiative neutrino models, one of the simplest realizations is the so-called *scotogenic model* (ScM) [103]. It imposes a  $\mathbf{Z}_2$  symmetry in order to forbid the tree-level neutrino mass generation, hence the lightest among the newly introduced particles can be a viable dark matter (DM) candidate [182–186]. The success of thermal leptogenesis in this model has also been demonstrated in Refs. [187–193]. In addition, recently it was shown by previous work of the author that light DM and leptogenesis via the *Akhmedov-Rubakov-Smirnov* (ARS) mechanism [194], i.e. the dynamical creation of a baryon asymmetry via CP-violating oscillations among RH neutrinos (RHN), can be embedded simultaneously in this framework [2]. It was found that the spectrum of new particles can be below the TeV-scale, while bounds from cosmology require the mass of the light DM to be below  $\mathcal{O}(10\text{ keV})$ . This raises the question whether we can test this model setup at present and future colliders, where the accessible energy range exceeds the masses of all newly introduced particles. Moreover, the light DM candidate can lead to interesting consequences for the early Universe, which will be discussed in the second part of this thesis.

In this chapter we will focus on collider searches at the (HL-)LHC and the future facilities FCC-hh and CLIC to project exclusion bounds on the model parameter space. For this purpose we are going to investigate pair production of the charged new scalar, which decays further either into  $e$  or  $\mu$  and missing transverse energy,  $\cancel{E}_T$ , or into tau leptons and  $\cancel{E}_T$  as the designated final state for the experiments under consideration.

This chapter is organized as follows: we briefly motivate our model spectrum in Section III.2 before we introduce the model in Section III.3. Section III.4 is dedicated to a projected HL-LHC analysis based on existing searches. Going beyond, we discuss the results for the future colliders FCC-hh and CLIC in Section III.5. We summarize our results in Section III.6.

## III.2 Motivation

The idea to setup a dedicated search for this specific model was sparked by previous research results presented in Ref. [2]. In this paper it has been shown that it is possible to combine an explanation for neutrino masses and a light RHN  $N_1$  as a DM candidate with a dynamical generation of the observed baryon asymmetry of the Universe (BAU) by applying a process known as leptogenesis. Generally, in this framework, CP violating decays or oscillations of heavy RHN are used to create an asymmetry in the SM lepton sector at high temperatures early in the Universe which is then transferred via non-perturbative processes, so-called sphalerons, to the baryon sector before the electroweak symmetry breaking takes place at  $T \simeq 160$  GeV. More precisely, the considered production relies on a combination of the ARS mechanism and thermally enhanced CP violating decays of the  $\Sigma$  scalar (see Ref. [195]). Unlike standard thermal leptogenesis, the asymmetry is generated at lower scales of a few TeV instead of high scales of  $\sim 10^{12}$  GeV. This is possible due to an enhancement effect stemming from a tiny mass splitting between the heavy RHN  $N_2$  and  $N_3$  which is quantified by the parameter  $m_{N_3} - m_{N_2} \equiv \delta_M \ll 1$ .<sup>19</sup>

One of the challenges was to find regions in the parameter space for which the observed values of DM relic abundance and the baryon asymmetry are simultaneously reached. Generally, these two mechanisms have conflicting requirements on the strength of the Yukawa coupling which can be set by the parameter  $\eta$  (see Eq. (III.6)). In order to not overproduce DM from decays of the heavier RHN, sufficiently large Yukawa interactions are required. On the other hand, leptogenesis relies on weak interactions or otherwise washout effects would easily destroy any generated lepton asymmetry. This tension can be cured by imposing coannihilations between the RHN and the scalar particles by choosing their masses to be of similar size. Such a regime opens up new scalar annihilation channels which do not rely on the strength of the second and third generation Yukawa couplings. Therefore, a huge suppression of the relic density can be achieved for Yukawa couplings set low enough to generate a significant lepton asymmetry.

Employed with this mass spectrum we calculated the DM relic density for different scalar

<sup>19</sup> Besides this concrete model, there are other intriguing possibilities to generate the baryon asymmetry via degenerate RH neutrinos and intertwine it with other BSM physics explanations as well. For instance, the model considered in Ref. [196] delivers an explanation to the observed discrepancies in anomalies in  $b$  decays, the so-called  $b$ -anomalies (see Ref. [197] for an overview). By extending the SM group to a  $SU(4) \times SU(3) \times SU(2) \times U(1)$  and incorporating a scalar leptoquark which couples third generation quarks and leptons, it explains the observed  $\sim 3\sigma$  discrepancy in the  $b \rightarrow \ell \ell s$  [198, 199] and  $b \rightarrow c \tau \nu_\tau$  [200] decay rate. It features an inverse seesaw mechanism [201, 202] to explain the smallness of neutrino masses, i.e. it introduces in total six particles (3 RHNs and 3 gauge singlets), two of which form a nearly mass degenerate pseudo Dirac pair (PDP) with masses  $M_R$  and a coupling  $M_\nu^D = Y_\nu v$  to the SM leptons. Their mass difference is characterized by a small lepton number violating (LNV) parameter  $\mu$ . They are related to the light neutrino mass matrix  $M_l$  via  $M_l \approx M_\nu^D M_R^{-1} \mu (M_R^T)^{-1} (M_\nu^D)^T$ . Here, the smallness of the LNV parameter guarantees an adaption of the ARS mechanism [203]. Assuming the mass of the lightest PDP to be of  $M_{R,1} \simeq \mathcal{O}(\text{MeV})$  and choosing appropriately small couplings  $Y_\nu$ , we find a space of parameter region which successfully explains the BAU. It can be enlarged by demanding further couplings between the gauge singlets and leptons. We checked that the corresponding PMNS mixing matrix does not violate unitarity bounds and further that the lightest PDP does not thermalize due to mixing with the heavier states. The later requirement is crucial for the success of the ARS mechanism; it relies on a freeze-in of the PDP in order to generate an asymmetry via oscillations among the mass degenerate states.

mass choices and further evaluated the corresponding baryon asymmetry in a range of the heavy RHN mass,  $m_{N_2}$ , and the strength of the Yukawa coupling. The results can be seen in Fig. III.1, where we have fixed the DM mass  $m_{N_1}$  to be 6 keV and  $\delta_M = 10^{-11}$ . The blue line indicates the region which gives a too small baryon asymmetry to explain for the observed value.<sup>20</sup> On the other hand, the red shaded region is ruled out because this parameter choice would spoil the formation of light nuclei due to late-time production of highly energetic DM. Here we adopted the limits on leptonic decays from [204]. There are several things we would like to point out. First, the final baryon asymmetry only mildly depends on the involved particle masses and in general larger mass scales will only lead to a slight decrease as can be seen from the slope of the BAU line in Fig. III.1. In contrast, choosing a higher mass scale slightly weakens the BBN bounds and broadens up the available parameter region. On the other hand, allowing for a slightly larger degeneracy between right-handed neutrinos, such as  $\delta_M = 10^{-10}$ , would correspond to a shift of the blue exclusion curve in Fig. III.1 towards the BBN bound at the left. For  $\delta_M \geq 10^{-10}$  and DM masses of  $\sim 6$  keV the corresponding parameter space is completely constrained either by BBN or BAU requirements.

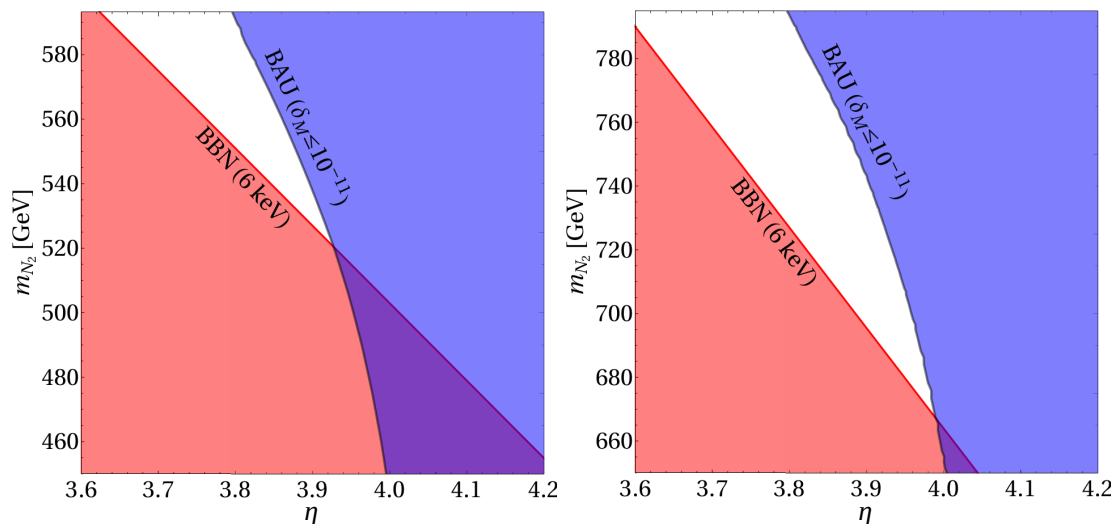


Figure III.1: Allowed region in the  $\eta$ - $m_{N_2}$  parameter space for a charged scalar mass  $m_{\pm} \simeq 590$  GeV (left) and  $m_{\pm} \simeq 795$  GeV (right). The BBN exclusion limits are shown in red, while the blue shaded region does not produce a sufficiently large baryon asymmetry. We observe that there is a region consistent with BBN limits in which the correct amounts of DM and baryon asymmetry can be obtained.

We have also observed the dependence of BBN limits on the maximum allowed DM mass. For scalar masses in the range 300–1000 GeV, we found a maximal value of the DM mass of 9.4 keV. Generally, choosing higher degeneracies will open up the available parameter space to some extent, thus allowing for larger DM masses.<sup>21</sup> However, even in such cases we estimated the maximal allowed DM mass to be at most  $\mathcal{O}(10$  keV).

In summary, we identified the parameter space in which the produced DM abundance and BAU are in accord with the observed values. We have seen that the most stringent constraints arise from BBN considerations, which can be relaxed by employing coannihilation

<sup>20</sup> In principle the observed asymmetry is only reproduced on the blue line. However, since we maximized the CP violating parameters, it is possible to adjust them such that the correct asymmetry can be achieved for the parameter region left to the blue line.

<sup>21</sup> Although smaller mass differences provide an increase in asymmetry, this effect breaks off at a certain value of the difference, and the asymmetry cannot be increased further. In our case this is  $\delta_M \approx 10^{-13}$

processes between RH neutrinos and scalars which effectively put an upper bound on the allowed mass for the DM. We found that the DM production in our model is mainly driven by the freeze-in. These results sparked the question of whether this scenario could potentially be tested by searches at collider experiments, given that the masses of the particles involved are below the TeV scale.

### III.3 The model and neutrino mass generation

In addition to the SM field content, the ScM contains one scalar doublet  $\Sigma = (\sigma^+, \sigma^0)^T$  as well as three generations of RHNs  $N_i$  ( $i = 1, 2, 3$ ). In addition to these new fields, the model requires a discrete  $\mathbf{Z}_2$  symmetry under which the new particle fields have an odd charge. The part of the Lagrangian containing newly introduced fields is

$$\mathcal{L} \supset \frac{i}{2} \bar{N}_i \not{\partial} N_i - \left( y_{i\alpha} \bar{N}_i \tilde{\Sigma}^\dagger L_\alpha + \frac{1}{2} m_{N_i} \bar{N}_i N_i^c + \text{h.c.} \right) + (D_\mu \Sigma)^\dagger (D^\mu \Sigma) - V(\Phi, \Sigma), \quad (\text{III.1})$$

where  $y_{i\alpha}$  is the Yukawa coupling between a RHN  $N_i$ ,  $\Sigma$  and a SM lepton doublet  $L_\alpha = (\nu_\alpha, \alpha^-)^T$ , ( $\alpha = e, u, \tau$ ),  $m_{N_i}$  is the mass of  $i$ -th RHN,  $D_\mu$  is the covariant derivative,  $\Phi = (\phi^+, \phi^0)^T$  is the SM Higgs doublet, and  $V(\Phi, \Sigma)$  represents the scalar potential

$$\begin{aligned} V(\Phi, \Sigma) = & \mu_1^2 \Phi^\dagger \Phi + \mu_2^2 \Sigma^\dagger \Sigma + \frac{1}{2} \lambda_1 (\Phi^\dagger \Phi)^2 + \frac{1}{2} \lambda_2 (\Sigma^\dagger \Sigma)^2 + \lambda_3 (\Phi^\dagger \Phi)(\Sigma^\dagger \Sigma) \\ & + \lambda_4 (\Phi^\dagger \Sigma)(\Sigma^\dagger \Phi) + \frac{\lambda_5}{2} \left( (\Phi^\dagger \Sigma)^2 + \text{h.c.} \right). \end{aligned} \quad (\text{III.2})$$

The couplings in the scalar sector are constrained by vacuum stability requirements, i.e. the potential should not diverge for large field values [183, 205],

$$\lambda_3 > -\sqrt{\lambda_1 \lambda_2}, \quad \lambda_3 + \lambda_4 - |\lambda_5| > -\sqrt{\lambda_1 \lambda_2}, \quad \lambda_{1,2} > 0. \quad (\text{III.3})$$

From Eq. (III.2), we can directly infer the masses of novel scalar degrees of freedom after electroweak symmetry breaking (EWSB):

$$\begin{aligned} m_\pm^2 &= \mu_2^2 + \lambda_3 v^2, \\ m_S^2 &= \mu_2^2 + (\lambda_3 + \lambda_4 + \lambda_5) v^2, \\ m_A^2 &= \mu_2^2 + (\lambda_3 + \lambda_4 - \lambda_5) v^2, \end{aligned} \quad (\text{III.4})$$

where  $v = 246/\sqrt{2}$  is the vacuum expectation value (VEV) of the Higgs field. The mass of the charged scalar is given in the first line of Eq. (III.4), whereas the latter two masses correspond to the CP-even ( $S$ ) and CP-odd ( $A$ ) neutral scalars, defined as  $\sigma^0 = (S + iA)/\sqrt{2}$ .

Since the exact  $\mathbf{Z}_2$  symmetry forbids a generation of neutrino masses at tree-level, they are realized radiatively with the following expression obtained by calculating self-energy corrections to the neutrino propagator from the exchange of neutral scalar fields  $S$  and  $A$  [103, 206, 207],

$$\begin{aligned} (m_\nu)_{\alpha\beta} &= \sum_i \frac{y_{i\alpha} y_{i\beta} m_{N_i}}{32\pi^2} \left[ \frac{m_S^2}{m_S^2 - m_{N_i}^2} \ln \left( \frac{m_S^2}{m_{N_i}^2} \right) - \frac{m_A^2}{m_A^2 - m_{N_i}^2} \ln \left( \frac{m_A^2}{m_{N_i}^2} \right) \right] \\ &\equiv \sum_i y_{i\alpha} y_{i\beta} \Lambda_i. \end{aligned} \quad (\text{III.5})$$

Here, the summation index runs over the RHN generations and in the last equality we abbreviated this formula with  $\Lambda_i$ . In the model spectrum considered in the following, the

mass of the lightest RHN is  $\mathcal{O}(10 \text{ keV})$  with  $y_{1\alpha} \simeq \mathcal{O}(10^{-8})$  and this state effectively does not participate in the neutrino mass generation. This makes the lightest active neutrino effectively massless, which is a viable scenario, consistent with the data from neutrino oscillation experiments that are probing only mass squared differences. In this case,  $N_1$  is decoupled from the mass generation and consequently only the elements of a  $2 \times 3$  submatrix of  $y$ , which we denote by  $y'$ , enter in Eq. (III.5).

In order to properly account for low-energy neutrino data in the analysis, we employ the Casas-Ibarra parametrization which imposes the following expression for the Yukawa sub-matrix [208]

$$y' = i \left( \sqrt{\Lambda^{\text{diag}}} \right)^{-1} R \sqrt{m_\nu^{\text{diag}}} U_{\text{PMNS}}^\dagger, \quad (\text{III.6})$$

where  $\Lambda^{\text{diag}} = \text{diag}(\Lambda_2, \Lambda_3)$ , and  $R$  is an orthogonal matrix parametrized with a complex angle  $\theta = \omega - i\eta$

$$R = \begin{cases} \begin{pmatrix} 0 & \cos \theta & -\sin \theta \\ 0 & \sin \theta & \cos \theta \end{pmatrix}, & \text{for normal neutrino mass ordering (NO)}, \\ \begin{pmatrix} \cos \theta & -\sin \theta & 0 \\ \sin \theta & \cos \theta & 0 \end{pmatrix}, & \text{for inverted neutrino mass ordering (IO)}. \end{cases} \quad (\text{III.7})$$

The remaining ingredients in Eq. (III.6) are the neutrino masses

$$m_\nu^{\text{diag}} = \begin{cases} \text{diag} \left( 0, \sqrt{m_{\text{sol}}^2}, \sqrt{m_{\text{atm}}^2} \right), & \text{for NO}, \\ \text{diag} \left( \sqrt{m_{\text{atm}}^2}, \sqrt{m_{\text{sol}}^2 + m_{\text{atm}}^2}, 0 \right), & \text{for IO}, \end{cases} \quad (\text{III.8})$$

where  $m_{\text{sol}}^2$  and  $m_{\text{atm}}^2$  are solar and atmospheric mass squared differences, and the leptonic mixing matrix,  $U_{\text{PMNS}}$ , which is parameterized as in Ref. [209]. The relevant parameters for us are one Dirac phase,  $\delta$ , and two Majorana CP phases,  $\alpha_1$  and  $\alpha_2$ . While the mixing angles are relatively precisely determined, the value of the Dirac CP phase is practically unconstrained, and Majorana phases are not testable at neutrino oscillation facilities. We use the values from Ref. [210] in the following:

$$\begin{aligned} m_{\text{sol}}^2 &= 7.39 \times 10^{-23} \text{ GeV}^2, & m_{\text{atm}}^2 &= 2.525 \times 10^{-21} \text{ GeV}^2, \\ \theta_{12} &= 33.62^\circ, & \theta_{23} &= 47.2^\circ, & \theta_{13} &= 8.54^\circ. \end{aligned} \quad (\text{III.9})$$

The size of the elements of the Yukawa sub-matrix  $y'$  are constrained from above due to non-observation of lepton flavor violating processes (LFV) such as  $\ell \rightarrow \ell' \gamma$  and  $\ell \rightarrow 3\ell'$  where  $\ell$  and  $\ell'$  denote different species of charged leptons. The upper bounds on the branching ratios (BR) for these types of decays are given in Ref. [209] and also compiled in Table 1 in Ref. [2]. While we have implemented all available constraints from LFV decays it is worthwhile pointing out that the dominant effect arises from the lack of observation of  $\mu \rightarrow e \gamma$  process. The upper bound on the BR for this process is  $4.2 \times 10^{-13}$  which converts to [206],

$$\left| \sum_{i=2,3} y_{i\mu} y_{ie}^* \right| \lesssim 4.3 \times 10^{-3} \left( \frac{m_\pm}{1 \text{ TeV}} \right)^2, \quad (\text{III.10})$$

for  $m_{N_{2,3}} \simeq 0.1 \text{ TeV}$ .

Finally, the neutrino mass matrix in Eq. (III.5) depends on  $\lambda_5$  which enters in the expression for  $m_S$  and  $m_A$  (see again Eq. (III.4)). This formula actually features a linear

dependence between the neutrino masses and  $\lambda_5$  for small values of  $\lambda_5$  [103]. The parameter  $\lambda_5$  and the entries of  $y'$  depend on each other and jointly set the scale for neutrino mass as  $\sim 0.1$  eV. This means that there is a lower bound  $\lambda_5 \gtrsim \mathcal{O}(10^{-7})$ , calculated for  $m_{\pm} = \mathcal{O}(\text{TeV})$ . In general, the  $\mathbf{Z}_2$ -odd scalar doublet can affect electroweak precision observables, but constraints arising from electroweak precision data [211] are not competitive to the above discussed ones and thus we do not include them in our discussion.

### III.4 Projections for the HL-LHC

In this section we explore the di-lepton and di-tau signatures with missing transverse energy (denoted as  $\cancel{E}_T$ ) due to non-detectable  $N_i$  from  $\sigma^{\pm}$  decays in the final state (see Fig. III.2):<sup>22</sup>

$$pp \rightarrow \sigma^+ \sigma^- \rightarrow \begin{cases} \sigma^{\pm} \rightarrow \ell^{\pm} N_i (\ell = e^{\pm} \text{ or } \mu^{\pm}), \\ \sigma^{\pm} \rightarrow \tau^{\pm} N_i. \end{cases} \quad (\text{III.11})$$

For these event topologies,  $\cancel{E}_T$  is calculated by summing over the observed transverse momenta,

$$\cancel{E}_T \equiv \left| \sum_{\text{vis}} p_T^i \right| = \left| \sum_{\text{vis}} \sqrt{(p_x^i)^2 + (p_y^i)^2} \right|. \quad (\text{III.12})$$

The former signature, for instance, was already applied to the ScM in Ref. [212], where the authors used data from LHC Run-1 to set their limits. Our aim is to extend this search by calculating the projected sensitivities for the HL-LHC using the same analysis techniques as presented in recent ATLAS publications, [213] and [214] for the di-lepton and di-tau channel, respectively. In particular, we are using the results from Run-2 with an integrated luminosity of  $36.1 \text{ fb}^{-1}$  at  $\sqrt{s} = 13 \text{ TeV}$ .<sup>23</sup> Furthermore, we will present both *optimal* and *realistic* projections; the first one is defined such that the BR for a charged scalar decaying into a RHN and a charged lepton considered in the search is set to 1. This case is, however, not feasible in our model, due to the requirement to reproduce the observed neutrino mass differences and mixing angles. Therefore, we also define realistic projections by maximizing the respective Yukawa couplings. This will lead to BRs smaller than one.

The model files were created with `FeynRules` [216]. The signal processes, as shown in Fig. III.2, were simulated at leading order with `MadGraph5_aMC@NLO_2.6.3.2` [217] interfaced with `Pythia8` [218] for showering the events and `Delphes_3.4.1` [219] was used for a fast detector simulation. By using these tools, we were able to reproduce the results given in Refs. [213, 214].

In Fig. III.3 we show the expected cross section for  $pp \rightarrow \sigma^{\pm} \sigma^{\mp}$  pair production,  $\sigma^{\text{prod}}$ , for different center-of-mass energies and masses. One can already conclude that large luminosities are needed to see a significant number of events inside the detector. For definiteness we have fixed the portal couplings to

$$\lambda_3 = 0.3, \quad \lambda_4 = 0.5, \quad \lambda_5 = 10^{-4}. \quad (\text{III.13})$$

For us, the most relevant parameter in the scalar sector is the physical mass of the charged scalar,  $m_{\pm}$ , and it is this quantity that will appear in all our sensitivity projections.

<sup>22</sup> We did not consider the additional  $A^0$  and  $S^0$  production, because they are sub-dominant compared to  $\sigma^{\pm}$  pair production.

<sup>23</sup> Meanwhile, the ATLAS collaboration published new results for the di-lepton final state based on a search at  $139 \text{ fb}^{-1}$  [215]. Although this analysis can place stronger limits on the parameter range studied, we have not explicitly included it because we are primarily focused on future experiments. With an in-depth analysis, it may be possible to test at least a small portion of the parameter range of our model with available data.

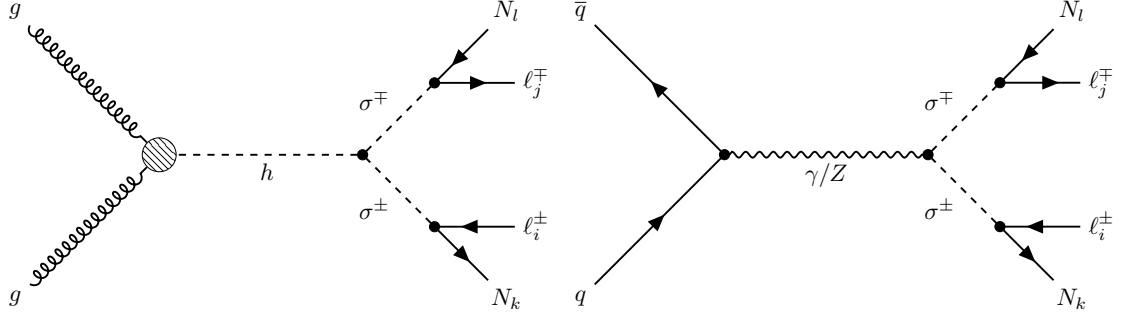


Figure III.2: Production channels for the  $\ell_i \ell_j + \cancel{E}_T$  process at the LHC. Pair produced charged scalars decay into heavy leptons  $N_{2,3}$  and charged SM leptons ( $e, \mu$  or  $\tau$ ).

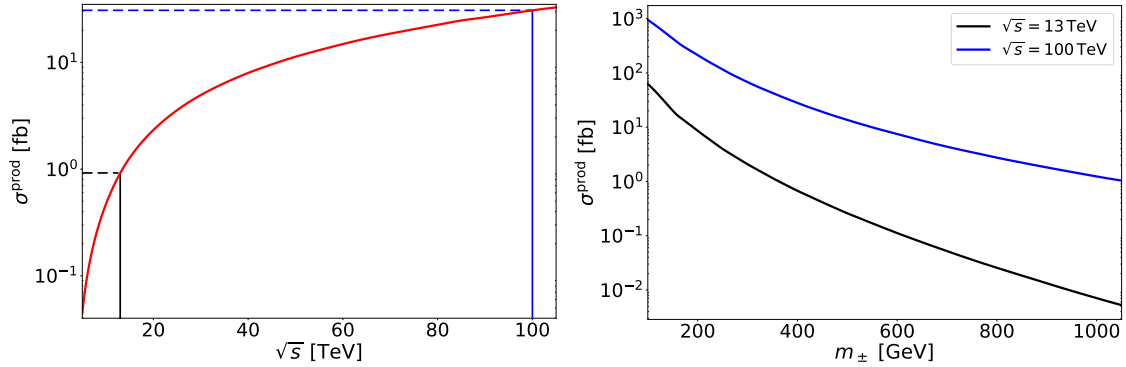


Figure III.3: Cross section  $\sigma^{\text{prod}}$  for pair production of charged scalars  $\sigma^\pm$ . The left panel shows the increase of  $\sigma^{\text{prod}}$  for different center-of-mass energies and fixed scalar mass,  $m_\pm = 400$  GeV. The black (blue) vertical lines indicate the energy range of the LHC (FCC-hh) and dashed lines indicate to the respective cross section of the experiment. In the right panel we show  $\sigma^{\text{prod}}$  for different scalar masses and fixed energy. By increasing  $m_\pm$  the cross section drops significantly.

We assume that  $m_{N_2} = m_{N_3}$  in the following, but in general we could take a hierarchical spectrum as well, i.e.  $m_{N_2} < m_{N_3}$  or vice versa. A hierarchical spectrum would, however, weaken the search strategy because in this case decays  $\sigma^\pm \rightarrow \ell^\pm N_3$  are more likely to yield soft leptons due to the smaller mass gap between  $\sigma^\pm$  and  $N_3$ . On the other hand, this could give rise to interesting event topologies, because  $N_3$  can decay inside of the detector into two leptons and  $N_2$  and this would possibly create multi-lepton +  $\cancel{E}_T$  signatures. However, we are going to focus on the di-tau +  $\cancel{E}_T$  and di-lepton +  $\cancel{E}_T$  searches within the degenerate spectrum.

### III.4.1 Di-tau + $\cancel{E}_T$ signature

Following the procedure outlined in Ref. [214], the following cuts were applied after event reconstruction: events shall contain no  $b$ -jet but at least two tau leptons with opposite charges. The invariant mass of every tau pair has to be larger than 12 GeV and must be 10 GeV away from the mean visible  $Z$  boson mass, set at 79 GeV.<sup>24</sup> Then, two different trigger setups are defined. The asymmetric trigger requires  $p_T^1 > 85$  GeV and  $p_T^2 > 50$  GeV for the first two  $p_T$  ordered tau leptons. Second, there is the  $\cancel{E}_T$  trigger set by  $p_T^1 > 35$  GeV,  $p_T^2 > 25$  GeV and  $\cancel{E}_T > 50$  GeV. For further discrimination from SM background, the so-

<sup>24</sup> The mean visible mass of the  $Z$  boson is smaller than its physical mass, because is reconstructed from a sample of  $Z \rightarrow \tau^+ \tau^-$  events [214].

called *transverse* mass [220, 221],  $m_{T_2}$ , is introduced. It is of particular interest in event topologies where pair produced particles decay into a directly visible final state and an invisible one. It is defined by

$$m_{T_2}^2 \equiv \min_{\mathbf{p}_1 + \mathbf{p}_2 = \mathbf{p}_T} [\max \{m_T^2(\mathbf{p}_{T\ell^-}, \mathbf{p}_1), m_T^2(\mathbf{p}_{T\ell^+}, \mathbf{p}_2)\}] \quad (\text{III.14})$$

$$\text{with } m_T(\mathbf{p}_T, \mathbf{q}_T) = \sqrt{2(p_T q_T - \mathbf{p}_T \cdot \mathbf{q}_T)},$$

where we have to minimize the larger of the two transverse masses  $m_T$  using the two-dimensional transverse momenta  $\mathbf{p}_1$  and  $\mathbf{p}_2$  such that their sum reproduces the observed missing momentum  $\mathbf{p}_T$ . Further,  $\mathbf{p}_{T\ell^-}$  and  $\mathbf{p}_{T\ell^+}$  are the transverse momenta of the visible charged leptons.

Finally, two signal regions based on  $m_{T_2}$  and  $\cancel{E}_T$  cuts were defined as shown in Table III.1. They are chosen such that different mass gaps between  $\sigma^\pm$  and  $N_{2,3}$  can be covered, due

SR-lowMass	SR-highMass	
$m_{T_2} > 70 \text{ GeV}$	$m_{T_2} > 70 \text{ GeV} \ \& \ m(\tau_1, \tau_2) > 110 \text{ GeV}$	
$\cancel{E}_T$ trigger	$\cancel{E}_T$ trigger	asymmetric trigger
$\cancel{E}_T > 150 \text{ GeV}$	$\cancel{E}_T > 150 \text{ GeV}$	$\cancel{E}_T > 110 \text{ GeV}$
$p_T^1 > 50 \text{ GeV}$	$p_T^1 > 80 \text{ GeV}$	$p_T^1 > 95 \text{ GeV}$
$p_T^2 > 40 \text{ GeV}$	$p_T^2 > 40 \text{ GeV}$	$p_T^2 > 65 \text{ GeV}$

Table III.1: Signal regions with the corresponding cuts on final state momenta used in the di-tau analysis. The definition of the respective triggers are explained in the text.

to the different cuts employed on the  $p_T$  of the tau final states. The 95% CL upper limits on the cross sections are summarized in Table III.2.

signal region	$N_{\text{obs}}$	obs. $\sigma_{\text{vis}}^{95} [\text{fb}]$
SR-lowMass	10	0.26
SR-highMass	5	0.20

Table III.2: 95% CL limits on the non-SM cross section for the di-tau +  $\cancel{E}_T$  analysis.

The final cross section in our model is determined by the product

$$\sigma(pp \rightarrow \ell_i^\pm \ell_j^\mp N_k N_l) = \sigma(pp \rightarrow \sigma^\pm \sigma^\mp) \times \text{BR}(\sigma^\pm \rightarrow \ell_i^\pm N_k) \times \text{BR}(\sigma^\mp \rightarrow \ell_j^\mp N_l). \quad (\text{III.15})$$

The cross section can be increased by maximizing the respective BRs. The latter can be achieved by making use of unconstrained parameters. In particular, we took the complex angle  $\theta = \omega - i\eta$  (see Eq. (III.7)), the Majorana phase  $\alpha_2$  and the CP phase  $\delta$  as free parameters<sup>25</sup> and maximized the expression

$$\frac{y_{2\tau}(\omega, \eta, \alpha_2, \delta)^2 + y_{3\tau}(\omega, \eta, \alpha_2, \delta)^2}{\sum_{k=2,3} \sum_i y_{ki}(\omega, \eta, \alpha_2, \delta)^2}. \quad (\text{III.16})$$

The parameter values that correspond to the extremum are in what follows denoted as  $\omega_0, \eta_0, \alpha_2^0, \delta_0$ . We have performed this procedure for both NO and IO neutrino masses and the corresponding minimization results are given in Table III.3.

For calculating the sensitivity curves we fixed the portal couplings  $\lambda_i$  (see Eq. (III.13))

<sup>25</sup> We allowed  $\delta$  to float in the range  $(135^\circ, 366^\circ)$  which corresponds to a  $3\sigma$  range from recent fits. We found that the second Majorana phase  $\alpha_1$  does not affect the minimization.



	$\omega_0$	$\eta_0$	$\alpha_2^0$	$\delta_0$	$\text{BR}(\sigma^\pm \rightarrow \tau^\pm N_k)$
NO	1.61	$> 2$	$\pi$	$2\pi$	38.26 %
IO	1.31	$> 2$	$-\pi$	$\pi$	27.30 %

Table III.3: Largest possible BRs for the decay of  $\sigma^\pm$  into  $\tau$  and  $N_{2,3}$ . Above the given value for  $\eta_0$ , the BRs are to a good approximation independent of this parameter. As can be seen, the IO gives rise to smaller BRs compared to NO.

such that  $\sigma^\pm$  is the lightest  $\mathbf{Z}_2$ -odd scalar, forbidding possible decays into the other scalars. We scanned over the charged scalar mass as well as the heavy lepton masses  $m_{N_{2,3}}$ ; our grid spans  $m_\pm \in (150 \text{ GeV}, 600 \text{ GeV})$  and  $m_{N_{2,3}} \in (10 \text{ GeV}, m_\pm)$  and we simulated  $10^4$  events for each point.

We compared the simulation with the ATLAS results derived at  $36.1 \text{ fb}^{-1}$  and found that the corresponding sensitivities are not strong enough to place limits. The reason is twofold: first, the cross section for the pair production in the model is significantly smaller than the one in the simplified model used in the ATLAS analysis. Second, the analysis uses specific cuts on kinematic variables which do suppress SM background but unfortunately also cut away a significant portion of signal events. For instance, the “best case” benchmark point, where we set the BR into tau leptons equal to one) features only a small surviving cross section:

$$m_{N_{2,3}} = 10 \text{ GeV}, m_\pm = 200 \text{ GeV} \quad \Rightarrow \quad \text{SR-highMass: } \sigma_{\text{vis}} = (0.15 \pm 0.06) \text{ fb.}$$

Taking the Casas-Ibarra parametrization into account and inserting model-dependent BRs, the situation gets even worse as the cross section is further reduced due to non-maximal BR into tau leptons.

This finding motivated us to go beyond the current experimental results and consider a similar search at the foreseen HL-LHC facility at CERN which will deliver a final integrated luminosity of up to  $4000 \text{ fb}^{-1}$  at  $\sqrt{s} = 14 \text{ TeV}$  [222]. This would lead to a huge increase in potential signal events. To estimate the potential of HL-LHC to test the ScM we conduct a similar analysis as in Ref. [214] but use a projected sensitivity,

$$\mathcal{S} = \frac{S}{\sqrt{S+B}}, \quad (\text{III.17})$$

instead, where  $S$  and  $B$  represent signal and background events, respectively. This formula is derived in the limit  $S/B \ll 1$  from the general expression for the case of exclusion limits,

$$\mathcal{S}_1 = \sqrt{2 \left( S - B \log \left( 1 + \frac{S}{B} \right) \right)}, \quad (\text{III.18})$$

obtained using the procedure described in Ref. [223].

By using the same signal regions as in the previous analysis and assuming a similar scaling of signal and background for the increased center of mass energies and luminosities we can now redo the cut and count analysis for the increased event rates. As can be seen in Fig. III.4, where we show the corresponding exclusion limits as solid lines, this allows us to significantly enhance the testable parameter space. For such high luminosities, scalar masses of up to 420 GeV and respective RHN masses of 170 GeV can be tested and there is even a potential discovery region for scalar masses between 200 and 300 GeV. The sharp drop for large masses is due to a decrease in the pair production cross section. The cuts on the kinematic variables, such as transverse momentum  $p_T$  and transverse mass  $m_{T2}$ ,

need a sufficiently large mass gap between  $\sigma^\pm$  and  $m_{N_{2,3}}$  which bounds the accessible parameter space from above and also from the left, because charged scalar cannot not be too light, as in this regions leptons are too soft. We also show in dashed the corresponding sensitivity curves for the optimal case where the BR into tau is equal to one. As expected, the sensitivities improve in this case, however we have not found such scenario in our numerical procedure (see Table III.3); the BRs for the decay into pair of tau leptons can be at most around 40%.

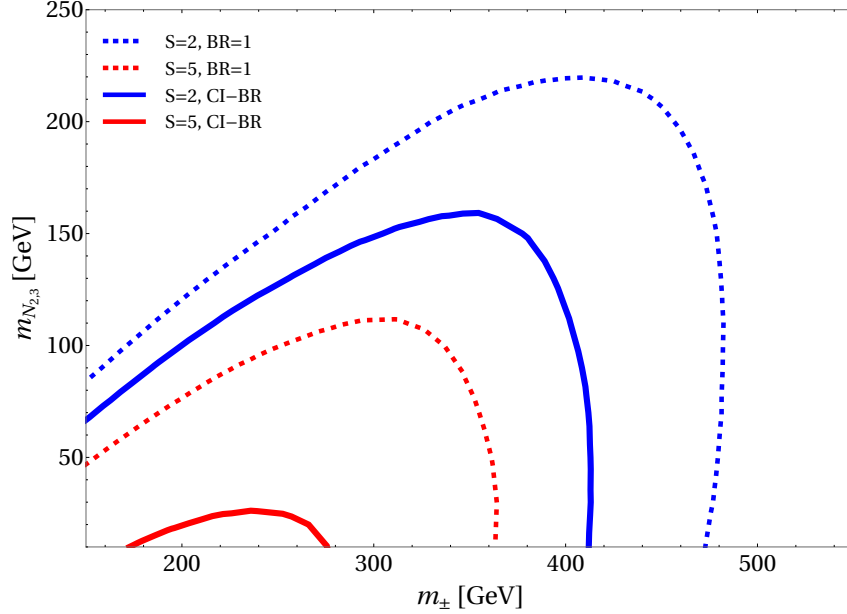


Figure III.4: Projected sensitivities for HL-LHC using  $\mathcal{L} = 4000 \text{ fb}^{-1}$  and the same analysis techniques as in Ref. [214]. Given in blue are exclusion limits,  $\mathcal{S} = 2$ , and shown in red are discovery limits, where  $\mathcal{S} = 5$ . The dashed lines correspond to a 100% BR into tau leptons using the Casas-Ibarra parametrization, whereas the solid lines represent the case in which the maximized BR for NO (shown in Table III.3) is employed.

### III.4.2 Di-lepton + $\cancel{E}_T$ signature

Now we turn our attention to the di-lepton +  $\cancel{E}_T$  channel: following the procedure outlined in Ref. [213], the following cuts were applied after event reconstruction and preselection: the invariant di-lepton mass  $m_{\ell\ell}$  should be larger than 40 GeV. Events should not contain any  $b$ -jet with  $p_T > 20$  GeV nor a jet with  $p_T > 60$  GeV. In the  $2\ell + 0\text{jets}$  channel, six different signal regions were defined: four are aiming for different flavor (DF) leptons in the final states and two for leptons with the same flavor (SF). All regions are inclusively defined and mainly separated by increasing cuts on the invariant mass of the lepton pair and  $m_{T2}$ , ranging from  $m_{\ell\ell} > 110$  GeV to  $m_{\ell\ell} > 300$  GeV and  $m_{T2} > 100$  GeV to  $m_{T2} > 300$  GeV. The 95% CL upper limits on the cross sections are summarized in Table III.4.

In contrast to Section III.4.1 we now want to minimize the expression given in Eq. (III.16) in order to maximize the possible BRs into leptons. Under the same assumptions as before and taking both, NO and IO regimes into account we obtain the results given in Table III.5. From the respective BRs we can calculate the suppression factor  $B$  of the pair production cross section according to

$$B \equiv \sum_{\substack{k=2,3 \\ i=e,\mu}} \text{BR}(N_k \ell_i)^2 + \sum_{\substack{k,l=2,3 \\ i,j=e,\mu \\ k \neq l \vee i \neq j}} \text{BR}(N_k \ell_i) \text{BR}(N_l \ell_j). \quad (\text{III.19})$$

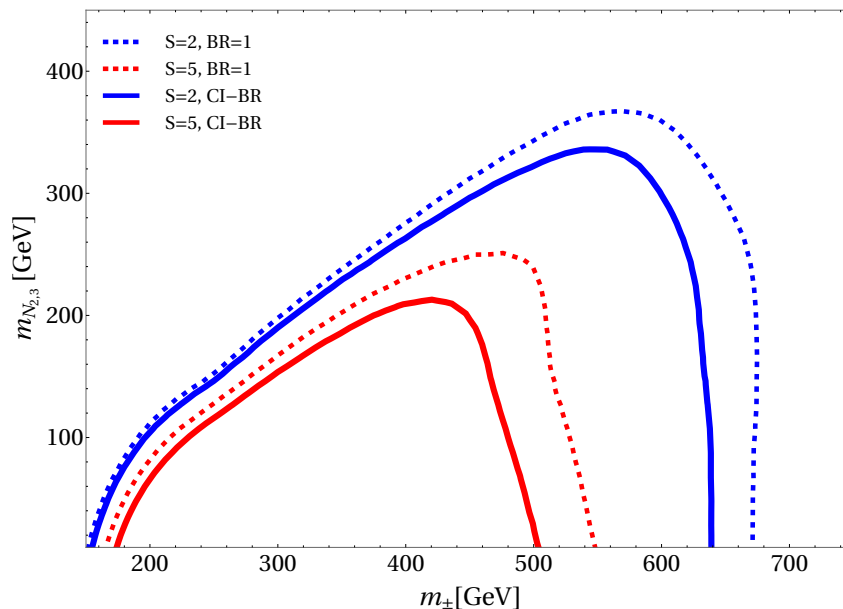
signal region	$m_{\ell\ell}$ [GeV]	$m_{T_2}$ [GeV]	$N_{\text{obs}}$	obs. $\sigma_{\text{vis}}^{95}$ [fb]
SF-loose	$> 100$	$> 111$	153	2.02
SF-tight	$> 130$	$> 300$	9	0.29
DF-100	$> 100$	$> 111$	78	0.88
DF-150	$> 150$	$> 111$	11	0.32
DF-200	$> 200$	$> 111$	6	0.33
DF-300	$> 300$	$> 111$	2	0.18

 Table III.4: 95% CL limits on the non-SM cross section for the di-lepton +  $\cancel{E}_T$  analysis.

	$\omega_0$	$\eta_0$	$\alpha_2^0$	$\delta_0$	BR( $\sigma \rightarrow \ell_i N_k$ )
NO	2.37	$< -2$	$\pi$	$2\pi$	86.42%
IO	3.07	$< -2$	$-\pi$	$\pi$	99.75%

 Table III.5: Largest possible BRs for the decay of  $\sigma^\pm$  into  $e^\pm, u^\pm$ . Below the given value for  $\eta_0$ , the BRs are to a good approximation independent of this parameter. Interestingly, the IO regime can feature a situation with a very small BR into tau's, implying approximate zeros in the third column of the Yukawa matrix.

The first sum corresponds to SF lepton channels, whereas the second term sums over DF leptons as final state particles. We introduced the shorthand notation  $\text{BR}(N_k \ell_i) \equiv \text{BR}(\sigma^\pm \rightarrow \ell_i^\pm N_k)$ . Inserting for instance the BR for NO (Table III.5), the final suppression factor is  $B \approx 75\%$ . While IO yields larger  $B$  values, we present our results for NO, as we did in Section III.4.1, since NO is favored by roughly  $3\sigma$  by a global fit analysis of neutrino oscillation data [210]. The sensitivities are shown in Fig. III.5 and by comparing


 Figure III.5: Projected sensitivities for HL-LHC using  $\mathcal{L} = 4000 \text{ fb}^{-1}$  and the same analysis techniques as [213]. Given in blue are exclusion limits,  $\mathcal{S} = 2$ , and shown in red are discovery limits, where  $\mathcal{S} = 5$ . The dashed lines correspond to optimal BR into leptons, whereas to obtain the solid lines we used the value for NO given in Table III.5.

them to the results from Fig. III.4 it can be seen that the di-lepton search offers stronger sensitivities for the parameter space. This is a result of the much cleaner signature resulting

from light leptons in the final state. Unlike taus, they do not decay hadronically and can be reconstructed more easily, which prevents misidentification of events.

The di-lepton search constrains scalar masses up to 650 GeV and it is interesting to go beyond the energy range of the HL-LHC and consider proposed future hadron and lepton colliders to check how much of the parameter space can be probed in the future. In the following, we will stick to the di-lepton search only, as the results from this section clearly indicate stronger sensitivities compared to the di-tau analysis.

## III.5 Projections for future colliders

The HL-LHC projections presented in Section III.4 allow us to test a sizeable region of parameter space below  $\mathcal{O}(\text{few } 100 \text{ GeV})$  for scalar masses, but to reach the TeV-scale and go even beyond requires future hadron and lepton colliders. We will discuss the corresponding projections in the following section.

### III.5.1 FCC-hh

We start by discussing the ScM in the context of a future circular hadron collider, dubbed FCC-hh [224]. For this purpose, we follow Ref. [225], where an opposite-sign-di-lepton (OSDL) final state with missing energy is discussed with the goal of finding TeV-scale winos and light binos. In contrast to the previous analyses, the following variables were used in the analysis to define cuts: first,  $M_{\text{eff}}$ , which is the scalar sum of the  $p_T$  of leptons, jets and missing transverse energy,

$$M_{\text{eff}} = \sum_{\text{leptons}} p_T + \sum_{\text{jets}} p_T + \cancel{E}_T. \quad (\text{III.20})$$

Based on this variable,  $M'_{\text{eff}} = M_{\text{eff}} - p_T(\ell_1)$  is introduced, where  $p_T(\ell_1)$  is the  $p_T$  value of the harder of the two final state leptons. Further, the invariant mass of the same flavor opposite sign (SFOS) lepton pair, mSFOS, is used and, finally, the transverse mass  $m_T$ . We simulated signal events for different mass parameters using the same pipeline as in Section III.4. To ensure that our simulations are comparable to those in Ref. [225], the most dominant backgrounds from di-boson intermediate states,  $WW$  and  $WZ$ , were also simulated and compared to the cut flow given in Ref. [225]. Our results are presented in Table III.6. Besides the cuts explicitly mentioned, the *Baseline* cut requires additionally that SFOS di-leptons have  $\text{mSFOS} > 12 \text{ GeV}$  and that the mSFOS closest to the  $Z$  mass,  $m_Z$ , denoted by  $\text{mSFOS}(Z)$ , fulfills  $|\text{mSFOS} - m_Z| > 30 \text{ GeV}$ . Further, the transverse momentum of the lepton pair,  $p_T(\ell\ell)$ , should be larger than 30 GeV. Finally, it is required that either  $\cancel{E}_T > 100 \text{ GeV}$  or that  $p_T(\ell_1) > 100 \text{ GeV}$ .

Since we generally find that the number of events for signal and background are of the same order, the significance given in Eq. (III.17) is not a good approximation and, hence, for exclusions we use Eq. (III.18), while for discoveries we employ [223]

$$\mathcal{S}_0 = \sqrt{2 \left( (S + B) \log \left( 1 + \frac{S}{B} \right) - S \right)}. \quad (\text{III.21})$$

We summarize our results on the parameter space exclusion capability at FCC-hh with two different luminosities,  $\mathcal{L} = 3 \text{ ab}^{-1}$  and  $\mathcal{L} = 30 \text{ ab}^{-1}$  in Fig. III.6. Both contours corresponding to  $\mathcal{S}_1 = 2$  and  $\mathcal{S}_0 = 5$  are derived for the maximal BRs into electrons and muons for the case of NO (see Table III.5). This scenario is dubbed “best case” in Fig. III.6 and it can be inferred that for such couplings FCC-hh will provide the possibility to probe a large portion of parameter space. In the final luminosity stage, it will be possible to test scalar masses up to 2 TeV and RHN masses of 1.4 TeV.

Cut	$S$	$B$	$\mathcal{S}_0$	$\mathcal{S}_1$
Baseline	351	$5.9 \times 10^5$	0.5	0.5
$M'_{eff} > 1100$ GeV	90	625	3.5	3.4
$m_T(\cancel{E}_T, l_1 + l_2) > 1100$ GeV	90	234	5.5	5.3
$\cancel{E}_T / M_{eff} > 0.36$	33	63	3.9	3.6
$p_T(l_2)/p_T(l_1) > 0.24$	19	18	3.8	3.4

Table III.6: Cuts made for distinguishing signal and background at FCC-hh with a luminosity of  $3 \text{ ab}^{-1}$ . We show the number of signal and background events for  $m_{N_{2,3}} = 500$  GeV and  $m_{\pm} = 1$  TeV. In contrast to Eq. (III.13),  $\lambda_3 = -0.27$  was used in this analysis. No systematic errors on the background were assumed for this analysis.

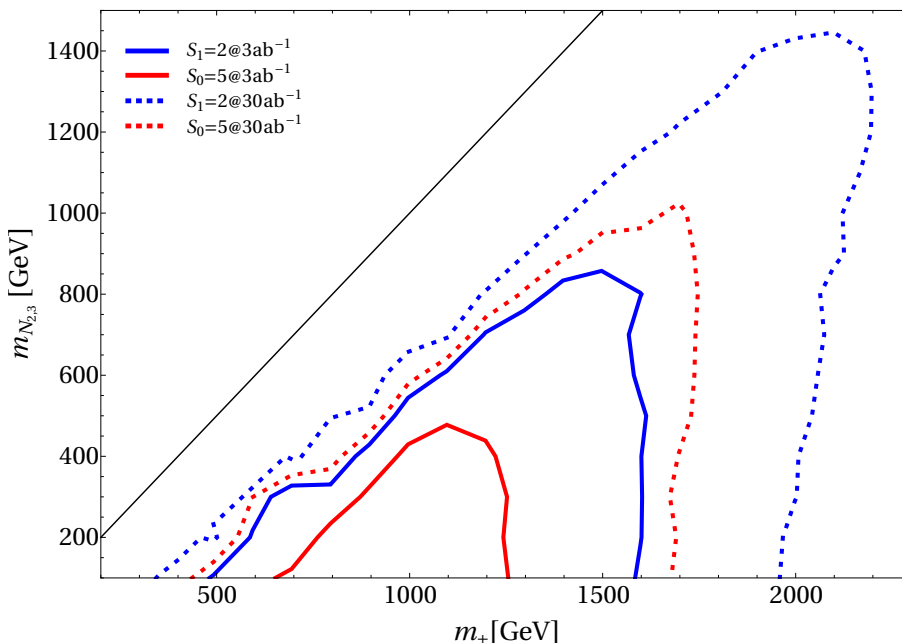


Figure III.6: Sensitivity of FCC-hh with  $\mathcal{L} = 3 \text{ ab}^{-1}$  ( $30 \text{ ab}^{-1}$ ) is shown with solid (dashed) lines. The analysis is based on a proposed search for a supersymmetric (SUSY) model presented in Ref. [225]. The red and blue curves correspond to the “best case” scenario with maximized couplings to  $e, \mu$ , indicating that a significant portion of the parameter space can be probed at FCC-hh. The situation further improves for larger luminosity. The thin black line corresponds to  $m_{N_{2,3}} = m_{\pm}$ .

### III.5.2 CLIC

The Compact Linear Collider (CLIC) [226] is a proposed  $e^+e^-$  collider that will operate in three stages with  $\sqrt{s} = 380$  GeV, 1.5 TeV, and 3 TeV, respectively [226, 227]. In the following, however, we restrict ourselves to the latter case as it offers the possibility to test the largest parameter space of  $\mathbf{Z}_2$ -odd particle masses in comparison to the two other stages. As for the FCC-hh analysis, we consider the di-lepton +  $\cancel{E}_T$  signal.

At  $e^+e^-$  colliders there are two complementary processes to produce  $\sigma^{\pm}$  in our model as shown in Fig. III.7: one is through the exchange of a  $Z$  boson or a photon in the  $s$ -channel,<sup>26</sup> another possibility is via RHNs in the  $t$ -channel. In the latter case, the

<sup>26</sup> In this case, the  $s$ -channel Higgs exchange diagram is negligible, because of the small Higgs-electron Yukawa couplings.

production cross section is proportional to the corresponding Yukawa coupling  $y_{m1}$  and we have checked that this production channel is subdominant for the size of Yukawa couplings employed in this work.

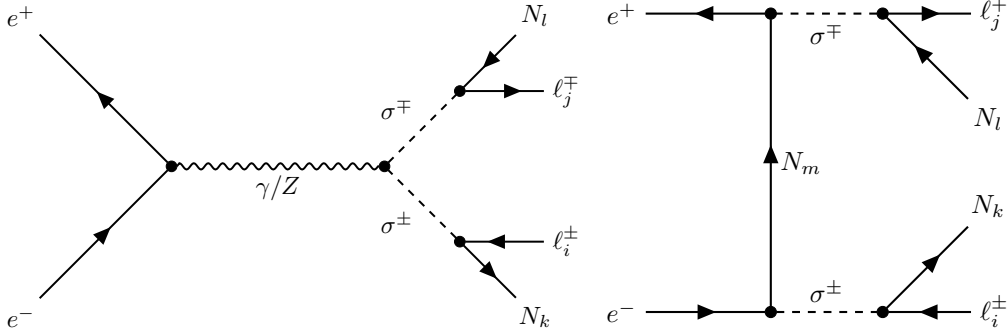


Figure III.7: Production channels for the  $\ell_i \ell_j + \cancel{E}_T$  process at CLIC. The left process is similar to hadron colliders, except for electrons in the initial state. Additionally, production via  $e^+e^-$  collision can happen via a RHN mediated  $t$ -channel diagram, although it is suppressed due to Yukawa couplings  $y$ .

The most outstanding advantage that lepton colliders offer with respect to hadron colliders is the clean signal; without parton distribution functions to be considered, missing energy and momentum can be reconstructed to a large precision and the distributions of the corresponding kinematic variables are not as smeared out as for parton collision where a wide range of energies is involved. Furthermore, background events due to quantum chromodynamics (QCD) processes are reduced compared to pure electroweak processes which is particularly relevant for our search analysis.

For general background rejection, we make the following preselection cuts: to remove QCD processes, we require the final state to contain no jets. Furthermore, we require exactly two leptons of opposite charge and that  $\cancel{E}_T$  exceeds 100 GeV. The last cut suppresses most of the  $e^+e^- \rightarrow \ell^+ \ell^-$  background.

The dominant background after the preselection cuts is  $e^+e^- \rightarrow \ell^+ \ell^- \nu \bar{\nu}$  and in the following this is the only background process we consider. In the case of  $\tau$  leptons in the final state, only those events in which  $\tau$  decay leptonically are considered; thus in this case there are four final state neutrinos. We have checked that any other SM background gives a negligible contribution after the above preselection cuts. A very promising result for the exclusion limits was found by choosing cuts as given in Table III.7.

The variables  $m_{\text{SFOS}}$  and  $M_{\text{eff}}$ , already employed for our FCC-hh analysis, were reused for CLIC because of their great potential for discriminating the ScM, with its comparatively large masses of  $\mathbf{Z}_2$ -odd particles, against the SM. Their cuts are parameter dependent, because they are derived by maximizing  $\mathcal{S}_1$  for different parameter choices in the considered mass range. Furthermore, the pseudorapidity of the first lepton,  $\eta(\ell_1)$ , turns out to be a very useful variable; it peaks at large values for the SM background while most of the signal events are more central in this variable. It is defined in terms of the angle  $\phi$  between lepton track and beam pipe by  $\eta(\ell_1) = -\ln \tan(\phi/2)$ .

A further suppression of the background can be made by utilizing the kinematics of this process. In the di-lepton search at CLIC, we can reconstruct the four-momenta of the two RHNs (denoted by  $p_{3,4}^\mu$  in what follows) by using only the initial state energy  $\sqrt{s}$  and the known four-momenta of the two charged leptons ( $p_{1,2}^\mu$ ). Four out of these eight unknowns are fixed by four-momentum conservation, namely  $\sum_{i=1}^4 p_i^\mu = (\sqrt{s}, 0, 0, 0)$ . Furthermore,

Cut	SR “best case”			
	$S$	$B$	$\mathcal{S}_0$	$\mathcal{S}_1$
preselection	4101	$1.0 \times 10^6$	4.1	4.1
$M_{eff} > 0.5 \mu_2 - 1.2 m_{N_{2,3}} + 1000 \text{ GeV}$	3442	$2.7 \times 10^5$	6.6	6.6
$m\text{SFOS} > -0.1 \mu_2 - 0.3 m_{N_{2,3}} + 530 \text{ GeV}$	3260	$2.2 \times 10^5$	6.9	6.8
$ \eta(l_1)  < 0.6$	2502	$2.1 \times 10^4$	16.9	16.6
kinematics	2136	908	55.6	45.6
Cut	SR “worst case”			
	$S$	$B$	$\mathcal{S}_0$	$\mathcal{S}_1$
preselection	1188	$1.0 \times 10^6$	1.2	1.2
$m\text{SFOS} > -0.3 m_{N_{2,3}} + 130 \text{ GeV}$	1153	$9.7 \times 10^5$	1.2	1.2
$ \eta(l_1)  < 0.6$	800	$1.2 \times 10^5$	2.3	2.3
kinematics	386	2806	7.1	7.0

Table III.7: Signal regions used for an analysis at CLIC with a center of mass energy of 3 TeV and a luminosity of  $5 \text{ ab}^{-1}$ . We show the number of signal and background events together with the corresponding sensitivities for a benchmark point  $m_{N_{2,3}} = 500 \text{ GeV}$  and  $m_{\pm} = 1 \text{ TeV}$ . The results are shown both for “best” and “worst” case scenarios which correspond to maximizing couplings to  $e$ ,  $\mu$  and  $\tau$  lepton, respectively.

imposing that all intermediate and final state particles are on-shell yields the following relations:

$$(p_1 + p_3)^2 = m_{\pm}^2 = (p_2 + p_4)^2, \quad p_3^2 = p_4^2 = m_{N_{2,3}}^2. \quad (\text{III.22})$$

In total, we end up with a solvable system of equations. For separating signal and background events we use that the latter ones typically have different kinematic properties, since the mass of the intermediate particle is for instance set by the  $W$  boson mass. After requiring that there is a physical solution to the aforementioned equations, i.e. we demand the momenta of the invisible particles to be real valued and that there is no real valued solution if  $m_{\pm}^2$  and  $m_{N_{2,3}}^2$  in Eq. (III.22) get replaced with the  $W$  boson and active neutrino mass, respectively, we reach the following effect: the number of signal events typically decreases only by  $\simeq 30\%$ , whereas background is strongly reduced, at most only a few percent of such events survive this cut. In reality, the four-momenta in Eq. (III.22) are only known to a finite precision. So it is crucial to include the finite detector resolution by using the respective `Delphes` card for the CLIC detector which is based on Ref. [228]. For this reason, the simulated  $p_T$  values experience a smearing with respect to the detector resolution. This last step allows for an efficient background suppression as can be seen in Table III.7.

We wish to stress that the cuts on  $m\text{SFOS}$  and  $M_{\text{eff}}$  are not optimal for each parameter point since we only used a simple function of the model parameters. Still, the resulting exclusion limits, shown in Fig. III.8, already indicate the great potential for testing this model setup at CLIC. For this case,  $\mathcal{S}_1 = 2$  and  $\mathcal{S}_0 = 5$  curves reach similar limits for these two cases. This is a consequence of the aforementioned use of kinematics: due to the suppression of background events, we find large sensitivity values across the parameter space. Although the “worst case” features fewer event rates due to smaller BRs, it still yields a sizable sensitivity after cutting the background, in contrast to FCC sensitivities. Even for the “worst case” with a large number of surviving background events, systematic uncertainties are negligible, because according to Ref. [226], they amount only to 0.3%.

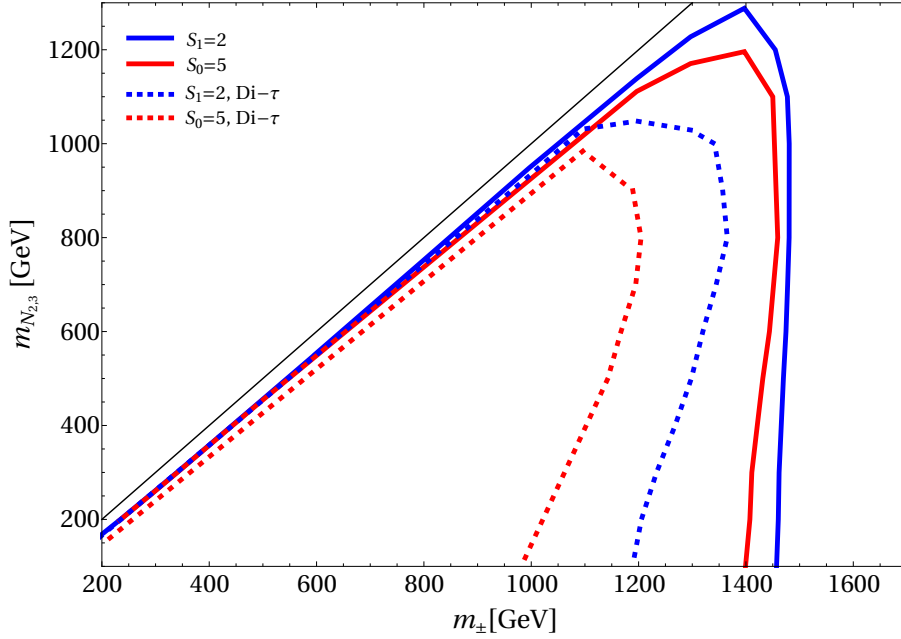


Figure III.8: CLIC sensitivity for the di-lepton search. Using maximized couplings to  $e, \mu$  we obtained the red solid contour that corresponds to a  $5\sigma$  discovery and the blue one that represents  $2\sigma$  exclusion. The corresponding dashed contours are for the case where  $\tau$  couplings are maximized. The thin black line indicates  $m_{N_{2,3}} = m_{\pm}$ .

In comparison with FCC-hh sensitivities at  $3 \text{ ab}^{-1}$ , CLIC can test for higher RHN masses while being less sensitive to  $\sigma^{\pm}$  masses larger than 1400 GeV. However, with a total center of mass energy of 3000 GeV this is expected. Overall, CLIC offers a testable parameter space which is comparable to the FCC-hh result. While the reach at CLIC is not as large in comparison to FCC-hh with  $30 \text{ ab}^{-1}$ , we note that, unlike FCC-hh, CLIC can nearly close the available kinematic window in the vicinity of  $m_{N_{2,3}} = m_{\pm}$ .

In conclusion, we have shown in this section that both lepton and hadron colliders offer promising and complementary ways to look for the considered ScM spectrum.



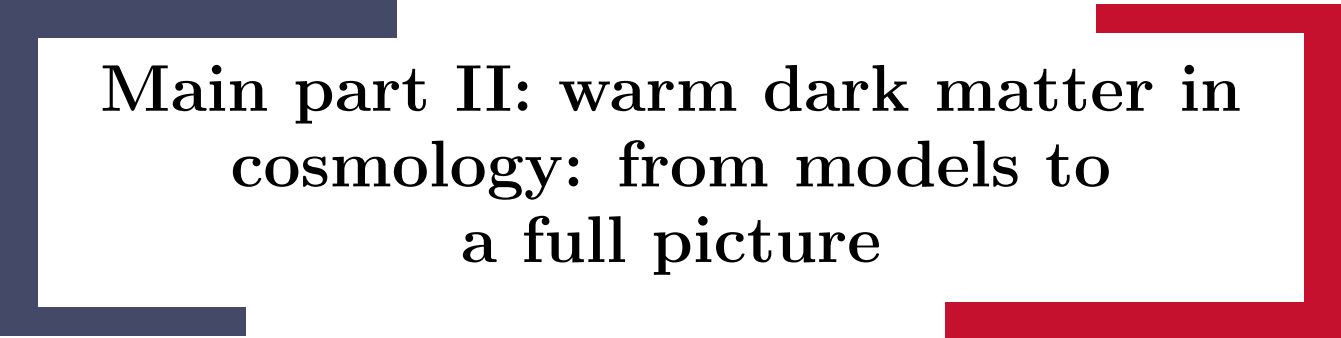
## III.6 Summary of Chapter III

The ScM is a very popular extension of the Standard Model which can explain both neutrino masses and the origin of DM. In this chapter we focused on the case of keV-scale fermionic DM with the mass of remaining  $\mathbf{Z}_2$ -odd fermion and scalar degrees of freedom at  $\mathcal{O}(100)$  GeV and explored the collider phenomenology of this model setup. In particular we studied  $pp \rightarrow \sigma^\pm \sigma^\mp \rightarrow \ell^\pm \ell^\mp + \cancel{E}_T$  channels. We demonstrated that testing this model at colliders strongly relies on forthcoming stages of the LHC as well as future colliders since we were not able to extract robust bounds by using  $36.1 \text{ fb}^{-1}$  data. Although the LHC delivered now  $139 \text{ fb}^{-1}$  of data at the end of its second run, we were considering HL-LHC with a final luminosity of  $4 \text{ ab}^{-1}$  at  $\sqrt{s} = 14 \text{ TeV}$ , FCC-hh with  $3 \text{ ab}^{-1}$  and  $30 \text{ ab}^{-1}$  at  $\sqrt{s} = 100 \text{ TeV}$  and CLIC with  $5 \text{ ab}^{-1}$  at a center-of-mass energy of  $3 \text{ TeV}$  to set parameter limits as large as possible. For the HL-LHC, we have found that the testable region covers a range up to  $650 \text{ GeV}$  for scalar and up to  $350 \text{ GeV}$  for RHN masses in the di-lepton +  $\cancel{E}_T$  analysis which gives stronger constraints compared to the di-tau +  $\cancel{E}_T$  signature. Designing our own analysis setup to extract constraints based on the future experiment CLIC and FCC-hh we were able to probe a large region of parameter space. The sensitivity reach of CLIC exceeds  $1 \text{ TeV}$  for both RHN and charged scalar masses and FCC-hh with  $3 \text{ ab}^{-1}$  would reach similar limits for the scalar and even larger RHN masses, and this further improves for  $30 \text{ ab}^{-1}$  where RHN masses up to  $2 \text{ TeV}$  would be probed. In particular, we found that CLIC offers the potential to test a compressed ScM spectrum, which, as we discussed in Section III.2, is of particular interest to address several open questions of the SM and explain them in a single BSM framework.

Despite the great discovery and exclusion potential of these experiments, they are nearly independent of the underlying light DM properties. As discussed in Section V.2,  $N_1$  effectively decouples from the spectrum and thus the chance to observe it directly at a collider are virtually absent, as long as the respective BR of  $\sigma^\pm \rightarrow N_1 \ell_\alpha^\pm$  is negligibly small. We will see in the next section, that this is guaranteed by the very small Yukawa couplings required to generate the observed DM abundance. Only by inverting the mass spectrum such that  $m_\pm < m_{N_{2,3}}$ , or for DM with masses of  $\mathcal{O}(\text{MeV})$ , there is the possibility to have  $\sigma^\pm$  particles which travel a few mm before decaying, hence offering the potential for dedicated displaced vertex studies. On the other hand, DM can be pair produced at  $e^+e^-$  colliders, but again the smallness of the corresponding  $N_1$  coupling would make a successful  $\cancel{E}_T + X$  search, where  $X$  can be for instance a photon or a jet, very unlikely.

Luckily, such light DM candidate with masses  $\mathcal{O}(10 \text{ keV})$  leaves an imprint in the history of the early Universe and the formation of structures and we will show in the next chapter how we can use cosmological observations to constrain the model parameter space further, taking the nature of DM into account as well.





**Main part II: warm dark matter in  
cosmology: from models to  
a full picture**

In the first part of the thesis we have seen that it can be quite challenging to observe light and only weakly coupled DM at collider experiments. In the context of the scotogenic model (ScM), collider searches allowed to place limits only on the heavy particles in the model spectrum up to 2 TeV. Direct experimental validation of such light DM candidates requires different setups and search strategies. For example, there are dedicated experiments at the high-luminosity frontier that do not aim for the highest energies, but aim to achieve as many particle collisions as possible to detect rare interactions and elusive particles. Another setup are beam-dump experiments, where highly energetic protons are dumped into dense material to absorb their remnants as much as possible and filter out long-lived stable or at least sufficiently long lived particles which are detected at a distant detector.

Nevertheless, these searches require that a potential light DM candidate has at least some coupling to the SM in order to detect it. If it interacts only gravitationally or evades detection due to too weak couplings, it will still be possible to observe its effects in cosmological observations (if light enough). In the Standard Model of cosmology, the  $\Lambda$ CDM, DM is supposed to be non-relativistic throughout the history of the early Universe and thus it plays a crucial role as the dominant driving force responsible for the formation of structures. On the other hand, light DM can stay relativistic during a significant amount of time in the early Universe which in turn leads to a suppression of structures below a certain scale. Observations targeting the matter profile of the Universe across a wide range of scales allow to search for deviations from the standard scenario due to light DM. Conversely, such surveys can be used to obtain limits on the allowed light DM parameter space; in particular, this can be used to exclude models that would induce more suppression of structures as observed.

Chapter IV is dedicated to explore the phenomenology of light DM in the context of the ScM. We study the impact of late-time produced keV-scale right-handed neutrinos on the formation of light nuclei during Big Bang Nucleosynthesis (BBN) and the suppression of the corresponding matter power spectrum. Further, the contribution to the effective number of relativistic particle species,  $N_{\text{eff}}$  is calculated and we overlap our findings with the results from Chapter III. In Chapter V we consider a light axion-like particle (ALP) DM candidate produced via a freeze-in mechanism in two different scenarios: either the ALP is coupled to photons or SM fermions. Using a half-mode analysis and counting the number of MW subhalos we can place limits on the allowed ALP mass. Finally, in Chapter VI we are following a model-independent as possible approach to analyze DM models, where different production mechanisms can lead to DM subsets with two associated temperatures. The results allow to adapt our limits derived from a MW subhalo count and Lyman- $\alpha$  data for a wide setup of such models.

# The scotogenic model and cosmology

## IV.1 Introduction

In the previous chapter, we have shown that future collider facilities are a promising way to test the scotogenic model (ScM) which is a phenomenological interesting extension of the SM. Although these searches will be able to constrain the masses of the new scalars and right-handed neutrinos (RHN), they do not offer a way to probe the lightest particle,  $N_1$  which is considered to have a mass of  $\mathcal{O}(10 \text{ keV})$ . In fact, from the point of view of experimental validation by these experiments, this particle is effectively detached from the spectrum and the obtained collider limits are essentially independent of the DM properties.

An intriguing and complementary way to constrain DM in the mass window we consider is to turn the gaze away from Earth-based experiments and towards the stars. Information on the distribution of matter in the Universe obtained from various surveys, such as Lyman- $\alpha$  forest probes allow to gather information on structures at different scales and constrain the light DM parameter space. Additionally, light DM which stays relativistic for sufficiently long times can contribute to the effective number of relativistic particle species,  $N_{\text{eff}}$ . We have to consider two different DM production mechanisms: first, we can produce  $N_1$  via a freeze-in of thermalized  $\mathbf{Z}_2$ -odd scalars and, second, via late-time three-body decays of heavy RHNs  $N_{2,3}$ . The latter turns out to create highly energetic, i.e. “hot” DM and thus can have a drastic impact on the considered cosmological quantities. Further, these decays have to happen before the formation of light nuclei takes place during the epoch of big bang nucleosynthesis (BBN) starting at  $T \approx 1 \text{ MeV}$ , or otherwise the abundances of newly formed nuclei are altered by the presence of relativistic DM particles.

This chapter is organized as follows: in Section IV.2 we will review the DM production and explain the constraints from cosmology in Section IV.3. Afterwards, we combine our results from collider searches and limits on the parameter space from cosmological observations in Section IV.4. We summarize our results in Section IV.5.

## IV.2 Light dark matter in the scotogenic model

Since the lightest of the newly introduced particles is stable, it is natural to consider whether it can account for the observed amount of DM in the Universe. In the ScM there are neutral particles both in the fermionic and scalar sector, making them potential candidates. Motivated by the results in the previous chapter, we consider fermionic DM and keep the scalars heavier than the RHNs. It was shown in Refs. [2, 182] that in the ScM with fermionic DM with mass  $\mathcal{O}(100 \text{ GeV})$ , the relic abundance from freeze-out generally strongly exceeds the measured values. There are, however, options how to solve

this problem: first, if additional processes, namely coannihilations of heavy DM with the other new particles, are involved, DM can stay longer in the thermal equilibrium and freeze-out with a much smaller abundance (see for instance Fig. 2 in Ref. [2]). The coannihilations are only effective if the splitting between the DM and scalar mass is tiny. However, considering searches with two leptons in the final state stemming from decays of pair-produced new scalars (see Sections III.4 and III.5), such a scenario would yield soft leptons which are hard to reconstruct and hence freeze-out of  $\mathcal{O}(100 \text{ GeV})$  DM is not compatible with the signatures at hadron colliders that were studied in Chapter III. This conclusion changes for the case of the future lepton collider CLIC, for which we have shown in Section III.5 that this regime can be probed in principle.

Second, the overproduction problem can be solved by considering light, non-thermally produced DM. Such DM can be produced either via freeze-in [76, 229] via decays of neutral and charged scalars in the  $\Sigma$  doublet or by decays of frozen-out next-to-lightest RHN, i.e.  $N_2$ .<sup>27</sup> However, the latter mechanism is also constrained by requiring  $N_2$  to decay before the time of BBN. Namely, if  $N_2$  is too long lived, the abundances of light nuclei will be altered. This production mechanism also leads to too hot momentum distributions and therefore needs to be subdominant with respect to the scalar decay contribution. We elaborate on this in the present section.

Generally, in the freeze-in scenario there is some freedom to choose the DM mass. On the contrary, in this model there is an upper bound from demanding that the DM production has stopped before BBN takes place, as will be discussed in the last part of Section IV.3. From the point of view of freeze-in DM production, a RHN  $N_1$  with masses up to few MeV is a perfectly viable DM candidate, as there are no direct upper mass limits. However, in the following we will consider the DM mass to be  $\mathcal{O}(10 \text{ keV})$ . This particular choice is motivated by our findings in the previous chapter, where we identified an interesting open window in parameter space to successfully incorporate a resonantly enhanced leptogenesis mechanism as well. At the end of Section IV.5 we will come back to the question of DM mass in the context of interpreting our cosmological limits.

## IV.2.1 Dark matter production mechanisms

The processes through which keV-scale  $N_1$  are frozen-in are (see left figure of Fig. IV.1),

$$A, S \rightarrow N_1 \nu_\alpha, \quad \sigma^\pm \rightarrow N_1 l_\alpha^\pm. \quad (\text{IV.1})$$

The corresponding Boltzmann equation for the DM yield,  $Y_{\text{FI}}$ , which is the ratio of DM number density and entropy density, reads [2, 76],

$$\frac{dY_{\text{FI}}}{dr} = \frac{135 M_0 |y_1|^2}{64 \pi^5 (g_*^s)^{3/2} m_\pm} r^3 \left( 2 K_1(r) + \epsilon_A^3 K_1(\epsilon_A r) + \epsilon_S^3 K_1(\epsilon_S r) \right). \quad (\text{IV.2})$$

Here,  $M_0 \simeq 7.35 \times 10^{18} \text{ GeV}$ , and the number of effective entropic degrees of freedom (DOF) across relevant temperatures is fixed to  $g_*^s(T) \equiv g_*^s = 114.25$ , taking new particle DOF into account. For simplicity, we assumed that the Yukawa couplings of  $N_1$  are flavor universal, i.e.  $y_{1\alpha} \equiv y_1$ . Furthermore, the abbreviations  $\epsilon_A \equiv m_A/m_\pm$  and  $\epsilon_S \equiv m_S/m_\pm$  are introduced to account for all three scalar decay production channels.<sup>28</sup>  $K_1(r)$  is the modified Bessel function of the second kind and a dimensionless temperature  $r = m_\pm/T$  is introduced. In the computation, we use Maxwell-Boltzmann (MB) distributions for all

<sup>27</sup> A similar scenario was already outlined and discussed in Ref. [182], where the authors presented the available parameter space for freeze-in production.

<sup>28</sup> In this chapter we fix the scalar couplings to the same values as given in Eq. (III.13).

thermalized  $\Sigma$  particles. Finally, we assume the initial DM number density to vanish and this simplifies the computation of the DM abundance, because, instead of solving a differential equation, a straightforward integration is possible.

We can obtain the expression for  $Y_{\text{FI}}$  by simply integrating Eq. (IV.2) between the temperature at the end of inflation and the present one, where the former is associated to the reheating temperature which is assumed to be larger than all particle masses in the model. Practically, this allows us to use  $x = 0$  and  $x = \infty$  as the respective integration boundaries. We obtain

$$Y_{\text{FI}} = \frac{405 M_0 |y_1|^2}{128\pi^4 (g_*^s)^{3/2} m_{\pm}} \frac{2\epsilon_A \epsilon_S + \epsilon_S + \epsilon_A}{\epsilon_A \epsilon_S}. \quad (\text{IV.3})$$

Taking  $\lambda_4 = \lambda_5 = 0$  for a moment allows to simplify above expression by  $\epsilon_S = \epsilon_A = 1$  and by using the relation between DM yield and relic abundance,  $\Omega_{\text{FI}} h^2 = 2.742 \times 10^2 (m_{N_1}/\text{keV}) Y_{\text{FI}}$ , we arrive at the analytical estimate for the DM relic abundance,

$$\Omega_{\text{FI}} h^2 \approx 0.12 \left( \frac{|y_1|}{2.36 \times 10^{-8}} \right)^2 \left( \frac{m_{N_1}}{1 \text{ keV}} \right) \left( \frac{1 \text{ TeV}}{m_{\pm}} \right), \quad (\text{IV.4})$$

from which we infer that in order to have scalar decays as a dominant DM production mechanism, the required DM Yukawa couplings need to be  $\mathcal{O}(10^{-8})$  for  $\mathcal{O}(\text{TeV})$  masses of new scalars and keV-scale  $N_1$ .

In addition to the described freeze-in mechanism, DM in this model can be produced from the decays of next-to-lightest  $\mathbf{Z}_2$ -odd particle,  $N_2$  (see right figure of Fig. IV.1). The Yukawa couplings  $y_{2\alpha}$ , that are required for the successful generation of neutrino masses via the mechanism described in Section III.3, are sufficiently strong to put this particle in thermal equilibrium with the SM bath. Hence,  $N_2$  will freeze-out at  $r' \equiv m_{N_2}/T \lesssim 15$ . Additionally, the  $\mathbf{Z}_2$ -odd scalars are also in thermal equilibrium due to their gauge interactions with SM particles. Still, all heavy  $\mathbf{Z}_2$ -odd particles will eventually decay into  $N_2$  and hence one effectively needs to solve a single Boltzmann equation for the yield of  $N_2$  [57]:

$$\frac{dY_{N_2}}{dr'} = \sqrt{\frac{\pi g_*^s}{45}} \frac{M_{\text{Pl}} m_{N_2}}{r'^2} \langle \sigma_{\text{eff}} v \rangle (Y_{\text{EQ}}^2 - Y_{N_2}^2), \quad (\text{IV.5})$$

where  $\langle \sigma_{\text{eff}} v \rangle$  accounts for the annihilations and coannihilations in the  $\mathbf{Z}_2$ -odd sector, and  $M_{\text{Pl}} \simeq 1.22 \times 10^{19} \text{ GeV}$  is the Planck mass. The equilibrium yield for a thermalized fermionic species,  $Y_{\text{EQ}}$ , is given by  $Y_{\text{EQ}} = 45 r'^2 K_2(r') / (2\pi^4 g_*^s)$ . We use micrOMEGAS 5.1 [230] to evaluate Eq. (IV.5) numerically. We refer the reader to Ref. [2] for a detailed description and derivation of Eq. (IV.5); in particular, the suppression of the  $N_2$  freeze-out abundance due to possible coannihilation channels with  $\mathbf{Z}_2$ -odd scalars has been outlined. After freeze-out,  $N_2$  decays into  $N_1$  and a pair of charged or neutral leptons with the rate [182],

$$\Gamma(N_2 \rightarrow \ell_{\alpha} \bar{\ell}_{\beta} N_1) = \frac{m_{N_2}^5}{6144 \pi^3 M^4} \left( |y_1|^2 |y_{2\alpha}|^2 + |y_1|^2 |y_{2\beta}|^2 \right), \quad (\text{IV.6})$$

where  $M$  stands for the mass of the scalar particle that is exchanged in the process and  $\alpha$  and  $\beta$  denote the flavor of final state leptons. The decay of  $N_2$  gives a contribution to the total DM abundance of the form,

$$\Omega_{N_2 \rightarrow N_1} h^2 = 10^{-7} \left( \frac{100 \text{ GeV}}{m_{N_2}} \right) \left( \frac{m_{N_1}}{10 \text{ keV}} \right) \Omega_{N_2} h^2, \quad (\text{IV.7})$$

where  $\Omega_{N_2} h^2$  is the freeze-out abundance of  $N_2$  which is set by the corresponding yield,  $Y_{N_2}$ , calculated by solving Eq. (IV.5).

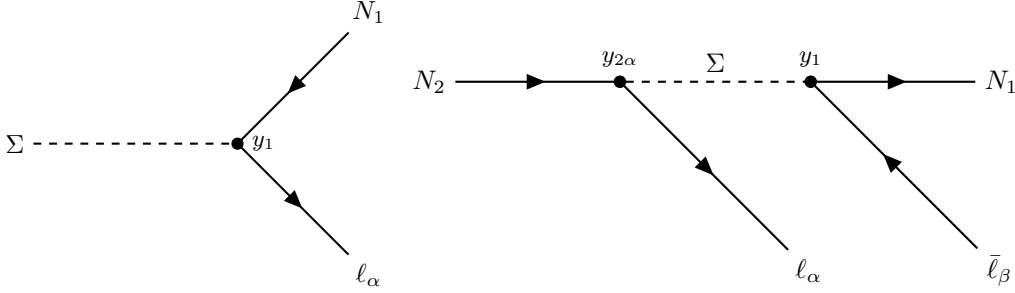


Figure IV.1: Production of the light DM  $N_1$  either via two-body decays of heavy scalars (left figure) or three-body decays of heavy  $N_{2,3}$  (right figure). Here,  $\Sigma$  stands for all scalar particles:  $\sigma^\pm$  and  $\sigma^0$ .

Even though these  $N_2$  decays give an extra source of DM, this production mechanism actually has two side effects:

- $N_2$  decays occur after freeze-out, at temperatures much lower than  $m_{N_2}$  and this leads to the production of DM particles with a hot momentum distribution, i.e. they feature large averaged momenta. In particular, it occurs for our considered parameter choices, although it is not a generic property of the model. As explained in Section II.2.6 this can drastically suppress the formation of structures at galactic scales and may not be compatible with observations.
- The decays of  $N_2$  should be fast enough in order not to violate BBN predictions for the abundance of light nuclei such as D,  ${}^3\text{He}$ ,  ${}^4\text{He}$  and  ${}^7\text{Li}$ . For  $N_2$  decays to tau leptons, which dominantly decay hadronically, the decay time needs to be  $\tau_{N_2 \rightarrow N_1} \lesssim 1$  s, whereas decays into the first and second generation leptons lead to less stringent limits, requiring only  $\tau_{N_2 \rightarrow N_1} \lesssim 100$  s [204].

## IV.3 Cosmological constraints

### IV.3.1 Constraints from structure formation

In this section we consider whether DM produced by the two previously described mechanisms is compatible with structure formation observations. The structure formation limits on keV-scale sterile neutrino DM are commonly derived for non-resonant production, so-called *Dodelson-Widrow* production [80], for which non-zero mixing between active and sterile states is required. Currently, the most stringent structure formation limit on the mass of non-resonantly produced particles,  $m_{\text{NRP}}$ , arises from Lyman- $\alpha$  forest data and yields  $m_{\text{NRP}} \gtrsim 28.8$  keV [231]. However, this limit may be too constraining, because the Lyman- $\alpha$  forest absorption spectra can be altered by effects stemming from gas dynamics in the intergalactic medium [232]. On the other hand, constraints arising from Milky Way satellite counts give  $m_{\text{NRP}} \gtrsim 10$  keV [233].

In order to derive constraints from these observations for our model, we evaluate the DM momentum distribution function  $f_{N_1}(x, r)$  which is calculated as a function of the dimensionless variables  $x \equiv p/T$  and  $r \equiv m_P/T$ . Here,  $m_P$  stands for the mass of a parent particle, which is either a heavy scalar in the case of freeze-in or  $N_2$  in late-time next-to-lightest particle decays. For scalar decays we are following the discussion in Ref. [234], whereas for the case of  $N_2$  decays we employ the procedure outlined in Ref. [235]. The total distribution function is hence given as a sum of the two contributions,

$$f_{N_1}(x, r) = f_{N_1}^\Sigma(x, r) + f_{N_1}^{N_2}(x, r), \quad (\text{IV.8})$$



where we indicate the production mechanisms of  $N_1$  with corresponding superscripts. In the following we discuss the calculation of both components. The general expression for  $f_{N_1}^\Sigma(z, r)$  assuming a MB distribution is given by [234, 235]

$$f_{N_1}^\Sigma(x, r) = 4 C_\Gamma^\Sigma \left( \frac{e^{-x} \sqrt{\pi} \operatorname{Erf} \left[ \frac{r}{\sqrt{4x}} \right]}{2\sqrt{x}} - e^{-x \left( \frac{r^2}{4x^2} + 1 \right)} \frac{r}{2x} \right) \xrightarrow{r \rightarrow \infty} 4 C_\Gamma^\Sigma \sqrt{\frac{\pi}{x}} e^{-x}, \quad (\text{IV.9})$$

where  $C_\Gamma^\Sigma = M_0 \Gamma_\Sigma / m_\pm^2$  is the effective decay width, originating from rescaled two-body decays of the  $\Sigma$  particles,

$$C_\Gamma^\Sigma = \frac{M_0}{g_*^s(T) m_\pm^2} \left( \frac{6|y_1|^2 m_\pm}{16\pi} + \frac{3|y_1|^2 m_S}{16\pi} + \frac{3|y_1|^2 m_A}{16\pi} \right), \quad (\text{IV.10})$$

An important property for a production mechanism with an associated momentum distribution function is the averaged momentum:

$$\langle x \rangle^{\text{prod}} = \frac{\int_0^\infty dx x^3 f(x, r)}{\int_0^\infty dx x^2 f(x, r)}. \quad (\text{IV.11})$$

For  $f_{N_1}^\Sigma(x, r)$  the averaged DM momentum is given by  $\langle x \rangle_{\text{FI}}^{\text{prod}} \approx 2.5$ . This result, together with the information that the production dominantly occurs at temperatures  $T \sim m_\Sigma/3$  (see for instance Fig. 1 in Ref. [2]), allows us to estimate the limit on  $m_{N_1}$  by using [234]

$$m_{N_1} = \frac{\langle p/T \rangle^{\text{prod}}}{3.15} \left( \frac{10.75}{g_*^s(T_{\text{prod}})} \right)^{1/3} m_{\text{NRP}}, \quad (\text{IV.12})$$

and assuming that the freeze-in DM production dominates. Here, the entropy dilution factor  $(10.75/g_*^s(T_{\text{prod}}))^{1/3}$  takes into account that the DM production happens at early times where  $g_*^s(T_{\text{prod}}) = 106.75$ . Taking the aforementioned limits  $m_{\text{NRP}} \gtrsim 10$  keV and  $m_{\text{NRP}} \gtrsim 28.8$  keV, we obtain  $m_{N_1} > 3.7$  keV and  $m_{N_1} > 10$  keV, respectively. Hence we are going to set  $m_{N_1} = 6$  keV as our limit on the DM mass in the following.<sup>29</sup> The combination of this limit and Eq. (IV.4) sets the upper bound on the magnitude of  $y_1$ .

If decays of  $\mathbf{Z}_2$ -odd scalars were the only source of DM production, our structure formation analysis would end here. However, decays of  $N_2$  significantly complicate the picture. To calculate the DM distribution function for the production via  $N_2$  decays, we apply the procedure from [235] and evaluate the equation<sup>30</sup>

$$f_{N_1}^{N_2}(x, r) = \int_{r_{\text{FO}}}^r d\hat{r} C_\Gamma^{N_2} \frac{\hat{r}^2}{x^2} \int_{|x-\hat{r}^2/(4x)|}^\infty d\hat{x} \frac{\hat{x}}{\sqrt{\hat{x}^2 + \hat{r}^2}} f_{N_2}(\hat{x}, \hat{r}). \quad (\text{IV.13})$$

Typically, the freeze-out temperature  $r_{\text{FO}}$  ranges between 8–16 and  $C_\Gamma^{N_2}$  is the effective decay width given by  $C_\Gamma^{N_2} = M_0 \Gamma / (g_*^s(T) m_{N_2}^2)$ , where  $\Gamma$  is the decay width of  $N_2$  into  $N_1$

<sup>29</sup> Compared to the updated analysis using a MW subhalo count and Lyman- $\alpha$  forest data done in Sections V.3 and VI.3.2 this limit is more conservative.

<sup>30</sup> Actually this equation was derived for two-body decay kinematics, but we are dealing with three-body decays instead. Consequently, this treatment gives rise to momentum distribution functions with larger averaged momenta  $\langle x \rangle$  compared to actual three-body decays. However, our discussion of a more general setup in Chapter VI shows that this simplified ansatz still yields robust limits: while  $\langle x \rangle$  would decrease in the case of three-body kinematics (see Section VI.4.3), this is compensated for by taking into account the time dependence of  $g_*^s(T)$  which shifts the averaged momentum to higher values (see Section VI.4.2). We will discuss and compare both approaches in Section VI.6.2.

and a pair of leptons given in Eq. (IV.6). The expression for the distribution function of  $N_2$  after freeze-out is [235]

$$f_{N_2}(x, r) = \exp[-(x^2 + r_{\text{FO}}^2)] \left( \frac{r + \sqrt{r^2 + x^2}}{r_{\text{FO}} + \sqrt{r_{\text{FO}}^2 + x^2}} \right)^{C_{\Gamma}^{N_2} x^2 / 2} \times \exp \left[ -C_{\Gamma}^{N_2} / 2 \left( r \sqrt{x^2 + r^2} - r_{\text{FO}} \sqrt{x^2 + r_{\text{FO}}^2} \right) \right], \quad (\text{IV.14})$$

where a MB distribution for  $N_2$  is assumed.

In Fig. IV.2 we show  $f_{N_1}(x, r) x^2$  for two  $N_2$  masses, namely  $m_{N_2} = 100$  GeV and 400 GeV, while the charged scalar mass is set to  $m_{\pm} = 600$  GeV. The red curves represent  $f_{N_1}^{N_2}(x, r) x^2$ , obtained by solving Eq. (IV.13) and fixing  $r$  to sufficiently large values in order to capture the effect of decaying  $N_2$ . For comparison, we also show the distribution function corresponding to the production via freeze-in (blue), taking  $r \rightarrow \infty$ . Clearly, the peak of  $f_{N_1}^{N_2}(x, r) x^2$  is shifted to very large values of  $x$  indicating that  $N_2$  decays yield a ‘‘hot’’ DM component. However, we also see from the figure that its amplitude is greatly suppressed with respect to  $f_{N_1}^{\Sigma}(x, r) x^2$ , implying that this component is subdominant for the selected benchmark point. Quantitatively, the distribution shown in the left panel yields  $\Omega_{N_2 \rightarrow N_1} h^2 = 0.03 \Omega_{\text{DM}} h^2$ , whereas for  $m_{N_2} = 400$  GeV it follows that less than 1 per mille of the observed DM abundance is produced in  $N_2$  decays. Further, the parameter choice in the left figure features a more prominent peak for  $f_{N_1}^{N_2}(x, r)$  compared to the other case, because  $N_2$  decays at later time where  $g_*(T)$  are decreasing, thus affecting the effective decay width  $C_{\Gamma}^{N_2}$ . In the following we are using an approach based on the

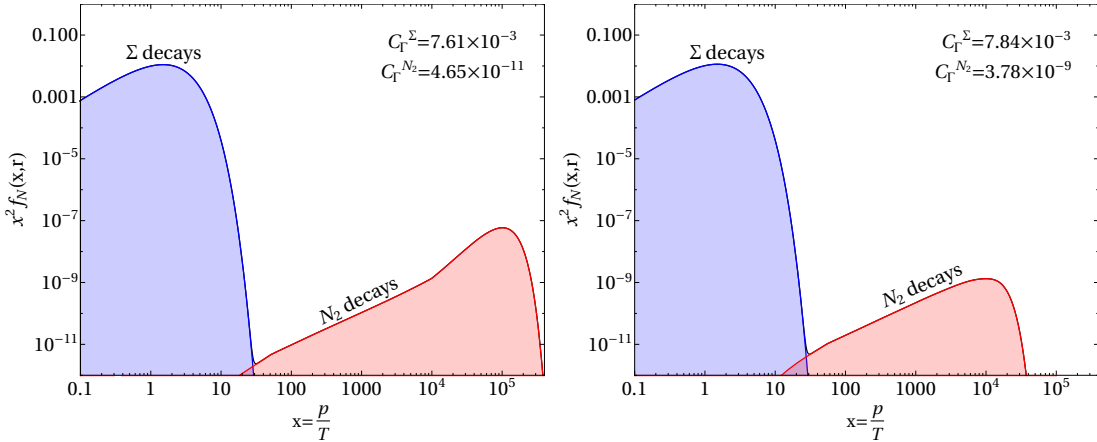


Figure IV.2: In the left (right) panel we show the DM momentum distribution function  $f_{N_1}(x, r) x^2$  including both DM production mechanisms, taking  $m_{\pm} = 600$  GeV and  $m_{N_2} = 100$  GeV ( $m_{N_2} = 400$  GeV). The blue and red curve correspond to early  $\Sigma$  decays and  $N_2$  late-time decays, respectively.

half-mode analysis explained in Section II.2.6.1 to constrain our model. We evaluate the transfer function  $T(k)$ , given by the power spectrum ratio,

$$T^2(k) = \frac{P(k)}{P(k)_{\Lambda\text{CDM}}}, \quad (\text{IV.15})$$

where  $P(k)$  is the matter power spectrum calculated from  $f_{N_1}(x, r)$  using CLASS [145, 146] and  $P(k)_{\Lambda\text{CDM}}$  is the corresponding  $\Lambda\text{CDM}$  power spectrum. The transfer function indicates at which scales non-cold DM will lead to deviations in comparison to cosmological

observations. The temperature of the DM species,  $T_{N_1}$ , relative to the photon temperature,  $T_\gamma$ , is relevant for the evaluation of the matter power spectrum: since we have two different mechanisms for DM production in the model, we are left with two independent dark sector temperatures.

The smaller one of the temperatures is set by the time when  $N_1$  is produced via a freeze-in mechanism from the decays of heavy scalars. These processes occur when the heavy scalars are still in thermal equilibrium implying that DM particles are produced with temperatures identical to those of the SM sector. After production,  $N_1$  is decoupled and does not experience reheating when SM DOF drop out of equilibrium. The temperature ratio, governed by the entropy dilution factor, yields

$$T_{N_1}^{\text{freeze-in}} \approx \left( \frac{g_*^s(T_0)}{g_*^s(T_{\text{prod}})} \right)^{1/3} T_\gamma = \left( \frac{3.94}{114.25} \right)^{1/3} T_\gamma \approx 0.33 T_\gamma, \quad (\text{IV.16})$$

where  $T_{\text{prod}}$  roughly corresponds to  $\mathbf{Z}_2$ -odd scalar masses and  $T_0$  is the temperature of the Universe today.

Additionally, to evaluate the temperature of DM produced from out of equilibrium  $N_2$  decays, we estimate the temperature when these decays are taking place. We assume an instantaneous decay at  $\tau = 1/\Gamma$  and make use of the time-temperature relation for a radiation-dominated Universe,

$$t = 2.42 \frac{1}{\sqrt{g_*^s(T)}} \left( \frac{1 \text{ MeV}}{T} \right)^2 \text{ s}, \quad (\text{IV.17})$$

which allows us to obtain an expression for the temperature at which  $N_2$  particles decay,

$$T_\Gamma = (g_*^s(T_\Gamma))^{-1/4} \left( \frac{\Gamma}{2.72 \times 10^{-25} \text{ GeV}} \right)^{1/2} \text{ MeV}. \quad (\text{IV.18})$$

For the benchmark point already used for presenting momentum distributions in the right panel of Fig. IV.2, we obtain

$$\Gamma = 1.52 \times 10^{-22} \text{ GeV}, \quad \Omega_{N_2} h^2 = 5.61 \times 10^3, \quad T_\Gamma = 13 \text{ MeV}. \quad (\text{IV.19})$$

At  $T \sim T_\Gamma$ , RHNs are at rest and each decay product has an energy  $E \approx m_{N_2}/3 \approx \mathcal{O}(100 \text{ GeV})$ . Note that by dividing this energy with  $T_\Gamma$  in Eq. (IV.19) we obtain  $x \simeq 10^4$  and this explains the approximate position of the  $N_2$  decay peak in the momentum distribution (see Fig. IV.2). Finally, we have to take into account that the SM bath is reheated when the epoch of electron-positron annihilation occurs. In summary, the temperature of this DM contribution is given by

$$T_{N_1}^{\text{decay}} \simeq \frac{m_{N_2}}{3T_\Gamma} \left( \frac{4}{11} \right)^{1/3} T_\gamma \approx 7300 T_\gamma, \quad (\text{IV.20})$$

where the temperature is evaluated for the aforementioned benchmark point.

In order to assess the cosmological viability of particular benchmark points, we compare the calculated  $T^2(k)$  against the function corresponding to the constraint stemming from Lyman- $\alpha$  forests. For the latter, we adopt an analytical fit for the transfer function [148] (see Eq. (II.45)), taking  $m_{\text{NRP}} \simeq 10 \text{ keV}$  which corresponds to a thermal relic mass of  $m_{\text{TR}} = 2 \text{ keV}$ ; the mass relation between non-resonantly produced particles and a thermal relic is given by  $m_{\text{NRP}} = 4.35 (m_{\text{TR}}/\text{keV})^{4/3}$  [234]. We are using an adapted version of the half-mode criterion (see Eq. (II.48)): since we are dealing with a momentum distribution with two peaks, we are expecting two associated wavenumbers at which  $P(k) < P(k)_{\Lambda\text{CDM}}$ .

This is illustrated in Fig. IV.2 by the red line that deviates from 1 early on, but reaches a plateau at intermediate wavenumbers, before it drops to 0 at large  $k$ . To take this early deviation into account (and not excluding too much of our parameter space), we define a new reference  $P(k)_{\Lambda\text{CDM}}$  where  $N_{\text{eff}}$  is larger than the SM value; precisely, we use bounds stemming from the epoch of BBN. As we will discuss in Section IV.3.2, they are stronger than corresponding  $N_{\text{eff}}$  limits from measurements of the cosmic microwave background (CMB). Then we calculate  $T^2(k)$  based on this new reference matter power spectrum and compare it against a limiting transfer function,  $T_{\text{lim}}^2(k)$  (see Section II.2.6.1). Consequently, a parameter choice is allowed if and only if

$$T^2(k) - T_{\text{lim}}^2(k) > 0 \text{ for } k \in \{0.02, 1\} h \text{ Mpc}^{-1}, \quad (\text{IV.21})$$

is fulfilled. This analysis technique may seem somewhat unconventional compared to the one used in Eq. (II.49), but our method is motivated by two observations: first, some transfer functions feature small bumps at wavenumbers  $k \simeq 0.1 h/\text{Mpc}$  in  $T^2(k)$ , as seen in Fig. IV.2 and we want to avoid this region when comparing the corresponding  $T^2(k)$  against each other. Second, in this analysis we are not necessarily interested in a lower mass limit for the DM, but want to primarily study the influence of the hot DM component produced by late-time  $N_2$  decays on wavenumbers  $k < 1$ . At the end, we are going to present two separate exclusion limits based on this transfer function formalism.

In Fig. IV.3 we show in red (green) the calculated transfer function for  $f_{N_1}(z, r)$  with  $m_{\pm} = 600 \text{ GeV}$  and  $m_{N_2} = 100 \text{ GeV}$  ( $m_{N_2} = 400 \text{ GeV}$ ); these are identical benchmark points as those from Fig. IV.2. If a given curve lies below the Lyman- $\alpha$  limit (blue curve) the corresponding parameter point is disfavored. We observe that the scenario with lighter mass of  $N_2$  is excluded since the abundance of hot DM is too large in this case and hence larger cosmological scales than observed are affected. In fact for these benchmark point the DM carries so much energy, it effectively acts as dark radiation. On the other hand, the green curve is in agreement with observational data; it seems to “overshoot” the  $\Lambda\text{CDM}$  reference, because the transfer function is defined with respect to a different reference  $P(k)_{\Lambda\text{CDM}}$  with  $N_{\text{eff}} = 3.046 + 0.28$ . One should note that both curves drop to zero at roughly the same point, because this wavenumber is set by the temperature of the dominant, frozen-in, DM component. If  $N_1$  would freeze-in at later times the curves would shift to the left. For this analysis and in what follows, we choose the Yukawa couplings  $y_{2i}$  to be as large as possible due to LFV constraints (see Eq. (III.10)). Smaller couplings would give rise to stronger constraints due to DM production via  $N_2$  decays at later times.

In addition to the published version, we determine similar limits on the parameter range using the  $\delta A$  method (see Section II.2.6.2 for a detailed explanation). For this we use the conservative limit  $m_{\text{TR}} = 2 \text{ keV}$  to define a reference WDM model and choose  $k = 100 h/\text{Mpc}$  as an upper limit for Eq. (II.50). Further, for typical surveys the  $k$ -range is between  $k_{\text{min}} = 0.5 h/\text{Mpc}$  and  $k_{\text{max}} = 10 h/\text{Mpc}$ . Using all these ingredients we find a reference suppression factor,  $\delta A_{\text{ref}} = 0.45$ , as the exclusion criterion. We are going to compare and discuss the results of both analysis techniques in the next section.

### IV.3.2 Constraints from additional radiation contribution

When discussing possible implications on the formation of structures in the early Universe, we should also take into account that keV-scale DM could change the number of relativistic non-photonic DOF,  $N_{\text{eff}}$ . This number enters in the expression for the radiation density

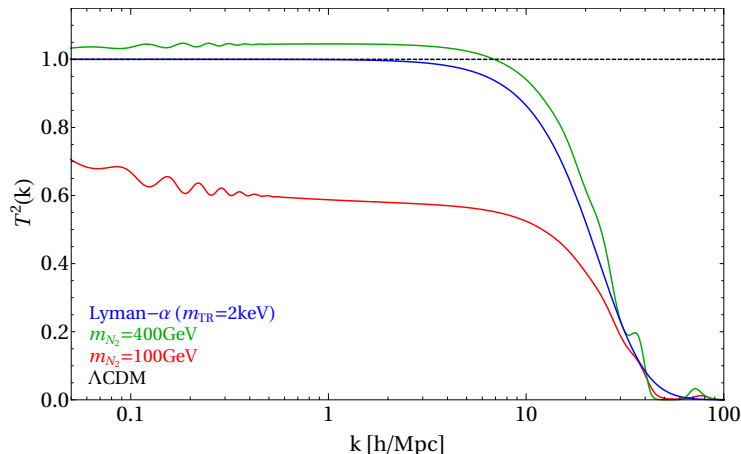


Figure IV.3: Transfer function  $T^2(k)$  for the same benchmark points as in Fig. IV.2. The constraint from structure formation, using Eq. (II.45) with  $m_{\text{TR}} = 2 \text{ keV}$  is shown in blue. RHN masses of around 100 GeV clearly violate this constraint while the green line, corresponding to  $m_{N_2} = 400 \text{ GeV}$ , is consistent with the data. The black dashed line represents  $\Lambda\text{CDM}$ .

$\rho_{\text{rad}}$ , which is, after electron-positron annihilation, given by

$$\rho_{\text{rad}} = \left[ 1 + \frac{7}{8} \left( \frac{4}{11} \right)^{4/3} N_{\text{eff}} \right] \rho_{\gamma}, \quad (\text{IV.22})$$

where  $\rho_{\gamma}$  represents the energy density of photons. In the SM,  $N_{\text{eff}} = 3.046$  [236] and thus we denote contributions from additional relativistic species as  $\Delta N_{\text{eff}} = N_{\text{eff}} - 3.046$ . The contribution to  $\Delta N_{\text{eff}}$  from  $N_1$  can be estimated by comparing its energy density against the one corresponding to a fully relativistic neutrino with temperature  $T_{\nu}$  [235]:

$$\begin{aligned} \Delta N_{\text{eff}}(T_{\nu}) &= \frac{60}{7\pi^4} \frac{g_*^s(T_{\nu})}{g_*^s(T_{\text{prod}})} \frac{m_{N_1}}{T_{\nu}} \int_0^{\infty} dx \left[ \sqrt{1 + \left( \frac{x T_{\nu}}{m_{N_1}} \right)^2} - 1 \right] x^2 f_{N_1}(x, T_{\nu}) \times \\ &\times \begin{cases} 1, & \text{if } T_{\nu} > 1 \text{ MeV} \\ \left( \frac{11}{4} \right)^{4/3}, & \text{if } T_{\nu} < 1 \text{ MeV} \end{cases}. \end{aligned} \quad (\text{IV.23})$$

Using as an example the benchmark points employed in Fig. IV.2, we can derive the following values:

$$m_{N_2} = 100 \text{ GeV} \rightarrow \Delta N_{\text{eff}} \sim 263, \quad m_{N_2} = 400 \text{ GeV} \rightarrow \Delta N_{\text{eff}} \sim 0.07. \quad (\text{IV.24})$$

Clearly, large mass gaps between  $N_2$  and  $\sigma^{\pm}$  are disfavored. The reason is that such cases would lead to larger abundances of  $N_2$  and therefore the hot DM component becomes more prominent in the spectrum.

Current measurements by the Planck collaboration allow for an upper limit of  $\Delta N_{\text{eff}} = 0.28$  (95% CL) (TT, TE, EE+lowE+lensing+BAO), which we refer to as ‘‘CMB strong’’. Including the present tension in the measurement of the Hubble constant, this value increases to  $\Delta N_{\text{eff}} = 0.52$  (95% CL) (TT, TE, EE+lowE+lensing+BAO+R18) [52], thus called ‘‘CMB weak’’. Another bound can be derived from the BBN epoch, at which  $\Delta N_{\text{eff}} = 0.344$  (95% CL) [237]. In contrast to the analysis done in Ref. [1] where we did not include the entropy dilution factor in Eq. (IV.23), we are going to use the later bound on  $\Delta N_{\text{eff}}$ . Since BBN takes place way before the CMB epoch in the early Universe, the

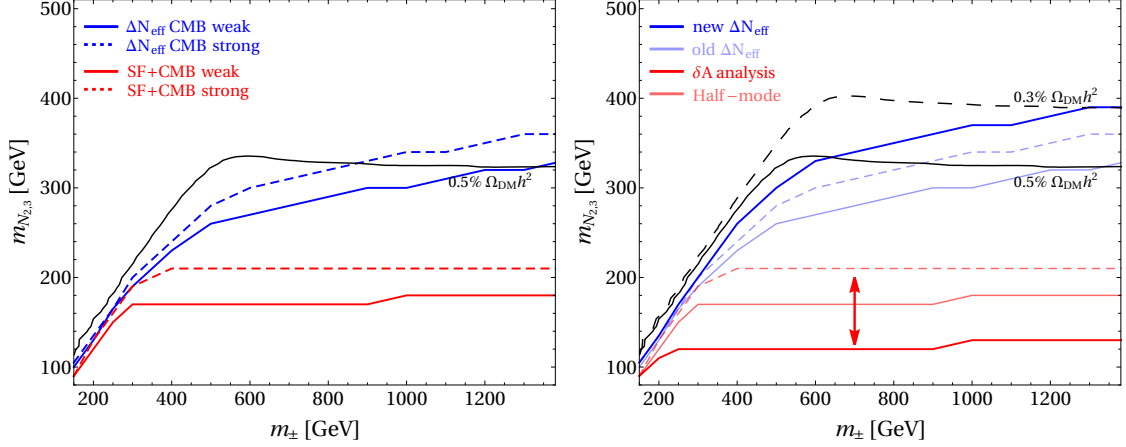


Figure IV.4: *Left figure:* constraints from structure formation (red curves) confronted with  $N_{\text{eff}}$  limits (blue curves) derived using Eq. (IV.23). The solid curves correspond to the ‘‘CMB weak’’ and dashed ones to the ‘‘CMB strong’’ choice of  $\Delta N_{\text{eff}}$ . Note that our structure formation limits also indirectly depend on  $\Delta N_{\text{eff}}$  as it is an input parameter for CLASS. Clearly,  $N_{\text{eff}}$  yields much stronger limits in comparison to those arising from structure formation. Shown in black solid is the curve for  $\Omega_{N_2 \rightarrow N_1} h^2 = 0.6 \times 10^{-3}$ . *Right figure:* same as left figure, whose contours are shown faded. The blue line indicates the new updated bound coming from the BBN limit on  $\Delta N_{\text{eff}}$  while the red line stems from a  $\delta A$  structure formation analysis as explained in Section IV.3.1. Additionally, the black dashed line indicates  $\Omega_{N_2 \rightarrow N_1} h^2 = 0.36 \times 10^{-3}$ .

DM has less time to cool down and thus it gives rise to stronger constraints.

By using Eq. (IV.23), we can estimate which parameter choices lead to  $\Delta N_{\text{eff}}$  values that exceed the bound. We have performed a scan and have deduced the following condition:

$$\frac{\Omega_{N_2 \rightarrow N_1} h^2}{\Omega_{\text{DM}} h^2} \lesssim 0.4\%, \quad C_{\Gamma}^{N_2} \gtrsim 5 \times 10^{-10} \text{ GeV}, \quad (\text{IV.25})$$

necessary for consistency with cosmology, which is further indicated by the black curve in Fig. IV.4.

Due to the above mentioned correction for  $N_{\text{eff}}$  compared to the published version, we compare the two results from Ref. [1] with the new single limit resulting from the BBN limit on  $\Delta N_{\text{eff}}$ . As can be seen, the BBN limit on  $\Delta N_{\text{eff}}$  provides slightly stronger constraints on  $m_{N_{2,3}}$  compared to the results quoted in Ref. [1]. We have updated all corresponding plots with this new limit. Furthermore, in Fig. IV.4 we compare the results from the two different structure formation analyses: the faded red lines correspond to the adapted half-mode analysis, while the thick red line corresponds to a  $\delta A$  analysis with  $\delta A_{\text{ref}} = 0.45$ . As indicated by the red arrow, the latter yields weaker limits on the neutrino mass, which is ultimately due to our conservative choice for  $m_{\text{TR}}$ .

In Fig. IV.3 and Eq. (IV.24) we demonstrate that one of the chosen benchmark points is excluded by both structure formation and  $N_{\text{eff}}$  limits. Comparing both probes in Fig. IV.4 we conclude that the BBN  $\Delta N_{\text{eff}}$  bound generally leads to stronger exclusion limits. Hence, in Section IV.4 we will compare regions in parameter space that are accessible at colliders, with this  $\Delta N_{\text{eff}}$  limit. For instance, taking  $m_{\pm} = 1 \text{ TeV}$ , the lower bound on the heavy lepton mass is  $m_{N_2} \gtrsim 340 \text{ GeV}$ .<sup>31</sup>

<sup>31</sup> There is a caveat as we have a freedom to choose the couplings between  $N_{2,3}$  and the charged leptons. Throughout this section we assume couplings to tau leptons to be subdominant.

### IV.3.3 Constrains from big bang nucleosynthesis

As we have seen in the previous section,  $N_2$  decays produce SM leptons with large momenta, which can inject a lot of energy into the plasma, thus affecting the primordial abundances of light nuclei. Specifically, we need to ensure that  $N_2$  decays are fast enough such that these highly energetic particles can thermalize with the plasma and thus the abundances of light nuclei essentially remain unaffected during the BBN epoch. The corresponding decay rate of  $N_2$  into  $N_1$  and a pair of leptons is proportional to two powers of the small Yukawa coupling  $y_1$  (see Eq. (IV.6)).

In order to obtain the BBN limits in the considered scenario, we adopt the results from [204] where the authors studied the impact of decaying hidden sector particles to the abundances of light nuclei. The channels of our interest are those containing charged leptons. Decays of  $N_2$  into electrons and muons can take as long as  $\mathcal{O}(100\text{ s})$ , since they mainly induce electromagnetic cascades, which affect BBN at later times only. In contrary, tau leptons decay mostly hadronically and this can significantly alter the abundances of light nuclei due to a change in the neutron-proton ratio. Hence, unless the abundance of  $N_2$  is strongly suppressed, the  $N_2$  decay time has to be  $\lesssim 1\text{ s}$ .

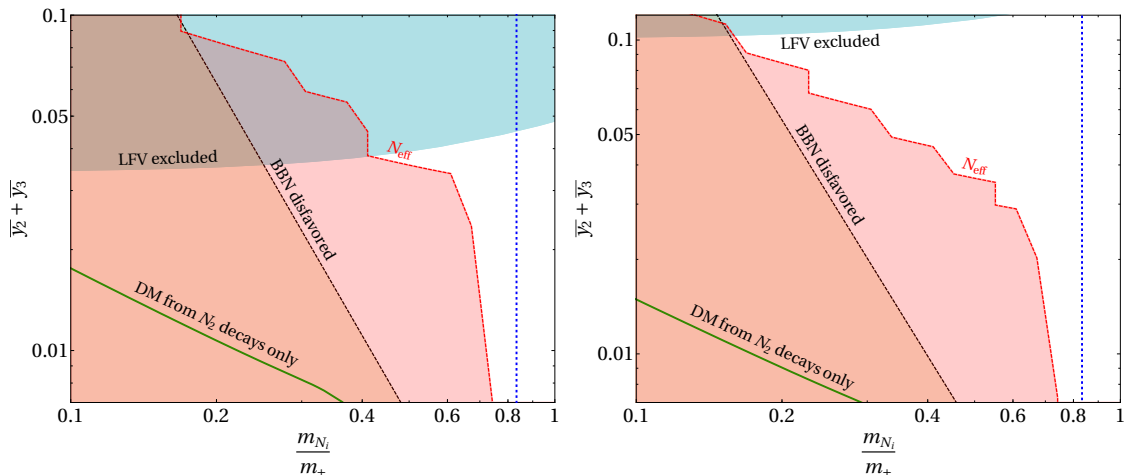


Figure IV.5: BBN constraints for the case where  $N_2$  dominantly decays into electrons and muons (left panel) and taus (right panel) are disfavoring parameter space below the black lines. The regions excluded by the BBN epoch limit on  $\Delta N_{\text{eff}}$  are shown in red. The solid green curve indicates the parameter space for a limiting case in which all of the DM is produced by  $N_2$  decays. The regions in blue represent constraints from LFV experiments. Finally, the region to the left of the vertical blue dashed line is favored by our collider analysis in the sense that the mass gap between  $\sigma^\pm$  and  $N_{2,3}$  is sufficiently large. The value of the charged scalar mass in both panels is fixed to  $m_\pm = 600\text{ GeV}$ . On the y-axis we show the average Yukawa coupling of  $N_2$  and  $N_3$ , defined as  $\bar{y}_2 + \bar{y}_3 \equiv \sqrt{\sum_\alpha (|y_{2\alpha}|^2 + |y_{3\alpha}|^2)}/3$ .

To be conservative, we impose the decay time to be shorter than 1 s for all  $N_2$  decay channels.<sup>32</sup> The corresponding results for different Yukawa coupling strengths and RHN masses are shown in Fig. IV.5, where black lines indicate BBN exclusion limits for a representative value of  $m_\pm = 600\text{ GeV}$ . The left panel corresponds to the dominant decay

<sup>32</sup> Additionally, this ensures that SM neutrinos produced in these decays thermalize with the SM bath. For temperatures  $T < 1\text{ MeV}$  their interaction with the plasma is not strong enough such that they reach thermal equilibrium.

into  $e^\pm/\mu^\pm$  and in the right panel the case where  $N_2$  decays prominently into  $\tau^\pm$  pairs is shown. These channels are motivated by the di-lepton and di-tau searches at colliders which were presented and discussed in Chapter III. In addition, the red shaded areas are excluded by the  $\Delta N_{\text{eff}} < 0.344$  limit, which generally limits the parameter space the most. Decreasing the magnitude of the corresponding Yukawa coupling, both, BBN and  $\Delta N_{\text{eff}}$  yield stronger constraints on  $m_{N_{2,3}}$  with respect to the charged scalar mass, because according to Eq. (III.5) smaller couplings have to be compensated by larger RHN masses in order to get the observed SM neutrino masses. Further, by increasing  $m_\pm$ , larger  $y_1$  are required for DM production through  $\Sigma$  decays and hence the BBN bounds get weaker. LFV bounds (blue regions) are then also relaxed, see Eq. (III.10). Moreover, the LFV bounds are weaker for maximized coupling to  $\tau$ , because the most stringent limits stem from transitions between second and first family leptons.

The thick green solid line indicates a parameter space corresponding to the DM production only through  $N_2$  decays and such a scenario is clearly excluded. Finally, in the parameter region to the left of the blue vertical dashed line, energies of would-be final state leptons at colliders, arising from  $\sigma^\pm \rightarrow N_2 \ell_\alpha^\pm$  are below 100 GeV, making them hard to detect.

Here we have shown that there are regions of parameter space, in particular the region  $m_\pm \rightarrow m_{N_i}$ , unconstrained by collider searches but which can still be excluded by  $N_{\text{eff}}$  and BBN limits. They start to be competitive at small sizes of the involved Yukawa couplings, because the collider searches are effectively independent on these parameters.

## IV.4 Combining collider and cosmological limits

Having examined the impact of the corresponding light DM on cosmology in this chapter and explored the capability of the HL-LHC, as well as future hadron (FCC-hh) and lepton (CLIC) colliders for testing the ScM in Chapter III, we are going to summarize the limits in the following. We start to discuss the implications for the parameter space available at the HL-LHC. The left figure of Fig. IV.6 contains the sensitivity limits from the di-tau search at the HL-LHC overlapped with bounds from BBN and  $\Delta N_{\text{eff}}$  and the right figure is the corresponding di-lepton case. Considering the di-tau scenario, it turns out that the discovery region is in tension with cosmological probes. Only a small part of the parameter space around  $m_{N_{2,3}} \simeq 100$  GeV is not excluded for the optimal case while the sensitivity for the realistic case is disfavored by cosmological limits. However, a certain portion of the potential exclusion parameter region around  $m_{N_{2,3}} \simeq 100\text{--}150$  GeV and  $m_\pm \simeq 200\text{--}400$  GeV is not constrained by cosmological data.

In the case of the di-lepton scenario, cosmology disfavors even more significant parts of the available parameter space. It can be seen by comparing both plots of Fig. IV.6 that  $N_{\text{eff}}$  limits are stronger for the di-lepton case. This is due to the fact, that we can have larger couplings in the di-tau case, because LFV processes yield less stringent bounds on the Yukawa couplings for the third lepton generation. Hence,  $N_{\text{eff}}$  bounds are weakened in such a case since larger interaction rates give rise to a smaller freeze-out abundance of  $N_2$ , suppressing the hot DM component. This is the same reason why the BBN limit is stronger for the di-lepton scenario, although, in contrast to the di-tau parametrization, it cannot compete with the  $\Delta N_{\text{eff}}$  bound. The fact that the projected HL-LHC results are covered by current cosmological observations is another motivation to consider facilities with higher energies, as the most dominant  $N_{\text{eff}}$  bound starts to flatten for  $m_\pm > 600$  GeV.



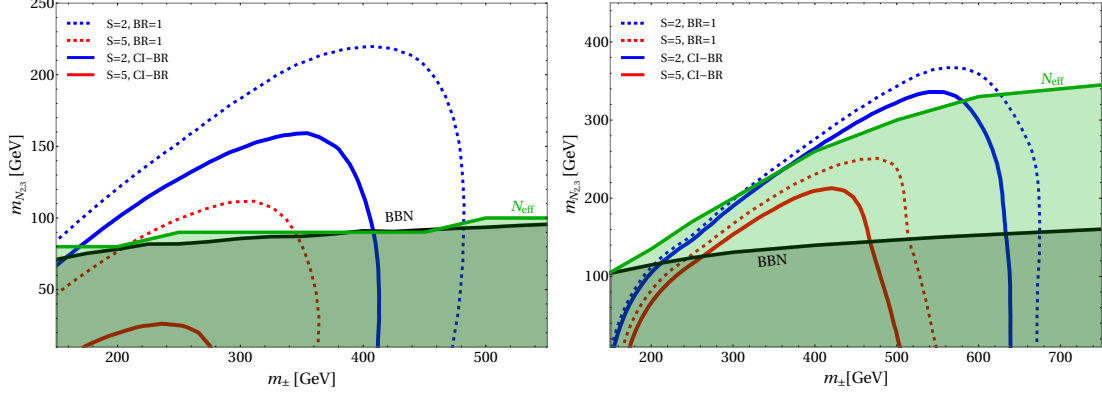


Figure IV.6: Same figures as shown in Figs. III.4 and III.5, but now overlapped with BBN constraints discussed in Section IV.3.3 and  $N_{\text{eff}}$  limits discussed in Section IV.3.1. For the di-lepton scenario (right picture), cosmological constraints already exclude most of the potential exclusion region while the discovery region is completely covered for both cases.

A compilation of all derived constraints is shown in Fig. IV.7. The figure contains all sensitivity curves already presented in Figs. III.4 to III.6 and III.8 as well as BBN and  $\Delta N_{\text{eff}}$  limits indicated by a black and gray line, respectively. While a potential discovery at HL-LHC is less likely due to the tension with cosmological limits, the future colliders offer a more promising situation in which large portions of the parameter space can be tested.

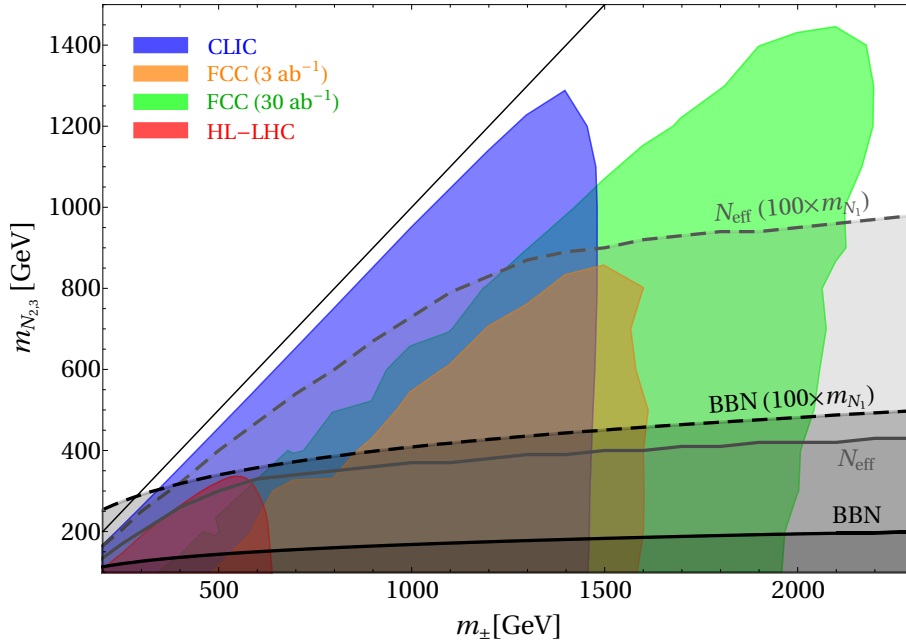


Figure IV.7: Summarized sensitivity curves for  $\mathcal{S}_0 = 2$  as discussed in Sections III.4.2, III.5.1 and III.5.2 for the HL-LHC (red shaded region) with  $4 \text{ ab}^{-1}$  (red shaded region), CLIC with  $5 \text{ ab}^{-1}$  and (blue shaded region) and FCC-hh with  $3 \text{ ab}^{-1}$  and  $30 \text{ ab}^{-1}$  luminosity (orange and green shaded regions). Again, the thin black line indicates  $m_{N_{2,3}} = m_{\pm}$ , whereas the thick black line shows BBN constraints and the gray solid curve represent  $N_{\text{eff}}$  constraints for  $m_{N_1} = 6 \text{ keV}$ . The corresponding dashed contours indicate BBN and  $N_{\text{eff}}$  constraints for a DM particle with  $m_{N_1} = 600 \text{ keV}$ . We assumed a maximal coupling to  $e$  and  $\mu$  in this case.

On the contrary, the non-collider limits shown in Fig. IV.7 depend on the magnitude of the involved coupling  $y_{i\alpha}$  and the DM mass  $m_{N_1}$ , while the collider searches do not depend on them, as long as the BRs are staying the same. First, the BBN bound depends on the lifetime  $\tau$  of  $N_2$  given by  $\tau \propto \Gamma^{-1} \propto (y_1 y_{2\beta})^2$  (using Eq. (IV.6)). Thus, if smaller couplings than anticipated are used, this bound will strengthen accordingly. It further features an implicit DM mass dependence, because it is related to  $\tau$  via  $y_1^2 \propto m_{N_1}^{-1}$  due to the DM abundance given by Eq. (IV.4).

Second, the  $\Delta N_{\text{eff}}$  bound depends on the DM temperature  $T_{N_1}^{\text{dec}} \propto (y_1 y_{2\beta})^{-1} T_\gamma$  (see Eq. (IV.20)) and the DM mass. However, for large  $T_{N_1}^{\text{dec}}$ , Eq. (IV.23) can be significantly simplified and the explicit DM mass dependence vanishes if  $\Delta N_{\text{eff}}$  is evaluated at the BBN epoch and thus the limit is expected to scale similarly to the BBN bound.

Only the results of the half-mode analysis do dependent on  $m_{N_1}$ : again,  $T_{N_1}^{\text{dec}}$  is important for evaluating the suppression of the corresponding matter power spectrum  $P(k)$  and the impact of different  $y_{2\alpha}$  is rather simple, while the influence of  $m_{N_1}$  is more subtle. On the one hand, an increase in the DM temperature due to smaller  $y_1$  is compensated by larger DM masses.<sup>33</sup> On the other hand, having larger DM masses increases the  $N_2$  decay contribution (see Eq. (IV.7)) and hence the hot subcomponent becomes more important. In summary, also this bound gives stronger constraints, and the cosmological bounds will persist even when  $N_1$  is heavier than we assumed in our analysis. Although substantial larger DM masses are not directly motivated by our findings in Section III.2, we consider a more general model setup and illustrate this effect by calculating the corresponding limits for  $m_{N_1} = 600 \text{ keV}$  and show the results in Fig. IV.7 as dashed lines. For this DM mass choice, it can be observed that the cosmological bounds increase by up to a factor  $\sim 2.5$  compared to  $m_{N_1} = 6 \text{ keV}$ , since the corresponding decrease in  $y_1$  has to be compensated for by a smaller abundance of DM produced in  $N_2$  decays.

In the following, we list upcoming cosmological and terrestrial searches which will provide stronger limits on the above mentioned parameters, allowing for a complementary probe of the parameter regions covered by future collider experiments.

- New searches for LFV processes can lower the bounds on Yukawa couplings  $y_{2\alpha}$  and  $y_{3\alpha}$ . For instance the MEG II experiment [238] features a projected sensitivity of  $\text{BR}(\mu \rightarrow e \gamma) < 6 \times 10^{-14}$ ; an improvement of about an order of magnitude compared to the previous bound, which in turn would give rise to even later DM production via  $N_2$  decays due to smaller Yukawa couplings.
- New observations of small scale structures in combination with detailed simulations of warm DM will push  $m_{\text{NRP}}$  to larger values and this in turn requires smaller  $y_1$  to produce the observed DM abundance via freeze-in, which will also impact BBN limits. Some of these updated mass limits will be discussed in the next sections.
- The upcoming CMB-S4 experiment will measure  $N_{\text{eff}}$  to a precision of  $\Delta N_{\text{eff}} = 0.06$  [239] which leaves less room for a hot DM subcomponent.

To summarize, these rather complementary searches would probe the parameter space up to even smaller mass ratios between  $\sigma^\pm$  and RHNs. They directly or indirectly set a stricter upper limit on the abundance of  $N_2$  which is crucial for cosmology. Hence, in the near future these experiments will offer novel relations between collider searches and cosmological observations.

In particular, we want to point out, that this is the kinematic window in which coannihilations are very effective and this can strongly suppress the “hot” DM component, relaxing

<sup>33</sup> A DM species with mass  $m_{\text{DM}}$  and temperature  $T_{\text{DM}}$  has the same matter power spectrum as another DM species with larger mass  $\alpha m_{\text{DM}}$  and higher temperature  $\alpha T_{\text{DM}}$ , where  $\alpha > 1$ .

the  $\Delta N_{\text{eff}}$  limits, while BBN limits still play a role. We wish to stress that such small splitting between  $\mathbf{Z}_2$ -odd fermions and scalars at mass scales of  $\simeq 1$  TeV is exactly the setup that the observed amounts of DM and baryon asymmetry of the Universe can be simultaneously explained within the ScM, as shown in [2]. It is very intriguing that future lepton colliders will offer the potential to search for such scenarios.

## IV.5 Summary of Chapter IV

Compared to the first chapter of this thesis, dedicated to collider searches, we focused in this chapter on the cosmological implications of keV-scale fermionic DM  $N_1$  within the ScM. In this setup there are two distinct DM production mechanisms: freeze-in through the decays of heavy scalars and the production from the decay of the next-to-lightest  $\mathbf{Z}_2$ -odd particle  $N_2$ , which itself is produced via a freeze-out. The large mass gap between the DM and  $N_2$  generally allows for a sufficient suppression of the abundance arising from the latter mechanism. This is crucial, because this DM subcomponent features a corresponding momentum distribution function with large momenta and could hence lead to washout of structures at small scales. We showed that even stronger constraints arise from the contribution of such hot DM to the effective number of relativistic species,  $\Delta N_{\text{eff}}$  at the epoch of BBN. We also derived BBN bounds from the requirement that  $N_2$  particles decay within  $\sim 1$  second, or otherwise they would hinder the formation of light nuclei during this epoch.

For a DM mass of 6 keV and Yukawa couplings allowed by LFV experiments, we found that the limit  $\Delta N_{\text{eff}} < 0.344$  constrains the parameter space the most. In particular, hot DM from  $N_2$  decays can contribute at most  $\simeq 0.1\%$  to the total DM density. We overlapped these cosmological limits with the projected collider exclusion results, derived in the previous chapter, and were able to show that both approaches allow for a complementary probe of the parameter space. In fact, these cosmological limits already constrain a significant part of the collider accessible parameter space, in particular for the HL-LHC. Further, we discussed how these cosmological bounds strengthen with larger  $m_{N_1}$  and/or smaller couplings  $y_2$ , as these cases lead to an even later production of DM particles and hence a further suppression of this subcomponent is necessary. The same does not hold for the collider limits; they are effectively independent of the associated  $N_1$  DM phenomenology.

In summary, we have shown that if the scotogenic model is realized in Nature, there is a number of complementary tests, stemming from terrestrial experiments to cosmological surveys, indicating a rich model phenomenology and a very promising discovery potential in the near future.



## Chapter V

# The cosmology of frozen-in axion-like particle dark matter

## V.1 Motivation

Strong experimental limits severely constraint a weakly interacting massive particle (WIMP) as a viable dark matter (DM) candidate [240] and this shifts DM research towards alternative realizations. For instance, non-thermally produced light DM in form of sterile neutrinos [80, 100, 241–243], fuzzy DM [244, 245], hidden photons [246, 247] and ALPs [136, 248, 249] is not only receiving a significant attention with regards to existing and forthcoming terrestrial experiments [250], but also has the potential to resolve discrepancies between observations and simulations, as for instance for properties of halo formation [251]. Additionally, non-thermal DM candidates can be related to new solutions of other open questions in the standard model (SM), such as the hierarchy problem in the case of relaxion DM [252–254].

In this chapter, we focus on ALP DM with  $\mathcal{O}(1\text{--}100\text{ keV})$  mass, which is the scale motivated by hints in gamma-ray data [93, 94] as well as the recent measurement of an excess in electron recoil spectrum performed by the XENON1T collaboration [128]. In fact, the former measurement can be explained by an ALP-photon coupling [248], while for the latter, an ALP-fermion coupling, in particular to electrons, suffices [253]. In light of these hints, we study ALP production via freeze-in through feeble interactions with SM gauge bosons and fermions. Our main goal is to compute the structure formation limits that have not been derived to date for keV-scale ALPs. For this purpose we use recent data from Lyman- $\alpha$  forests as well as the observed number of MW subhalos. These limits are widely scrutinized for light sterile neutrino DM [99, 233]. While using the results from these studies would allow us to get a very rough estimate on the structure formation limits for ALP DM, we find it valuable, especially in light of aforementioned experiments that may start to detect DM, to perform a dedicated study and determine with large precision a viable parameter space for the considered model. We also point out that for bosonic DM such bounds are important irrespective of their strength, because the Tremaine-Gunn bound on the DM mass does not apply, in contrast to fermionic DM [54].

This chapter is organized as follows: in Section V.2 we introduce the model and discuss production channels for ALP DM. Following this, we calculate the DM momentum distribution in V.2.1, where we use Maxwell-Boltzmann (MB) statistics to describe SM bath particles and discuss briefly the case when quantum statistics are used instead. Then, in Section V.3 we discuss experimental observations that allow us to constrain the ALP DM parameter space. In Section V.4 we discuss theoretical aspects of ALP DM in the early Universe, focusing on the interplay between misalignment and freeze-in production. In Section V.5 our main results are presented and summarize in Section V.6.

## V.2 The model setup

The part of the Lagrangian relevant for the subsequent analysis is given by

$$\begin{aligned} \mathcal{L} = & \frac{1}{2} \partial_\mu a \partial^\mu a + \frac{1}{2} m_a^2 a^2 + \bar{f} (i \not{\partial} - m_f) f - \frac{1}{4} F_{\mu\nu} F^{\mu\nu} \\ & - q e \bar{f} \not{A} f + \frac{c_{a\gamma\gamma}}{4f_a} a F_{\mu\nu} \tilde{F}^{\mu\nu} + \frac{c_{aff}}{f_a} \partial_\mu a \bar{f} \gamma^\mu \gamma_5 f. \end{aligned} \quad (\text{V.1})$$

The first two terms are the kinetic and mass term for the pseudoscalar ALP field  $a$ . The following three terms describe quantum electrodynamics (QED), namely a SM fermion  $f$  with an electric charge  $q$  interacting with photon field  $A^\mu$  whose corresponding (dual) field strength tensor is denoted by  $F^{\mu\nu}$  ( $\tilde{F}^{\mu\nu}$ ). Finally, the last two terms describe the interaction of an ALP with  $A^\mu$  and  $f$ , respectively. We will focus on analyzing the ALP coupling to photons and fermions separately, i.e. working under the assumption that either  $c_{aff}$  or  $c_{a\gamma\gamma}$  vanishes. These scenarios are dubbed as *photophilic* and *photophobic*, respectively.

Regarding the photophilic case, at temperatures above  $\sim 160$  GeV the electroweak (EW) symmetry  $SU(2)_L \times U(1)_Y$  is restored, and we have to work in the  $\{B_\mu, W_\mu^a\}$  basis instead, where  $B_\mu$  is the hypercharge gauge boson, whereas the  $W_\mu^a$  are the three corresponding  $SU(2)_L$  gauge bosons. In the following, we assume for simplicity that the ALP couples only to the  $U(1)_Y$  gauge field via the corresponding field strength tensor  $B_{\mu\nu}$ ,

$$\frac{c_{aBB}}{4f_a} a B_{\mu\nu} \tilde{B}^{\mu\nu}. \quad (\text{V.2})$$

The  $c_{aBB}$  coupling is related to the ALP-photon coupling via the weak mixing angle  $\theta_W$ ,  $c_{aBB} \cos(\theta_W) = c_{a\gamma\gamma}$ , where  $\cos\theta_W \sim 0.88$ .

The inclusion of the  $W_\mu^a$  and gluon fields would increase the production rate of ALPs, but for the moment we consider only a coupling to photons, which is the scenario typically considered in the literature for heavy ALP searches [255–258]. We will come back to this case when discussing our results in Section V.5.

In the photophobic case, using the equations of motion, we can replace the last term in Eq. (V.1) with the term proportional to the fermion mass [125],  $(2m_f/f_a) a \bar{f} \gamma_5 f$ . This does not imply that such coupling is only present once EW symmetry is broken. After a phase redefinition of the quark fields  $f$  and Higgs field  $H$ , a term  $iy_f (c_f a/f_a) \bar{Q}_L H q_R$  is generated [259], where  $Q_L$  is a left-handed (LH) quark doublet,  $q_R$  is a right-handed (RH) quark field and  $c_f$  is a free dimensionless parameter. In general, such coupling exists for all SM quarks, but since it is proportional to the Yukawa coupling of the respective quark, all contributions except the top quark are negligible due to their small coupling strength. However, thanks to the large top Yukawa, the term  $iy_t (c_t a/f_a) \bar{Q}_3 H t_R$  contributes very efficiently to the ALP production, and it can be the dominant source when all ALP couplings to SM particles have the same order of magnitude.

In this work, however, we limit ourselves to sub-TeV values of the reheating temperature in the photophobic scenario, namely  $T_{\text{RH}} < 160$  GeV. In that regime, the top quark is Boltzmann suppressed and does not contribute to ALP production. Since the ALP-fermion coupling is proportional to the fermion mass  $m_f$ , relevant for ALP production are the heaviest fermions after the top quark, namely bottom and charm quarks as well as tau leptons.

The kinetic and interaction terms in Eq. (V.1) enable ALP production from thermalized fermions and vector bosons  $V$  (the photon, a gluon, or the  $U(1)_Y$  gauge field) through

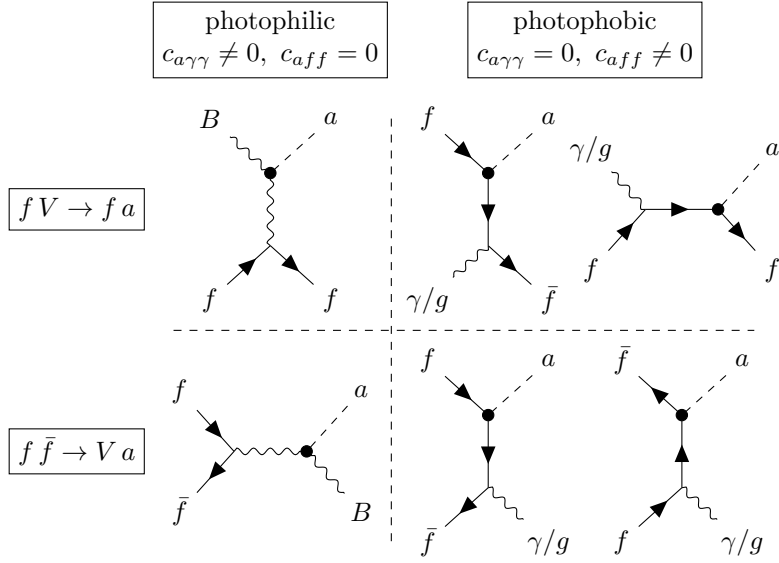


Figure V.1: Tree level Feynman diagrams for the two processes of interest,  $fV \rightarrow fa$  (top) and  $\bar{f}f \rightarrow Va$  (bottom), in the photophilic (left) and photophobic (right) cases. *Image credits:* Enrico Morgante

$Vf \rightarrow af$  and  $\bar{f}f \rightarrow Va$  channels. For both of these processes there are one photon- and two  $f$ -mediated Feynman diagrams contributing at tree level (see Fig. V.1). We note that for mixed scenarios where  $c_{aff} \sim c_{a\gamma\gamma}$ , our results turn out to be driven by couplings to photons, namely they effectively match the photophilic scenario. This is because in the photophobic case, the ALP interaction operator is proportional to the fermion mass, and thus the production rate is suppressed with respect to the photophilic case by a factor  $m_f/T_{\text{RH}}$ .

Independently of the scenario under consideration, the production of keV-scale ALP DM through the processes depicted in Fig. V.1 should occur via “freeze-in” [76], because for  $m_a \gtrsim 100$  eV the freeze-out would lead to DM relic abundance that greatly exceeds present measurements [260]. The relic abundance of non-thermalized ALP DM is given by [248]

$$\Omega_{\text{ALP}} h^2 \simeq 0.12 \frac{m_a}{154 \text{ eV}} \frac{106.75}{g_*^s(T_{\text{RH}})} \frac{\Gamma}{H} \Big|_{T_{\text{RH}}}, \quad (\text{V.3})$$

and a freeze-in scenario requires that  $\Gamma < H$  during reheating, or otherwise the ALP DM would thermalize instead.

### V.2.1 Calculation of the momentum distribution function

Equipped with the model Lagrangian we will derive the ALP DM momentum distribution function  $f(p_a, t)$  in this section. It is a key ingredient needed to calculate the properties of ALP DM and its influence on structure formation and can be obtained by solving the Boltzmann equation, which, for the process  $1 + 2 \rightarrow 3 + a$ , reads:

$$\left[ \frac{\partial}{\partial t} - H p_a \frac{\partial}{\partial p_a} \right] f(p_a, t) = \mathcal{C}(p_a). \quad (\text{V.4})$$

The collision term on the r.h.s depends on the DM production mechanism and is given by

$$\mathcal{C}(p_a) = \frac{1}{2E} \int \frac{d^3 p_1}{(2\pi)^3 2E_1} \frac{d^3 p_2}{(2\pi)^3 2E_2} \frac{d^3 p_3}{(2\pi)^3 2E_3} (2\pi)^4 \delta^4(P_1 + P_2 - P_3 - P_a) \times \\ \times \overline{|\mathcal{M}|^2} f_1(E_1, T) f_2(E_2, T) (1 - f_3(E_3, T)). \quad (\text{V.5})$$

Here,  $\overline{|\mathcal{M}_A|^2}$  is the averaged squared amplitude for the considered process. In what follows, we present the computation of the ALP DM distribution function for the case of MB statistics describing the SM bath and highlight some differences compared to a quantum statistical treatment.

Using MB statistics and assuming  $f_i \ll 1$  for all particles involved, simplifies the Boltzmann equation considerably [234]. Indeed, we can approximate  $f_1(E_1) f_2(E_2) (1 - f_3(E_3)) \approx \exp[-(E_1 + E_2)/T] = \exp(-P_0/T)$ , where  $P = P_1 + P_2 = P_3 + P_4$  and  $P_0$  is the first component of the four-vector  $P$ . The collision term can then be factorized as

$$\mathcal{C}(p_a) = \frac{1}{2E} \int \frac{d^4 P}{(2\pi)^4} \frac{e^{-P_0/T}}{2E_3} (2\pi) \delta(E_3 + E_a - P_0) \times \\ \times \int \frac{d^3 p_2}{(2\pi)^3 2E_2} \frac{d^3 p_3}{(2\pi)^3 2E_3} (2\pi)^4 \delta^4(P_1 + P_2 - P) \overline{|\mathcal{M}_A|^2}. \quad (\text{V.6})$$

Neglecting any CP violation, the second line is nothing but the reduced cross section,  $\hat{\sigma}$ , of the inverse process  $3 + a \rightarrow 1 + 2$ , multiplied by a phase space factor  $\lambda(s, m_1^2, m_2^2)^{1/2}/s$ . It is related to the usual cross section through  $\hat{\sigma} = 2[\lambda(s, m_1^2, m_2^2)/s] \sigma$ , where  $s$  is a Mandelstam variable and  $\lambda$  is the *Källén* function. This function is approximated by  $\lambda \approx s^2$  for masses  $m_a, m_f \lesssim \sqrt{s} \sim T$  which is the case for the relevant epoch in the early Universe associated to ALP DM production. The second line of Eq. (V.6) is invariant under longitudinal boosts, which allows us to compute it in the center-of-mass frame.

We calculate  $\hat{\sigma}$  analytically at tree level considering the diagrams shown in Fig. V.1. For QED with one fermion of charge  $\pm 1$ , we obtain

$$\hat{\sigma}_{\bar{f}f \rightarrow \gamma a} = \frac{e^2}{12\pi} \frac{c_{a\gamma\gamma}^2}{f_a^2} s \left( 1 + 2 \frac{m_f^2}{s} \right) \sqrt{1 - \frac{4m_f^2}{s}} \\ - \frac{2}{\pi} e^2 m_f^2 \left( 2 \frac{c_{aff}^2}{f_a^2} + \frac{c_{aff} c_{a\gamma\gamma}}{f_a^2} \right) \log \left( \frac{s - 2m_f^2 - s\sqrt{1 - 4m_f^2/s}}{2m_f^2} \right), \quad (\text{V.7})$$

and

$$\hat{\sigma}_{f\gamma \rightarrow fa} = \frac{e^2}{16\pi} \frac{c_{a\gamma\gamma}^2}{f_a^2} s \left( 1 - \frac{m_f^2}{s} \right)^2 \left[ 4 \log \left( \frac{(s - m_f^2)^2}{s m_\gamma^2} \right) - 3 - 2 \frac{m_f^2}{s} + \frac{m_f^4}{s^2} \right] \\ - \frac{e^2}{2\pi} \left( 2 \frac{c_{aff}^2}{f_a^2} + \frac{c_{aff} c_{a\gamma\gamma}}{f_a^2} \right) m_f^2 \left( 1 - \frac{m_f^2}{s} \right) \left( 2 \log \left( \frac{s}{m_f^2} \right) - 3 + 4 \frac{m_f^2}{s} - \frac{m_f^4}{s^2} \right). \quad (\text{V.8})$$

Details on the derivation of the cross section starting from the matrix amplitudes of the corresponding Feynman diagrams are given in Section V.7. Here,  $m_\gamma \approx eT/3$  is the plasmon mass that serves as a regulator for the diagram including  $t$ -channel photon exchange. The expressions in Eqs. (V.7) and (V.8) are obtained for general cases of both  $c_{a\gamma\gamma}$  and  $c_{aff} \neq 0$  and have well defined limits if any of these two couplings vanishes. We note that Eq. (V.8) holds for both  $f$  and  $\bar{f}$  scattering off photons and thus it must be summed over twice.



The expressions in Eqs. (V.7) and (V.8) must be generalized to account for the presence of SM fermions. Additionally, in the photophilic scenario, in which the ALP population is generated at  $T \gg 160 \text{ GeV}$ ,  $e^2 c_{a\gamma\gamma}$  must be replaced by  $g'^2 c_{aBB} = g'^2 c_{a\gamma\gamma} / \cos^2 \theta_W$ , and the result must be multiplied by the sum over the hypercharge of SM fermions,  $g_Y \equiv \sum_L Y^2 n_c n_f n_L = 10$ , where the sum runs over all LH doublets ( $n_L = 2$ ) and RH singlets ( $n_L = 1$ ). The plasmon mass for a  $B$  gauge boson is given by  $(11/12)^{1/2} g' T$  [259].

On the contrary, in the photophobic scenario, the electric charge  $e^2$  should be multiplied by  $q^2 n_c$  for leptons, and replaced with  $q^2 n_c e^2 + 4g_s^2$  for quarks, and finally summed over the SM fermions involved (typically  $b, c, \tau$ ). Here,  $n_c$  is the number of colors of the fermion  $f$  and  $q$  its electric charge in units of  $e$ . For quarks, we take the diagrams with an external gluon into account as well. The diagrams involving an external gluon can be derived from the QED diagrams by replacing  $ie\gamma^\mu$  with  $ig_s\gamma^\mu T^a$  where  $T^a$  are  $SU(3)$  generators. Summing over initial and final states, we have to evaluate the trace  $\text{Tr}[T^a T^a]$  which gives the factor 4 in front of the second term of the substitution for quarks.

It is convenient to rewrite the Boltzmann equation (Eq. (V.6)) by defining dimensionless quantities,  $r = m_H/T$  and  $x = p/T$ , where  $m_H$  is a reference mass which we fix to be the Higgs mass; its actual value is irrelevant as  $m_H$  cancels in the calculation of physical quantities. Thus,  $r$  acts as a time variable, while  $x$  denotes the comoving ALP momentum. With this redefinition we obtain the expression given in Eq. (11) of [234] for an ALP DM distribution function,

$$f(x) = \frac{M_0}{16\pi^2 m_H x^2} \int_{r_i}^{r_f} dr \int_{y^*}^{\infty} dy \hat{\sigma} \left( \frac{m_H^2 y}{r^2} \right) \exp \left[ -x - \frac{y}{4x} \right], \quad (\text{V.9})$$

where  $M_0 = M_{\text{Pl}} \sqrt{45/(4\pi^3 g_*^s(T))}$  and  $M_{\text{Pl}} = 1/\sqrt{G_N} \approx 1.22 \times 10^{19} \text{ GeV}$  is the Planck mass;  $r_{i,f}$  are the lower and upper integration boundaries set by  $m_H/T_{\text{RH}}$  and  $m_H/m_f$ , respectively;  $y^* = 4rm_f^2/m_H^2$  for the fermion annihilation process and  $y^* = rm_f^2/m_H^2$  for fermion scattering. We would like to point out, that  $f(x)$  has no explicit time dependence, because it is evaluated at times  $r_f$ . Using this approach, the change of the number of effective entropic degrees of freedom (DOF),  $g_*^s(T)$ , is not taken into account but in the relevant high-temperature range (that is above the QCD phase transition at  $T \sim 100 \text{ MeV}$ ) such approximation is justified.

In Eq. (V.9) and in the following, we expand the expressions up to the first non-zero order in  $m_f$ , i.e. we set  $m_f = 0$  everywhere apart from the cross section where we keep the factor  $m_f^2$  multiplying the  $c_{aff}^2$  terms. We also keep only the first non-zero  $m_f$ -dependent term inside the logarithms (see Eqs. (V.7) and (V.8)). The same holds for the integration limits  $r_f$  and  $y^*$ , which can be sent, respectively, to infinity and to zero in the photophilic ALP case. Finally, we drop the interference terms  $\propto c_{a\gamma\gamma} c_{aff}$ , as we are going to consider separately the cases  $c_{a\gamma\gamma} = 0$  and  $c_{aff} = 0$ . Note that the interference terms in Eqs. (V.7) and (V.8) are proportional to the corresponding  $c_{aff}^2$  terms, and hence, even if considered, they would not lead to any major effect, in particular the energy dependence of the cross section would be unaltered.

The distribution function can thus be integrated analytically. We obtain

$$f(x) = \frac{g'^2}{12\pi^3 \cos^2 \theta_W} g_Y M_0 T_{\text{RH}} \frac{c_{a\gamma\gamma}^2}{f_a^2} e^{-x} \left\{ 1 + \frac{3}{2} \left[ 1 - 4\gamma_E + 4 \log \left( \frac{48x}{11g'^2} \right) \right] \right\}, \quad (\text{V.10})$$

in the photophilic and

$$f(x) = \sum_f \frac{1}{2\pi^3} M_0 \kappa_f \frac{c_{aff}^2}{f_a^2} \frac{e^{-x}}{x} \left\{ \left[ 2\sqrt{\pi x} (1 + \log 2) \text{erf} \left( \frac{1}{\sqrt{x}} \right) + 2\Gamma \left( 0, \frac{1}{x} \right) \right] \right\}$$

$$+ \left[ \sqrt{\pi x} \operatorname{erf} \left( \frac{1}{2\sqrt{x}} \right) + 2\Gamma \left( 0, \frac{1}{4x} \right) \right] \Big\}, \quad (\text{V.11})$$

in the photophobic scenario. In these expressions,  $\operatorname{erf}(x)$  is the error and  $\Gamma(a, x)$  is the incomplete Gamma function and the factor  $\kappa_f$  is equal to  $m_f n_c q^2 e^2$  for leptons and to  $m_f n_c q^2 e^2 + 4m_f g_s^2$  for quarks. The strong gauge coupling,  $g_s$ , is fixed to 1.31 which is obtained by averaging  $\alpha_s$  over the relevant energy range between the  $b$  and  $Z$  mass,

$$\alpha_s \equiv \frac{1}{m_Z - m_b} \int_{m_b}^{m_Z} d\mu \alpha_s(\mu) \approx 0.137, \quad (\text{V.12})$$

where the running of  $\alpha_s(\mu)$  is given by the corresponding renormalization group equation [261]. Finally, the parameter  $\kappa_f$  takes the approximate values  $\{0.16, 8.97, 29.0, 38.1, 38.9\}$  GeV for tau, charm, bottom, the sum over these three, and the sum over all SM fermions (excluding the top), respectively.

In both, Eq. (V.10) and Eq. (V.11), the first term in the curly brackets comes from the fermion annihilation process  $f\bar{f} \rightarrow Va$ , while the second arises from scattering  $fV \rightarrow fa$ .

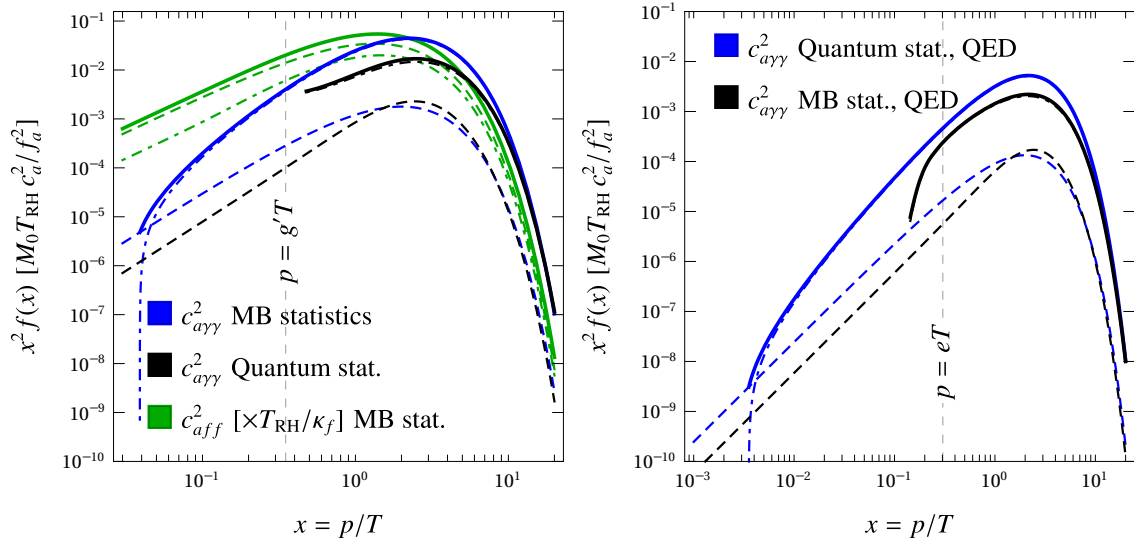


Figure V.2: The ALP momentum distribution function plotted as  $x^2 f(x)$ . *Left figure:* In blue we show the photophilic case for MB statistics; black lines represent the photophilic case with quantum statistics and in green we show the photophobic case for MB statistics. For each, the dashed (dot-dashed) line represents  $f\bar{f} \rightarrow Va$  ( $fV \rightarrow fa$ ) and the solid line is their sum. The vertical dashed line marks  $p = g/T$ , left of which thermal corrections should be added [262]. *Right figure:* Photophilic scenario for MB and quantum statistics in QED, namely, including only a single fermion carrying unit charge. *Image credits:* Enrico Morgante (adapted by author)

The left panel of Fig. V.2 shows the momentum distribution multiplied with  $x^2$  obtained for the photophilic (blue) and photophobic (green) ALP DM, in units of  $M_0 T_{\text{RH}} c_a^2 / f_a^2$ , where  $c_a$  denotes  $c_{a\gamma\gamma}$  or  $c_{aff}$ , respectively.

The dashed lines represent the contribution from fermion annihilation, the dot-dashed ones correspond to fermion scattering, and solid lines are the sum. We rescaled the photophobic ALP lines by  $T_{\text{RH}}/\kappa_f$ , as otherwise, for  $c_{a\gamma\gamma} \sim c_{aff}$  choice, green lines would not be visible on the same panel next to those corresponding to photophilic ALP. Moreover, since for the photophobic ALP,  $f(x) \propto m_f q^2 n_c$ , with such rescaling the computed green curve is

independent of the fermion choice. It can be seen from the plot that, if both  $c_{a\gamma\gamma}$  and  $c_{aff}$  are present, the contribution from  $c_{aff}$  is negligible as long as  $c_{aff} \lesssim c_{a\gamma\gamma} T_{\text{RH}}/m_f$ . Finally, the black lines are the results for  $f(x)$  when using quantum statistics for the involved particles, and we will discuss this case briefly at the end of this section.

Importantly, at  $p/T \simeq 4 \times 10^{-2}$  the dot-dashed blue line turns negative and hence the momentum distribution becomes unphysical for smaller values of  $p/T$ . The reason for that is a simplified treatment of the infrared (IR) divergence in the  $t$ -channel photon exchange diagram where we use the plasmon mass  $m_\gamma$  as a momentum cutoff. For the purpose of our computations, we make a sharp cut at the location where the function turns negative. In the case of a MB distribution, we infer this condition to be

$$p/T = \exp[-1/4 + \gamma_E] \frac{m_\gamma^2}{4T^2} \simeq 0.04. \quad (\text{V.13})$$

The same condition holds also for QED, with appropriately adjusted plasmon mass  $m_\gamma$ . Such a single fermion scenario is shown in the right panel of Fig. V.2 and we can observe the shift of the cutoff toward an order of magnitude smaller values of  $p/T$ ; this effect only arises due to different values for the plasmon mass in the full model and QED, respectively. In any case, for both panels, the cutoff occurs at a value of  $p/T$  at least two orders of magnitude smaller than the expected mean,  $\langle p/T \rangle$ . If the cutoff was at  $p/T \simeq \mathcal{O}(1)$ , the further calculation of structure formation based on this  $f(x)$  would not be justified.

Coming back to the left panel of Fig. V.2, we can infer that in the photophilic case, the annihilation process is subdominant, and as such it is often neglected in the literature (see for example Refs. [136, 260, 263]). On the other hand, in the photophobic case it yields a contribution comparable to scattering (see also Eqs. (V.21) and (V.22)). For the average momentum we obtain  $\langle p/T \rangle = 3.24$  for a photophilic ALP and  $\langle p/T \rangle = 2.36$  for a photophobic one. Up to higher order corrections, this result is independent of  $m_f$ .

The procedure described above is only approximate, and it fails to capture two features that may a priori be important. First, it cannot account correctly for the phase space regions where  $p_i \lesssim T$ , as in these regions MB statistics deviates from a quantum statistics treatment. Second, thermal field theory effects are important for  $p_i \lesssim eT$ , and must be correctly resummed. This is especially true for the process  $fB \rightarrow fa$ , which has a logarithmic IR divergence when  $|\mathbf{p}_\gamma - \mathbf{p}_a| \rightarrow 0$ . In that context, it is interesting to consider the question whether the usage of quantum statistics could in principle cure the occurrence of a negative momentum distribution function at low  $p/T$ . Following the procedure discussed in Ref. [263], we isolate the momentum  $\mathbf{k}$  flowing in the  $t$ -channel propagator and calculated the hard part of the process, by imposing an IR cutoff in the integration,  $|\mathbf{k}| > k_{\text{cut}}$ , which diverges for  $k_{\text{cut}} \rightarrow 0$ . By adding a soft term which is extracted from the ALP self-energy evaluated with a resummed photon propagator at finite temperature, the sum is finite since the cutoff drops out and only the thermal photon mass remains,  $\log(T/m_\gamma) = -\log(\sqrt{11/12}g')$ . More details on the calculation can be found in Ref. [3] and we are going to highlight two important consequences in the following: first, these expressions are only accurate for  $p_a > g'T$ , but they correctly account for the case  $p_{1,2,3} < g'T$ . Below this momentum, the ALP-photon vertex should be thermally corrected as well [262]. Second, obtaining the momentum distribution from the collision term by solving the Boltzmann equation (see Eq. (II.33)), which is most conveniently written in terms of already introduced dimensionless quantities

$$\frac{m_H^2}{M_{\text{Pl}} r} \frac{\partial}{\partial r} f_{\text{QS}}(x, r) = \mathcal{C}(x, r). \quad (\text{V.14})$$

we find that the corresponding distribution function is similar in shape compared to the one obtained with MB statistics (see again Fig. V.2). The overall normalization differs

by a factor  $\int d^3 p_a f_{\text{MB}} / \int d^3 p_a f_{\text{QS}} \sim 5$ , which is not relevant for the purpose of deriving structure formation limits. More importantly, the average momentum is very similar between the two cases; we obtain  $\langle p/T \rangle = 3.18$  for quantum statistics that is to be compared with 3.24 from MB yielding only a  $\approx 2\%$  difference.

Due to practically identical results on  $\langle p/T \rangle$  that stem from the two approaches and the fact that the cutoff to be imposed is at values of  $p/T$  that do not effectively impact  $\langle p/T \rangle$ , we proceed with the classical statistics description that allows us to work with fully analytical expressions when deriving limits from structure formation in Section V.5.

## V.2.2 Axion-like particle properties and production

In the following, we are going to use the ALP DM momentum distribution function  $f(x)$  given in Eqs. (V.10) and (V.11) to derive important quantities of the DM species such as its abundance for instance.

The first step is to verify, that the ALP does not thermalize in the early Universe. This implies that the reheating temperature,  $T_{\text{RH}}$ , should not exceed the temperature at which ALP decouples from the thermal plasma. This decoupling temperature,  $T_{\text{dec}}$ , can be estimated by equating the scattering rate  $\Gamma$  and the Hubble rate  $H(T)$  (see Eq. (II.28)). The scattering rate can be calculated from the momentum integrated collision term,  $C(x, r)$ , which can be derived from the production cross section by comparing Eq. (V.9) and Eq. (V.14), and the number density of SM fermions,  $n_f = 4(6 + 3 \cdot 6) \times 3\zeta(3)T^3/(4\pi^2) = 72\zeta(3)T^3/\pi^2$ , where we sum over all lepton and colored quark families and counting particles/antiparticles. The number density is derived from Eq. (II.22) using a Fermi-Dirac distribution in the highly relativistic limit. In the photophilic case we find for  $\Gamma$ ,

$$\begin{aligned} \Gamma &= \int \frac{d^3 p}{(2\pi^3)} \frac{C(x, r)}{n_f} \\ &= \frac{T^4}{8\pi^3 n_f} \int_0^\infty dx \int_{y^*}^\infty dy \hat{\sigma}(T^2 y) \exp\left[-x - \frac{y}{4x}\right] \\ &= \frac{g'^2 T^3}{1728\pi^3 \zeta(3) \cos^2 \theta_W} \frac{c_{a\gamma\gamma}^2}{f_a^2} g_Y \left(23 - 24\gamma_E - 12 \log\left(\frac{11g'^2}{48}\right)\right), \end{aligned} \quad (\text{V.15})$$

where  $\gamma_E$  is the Euler-Mascheroni constant. For the numerical values of the QED and  $U(1)_Y$  coupling constants,  $e$  and  $g'$ , we use  $\sqrt{4\pi}/137$  and 0.35, respectively and neglect the running of these parameters.

On the other hand, the requirement that the correct DM abundance is reproduced can be used to fix the reheating temperature in terms of  $c_{a\gamma\gamma}$  (see Eq. (II.31)),

$$T_{\text{RH}} = \frac{g_*^s(T_{\text{RH}})}{m_a} \frac{4\pi^4}{45} \frac{\rho_c}{s_0} \frac{12f_a^2 \pi^3}{g'^2 M_0 g_Y} \frac{\cos^2 \theta_w f_a^2}{c_{a\gamma\gamma}^2} \Omega_{\text{DM}} h^2 \left[23 - 24\gamma + 12 \log\left(\frac{11g'^2}{48}\right)\right]^{-1}. \quad (\text{V.16})$$

Comparing both temperatures gives the following ratio, where most prefactors dropped out,<sup>34</sup>

$$\frac{T_{\text{RH}}}{T_{\text{dec}}} \simeq 2 \times 10^{-4} \left(\frac{g_*^s(T)}{106.75}\right) \left(\frac{10 \text{ keV}}{m_a}\right). \quad (\text{V.17})$$

Hence, for  $m_a \sim \mathcal{O}(10 \text{ keV})$  it is guaranteed that the ALP DM never thermalizes. For the photophobic scenario,  $\Gamma/H(T)$  is largest for temperatures at  $T \simeq m_f$ : at higher

<sup>34</sup> This ratio slightly differs from the published version. Although it is roughly two times larger, it does not significantly affect the interpretation of the results based on it.

temperatures, the Hubble rate is stronger than  $\Gamma$ , while at  $T < m_f$  the scattering rate drops because of the Boltzmann suppression of the respective fermion. However, as we will show next, demanding that  $\Omega_{\text{DM}} h^2$  is matched, we require  $c_{aff}/f_a \lesssim 10^{-9} \text{ GeV}^{-1}$  for  $m_a = \mathcal{O}(10 \text{ keV})$  and with such feeble couplings it is guaranteed that photophobic ALP DM does not thermalize with SM species and thus freeze-in is viable.

Doing a momentum integration of the distribution function given in Eq. (V.10), we find for the contribution from  $\bar{f}f \rightarrow Ba$  in the photophilic scenario to the DM abundance,

$$\Omega_{\text{DM}}^{\bar{f}f \rightarrow Ba} h^2 \approx 0.12 \left( \frac{106.75}{g_*^s(T_{\text{prod}})} \right)^{3/2} \left( \frac{c_{a\gamma\gamma}/f_a}{10^{-17} \text{ GeV}^{-1}} \right)^2 \left( \frac{m_{\text{DM}}}{10 \text{ keV}} \right) \left( \frac{T_{\text{RH}}}{6.7 \times 10^{16} \text{ GeV}} \right), \quad (\text{V.18})$$

and the  $fB \rightarrow fa$  process yields

$$\Omega_{\text{DM}}^{fB \rightarrow fa} h^2 \approx 0.12 \left( \frac{106.75}{g_*^s(T_{\text{prod}})} \right)^{3/2} \left( \frac{c_{a\gamma\gamma}/f_a}{10^{-17} \text{ GeV}^{-1}} \right)^2 \left( \frac{m_{\text{DM}}}{10 \text{ keV}} \right) \left( \frac{T_{\text{RH}}}{2.7 \times 10^{15} \text{ GeV}} \right). \quad (\text{V.19})$$

Including both contributions we get

$$\Omega_{\text{DM}} h^2 \approx 0.12 \left( \frac{106.75}{g_*^s(T_{\text{prod}})} \right)^{3/2} \left( \frac{c_{a\gamma\gamma}/f_a}{10^{-17} \text{ GeV}^{-1}} \right)^2 \left( \frac{m_{\text{DM}}}{10 \text{ keV}} \right) \left( \frac{T_{\text{RH}}}{2.6 \times 10^{15} \text{ GeV}} \right). \quad (\text{V.20})$$

We keep  $g_*^s(T_{\text{prod}})$  fixed at the time of ALP DM production, i.e. the reheating temperature  $T_{\text{RH}}$ . Clearly, the scattering process  $fB \rightarrow fa$  is the dominant production channel in the photophilic scenario and hence will also be the more important process in the determination of structure formation limits. The reason for that lies in the logarithmic enhancement arising due to regularizing the  $t$ -channel  $B$ -mediated process with a thermal gauge boson mass which is absent for the production via fermion annihilation.

The equivalent equations to Eqs. (V.18) and (V.19) for the photophobic scenario read

$$\Omega_{\text{DM}}^{\bar{f}f \rightarrow Va} h^2 \approx 0.12 \left( \frac{80}{g_*^s(T_{\text{prod}})} \right)^{3/2} \left( \frac{m_{\text{DM}}}{10 \text{ keV}} \right) \left( \frac{\sum_f \kappa_f}{38.9 \text{ GeV}} \right) \left( \frac{c_{aff}/f_a}{9.6 \times 10^{-11} \text{ GeV}^{-1}} \right)^2, \quad (\text{V.21})$$

and

$$\Omega_{\text{DM}}^{fV \rightarrow fa} h^2 \approx 0.12 \left( \frac{80}{g_*^s(T_{\text{prod}})} \right)^{3/2} \left( \frac{m_{\text{DM}}}{10 \text{ keV}} \right) \left( \frac{\sum_f \kappa_f}{38.9 \text{ GeV}} \right) \left( \frac{c_{aff}/f_a}{1.2 \times 10^{-10} \text{ GeV}^{-1}} \right)^2, \quad (\text{V.22})$$

while the sum gives

$$\Omega_{\text{DM}} h^2 \approx 0.12 \left( \frac{80}{g_*^s(T_{\text{prod}})} \right)^{3/2} \left( \frac{m_{\text{DM}}}{10 \text{ keV}} \right) \left( \frac{\sum_f \kappa_f}{38.9 \text{ GeV}} \right) \left( \frac{c_{aff}/f_a}{7.6 \times 10^{-11} \text{ GeV}^{-1}} \right)^2. \quad (\text{V.23})$$

One can infer from Eqs. (V.21) and (V.22) that both  $\bar{f}f \rightarrow Va$  and  $fV \rightarrow fa$  are of similar strength in the photophobic scenario and thus both contributions are important when deriving limits from structure formation.

### V.3 Structure formation probes: Lyman- $\alpha$ forests and Milky Way satellites

As already discussed in Section II.2.6, a DM candidate which features a non-vanishing distribution function for rather large values of  $p/T$  can be considered to be “warm”. It starts to wash out structures at small scales and this can be quantified by the suppression of the matter power spectrum at such scales. The respective DM momentum distribution function  $f(x, r)$  is essential in the computation of the matter power spectrum,  $P(k)$  at wavenumbers  $k$ . Hence, computing the matter power spectrum is a starting point and the essence for assessing the structure formation limits. In the following, we are going to use the tools developed in Sections II.2.6.1 and II.2.6.3 to calculate the suppression effect on small scale structures for this warm ALP DM model, i.e we are going to use a half-mode analysis and counting the number of Milky Way (MW) subhalos to limit the ALP DM parameter space.

Qualitatively, the suppression of small scale structures due to ALP DM can be quantified by the average momentum  $\langle p/T \rangle$  of the respective momentum distribution function corresponding to both production channels for which we find:

$$\langle p/T \rangle_{\bar{f}f \rightarrow Va} = \frac{\int_0^\infty dx x^3 f_{\bar{f}f \rightarrow \gamma a}(x)}{\int_0^\infty dx x^2 f_{\bar{f}f \rightarrow \gamma a}(x)} = 3.0 \quad (2.31),$$

$$\langle p/T \rangle_{fV \rightarrow fa} = \frac{\int_0^\infty dx x^3 f_{f\gamma \rightarrow fa}(x)}{\int_0^\infty dx x^2 f_{f\gamma \rightarrow fa}(x)} \approx 3.24 \quad (2.44),$$

$$\Rightarrow \langle p/T \rangle \approx 3.24 \quad (V.24),$$

where  $f(x)$  is evaluated at  $r_f = m_H/m_f$  for the photophobic and at  $r \rightarrow 0$  for the photophilic scenario. The numbers in each line correspond to the photophilic and photophobic scenario, the latter given in brackets. The last line refers to the sum of the two processes, and it is the one which is physically relevant. Based on the averaged momentum the photophilic scenario is slightly “warmer” than the photophobic case.

We start by repeating some details for the respective analysis techniques. The starting point of a half-mode analysis is the transfer function  $T(k)$ ,

$$T(k) \equiv \sqrt{\frac{P(k)}{P(k)_{\Lambda\text{CDM}}}}, \quad (V.25)$$

where the subscript  $\Lambda\text{CDM}$  in the denominator denotes the reference matter power spectrum and the expression in the numerator is the corresponding power spectrum for ALP DM. In the following we calculate it numerically by providing analytical expressions for  $f(x)$  to CLASS [145, 146]. Furthermore, we have to take into account entropy dilution effects due to a change in  $g_*^s(T)$  between the time of production and today. This effect is quantified via an effective DM temperature  $T_{\text{DM}}$  which is related to the photon temperature  $T_\gamma$  by

$$T_{\text{DM}} = \left( \frac{g_*^s(T_0)}{g_*^s(T_{\text{prod}})} \right)^{1/3} T_\gamma = \left( \frac{3.94}{g_*^s(T_{\text{prod}})} \right)^{1/3} T_\gamma. \quad (V.26)$$

As can be seen this leads to a “cooling” of the ALP DM and the strength of this effect depends on the time of production  $T_{\text{prod}}$ . Above the electroweak phase transition we have  $g_*^s(T) = 106.75$  for the SM.

As explained in Section II.2.6.1, the computed transfer function is compared to an analytical fit of the transfer function of a warm thermal relic (TR) with mass  $m_{\text{TR}}$  and abundance

$\Omega_{\text{TR}}$  [148] (see Eqs. (II.45) and (II.46) for further details on the analytical expression). In the following, we use for the Hubble constant,  $h$ , and  $\Omega_{\text{TR}}$  the values quoted in Ref. [52]. We can relate the masses  $m_a$  and  $m_{\text{TR}}$  by equalizing the free-streaming length,  $\lambda_{\text{FS}}$ , for the ALP and TR model. In the thermal relic case,  $\lambda_{\text{FS}} \sim 0.22 \text{ Mpc} (\text{keV}/m_{\text{TR}})^{4/3}$ , whereas for the ALP [234],

$$\lambda_{\text{FS}} \sim \text{Mpc} \left( \frac{\text{keV}}{m_a} \right) \left( \frac{g_*^s(T_\nu)}{g_*^s(T_{\text{prod}})} \right)^{1/3}. \quad (\text{V.27})$$

Since we deal with large production temperatures,  $T_{\text{prod}}$ , we have  $g(T_{\text{prod}}) = 106.75$ , whereas the thermal relics decouple at a later time  $T_\nu$ , where  $g_*^s(T_\nu) = 10.75$ . This allows us to derive the following relation between the two masses:

$$(m_a)_{\text{min}} \simeq 2.1 \text{ keV} \left( \frac{m_{\text{TR}}}{1 \text{ keV}} \right)^{4/3}. \quad (\text{V.28})$$

Our averaged ALP DM momentum is similar to the result quoted in Ref. [264].

A better comparison can be done by utilizing the half-mode criterion (see Eqs. (II.48) and (II.49)). The reference transfer function,  $T_{\text{lim}}$ , is based on Eq. (II.45) and uses  $m_{\text{TR}}$  adopted from dedicated searches using limits from Lyman- $\alpha$  forest observations. The lower bounds on the mass of thermal relic,  $m_{\text{TR}}$ , span the range between  $m_{\text{TR}} = 1.9$  and  $5.58 \text{ keV}$  (see Refs. [56, 148, 231, 265, 266]). When showing our limits on the ALP DM parameter space, we will present both *weak* and *strong* bounds, corresponding to this mass range of  $m_{\text{TR}}$ . In Fig. V.3 we show the transfer function of ALP DM for a selection of different masses  $m_a$  as solid, dotted and dashed blue lines and compare them against the limits which exclude the red and light red shaded regions. One can infer that the more stringent limit ( $m_{\text{TR}} = 5.58 \text{ keV}$ ) is essentially excluding ALP masses  $m_a \lesssim 15 \text{ keV}$ , whereas by taking the weaker limit of  $m_{\text{TR}} = 1.9 \text{ keV}$ , only  $m_a \lesssim 5 \text{ keV}$  are disfavored. Using the corresponding half-mode wavenumber  $k_{\text{half}}$ , we can deduce a relation similar to Eq. (V.28). For the ALP model we derived  $k_{\text{half}}$  numerically from the matter power spectrum for different  $m_a$  and fitted the result with an exponential to get the relation

$$k_{\text{half}}^{\text{ALP}} = p_1 \left( \frac{m_a}{\text{keV}} \right)^{p_2}, \quad \text{with } p_1 = 0.87, p_2 = 3.56. \quad (\text{V.29})$$

In the case of a thermal relic, we can solve the equation  $T(k_{\text{half}})^2 = 1/2$  using Eq. (II.45) directly to find that

$$k_{\text{half}}^{\text{TR}} = \frac{(2^{\nu/10} - 1)^{1/(2\nu)}}{\alpha}, \quad (\text{V.30})$$

where  $\alpha$  depends on  $m_{\text{TR}}$ . Equating Eqs. (V.29) and (V.30) allows to derive a numerical relation between  $m_{\text{TR}}$  and our ALP DM mass,

$$(m_a)_{\text{min}} \simeq 2.1 \text{ keV} \left( \frac{m_{\text{TR}}}{1 \text{ keV}} \right)^{1.27}, \quad (\text{V.31})$$

which can be used to map limits from structure formation quoted in  $m_{\text{TR}}$  directly onto a limit  $(m_a)_{\text{min}}$ . Assuming a different value for  $g_*^s(T_{\text{prod}})$  we have to modify this relation by taking the entropy dilution (Eq. (V.26)) into account. Consequently, the previous equation is modified by an additional factor

$$(m_a)_{\text{min}} \simeq 2.1 \text{ keV} \left( \frac{m_{\text{TR}}}{1 \text{ keV}} \right)^{1.27} \left( \frac{106.75}{g_*^s(T_{\text{prod}})} \right)^{1/3}. \quad (\text{V.32})$$

Therefore, smaller values of  $g_*^s(T_{\text{prod}})$  have to be compensated by larger ALP DM masses. We will come back to this when discussing limits for the photophobic scenario.

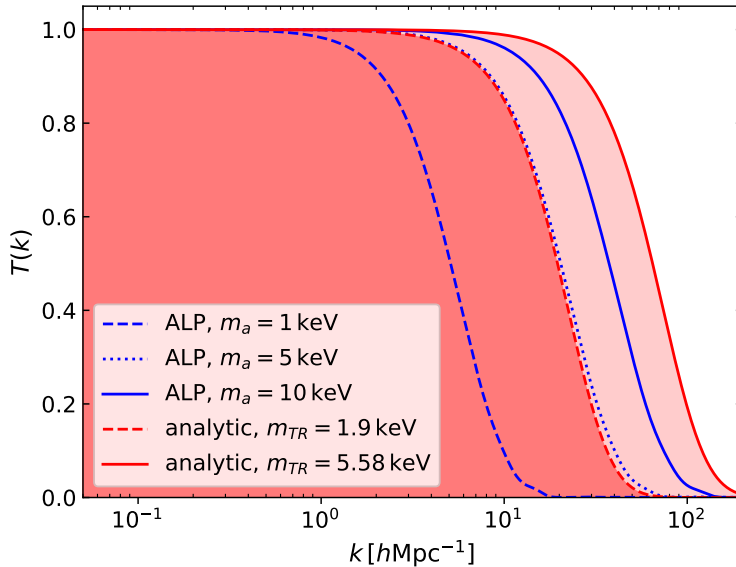


Figure V.3: Transfer function  $T(k)$  shown as blue lines for photophilic ALP DM with different masses compared to thermal relic limits presented as an analytic fit given in Eq. (II.45). Shaded in red is the weak limit whereas the light red shaded region is excluded by the strong limit. Hence, the weakest mass bound stemming from this analysis is  $m_a \simeq 5$  keV, as indicated by the dotted blue line.

As far as the number of MW satellites is concerned, ALP DM with a momentum distribution function which yields an averaged momentum as given in Eq. (V.24) would cause the occurrence of smaller number of subhalos compared to  $\Lambda$ CDM. The predicted number of satellites has an intriguing connection with the type of DM and its production and we are able to set limits on  $m_a$  by requiring that the number of satellites is not smaller than what was observed. As explained in Section II.2.6.3, we are going to set  $N_{\text{sub}} = 64$  as the number of observed subhalos and thus ALP DM scenarios which predict less subhalos will be excluded. However, there is some uncertainty associated to this number and therefore we will examine the influence of  $N_{\text{sub}}$  on our results in more detail in Section V.7.3.

A detailed discussion on the derivation of  $N_{\text{sub}}$  is given in Section II.2.6.3. In the following, we are going to calculate  $N_{\text{sub}}$  via the integral over the subhalo mass range (see Eqs. (II.58) and (II.59) for more details)

$$N_{\text{sub}} = \int_{M_{\text{min}}}^{M_{\text{MW}}} dM \frac{1}{34} \frac{1}{6\pi^2} \frac{M_{\text{MW}}}{M} \frac{P(1/R)}{R^3 \sqrt{2\pi(S - S_0)}}, \quad (\text{V.33})$$

which depends explicitly and implicitly via the variance  $S$  on the matter power spectrum  $P(k)$  of the underlying ALP DM model. Here, the integration boundaries are given by,  $M_{\text{min}} = 10^8 M_{\odot}$  and the MW mass,  $M_{\text{MW}}$ . Decreasing  $m_a$  leads to smaller variances  $S_i$  as well as a suppression of  $P(k)$  which then features an earlier drop. The latter effect is, however, stronger and therefore less subhalos  $N_{\text{sub}}$  are predicted.

We further note, that the prediction for  $N_{\text{sub}}$  clearly depends on the MW mass,  $M_{\text{MW}}$ . The precise value of this quantity is still under investigation and, depending on the analysis, the reported values range roughly between  $1 \times 10^{12} M_{\odot} < M_{\text{MW}} < 1.5 \times 10^{12} M_{\odot}$  (see Refs. [267–271] and references therein), using recent data from the GAIA survey. In the following, we will refer to the lower mass as *strong*, while the higher mass bound is



dubbed as *weak*, because a heavier MW mass allow for a larger number of subhalos in the considered ALP DM model. We want to stress the following two subtleties: first, the quoted MW masses are defined with respect to densities 200 times larger than the critical density, the so-called virial mass of the MW. For this reason, the constant  $C$  of Eq. (II.59) is given by  $C = 34$ . Second, Eq. (V.33) uses MW masses in units of  $M_\odot/h$  as an input and we have to take this additional factor into account.

## V.4 Suppressing production from misalignment and topological defects

An important assumption of our discussion is that the ALP DM is predominantly produced through a freeze-in process. This means that a contribution to the ALP abundance by the misalignment, as well as any ALP population produced from the decay of topological defects such as cosmic strings, must be suppressed. As we are going to show in what follows, this is not trivial for the photophilic ALP, as the requirement of a small misalignment energy density implies bounds on  $T_{\text{RH}}$  and  $f_a$  which are in contrast with what is needed in order to match the observed DM abundance with ALP production via freeze-in. If ALP DM features a significant contribution from misalignment, limits from structure formation will be weakened, because, in contrast to ALP DM produced by a freeze-in, this ALP behaves like “cold” DM (CDM) after the axion field relaxed to the potential minimum. For this reason, in order to justify the assumption that the misalignment energy density is suppressed, we will need some specific assumption about the axion potential and the specific symmetry breaking pattern through which it develops in the early Universe. This statement holds only for the photophilic axion, as we will discuss below.

The energy density from ALP misalignment, assuming a constant ALP mass, is [136]

$$\Omega_a h^2 = 1.61 \times 10^{-2} \left( \frac{m_a}{\text{eV}} \right)^{1/2} \left( \frac{a_i}{10^{11} \text{ GeV}} \right)^2. \quad (\text{V.34})$$

Requiring that this value does not exceed the observed DM abundance yields

$$a_i < 2.6 \times 10^{10} \left( \frac{10 \text{ keV}}{m_a} \right)^{1/4} \text{ GeV}, \quad (\text{V.35})$$

where  $a_i$  is the displacement of the ALP from the potential minimum when it starts to oscillate. It is related to the misalignment angle  $\theta_i$  via  $a_i = \theta_i f_a$ . If the ALP is present during inflation,<sup>35</sup> the minimal misalignment is set by quantum fluctuations during inflation,  $a_i > \sqrt{N_e} H_I / 2\pi$  [58]. Here,  $N_e$  is the number of e-folds<sup>36</sup> of inflation and  $H_I$  is the Hubble rate during the inflation epoch. This, combined with Eq. (V.35), results in a rather stringent upper limit for  $H_I$ . Recalling that the maximal reheating temperature is obtained under the assumption of instantaneous reheating, i.e. the case in which the entire energy density of inflation is converted into radiation, we obtain a bound on the reheating temperature,

$$T_{\text{RH}} < 1.2 \times 10^{14} \left( \frac{106.75}{g_*^s(T_{\text{prod}})} \right)^{1/4} \left( \frac{10 \text{ keV}}{m_a} \right)^{1/8} \left( \frac{60}{N_e} \right)^{1/4} \text{ GeV}. \quad (\text{V.36})$$

<sup>35</sup> If the ALP is the pseudo-Nambu-Goldstone boson (PNGB) of a spontaneously broken global symmetry, this corresponds to the scenario where the symmetry is broken before or during inflation, with  $H_I < f_a$ . In any case, this assumption is not crucial for our discussion.

<sup>36</sup> One e-fold is the time interval in which a patch of the Universe is grown by a factor of  $e$ . Hence, it acts as a time variable in inflation scenarios.

With such values of  $T_{\text{RH}}$  in the photophilic scenario, matching the DM abundance would typically be only achievable for large  $c_{a\gamma\gamma}/f_a$  couplings, disfavored by gamma-ray constraints for  $m_a \gtrsim 2 \text{ keV}$  (see  $T_{\text{RH}} = 10^{14} \text{ GeV}$  line in Fig. V.4). For the photophobic scenario instead, this bound is always satisfied in our considered parameter space.

In the following, we present two alternative ways in which the misalignment contribution can be suppressed without implying a low reheating temperature as in Eq. (V.36).

For instance, if the Peccei-Quinn (PQ) symmetry breaks after inflation, the Universe consists of many patches with different values for  $a_i$ . Thus, neglecting anharmonicities in the potential, the initial misalignment angle is given by the root mean average over all possible values for  $\theta_i$ ,  $\langle \theta_i^2 \rangle = \int_{-\pi}^{\pi} d\theta_i \theta_i^2 / 2\pi = \pi^2/3$ . After inserting this value into Eq. (V.34) and imposing  $\Omega_a h^2 < \Omega_{\text{DM}} h^2$  we obtain

$$f_a < 1.4 \times 10^{10} \left( \frac{10 \text{ keV}}{m_a} \right)^{1/4} \text{ GeV}. \quad (\text{V.37})$$

In this case we have no upper bound on the reheating temperature, because  $\langle a_i \rangle$  is fixed from the beginning. We only need to assume that the ALP-SM couplings are suppressed compared to  $f_a$ , i.e.  $c_{a\gamma\gamma}, c_{aff} \ll \alpha/(2\pi)$ , the r.h.s being the reference value of this coupling in typical axion models. Further, we need to make sure that the contribution from the decay of cosmic string is negligible. For the typical example of a PNCB from the breaking of a global  $U(1)$  symmetry, such as the standard QCD axion, the axion abundance from the decay of topological defects is similar in magnitude to the one from misalignment [124].<sup>37</sup> Assuming this is the case, we expect both contributions to be subdominant when Eq. (V.37) is satisfied.

The second way of suppressing the misalignment energy density is to have a very small angle from the start. This is achieved if the PQ symmetry is broken already during inflation and the axion is heavy,  $m_a > H_I$ , hence suppressing quantum fluctuations. If the axion mass is constant, this would imply a too strong upper bound on  $T_{\text{RH}}$ . Still, the mass of the axion could have been much larger during inflation than today, caused for instance by time evolving PQ breaking dynamics (see e.g. Refs. [272, 273] and references therein for some explicit realizations). In particular, for  $m_a \approx 10^{16} \text{ GeV}$ , the reheating temperature can be as large as  $10^{17} \text{ GeV}$  during inflation. If, after inflation, the ALP is light again, thermal fluctuations could in principle increase the energy density from the misalignment mechanism. This is, however, not the case for the photophilic scenario under our consideration as ALPs do not thermalize with the SM plasma.

We again stress that, for the photophobic ALP, the requirement of a vanishing misalignment energy density is easier to satisfy. If the axion is present during inflation, Eq. (V.36) applies, which is always satisfied for our choice  $T_{\text{RH}} \lesssim \mathcal{O}(100 \text{ GeV})$ . If, instead, the PQ symmetry is broken after inflation,  $f_a$  should satisfy Eq. (V.37). Comparing this requirement with the preferred value of  $c_{aff}/f_a$  shown in Fig. V.6, obtained by imposing that the freeze-in abundance matches the observed DM one, results in  $c_{aff} \lesssim \mathcal{O}(1)$ .

Nonetheless, we will briefly discuss the case of non-negligible misalignment production of ALP DM when discussing constraints from the MW subhalo count in the next section.

---

<sup>37</sup> So far, it is still not exactly known how large this additional abundance contribution is, but it is estimated to be at least of similar size as the contribution from axion misalignment production.

## V.5 Structure formation limits on the model parameter space

We use the distribution functions in Eqs. (V.10) and (V.11) to calculate the matter power spectrum using CLASS, derive the corresponding transfer function and the number of MW subhalos and finally compare against results from observations following the strategy outlined in Section V.3. As long as the observed DM abundance is matched, the result does not depend on the couplings  $c_{a\gamma\gamma}$  and  $c_{aff}$ . Therefore, we performed a scan over  $m_a$  to derive limits.

### V.5.1 Results for the photophilic scenario

The results for the Lyman- $\alpha$  forest and the MW subhalo count for the photophilic scenario are shown in Fig. V.4. For both analysis techniques, we show weak and strong bounds as discussed in Section V.3. The explicit values for the lower limits on the DM mass  $m_a$  are also quoted in Table V.1. For this scenario we set  $g_*^s(T_{\text{prod}}) = 106.75$  for all parameter choices because of the high reheating scale involved.

For the photophilic scenario we also show limits from gamma-ray searches which severely narrow the viable parameter space in the  $m_a \gtrsim 17$  keV region where structure formation constraints fade away. We have calculated gamma-ray limits on ALP DM by utilizing existing ones on keV-scale sterile neutrino DM [81] and matching them with the corresponding ALP decays into photons.

In the photophilic scenario, an ALP can decay directly into two photons and the decay width is given by [274]

$$\Gamma(a \rightarrow \gamma\gamma) = \frac{1}{64\pi} \frac{c_{a\gamma\gamma}^2}{f_a^2} m_a^3. \quad (\text{V.38})$$

Usually available limits from gamma-ray searches are quoted in the parameter space for sterile neutrinos, which decay into a photon and a SM neutrino. Using Eq. (II.14), we match existing bounds on the sterile mixing angle  $\vartheta$  onto the ALP-photon coupling by equating the corresponding decay widths,  $\Gamma(a \rightarrow \gamma\gamma) \equiv \Gamma(\nu_s \rightarrow \gamma\nu)/2$ . Here, the factor 2 compensates that  $\nu_s$  decays only into one  $\gamma$ . This yields a limit  $c_{a\gamma\gamma}^{\text{lim}}$  for the ALP-photon coupling,

$$\frac{c_{a\gamma\gamma}^{\text{lim}}}{f_a} = 9.55 \times 10^{-18} \text{ GeV}^{-1} \left( \frac{m_a}{\text{keV}} \right) \left( \frac{\sin^2(2\vartheta^{\text{lim}})}{10^{-8}} \right)^{1/2}, \quad (\text{V.39})$$

where  $\vartheta^{\text{lim}}$  denotes a mixing angle limit from a given gamma-ray survey. We use limits derived from INTEGRAL [275] (dark blue), NuSTAR [276] (orange) and M31 [277] (red shaded region) to constrain the ALP DM parameter space and show the results together with our own limits derived from structure formation indicated by the blue shaded regions in Fig. V.4. As already pointed out, the limits from structure formation are independent from the coupling  $c_{a\gamma\gamma}$  and constrain only  $m_a$ . The respective lower mass limits are given in Table V.1. Last but not least, the red line is a limit based on estimations of the sensitivity for an upcoming survey. We will briefly comment about this at the end of this section.

	<i>weak</i>	<i>strong</i>
Lyman- $\alpha$	4.9 keV	19.1 keV
MW subhalo	10.3 keV	17.4 keV

Table V.1: Structure formation limits on the ALP mass  $m_a$  in the *photophilic* scenario.

We want to point out one important thing: as explained in Eq. (V.16),  $T_{\text{RH}}$  is fixed by requiring the ALP to be abundant enough. This relation is indicated for the photophilic ALP by the gray lines in Fig. V.4, where we present three different choices:  $T_{\text{RH}} = 10^{14}$  GeV (solid),  $T_{\text{RH}} = 10^{16}$  GeV (dotted) and  $T_{\text{RH}} = m_{\text{Pl}} \equiv M_{\text{Pl}}(8\pi)^{-1/2}$  (dashed) based on the reduced Planck mass. The values of  $T_{\text{RH}}$  in the region below the solid gray line are violating the bound from Eq. (V.36). Although a substantial production from misalignment would invalidate such parameter space, we have shown in Section V.4 several ways to remedy such situation and suppress “cold” ALP DM production via misalignment. Such requirements are not even necessary in the region to the right of  $T_{\text{RH}} = 10^{14}$  GeV where the misalignment production is suppressed.

The other lines correspond to different upper limits on the reheating temperature: the limit on the tensor-to-scalar power ratio  $r$  obtained by Planck sets the bound  $T_{\text{RH}} \lesssim 10^{16}$  GeV [278] (dotted gray line). There can be inflationary scenarios in which this limit does not apply; in these cases the maximum allowed reheating temperature is set by  $m_{\text{Pl}}$ . That means, on the left of the  $T_{\text{RH}} = m_{\text{Pl}}$  dashed gray line, the value of the reheating temperature necessary to obtain  $\Omega_{\text{DM}} h^2 = 0.12$  exceeds the reduced Planck scale making this parameter space theoretically implausible. In summary, it is interesting to note, that limits from current gamma-ray surveys are able to probe most of the accessible photophilic ALP DM parameter region for  $m_a \gtrsim 2$  keV, if we consider only ALP-photon couplings.

On the other hand, taking more production channels into account, we can alleviate this bound on  $T_{\text{RH}}$ . For this purpose we are going to assume that the ALP couples not only to  $B_\mu$  bosons, but also to the SU(2) gauge bosons,  $W_\mu^a$ , via  $c_{aWW} = c_{a\gamma\gamma} \sin \theta_W$ . In that case, we can derive similar diagrams as shown in Fig. V.1, but they give rise to a larger contribution to the DM abundance. Compared to the cross section stemming from ALP- $B_\mu$  boson coupling,  $\sigma^{aBB}$ , the cross section including  $W_\mu^a$  couplings,  $\sigma^{aWW}$  is given by<sup>38</sup>

$$\frac{\sigma^{aWW}}{\sigma^{aBB}} \propto \frac{n_c n_f + n_f}{g_Y} \left( \frac{g_2}{g'} \right)^2 \left( \frac{\cos \theta_W}{\sin \theta_W} \right)^2 \frac{\sum_a \text{tr}(\sigma^a \sigma^a)}{4} \simeq 22. \quad (\text{V.40})$$

The first expression takes into account, that the  $W^a$  boson couple only to LH quark and lepton doublets; the second factor includes the SU(2) gauge coupling,  $g_2 \simeq 0.65$ , and the third the corresponding relations to  $c_{a\gamma\gamma}$ ; the last expression is a trace over two SU(2) generators where  $\sigma^a$  are the Pauli matrices. Including this additional production channel requires smaller  $T_{\text{RH}}$  by a factor of  $\simeq \sqrt{22}$ . We indicate the combination of  $B_\mu$  and  $W_\mu^a$  couplings by the corresponding light gray lines in Fig. V.4. For this case, structure formation can rule out ALP DM parameter space not covered by current gamma-ray searches. Future surveys such as the THESEUS mission [279] will be able to provide a complementary probe of this interesting parameter region. Nonetheless, we observe that for  $m_a \lesssim 2$  keV the structure formation limits are clearly leading, even taking only  $B_\mu$  couplings into account.

In light of our results, we want to briefly comment on the previously reported unidentified line at  $\sim 3.55$  keV in a gamma-ray data spectrum [93, 94]. It sparked lots of interest as a potential signal of decaying DM and one of the favored explanations is the decay of keV-scale sterile neutrinos, but a 7.1 keV ALP DM was discussed as well [248]. Our strong structure formation limits are, however, clearly disfavoring such an interpretation, while the weak ones are marginally consistent with it. We should still stress that our

---

<sup>38</sup> Since the  $W_\mu^a$  have a larger thermal mass,  $m_2 = (11/12)^{1/2} g_2 T$  compared to the  $B_\mu$  boson, the corresponding momentum distribution functions features a slightly larger averaged momentum  $\langle p/T \rangle \sim 3.33$ , but we neglect this effect here to allow for a simple rescaling.

findings are not in general disfavoring a DM interpretation of a 3.5 keV line and hold only for the freeze-in production of ALPs. For instance, scenarios where ALPs are dominantly produced via the misalignment mechanism are still viable in this regard.

As mentioned before, above reheating temperatures  $T_{\text{RH}} = 10^{14}$  GeV, we have to suppress ALP production by the misalignment mechanism. Keeping this in mind, we address the case for a photophilic ALP, where the production via scattering processes only contributes a fraction of “warm” ALP DM,  $F \equiv \Omega_a/\Omega_{\text{DM}}$ , to the total abundance, while the rest is “cold” ALP DM generated by the misalignment mechanism as described in Section V.4. In this case ALP DM consists of a mixture of two components with different temperatures and the limits on the ALP parameter space change accordingly.

The results are shown in Fig. V.5 where we vary  $F$  between 0.05 and 1 and derive the corresponding limits on  $m_a$  based on the MW subhalo count using the strong mass choice.<sup>39</sup> In particular, for  $F < 0.2$ , i.e. only a small “warm” ALP DM fraction, the mass limit starts to drop and effectively vanishes for very small fractions  $\lesssim 0.05$  since the larger “cold” ALP DM component dominates the matter power spectrum in this case. That means, if misalignment is not significantly suppressed, the mass limits in Fig. V.4 have to be rescaled and become significantly weaker.

### V.5.2 Results for the photophobic scenario

In this section, we apply the same techniques as above to the photophobic scenario. In that case we derived Eq. (V.11) by expanding Eq. (V.9) for small  $m_f$  assuming that  $T_{\text{RH}} \gg m_f$ . By doing so, the dependence on the reheating temperature actually drops out. We implicitly assumed that  $T_{\text{RH}} \lesssim 160$  GeV. However, for smaller reheating temperatures we have to keep the full expression and an explicit  $T_{\text{RH}}$  dependence is recovered, as we will discuss later in this section.

Using Eq. (V.23), the accessible parameter space is then represented by a linear relation between  $m_a$  and  $c_{aff}$ ,

$$\frac{c_{aff}}{f_a} \simeq 7.49 \times 10^{-11} \left( \frac{10 \text{ keV}}{m_a} \right)^{1/2} \left( \frac{38.9 \text{ GeV}}{\kappa_f} \right)^{1/2} \text{ GeV}^{-1}. \quad (\text{V.41})$$

The results are shown in Fig. V.6 where the green diagonal lines denotes the viable parameter space of the model assuming couplings to different fermions. The upper line corresponds to a tau lepton contribution only, while the lower edge shows the sum of tau lepton,  $c$  and  $b$  quark contributions with equal coefficients, and the two lines in between indicates an exclusive coupling to either  $c$  or  $b$  quark.

The regions shown in blue are disfavored using Lyman- $\alpha$  forest limits and the MW subhalo counts. The strongest limit on the photophobic ALP arises from Lyman- $\alpha$  data (see also Table V.2) and reads  $m_a \approx 15$  keV. The derived constraints are slightly weaker compared to the photophilic case, because ALP DM produced in the photophobic scenario is slightly “cooler” compared to the other case (see Section V.2).<sup>40</sup> However, in the photophobic scenario we assumed  $T_{\text{RH}} \lesssim 160$  GeV and so we have to take a change in  $g_*^s(T_{\text{prod}})$  into account. The results were derived using  $g_*^s(T_{\text{prod}}) = 106.75$  and so the limits on the ALP

<sup>39</sup> The half-mode analysis is not particularly suited to constrain  $m_a$  for this setup, since the presence of the CDM component gives rise to a plateau in the transfer function and it is not clear how to define  $k_{\text{half}}$  properly. See Section VI.3.2 for further comments on this issue.

<sup>40</sup> A recent study including an updated number of MW satellites quotes stronger results in terms of  $m_{\text{TR}} > 6.5$  keV [280]. This allows us to use the ALP DM transfer function directly to derive mass bounds. After doing so we find  $m_a > 23.0$  keV for the photophilic and  $m_a > 17.5$  keV for the photophobic scenario, which extends even beyond the strong bounds derived in our own analysis.

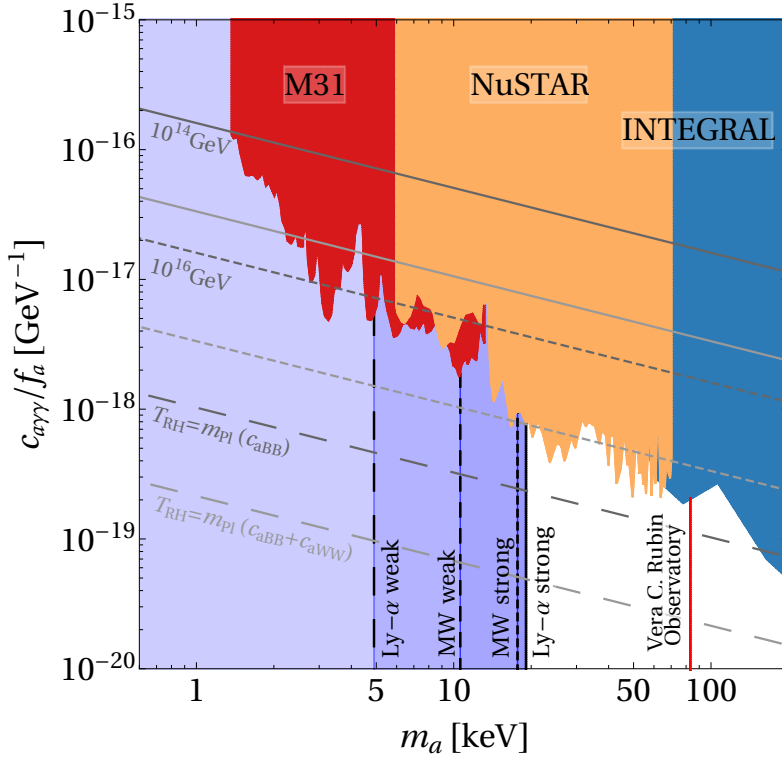


Figure V.4: The blue shaded regions are structure formation limits on the photophilic ALP parameter space derived using a half-mode analysis technique as well as a MW subhalo count. The former (latter) are denoted as Lyman- $\alpha$  (MW). For both, weak and strong limits are shown (see Section V.3 for further analysis details). Additionally, gamma-ray limits from INTEGRAL (dark blue shaded) [275], NuSTAR (orange shaded) [276] and M31 [277] (red shaded) are shown. The diagonal dashed lines indicate specific values of  $T_{RH}$ , calculated by the requirement of producing the observed amount of DM. The dark gray line assumes only couplings between ALP and  $B$  bosons, whereas the light gray lines takes an additional coupling  $c_{aWW}$  into account. Finally, the red line at  $m_a \sim 80$  keV is the projected sensitivity from the forthcoming Vera C. Rubin observatory. *Image credits:* Vedran Brdar (adapted by author)

mass have to be rescaled according to Eq. (V.32). For instance, if  $g_*^s(T_{\text{prod}}) = 80$ , all mass limits are increased by a factor  $\simeq 1.1$  compared to the results shown in Table V.2.

	<i>weak</i>	<i>strong</i>
Lyman- $\alpha$	3.7 keV	15.5 keV
MW subhalo	7.8 keV	13.3 keV

Table V.2: Structure formation limits on the ALP mass  $m_a$  in the *photophobic* scenario under the assumption that  $g_*^s(T_{\text{prod}}) = 106.75$ .

If the ALP has flavor universal couplings or if the strength of the ALP-fermion coupling is at least comparable for several flavors including electrons, further constraints have to be applied on the parameter space. First, if there is an ALP-electron coupling, ALPs are produced via Bremsstrahlung processes inside red giants (RG), would leave the core and lead to additional energy emission of RGs which can be detected. Recent bounds on such cooling effects during the Helium ignition phase of RGs, place a limit on the dimensionless coupling  $g_{ae} < 1.2 \times 10^{-13}$  [281]. Converting it to our parametrization gives

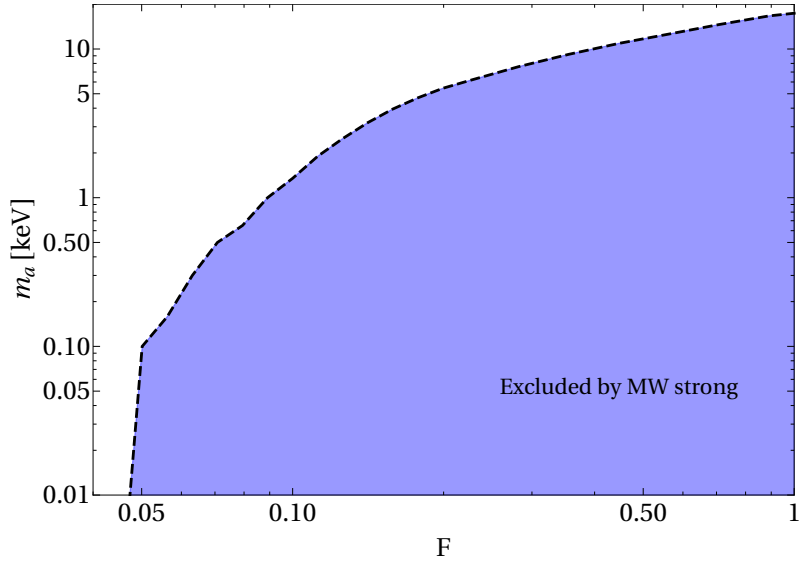


Figure V.5: Limits for the photophilic ALP  $F - m_a$  parameter plane stemming from a MW subhalo count assuming the strong MW mass choice. We considered that freeze-in contributes only a fraction  $F < 1$  to the total ALP DM abundance. The blue shaded region is excluded because these parameters yield  $N_{\text{sub}} < 64$ . As the cold ALP DM contribution increases, the limit on  $m_a$  decreases correspondingly and effectively vanishes for  $F \lesssim 0.05$ .

(see Ref. [282]),

$$\frac{c_{aee}}{f_a} = \frac{g_{ae}}{2m_e} < 1.2 \times 10^{-10} \text{ GeV}^{-1}. \quad (\text{V.42})$$

However, ALPs can only be produced inside RG, if they are light enough; assuming a RG core temperature of  $10^8$  K, the limits applies only for ALPs with mass  $m_a \lesssim 9$  keV. Second, recent electron recoil measurements from the XENON1T collaboration limits the ALP-electron coupling even further [128]. The latter is clearly more relevant for a larger span of ALP masses. Consequently, the XENON1T line is chiefly below the green band in the region  $m_a \lesssim 10$  keV, disfavoring the flavor universal ALP coupling scenario for such parameter choice.

Although a tree-level ALP-photon is absent in the photophobic scenario, there is still an effective coupling  $c'_{a\gamma\gamma}$  to photons due to fermion loops [125]. In the limit of  $m_a \rightarrow 0$  it is given by

$$\frac{c'_{a\gamma\gamma}}{f_a} \simeq -\frac{m_a^2 e^2}{24\pi^2} \sum_f \frac{n_c Q_f^2 c_{aff}}{m_f^2 f_a}, \quad (\text{V.43})$$

where we have to sum over all fermions  $f$  involved with their respective electric charges  $Q_f$  in units of  $e$ . Inserting the effective coupling into Eq. (V.38) allows to evaluate constraints from gamma-ray searches for the photophilic scenario as well. We have, however, found that such gamma-ray limits are only relevant if ALP couples to electrons, because the loop induced coupling to photons is suppressed by the mass ratio  $m_a^2/m_f^2$ . In this case, even parameter space above  $m_a \sim 10$  keV, unexcluded by XENON1T, would be disfavored in a flavor universal scenario. We note, however, that it was recently shown that by adding more new physics, destructive interference between loop-level diagrams contributing to decays into SM photons can be achieved; hence the limit can be relaxed substantially [283], particularly for higher values of  $m_a$ .

As already pointed out, keeping higher order terms of  $m_f$  in  $f(x)$  as opposed to Eq. (V.41) restores a  $T_{\text{RH}}$  dependence for the photophobic scenario as well and the viable param-

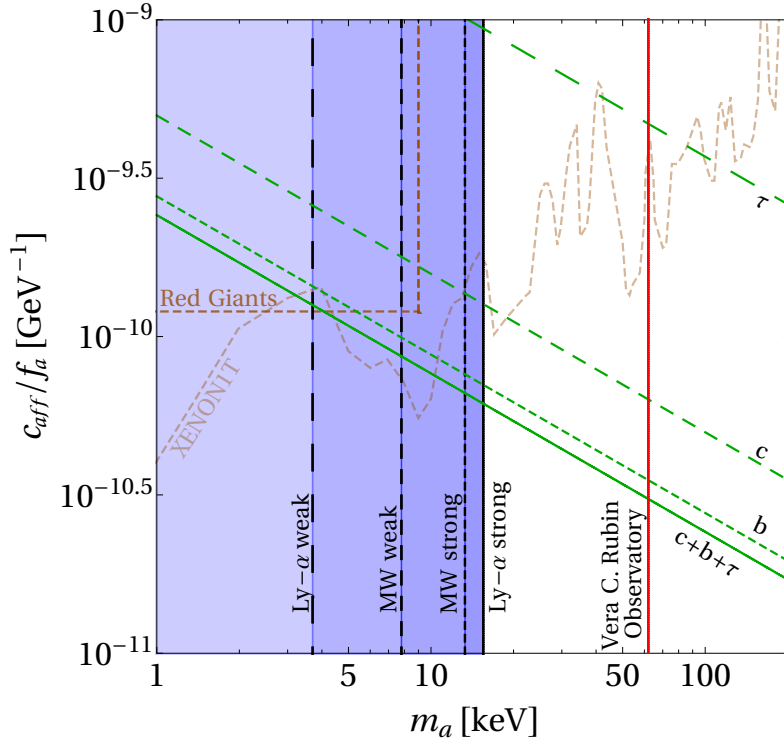


Figure V.6: As before, blue shaded regions are structure formation limits on the photophobic ALP parameter space derived using a half-mode analysis technique as well as a MW subhalo count. The former (latter) are denoted as Lyman- $\alpha$  (MW). For both, weak and strong limits are shown (see Section V.3 for further analysis details). The green lines indicate the viable parameter space based on Eq. (V.41). If the ALP couples only to tau leptons, the ALP needs large couplings indicated by the uppermost line, whereas the other lines correspond to couplings to  $c$  or  $b$  quark and the sum over all three fermions. If the ALP has a flavor universal coupling, additional bounds from red giant cooling and limits from XENON1T has to be taken into account. Finally, the red line at  $m_a \sim 60$  keV is the projected sensitivity from the forthcoming Vera C. Rubin observatory. *Image credits:* Vedran Brdar (adapted by author)

ter space, i.e. the green lines in Fig. V.6, does depend on the choice of the reheating temperature. The dependency is shown in Fig. V.7 where we have varied  $T_{\text{RH}}$  between 160 GeV and 10 GeV (shown as green dashed lines) for a photophobic ALP which couples exclusively to  $b$  quarks. Compared to Fig. V.6, lower reheating temperatures have to be compensated by slightly larger coupling coefficients  $c_{aff}$ . Further, we included the same entropy dilution factor as shown in Eq. (V.32), to take a decrease in  $g_*^s$  for smaller reheating temperatures into account: while the blue shaded regions correspond to mass limits for  $g_*^s(T_{\text{prod}}) = 106.75$ , the black lines are bend to higher masses, because the DM temperature increases compared to the thermal bath. For  $T_{\text{RH}} \rightarrow 10$  GeV this factor is set by  $\simeq 1.07$ . We have restricted the lower temperature limit to  $T_{\text{RH}} \gtrsim 2m_f$ , because at even lower reheating temperatures the fermion mass starts to become relevant and the  $b$  quark will not necessarily reach a thermal population.

We note here that our results constrain the relaxion<sup>41</sup> DM model of [252], in which the

<sup>41</sup>A relaxion is an ALP with special properties; it is constructed such that it can address the hierarchy problem of the SM. During the cosmological evolution, it scans the Higgs mass parameter range by providing a time-dependent effective Higgs mass term. Back-reactions will eventually stop the relaxion, hence allowing a natural realization of the weak scale Higgs mass.



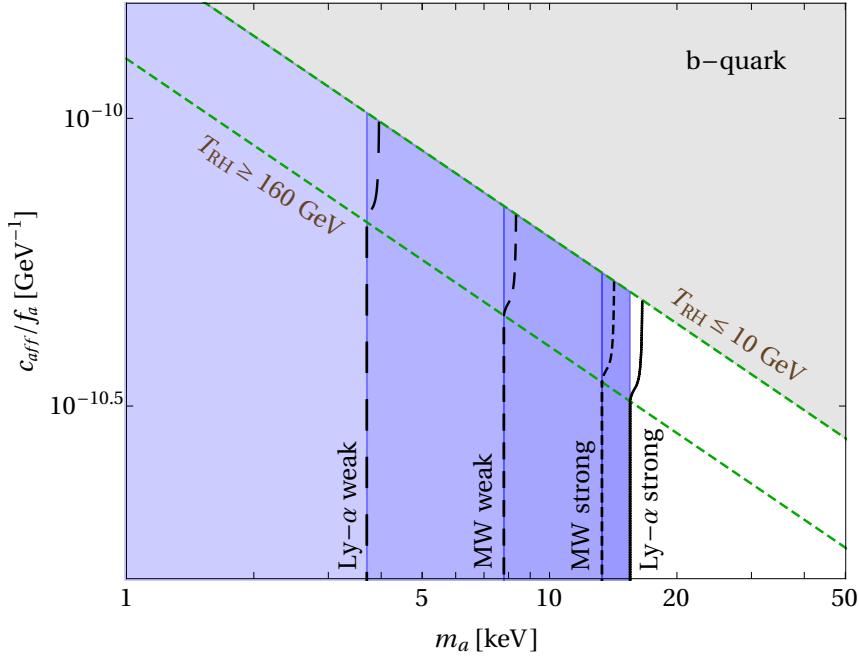


Figure V.7: Impact of  $T_{\text{RH}}$  on the viable parameter space of the photophobic ALP, assuming that it couples only to  $b$  quarks. A larger ALP-fermion coupling is needed to get the correct DM abundance for lower reheating temperatures. The blue shaded regions are the same mass limits as in Fig. V.6, where  $g_*^s(T_{\text{prod}}) = 106.75$ , while the black lines are computed taking a change in  $g_*^s(T_{\text{prod}})$  into account.

relaxion production occurs via freeze-in similar to the scenario considered here. The relaxion can constitute 100% of DM only if a large mass is allowed by a large hierarchy in the relaxion couplings. Even assuming the most conservative bounds from the number of MW subhalos, the model provides an explanation of the XENON1T anomaly only if the relaxion is responsible for a fraction of the DM abundance [253].

Finally, we are going to comment on future sensitivity projections. The Vera C. Rubin observatory is designed to go beyond the results derived from SDSS and among observing other properties, it can measure the MW mass halo function down to  $10^6 M_\odot$ . Hence, its resolution allows to detect more ultra-faint subhalos and it will improve limits dramatically. Using its projected limit on thermal relic DM,  $m_{\text{TR}} > 18 \text{ keV}$  [284, 285], we find that, for the photophilic case, the lower limit on the ALP DM mass would be pushed to  $m_a > 83 \text{ keV}$ . Similarly, we find  $m_a > 62 \text{ keV}$  for the photophobic case (both values are illustrated in Figs. V.4 and V.6 with red lines). It is rather intriguing that for the case of photophilic ALP, the structure formation limits offer a complementary probe to gamma-ray limits in the  $m_a \sim \mathcal{O}(100 \text{ keV})$  region.

## V.6 Summary of Chapter V

ALPs are currently one of the most popular extension of the SM, being studied and tested across a wide range of masses and couplings. In this section we studied keV-scale ALP DM produced via a freeze-in through feeble interactions with gauge bosons, such as photons,  $B_\mu$  bosons and gluons, and SM fermions. The respective momentum distribution function was calculated assuming MB statistics for the involved particles and we briefly discussed the implementation of quantum statistics and compared both methods with each other. Although these approaches did not capture the full picture at small values of  $p/T$ , they turned out to be robust for constraining the parameter space using the matter power spectrum derived from the respective momentum distribution function. Using Lyman- $\alpha$  forest data as well as the observed number of MW companions we derived structure formation limits that were missing to date. For the photophilic ALP DM, we found the most stringent limits to exclude ALP DM masses below  $\sim 19$  keV, complementing constraints from gamma-ray data. In particular, we have found these searches to severely limit our scenario where only  $B_\mu$  couplings are considered, because the corresponding reheating temperature necessary to achieve enough ALP DM abundance is too large. Thus, non-trivial inflation scenarios or additional production channels via a ALP- $W$  coupling are needed in order to avoid these astrophysical constraints.

We also discussed how to suppress an additional “cold” ALP DM production via misalignment which would weaken the derived limits on the ALP mass.

For the photophobic ALP, the obtained limits are somewhat milder, because in that case we found DM to be “cooler”, i.e. the averaged momentum is slightly smaller. Further, if the photophobic ALP does couple flavor-universal and not only to heavy fermions, the viable parameter space will be in tension with limits from gamma-ray data.

Utilizing measurements from the upcoming Vera Rubin observatory, we found that the mass bounds will be strongly improved up to  $m_a \gtrsim 60$  keV for both scenarios.

## V.7 Appendix of Chapter V

### V.7.1 Amplitudes for dark matter production channels

In the following chapters, we will go into more details regarding the calculation of the reduced cross sections  $\hat{\sigma}$  needed to determine the momentum distribution  $f(x, r)$  of the ALP DM. We discuss the ALP production via the scattering process first, before we turn on the production of ALPs via fermion annihilation. To keep the expressions as simple as possible, we mention only the coupling to photons in the following. However, the results can easily be generalized to the case of a  $B$  gauge boson or gluons.

#### V.7.1.1 Process A: $f\gamma \rightarrow fa$

This process, also-called Primakoff process for ALP-photon couplings only, comes with three separate diagrams: the first one involves a coupling to photons,  $c_{a\gamma\gamma}$ , we will refer to it as  $A1$ , whereas the other two are proportional to  $c_{aff}$  instead. We refer to the  $u$ -channel diagram as  $A21$  and the  $s$ -channel as  $A22$ . The corresponding production diagrams are shown in Fig. V.8. Following the procedure outlined in Ref. [234] we calculate the inverse process  $f(p_1)a(p) \rightarrow f(p_3)\gamma(p_2)$ .<sup>42</sup>

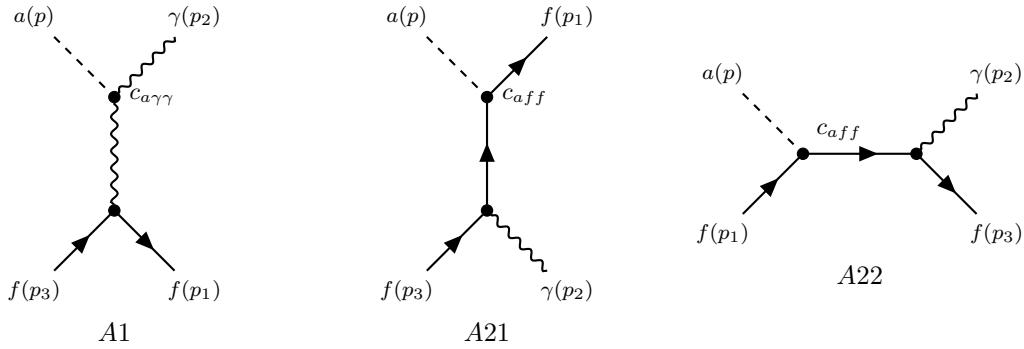


Figure V.8: Inverse production process of ALP DM via its coupling to photons ( $A1$ ) and fermions ( $A21$  and  $A22$ ). An ALP particle  $a$  is converted into a photon  $\gamma$  by scattering off a fermion  $f$ .

The matrix elements for the respective processes are given by

$$\mathcal{M}_{A1} = -e \frac{c_{a\gamma\gamma}}{f_a} \varepsilon_\nu^* \bar{u}(p_3) \gamma_\rho u(p_1) \left( -i \frac{g_{\rho\beta}}{(p-p_2)^2} \right) \times \epsilon^{\alpha\beta\mu\nu} (p_2 - p)_\alpha (-p_{2\mu}), \quad (\text{V.44})$$

$$\mathcal{M}_{A21} = -2iem_f \frac{c_{aff}}{f_a} \varepsilon_\nu^* \bar{u}(p_3) \gamma_5 \frac{i(\not{p}_3 - \not{p} + m_f)}{(p_3 - p)^2 - m_f^2} \gamma^\nu u(p_1), \quad (\text{V.45})$$

$$\mathcal{M}_{A22} = -2iem_f \frac{c_{aff}}{f_a} \varepsilon_\nu^* \bar{u}(p_3) \gamma^\nu \frac{i(\not{p} + \not{p}_1 + m_f)}{(p + p_1)^2 - m_f^2} \gamma_5 u(p_1). \quad (\text{V.46})$$

Here we have used the equations of motion to rewrite the axion-fermion coupling as

$$\frac{c_{aff}}{f_a} \partial_\mu a \bar{f} \gamma^\mu \gamma_5 f = -2im_f \frac{c_{aff}}{f_a} a \bar{f} \gamma_5 f, \quad (\text{V.47})$$

and the four-dimensional Levi-Civita tensor arises from the ALP-photon interaction term  $\frac{c_{a\gamma\gamma}}{f} a F_{\mu\nu} \tilde{F}^{\mu\nu}$ .

<sup>42</sup> Since we do not assume any CP violation this process is in fact the same as  $f(p_3)\gamma(p_2) \rightarrow f(p_1)a(p)$ .

The Mandelstam variables of this process are:

$$\begin{aligned} s &= (p + p_1)^2 = m_a^2 + m_f^2 + 2p \cdot p_1 \\ &= (p_2 + p_3)^2 = m_f^2 + 2p_2 \cdot p_3, \end{aligned} \quad (\text{V.48})$$

$$\begin{aligned} t &= (p_1 - p_3)^2 = 2m_f^2 - 2p_1 \cdot p_3 \\ &= (p - p_2)^2 = m_a^2 - 2p \cdot p_2, \end{aligned} \quad (\text{V.49})$$

$$\begin{aligned} u &= (p - p_3)^2 = m_a^2 + m_f^2 - 2p \cdot p_3 \\ &= (p_1 - p_2)^2 = m_f^2 - 2p_1 \cdot p_2. \end{aligned} \quad (\text{V.50})$$

They are related by

$$s + t + u = m_a^2 + 2m_f^2 \rightarrow u = m_a^2 + 2m_f^2 - s - t. \quad (\text{V.51})$$

Squaring the sum of Eqs. (V.44) to (V.46), summing over the polarizations of the outgoing photon and the spins of the initial fermions and setting  $m_a = 0$ , we find for the amplitude of process  $A$ :

$$\begin{aligned} |\overline{\mathcal{M}}_A|^2 &= -e^2 \frac{c_{a\gamma\gamma}^2}{f_a^2} \frac{(-4m_f^2 s + 2m_f^4 + 2s^2 + 2st + t^2)}{t} \\ &\quad - 8e^2 m_f^2 \left( 2 \frac{c_{aff}^2}{f_a^2} + \frac{c_{a\gamma\gamma} c_{aff}}{f_a^2} \right) \frac{t^2}{(m_f^2 - s)(s + t - m_f^2)}. \end{aligned} \quad (\text{V.52})$$

We used Eq. (V.51) to remove the dependence on the Mandelstam variable  $u$ .

### V.7.1.2 Process B: $f\bar{f} \rightarrow \gamma a$

This process involves three separate diagrams as well: one  $s$ -channel diagram with a coupling to photons, we will refer to it as  $B1$ , whereas the other two involves an ALP-fermion coupling instead. We refer to the  $t$ -channel diagram as  $B21$  and the  $u$ -channel as  $B22$ . The corresponding production diagrams are shown in Fig. V.9. The inverse process we are interested in is  $\gamma(p_1) a(p) \rightarrow f(p_3) \bar{f}(p_2)$ .

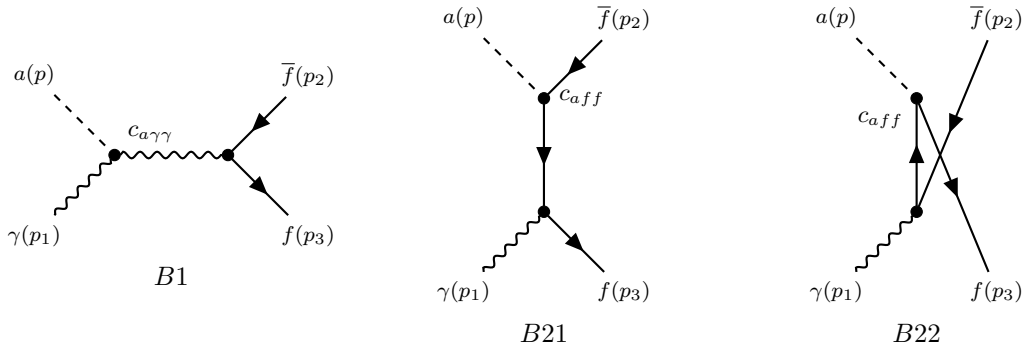


Figure V.9: Inverse production process of ALP DM via its coupling to photons ( $B1$ ) and fermions ( $B21$  and  $B22$ ). An ALP particle  $a$  annihilates with a photon  $\gamma$  into a fermion-antifermion pair.

The matrix elements for the respective processes are given by

$$\mathcal{M}_{B1} = -e \frac{g_{a\gamma\gamma}}{f_a} \bar{u}(p_2) \gamma^\rho v(p_3) \left( -i \frac{g_{\rho\beta}}{(p + p_1)^2} \right) \times \epsilon^{\alpha\beta\mu\nu} (-p - p_1)_\alpha p_{1\mu} \epsilon_\nu, \quad (\text{V.53})$$

$$\mathcal{M}_{B21} = -2iem_f \frac{c_{aff}}{f_a} \varepsilon_\nu \bar{u}(p_2) \gamma^5 \frac{i(\not{p}_1 - \not{p}_3 + m_f)}{(p_1 - p_3)^2 - m_f^2} \gamma^\nu v(p_3), \quad (\text{V.54})$$

$$\mathcal{M}_{B22} = -2iem_f \frac{c_{aff}}{f_a} \varepsilon_\nu \bar{u}(p_2) \gamma^\nu \frac{i(\not{p} - \not{p}_3 + m_f)}{(p - p_3)^2 - m_f^2} \gamma^5 v(p_3). \quad (\text{V.55})$$

As above we have used the equations of motion to rewrite the axion-fermion vertex. The Mandelstam variables of this process are:

$$\begin{aligned} s &= (p + p_1)^2 = m_a^2 + 2p \cdot p_1 \\ &= (p_2 + p_3)^2 = 2m_f^2 + 2p_2 \cdot p_3, \end{aligned} \quad (\text{V.56})$$

$$\begin{aligned} t &= (p_1 - p_3)^2 = m_f^2 - 2p_1 \cdot p_3 \\ &= (p - p_2)^2 = m_a^2 + m_f^2 - 2p \cdot p_2, \end{aligned} \quad (\text{V.57})$$

$$\begin{aligned} u &= (p - p_3)^2 = m_a^2 + m_f^2 - 2p \cdot p_3 \\ &= (p_1 - p_2)^2 = m_f^2 - 2p_1 \cdot p_2. \end{aligned} \quad (\text{V.58})$$

They fulfill the same relation as the Mandelstam variables of process  $A$  given in Eq. (V.51). Squaring the sum of Eqs. (V.53) to (V.55), summing over the polarizations of the outgoing photon and the spins of the initial fermions and setting  $m_a = 0$ , we find for the amplitude of process  $B$ :

$$\begin{aligned} |\overline{\mathcal{M}}_B|^2 &= e^2 \frac{c_{a\gamma\gamma}^2}{f_a^2} \frac{(-4m_f^2 t + 2m_f^4 + s^2 + 2st + 2t^2)}{s} \\ &\quad - 8e^2 m_f^2 \left( 2 \frac{c_{aff}^2}{f_a^2} + \frac{c_{a\gamma\gamma} c_{aff}}{f_a^2} \right) \frac{s^2}{(t - m_f^2)(s + t - m_f^2)}. \end{aligned} \quad (\text{V.59})$$

## V.7.2 Calculating the cross section

To find the momentum distribution we have to calculate the reduced cross section  $\hat{\sigma}$  of a  $a + 3 \rightarrow 1 + 2$  process first. It is given by [286]

$$\begin{aligned} \hat{\sigma} &= \frac{\lambda(s, m_3^2, m_a^2)}{s} \int \frac{d^3 p_1}{(2\pi)^3 2E_1} \frac{d^3 p_2}{(2\pi)^3 2E_2} (2\pi)^4 \delta^4(p_1 + p_2 - p_3 - p_a) |\overline{\mathcal{M}}|^2 \\ &\equiv \frac{\lambda(s, m_3^2, m_a^2)}{s} \Phi, \end{aligned}$$

where  $m_i$ , ( $i = 1, 2, 3$ ), is the mass of particle with momentum  $p_i$  and  $\lambda(x, y, z)$  is the *Källén* or *triangle* function,

$$\lambda(x, y, z) = x^2 + y^2 + z^2 - 2xy - 2xz - 2yz. \quad (\text{V.60})$$

For the calculation of the final state phase space integral,  $\Phi$ , it is convenient to use the center-of-mass frame and assign the following choices for the particle momenta:

$$\begin{aligned} \mathbf{p}_a &= (0, 0, k), \\ \mathbf{p}_3 &= (0, 0, -k), \\ \mathbf{p}_1 &= \mathbf{p}_3 + \ell, \quad |\mathbf{p}_1| \equiv q, \end{aligned} \quad (\text{V.61})$$

where  $\ell = (\sin \theta \cos \phi, \sin \theta \sin \phi, \cos \theta) \ell$

$$\mathbf{p}_2 = -\mathbf{p}_1.$$

The  $\ell$  integration will be done last in order to isolate possible IR divergences in the  $t$ -channel. Using the Mandelstam variable  $s = (p_1 + p_2)^2 = (p_3 + p_a)^2$ , we find for the squared particle momenta,

$$k^2 = \frac{s}{4} \left[ \left( 1 - \frac{m_3^2}{s} - \frac{m_a^2}{s} \right)^2 - 4 \frac{m_3^2 m_a^2}{s^2} \right], \quad (\text{V.62})$$

$$q^2 = \frac{s}{4} \left[ \left( 1 - \frac{m_1^2}{s} - \frac{m_2^2}{s} \right)^2 - 4 \frac{m_1^2 m_2^2}{s^2} \right]. \quad (\text{V.63})$$

They are related to  $\ell$  by

$$\cos \theta = \frac{k^2 - q^2 + \ell^2}{2k\ell}. \quad (\text{V.64})$$

The integration range for  $\ell$  can be derived by imposing  $\cos \theta < 1$  and  $\cos \theta > -1$ :

$$|k - q| < \ell < k + q. \quad (\text{V.65})$$

Finally, the Mandelstam variables  $t, u$  can be rewritten as

$$t = m_1^2 + m_3^2 - 2\sqrt{q^2 + m_1^2}\sqrt{k^2 + m_3^2} + k^2 + q^2 - \ell^2, \quad (\text{V.66})$$

$$u = m_1^2 + m_a^2 - 2\sqrt{q^2 + m_1^2}\sqrt{k^2 + m_a^2} - k^2 - q^2 + \ell^2, \quad (\text{V.67})$$

which, in the massless limit ( $m_i \rightarrow 0$ ), simplifies to

$$t = -\ell^2, \quad (\text{V.68})$$

$$u = \ell^2 - s. \quad (\text{V.69})$$

Now everything is expressed in terms of the integration variable  $\ell$  and we can compute the phase space integral  $\Phi$ . Using the three-dimensional  $\delta^3$ -distribution including the particle momenta and  $s = (p_3 + p_a)^2 = (E_3 + E_a)^2$ , it is given by

$$\Phi = \int d^3 p_1 \frac{1}{16\pi^2 E_1 E_2} \delta(E_1 + E_2 - \sqrt{s}) \overline{|\mathcal{M}|^2}. \quad (\text{V.70})$$

Changing integration variable from  $\mathbf{p}_1$  to  $\ell$ , the  $\delta$  distribution can be rewritten as

$$\begin{aligned} \delta(E_1 + E_2 - \sqrt{s}) &= \\ &= \delta(\sqrt{k^2 + \ell^2 - 2k\ell \cos \theta + m_1^2} + \sqrt{k^2 + \ell^2 - 2k\ell \cos \theta + m_2^2} - \sqrt{s}) \\ &= \frac{E_1 E_2}{k\ell \sqrt{s}} \delta\left(\cos \theta - \frac{k^2 - q^2 + \ell^2}{2k\ell}\right), \end{aligned} \quad (\text{V.71})$$

and the integral is given by

$$\begin{aligned} \Phi &= \int_0^{2\pi} d\phi \int_{-1}^1 d\cos \theta \int_{\ell_{\min}}^{\ell_{\max}} d\ell^2 \frac{\ell}{2} \frac{1}{16\pi^2 E_1 E_2} \frac{E_1 E_2}{k\ell \sqrt{s}} \delta\left(\cos \theta - \frac{k^2 - q^2 + \ell^2}{2k\ell}\right) \overline{|\mathcal{M}|^2} \\ &= \frac{1}{8\pi} \frac{1}{\lambda(s, m_3^2, m_a^2)^{1/2}} \int_{\ell_{\min}}^{\ell_{\max}} d\ell^2 \overline{|\mathcal{M}|^2}. \end{aligned} \quad (\text{V.72})$$

The integration boundaries are fixed by Eq. (V.65). Finally, the reduced cross section is

$$\hat{\sigma} = \frac{1}{8\pi s} \int_{\ell_{\min}}^{\ell_{\max}} d\ell^2 \overline{|\mathcal{M}|^2}. \quad (\text{V.73})$$

In the next step, we determine  $\hat{\sigma}$  for the two respective production processes.

### V.7.2.1 Cross section for process A

For this process we have to substitute the masses with  $m_1 = m_3 = m_f$ ,  $m_2 = 0$  and in the  $m_a \rightarrow 0$  limit, the integration boundaries (Eq. (V.65)) become

$$0 < \ell^2 < s \left(1 - \frac{m_f^2}{s}\right)^2. \quad (\text{V.74})$$

However, the  $c_{a\gamma\gamma}^2$  term from the  $t$ -channel diagram diverges logarithmically for  $\ell^2 \rightarrow 0$ . For this reason, this expression has to be regularized by introducing a finite thermal photon mass  $m_\gamma = eT/3 > 0$ .<sup>43</sup> The Mandelstam variables are given by

$$\begin{aligned} t &= -\ell^2, \\ u &= \ell^2 + 2m_f^2 - s. \end{aligned} \quad (\text{V.75})$$

Inserting these into Eq. (V.52) and adapting the  $\ell$  boundaries from Eq. (V.74) with the lower cutoff  $m_\gamma$ , the reduced cross section is given by

$$\begin{aligned} \hat{\sigma}_A &= \frac{e^2}{16\pi} \frac{c_{a\gamma\gamma}^2}{f_a^2} s \left(1 - \frac{m_f^2}{s}\right)^2 \left(4 \log \left(\frac{(s - m_f^2)^2}{s m_\gamma^2}\right) - 3 - 2\frac{m_f^2}{s} + \frac{m_f^4}{s^2}\right) \\ &\quad - \frac{e^2}{2\pi} \left(2\frac{c_{aff}^2}{f_a^2} + \frac{c_{aff}c_{a\gamma\gamma}}{f_a^2}\right) m_f^2 \left(1 - \frac{m_f^2}{s}\right) \left(2 \log \left(\frac{s}{m_f^2}\right) - 3 + 4\frac{m_f^2}{s} - \frac{m_f^4}{s^2}\right), \end{aligned} \quad (\text{V.76})$$

where we keep only the logarithmic dependence on  $m_\gamma$  in the  $c_{a\gamma\gamma}$  term. Expanding it for small  $m_f$  up to second order yields the simpler expression:

$$\begin{aligned} \hat{\sigma}_A &= \frac{e^2}{16\pi} \frac{c_{a\gamma\gamma}^2}{f_a^2} s \left(4 \log \left(\frac{s}{m_\gamma^2}\right) - 3\right) \\ &\quad + \frac{e^2}{2\pi} m_f^2 \left(2\frac{c_{aff}^2}{f_a^2} + \frac{c_{aff}c_{a\gamma\gamma}}{f_a^2}\right) \left(2 \log \left(\frac{s}{m_f^2}\right) - 3\right) + \mathcal{O}(m_f^3). \end{aligned} \quad (\text{V.77})$$

### V.7.2.2 Cross section for process B

For the second process, the masses are  $m_1 = m_2 = m_f$ ,  $m_3 = 0$  and for  $m_a \rightarrow 0$ , Eq. (V.65) becomes

$$\frac{1}{2}s \left(1 - \frac{2m_f^2}{s} - \sqrt{1 - \frac{4m_f^2}{s}}\right) < \ell^2 < \frac{1}{2}s \left(1 - \frac{2m_f^2}{s} + \sqrt{1 - \frac{4m_f^2}{s}}\right) \quad (\text{V.78})$$

and no cutoff has to be specified, because the finite fermion mass already serves as an IR regulator in the  $t$ -channel. The corresponding Mandelstam variables for process B are the same ones as in Eq. (V.75). The phase space integration can be straightforwardly evaluated:

$$\begin{aligned} \hat{\sigma}_B &= \frac{e^2}{12\pi} \frac{c_{a\gamma\gamma}^2}{f_a^2} s \left(1 + 2\frac{m_f^2}{s}\right) \sqrt{1 - \frac{4m_f^2}{s}} \\ &\quad - \frac{2}{\pi} e^2 m_f^2 \left(2\frac{c_{aff}^2}{f_a^2} + \frac{c_{aff}c_{a\gamma\gamma}}{f_a^2}\right) \log \left(\frac{s - 2m_f^2 - s\sqrt{1 - 4m_f^2/s}}{2m_f^2}\right). \end{aligned} \quad (\text{V.79})$$

<sup>43</sup> The more formal treatment is to regularize this expression by an IR cutoff  $\ell_{\text{cut}}$  for the  $\ell$  integration and include the thermal two-point function of the photon. At the end, a logarithmic dependence on  $m_\gamma$  is left, while the  $\ell_{\text{cut}}$  terms cancel with each other (see Ref. [263] for more details).

At second order in  $m_f$ , it reduces to

$$\hat{\sigma}_B = \frac{e^2}{12\pi} \frac{c_{a\gamma\gamma}^2}{f_a^2} s + \frac{2}{\pi} e^2 m_f^2 \left( 2 \frac{c_{aff}^2}{f_a^2} + \frac{c_{aff} c_{a\gamma\gamma}}{f_a^2} \right) \log \left( \frac{s}{m_f^2} \right) + \mathcal{O}(m_f^3).$$

### V.7.3 Impact of $N_{\text{sub}}$ on the mass limits

Regarding the MW subhalo count, we have already pointed out associated uncertainties in Section V.3. We have presented our limits on  $m_a$  for different choices of the MW mass (see Tables V.1 and V.2) but kept the requirement that  $N_{\text{sub}} \leq 64$ . As explained in Section II.2.6.3, this value is derived assuming an isotropic distribution of MW satellites seen by SDSS which may be too simplistic. Therefore, we examine how the ALP mass limits change for different numbers of MW subhalos in Fig. V.10. To illustrate this effect, we choose the photophilic ALP case and compare the corresponding limits for  $N_{\text{sub}} = 50$  (red lines) and  $N_{\text{sub}} = 80$  (blue lines) against the limits derived in Section V.5 shown as black lines. The lower part shows the results for the weak MW mass choice, whereas the upper part are the limits for a strong MW mass choice. Especially for the latter case, the mass limits clearly depend on the choice of  $N_{\text{sub}}$ : for  $N_{\text{sub}} = 80$ , ALP masses up to  $\simeq 48$  keV would be excluded, while the same requirement yields only a limit of  $m_a \simeq 14$  for the weak MW mass choice. The exact results are quoted in Table V.3.

MW \ $N_{\text{sub}}$	50	64	80
weak	8.8 keV	10.3 keV	13.6 keV
strong	12.3 keV	17.4 keV	47.6 keV

Table V.3: Limits on the ALP mass  $m_a$  for different choices of the observed amount of subhalos  $N_{\text{sub}}$  compared to the case  $N_{\text{sub}} = 64$  as used in this section, assuming a photophilic scenario.



This highlights how discoveries of new ultra-faint subhalos by future surveys will be able to probe the parameter space of freeze-in ALP DM and WDM in general. However, a precise measurement of the MW mass is additionally needed, as the interpretation of the results depends not only on the amount of observed subhalos, but on the properties of the MW as well.

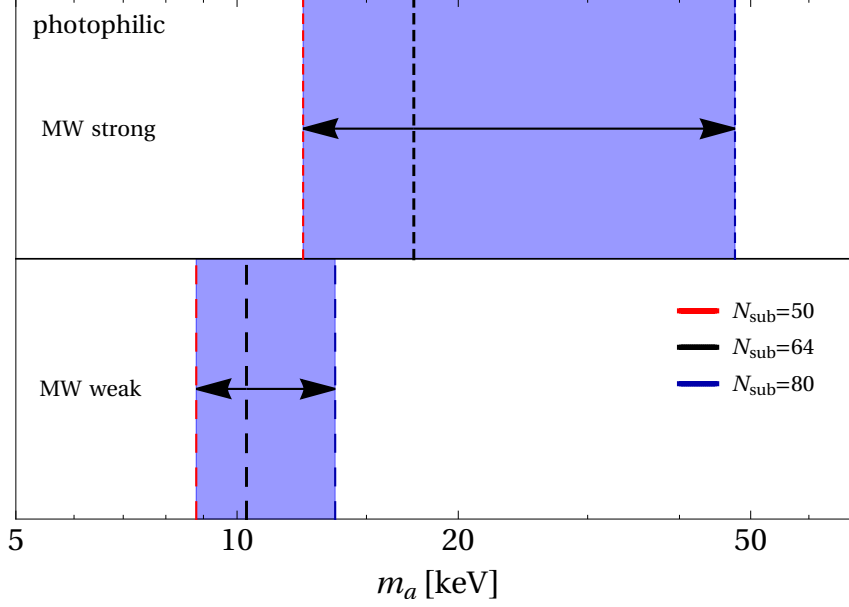


Figure V.10: Comparison of ALP DM mass limits for different choices of  $N_{\text{sub}}$  and MW masses in the photophilic scenario. The upper part is the strong MW mass and the lower the weak mass choice. The blue lines are  $m_a$  limits for  $N_{\text{sub}} = 80$  and the red lines are using  $N_{\text{sub}} = 50$  while the black lines are the results given in Tables V.1 and V.2.



# Two temperature dark matter: a general picture

## VI.1 Motivation

While the WIMP paradigm is strictly speaking not ruled out yet, it is under pressure from current direct detection results [62] and hence the last several years have seen a rise in interest of other avenues to explain the DM puzzle (see for instance Refs. [81, 148, 240, 287]). Specifically, the focus has shifted to DM candidates of lighter masses. While these particles allow for potential new experimental probes, they may have an impact on the cosmology of the early Universe as well. In fact, if DM is light enough such that it is still relativistic at sufficiently late times it has a non-vanishing free-streaming length and will thereby change the formation and the properties of galaxies compared to the standard  $\Lambda$ CDM paradigm [288] below this length scale.

Initially, the effect of such “hot” DM has been studied in the context of neutrino DM, which turned out to feature a too large free-streaming length, effectively erasing structures at far too large scales. Thus, attention has shifted to DM models which can be considered to be “warm” instead. Interestingly,  $N$ -body simulations of structure formation in the  $\Lambda$ CDM regime revealed small scale structures which are in tension with observations (for an overview, see Ref. [289]). These simulations predict too large numbers of accompanying galaxies of the Milky Way (MW) [156, 290], which is usually called the “missing satellite” problem. Further, the shape of galactic cores do not match with observations [291] (the *cusp versus core problem*) and lastly, the *too big too fail problem* [292, 293] addresses a mismatch in the dynamics of the brightest MW satellites. It is still under debate if these issues can be alleviated in the  $\Lambda$ CDM paradigm by including baryonic feedback in the simulations (see for instance [294–296]).

On the other hand, going beyond the  $\Lambda$ CDM paradigm, aforementioned tensions can be cured by invoking “warm” DM models which alter the small scale structures but agree with cold DM (CDM) at large scales. Of particular interest with respect to above mentioned questions, are DM mixtures of “cold” and “warm” DM species. Often, the “cold” component is considered to be of standard  $\Lambda$ CDM origin, while the “warm” component is made of something else: popular extensions involve sterile neutrinos [152, 154, 233], ultralight particles [150, 245], axions [251], fuzzy DM [297, 298] or non cold thermal relics [299, 300]. Some of the first models invoked neutrinos as a “hot” DM candidate mixed with a “cold” component (see for instance [301–305]).

In the following, we are mainly concerned with scenarios with only a single DM species, which, however, features a non-thermal momentum distribution, for example due to different production mechanisms contributing to its relic abundance.

Such scenarios of DM with a non-thermally produced warm admixture have been considered for instance in Refs. [1, 2, 234, 306–309] and we discussed examples in Chapters IV

and V, where we analyzed the scotogenic model (ScM) framework and axion-like particle (ALP) DM. Precisely, we will have a subset of DM characterized by a higher temperature such that it can be considered to be “warm” or even “hot”. The aim is to quantify our results in a way, that they can be matched for a wide variety of models which might feature other ways to produce DM at different times. A similar idea was done in Ref. [310], where the authors trained an emulator using the matter power spectrum of a mixed cold and warm DM model setup.

In particular, this chapter extends and refines the analysis of Chapter IV, where we used simplifying assumptions which are going to be relaxed in the following sections, especially with respect to the treatment of the effective number of entropic degrees of freedom (DOF),  $g_*^e(T)$ .

We introduce a model-independent parametrization of the DM momentum distribution function and use current observational limits on observables related to the matter power spectrum to set bounds on the allowed parameter space. In the following, we will refer to our framework as the *two temperature dark matter* (2TDM).

This chapter is organized as follows: in Section VI.2 we discuss how we parameterize the 2TDM and explain the assumptions we made when modeling the production mechanism. Section VI.3 consists of a discussion of constraints on the parameter space derived from cosmological observations. In Section VI.4 we discuss some modifications of the simplified description. Results are shown in Section VI.5 and an application of the matching to some sample models is given in Section VI.6. Lastly, we summarize our findings in Section VI.7.

## VI.2 Setup of the framework

We consider a framework where the observed DM density is explained via one particle species which is produced in two different production modes at separate times. Therefore, an intrinsic temperature can be assigned to both production possibilities. Consequently, the final DM abundance is made up by two shares of a single particle species each with its own temperature. For convenience we are going to refer to the earlier produced part as the *first subset*, while the other one is the *second subset*. A schematic representation of this is shown in Fig. VI.1. Crucially, the second DM subset whose production happens at a later time  $t_2$  features a significantly larger temperature than the first DM set which is produced earlier on at time  $t_1$ , that means we take that  $T_2 > T_1$ .<sup>44</sup> A scenario with these assumptions has important consequences for the behavior of DM. In fact, while the first subset might be cold, the second one will be warm or even hot DM. The question which arises is two-fold: how large can the temperature of the second subset be, and how much of it can be produced? To assess these questions, we will study the impact of the 2TDM on the structure formation at galactic scales. To be precise, as will be explained in Section VI.3.2, we are adopting observations of the Lyman- $\alpha$  forest and the observed number of MW subhalos to constrain the 2TDM.

A visualization of the parameters we are constraining is given in Fig. VI.2 (similar to the benchmark points presented Fig. IV.2 for the ScM), where we show an example of the DM momentum distribution functions weighted by the comoving momentum,  $x = p/T$ , squared,  $x^2 f(x)$ , which is a characteristic quantity for a given DM model. The spectrum features two distinctive peaks, which can be characterized by two quantities: first, the

---

<sup>44</sup> This does not have to be necessarily true for all cases. Depending on the properties of the parent species, one can have model setups, where the temperature of the latter produced DM subset is smaller compared to the temperature of the DM produced at earlier times. However, in that case one can change the naming  $1 \leftrightarrow 2$  for both DM subsets.

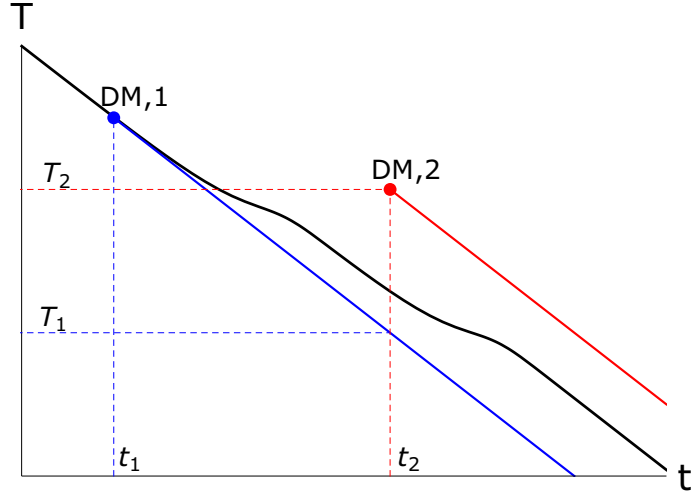


Figure VI.1: Schematic representation of our setup: given in black is the background temperature  $T_\gamma$  of the universe, while the blue and red curve represents the time evolution of the temperature of the first and second DM set, respectively. The first DM subset is produced at time  $t_1$  with a temperature similar to  $T_\gamma$ . After a while, the second DM subset is produced at  $t_2$  but it has a higher temperature  $T_2$  compared to  $T_1$ . The bumps in the solid black line mimics entropy dilution due to particle freeze-out in the SM thermal bath.

position of their peaks which is related to the respective DM temperature and second, their contribution to the total DM density  $\Omega_{\text{DM}} h^2$  which is set by the area under the respective curve. As can be seen, in this example the first share is the dominant contribution which contributes a part  $A_1$  to the total DM density (blue shaded region), while the hotter DM part contributes  $A_2$  (red shaded region).

### VI.2.1 Decay parametrization

The momentum distribution shown in Fig. VI.2 corresponds to DM freeze-in production via decays of thermalised (blue curve) and non-thermal particles (red curve). Following this, we are going to assume that DM in the 2TDM is produced via decays of heavy parent particles irrespective whether they were previously thermalized or not. Specifically, we are interested in the following two parameters:

$$\begin{aligned} \text{Temperature ratio: } \xi &\equiv \frac{T_2}{T_1} > 1, \\ \text{Abundance: } A_2 &\in (0, 1]. \end{aligned}$$

The abundance  $A_1$  of the first DM subset is fixed by the requirement  $A_1 = 1 - A_2$  such that the DM relic abundance is achieved.

It is important to note that we assume the temperature between both DM subsets to stay constant once produced during the subsequent time evolution of the universe. In principle, we could have entropy dilution in the dark sector similar to the SM thermal bath, but in the following we want to neglect such dilution effects for the dark sector.

### VI.2.2 Decay modeling

In the following, we model the production of the individual DM subsets by decays of particles  $P$ , which decay into a DM particle  $X$  via  $P \rightarrow X X$  and whose mass is  $m_P$ . More details on the DM production via decaying scalars can be found for instance in Refs. [109,

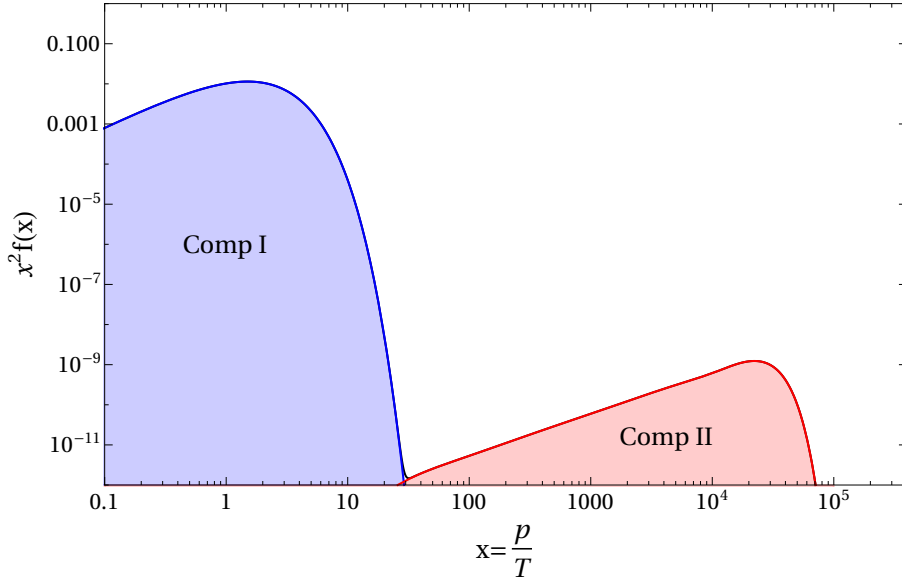


Figure VI.2: Example  $x^2 f(x)$  spectrum for a specific 2TDM scenario with two observable peaks calculated for times when DM production is finished. The blue area corresponds to a dominant subset whereas the red area refers to a subdominant DM share but with higher temperature with respect to the first set.

[111, 235, 241]. In the following we want to focus solely on analytical expressions derived in Ref. [235], similar to our procedure in Section IV.3.1, which corresponds to the following types of production:

- The parent particle decays while it is still in thermal equilibrium.
- For sufficiently small decay widths, the scalar particle freeze-out before it decays into DM.
- If the scalar is only weakly coupled to the SM, it never thermalizes before or during its decays, but freezes in instead.

Solving the Boltzmann equation for the DM momentum distribution yields [235]

$$f(x, r) = 2 \frac{C_\Gamma}{g_*^s(T_{\text{prod}})} \int_0^r ds \frac{s^2}{x^2} \int_{\tilde{x}_{\text{min}}}^\infty d\tilde{x} \frac{\tilde{x}}{\sqrt{\tilde{x}^2 + s^2}} f_P(\tilde{x}, s). \quad (\text{VI.1})$$

Here,  $C_\Gamma$  denotes an effective DM production rate via decays of  $P$ . Consequently, it is related to the decay width<sup>45</sup>  $\Gamma$  of  $P$  by  $C_\Gamma = M_0 \Gamma / m_P^2$ , where  $M_0 = 7.35 \times 10^{18}$  GeV. The factor of two in front of the expression has to be dropped if we look at processes  $P \rightarrow X S$  instead. Although it is implicitly assumed for this derivation that the number of entropic DOF,  $g_*^s(T)$ , are not changing at all, a dimensionless time variable  $r = m_P / T$  is introduced to track changes in  $g_*^s(T)$  during DM production; for a general discussion we refer to Section VI.4.2.

In the following, we present the result for parent particles decaying while maintaining thermal equilibrium, whereas the other two cases are given in Sections VI.8.1 and VI.8.2.

<sup>45</sup> We assume that there is only one decay channel for  $P$  and so  $\Gamma$  is a total decay width.

Assuming a Maxwell-Boltzmann (MB) distribution<sup>46</sup> for the parent particle,  $f_P(x, r) = \exp\left(-\sqrt{r^2 + x^2}\right)$ , we can derive the following expression for the DM momentum distribution [235]

$$f(x, r) = 8C_\Gamma e^{-x} \left( \frac{r}{2x} e^{-r^2/4x} + \frac{1}{2} \sqrt{\frac{\pi}{x}} \text{Erf} \left[ \frac{r}{\sqrt{4x}} \right] \right). \quad (\text{VI.2})$$

In the limit  $r \rightarrow \infty$ , Eq. (VI.2) reduces to

$$f(x, \infty) \equiv f(x) = 4C_\Gamma e^{-x} \sqrt{\frac{\pi}{x}}. \quad (\text{VI.3})$$

Inserting this expression into Eq. (II.31), we can derive the DM abundance

$$\Omega_{\text{DM}} h^2 = C_\Gamma K \frac{m_{\text{DM}}}{\text{GeV}} \frac{g}{g_*^s(T_{\text{prod}})}, \quad (\text{VI.4})$$

where  $K \simeq 3 \times 10^8$  and  $g$  denotes the internal DOF of the DM species. It may seem counterintuitive at first that the DM density is directly proportional to the decay width of  $P$ , but under this approximation the parents do not deviate from a MB distribution and hence DM can only be efficiently produced before the parent particles experience a Boltzmann suppression at temperatures  $T \approx m_P$ . The corresponding abundances for the other two production processes do not depend on the size of  $C_\Gamma$ .

Above formulas can be straightforwardly generalized to a DM scenario composed of  $i$  subsets, each with a temperature  $T_i$ . In that case we are defining a reference temperature  $T_1$  which we take to be given by the lowest temperature of the DM species and so the final momentum distribution for the DM,  $f_{\text{DM}}(x_i)$ , is given by the following sum:

$$f_{\text{DM}}(x_1) = \sum_i f_i(x_i) = 4 \sum_i C_{\Gamma,i} \sqrt{\frac{\pi}{x_i}} e^{-x_i} = 4 \frac{\pi}{\sqrt{x_1 T_1}} \sum_i C_{\Gamma,i} \sqrt{T_i} e^{-x_1 T_1 / T_i}. \quad (\text{VI.5})$$

Here each subspecies has its own decay width  $C_{\Gamma,i}$  and temperature  $x_i = p/T_i$ . For the 2TDM we find that

$$f_{\text{DM}}(x_1) = 4 \sqrt{\frac{\pi}{x_1}} \left( C_{\Gamma,1} e^{-x_1} + C_{\Gamma,2} \sqrt{\xi} e^{-x_1/\xi} \right), \quad (\text{VI.6})$$

$$\begin{aligned} \Omega_{\text{DM}} h^2 &= K \frac{m_{\text{DM}}}{\text{GeV}} g \left( \frac{C_{\Gamma,1}}{g_*^s(T_{\text{prod},1})} + \frac{C_{\Gamma,2}}{g_*^s(T_{\text{prod},2})} \xi^3 \right) \\ &\equiv \Omega_{\text{DM}} h^2 (A_1 + A_2). \end{aligned} \quad (\text{VI.7})$$

Thus, Eq. (VI.7) allows to relate  $A_1$  and  $A_2$  to the decay width  $C_{\Gamma,i}$  and demanding that the DM relic abundance is generated constrains  $C_{\Gamma,1}$ ,  $C_{\Gamma,2}$  and  $\xi$ . However, above expressions are only valid if the respective parent particles are in thermal equilibrium during their decay into DM.

In the following we will match our prescription onto DM produced by long-lived particles by defining a relation between the production rate  $C_\Gamma$  and the temperature ratio of the 2TDM. We start by comparing the averaged momentum  $\langle x_2 \rangle$  for the late-time produced particles against  $\langle x_1 \rangle$  stemming from DM production of thermalized parent particles. The respective averaged momenta are given by

$$\langle x_2 \rangle = \frac{\int_0^\infty dx_1 x_1^3 f(x_1/\xi)}{\int_0^\infty dx_1 x_1^2 f(x_1/\xi)} = 2.5 \xi = \xi \langle x_1 \rangle, \quad (\text{VI.8})$$

<sup>46</sup> This assumption is crucial to derive analytic results, while the inclusion of a Bose-Einstein or Fermi-Dirac distribution only marginally changes the result. Hence our discussion holds for all types of parent particles.

where the averaged value  $\langle x_2 \rangle$  is shifted by a factor  $\xi$  compared to  $\langle x_1 \rangle = 2.5$ . This is important for matching the temperature ratio  $\xi$  to a specific decay width of long-lived parent particles.

For this matching we assume the parent particles to be at rest when decaying and producing the DM. Further we assume an instantaneous decay at time  $\tau = t_{1/2} = \log 2/\Gamma$  set by the half-time of the parent particle, which can be converted into a temperature by the relation

$$\begin{aligned} \frac{T}{\text{MeV}} &= 1.55 g_*^s(T)^{-1/4} \left( \frac{\text{sec}}{\tau} \right)^{1/2} \\ &\simeq 8.5 \times 10^5 \frac{m_P}{\text{TeV}} g_*^s(T)^{-1/4} \sqrt{C_\Gamma}, \end{aligned} \quad (\text{VI.9})$$

where we used  $\Gamma = m_P^2 C_\Gamma/M_0$  in the last step. This temperature has to be compared to the energy of the DM which is roughly set by  $E \approx p = m_P/2$ .

Finally, we can equate  $p/T$  and Eq. (VI.8) to derive a relation between our model parameter  $\xi$  and the DM production rate  $C_\Gamma$ ,

$$\xi = \frac{m_P}{5T(C_\Gamma)} \implies \xi \simeq 0.24 C_\Gamma^{-1/2} g_*^s(T_{\text{prod}})^{1/4}. \quad (\text{VI.10})$$

The last expression is only valid, if  $g_*^s(T) \equiv g_*^s(T_{\text{prod}})$  is constant during DM production. As expected smaller decay widths give rise to a hotter second DM subset. The reason why we use the half-life  $t_{1/2}$  instead of  $1/\Gamma$ , stems from the matching between a production assuming a shifted MB distribution and an explicit long-lived particle production mechanism, which will be explained in Section VI.4.1. Therefore, such long-lived decays are well approximated by a suitable choice of  $\xi$  based on Eq. (VI.10) and we can use it as an input parameter for our simulations.

## VI.3 Constraints on the model parameter space

Depending on the temperature ratio  $\xi$ , the subdominant production mechanism may lead to a “warm” or even “hot” DM subset which could lead to a significant contribution to the effective number of relativistic species,  $N_{\text{eff}}$ , or alter small scale structures. Therefore the 2TDM can be constrained by cosmological and astrophysical observations and measurements. Stringent constraints arise from flux spectra analyses of the Lyman- $\alpha$  forest and the number of dwarf galaxies of the MW as well as the measured value for  $N_{\text{eff}}$ .

### VI.3.1 Limits from additional radiation

Similar to Section IV.3.2, there are parts of the parameter space, where the second DM subset effectively acts as radiation in the early universe and hence increases  $N_{\text{eff}}$  by an amount  $\Delta N_{\text{eff}}$ . For the SM,  $N_{\text{eff}} = 3.046$  [236] while measurements by the Planck collaboration yield  $N_{\text{eff}} = 2.99_{-0.33}^{+0.34}$  (95% CL) (TT, TE, EE+lowE+lensing+BAO) [52] from the cosmic microwave background (CMB) whereas at the onset of big bang nucleosynthesis (BBN),  $N_{\text{eff}} = 2.88 \pm 0.52$  (95% CL) [237]. Since BBN takes place at much earlier times the latter bound is more relevant for us, because the warm DM subset has more time to cool down until the CMB epoch.

We follow the procedure outlined in Section IV.3.2 and estimate  $\Delta N_{\text{eff}}$  by comparing the kinetic energy of the DM species with temperature  $T_2 = T_1 \xi$  to the energy density of a massless Dirac fermion with a temperature equal to the neutrino temperature  $T_\nu$ , given



by:  $\rho_{\text{ferm}} = 7\pi^2/120 T_\nu^4$ ,<sup>47</sup>

$$\Delta N_{\text{eff}} \equiv \frac{\rho(T_1) - n(T_1) m_{\text{DM}}}{2\rho_{\text{ferm}}} = \frac{60}{7\pi^4} \left(\frac{T_1}{T_\nu}\right)^4 \frac{m_{\text{DM}} g_*^s(T_1)}{T_1 g_*^s(m_P)} \times \int_0^\infty dz_1 z_1^2 \left( \sqrt{1 + \left(\frac{g_*^s(T_1)}{g_*^s(m_P)}\right)^{2/3} \left(\frac{z_1 T_1}{m_{\text{DM}}}\right)^2} - 1 \right) f(z_1/\xi), \quad (\text{VI.11})$$

$$\text{where } z_1 = x_1 \left( \frac{g_*^s(m_P)}{g_*^s(m_P/r)} \right)^{1/3},$$

is a redefinition of the comoving momentum  $x_1$  including  $g_*^s(T)$ , which was neglected in the corresponding discussion of Section IV.3.2. The dependence on the parameters  $A_2$  and  $\xi$  are encoded in  $f(z_1/\xi)$ . The prefactor  $(T_1/T_\nu)^4$  evaluates to  $(11/4)^{4/3}$  below temperatures of 1 MeV and can be dropped for temperatures above. In the temperature range we are interested in,  $T_1 \approx 1$  MeV, we can simplify Eq. (VI.11) by expanding the square root for small arguments. Using the expression for  $f(z_1/\xi)$  given in Eq. (VI.3) we find in this case

$$\Delta N_{\text{eff}} \simeq \frac{180}{7\pi^3} \left(\frac{g_*^s(T_1)}{g_*^s(m_P)}\right) C_{\Gamma,2} \frac{m_{\text{DM}}}{T_1} \left(\frac{5T_1}{2m_{\text{DM}}} \frac{g_*^s(T_1)}{g_*^s(m_P)}\right)^{1/3} \xi^4. \quad (\text{VI.12})$$

This expression has to be evaluated at temperatures  $T_1$  for given choices of  $\xi$  and  $A_2$  which are defined in  $C_{\Gamma,2}$ . Inserting Eq. (VI.7) we find an expression for  $\Delta N_{\text{eff}}$  only in terms of our model parameters:

$$\Delta N_{\text{eff}} \simeq 8.1 \times 10^{-4} \left(\frac{g_*^s(T_1)}{10.75}\right) \left(\frac{\Omega_{\text{DM}} h^2}{0.12}\right) \left(\frac{10 \text{ keV}}{m_{\text{DM}}}\right) \left(\frac{g_*^s(T_1)/10.75}{g_*^s(m_P)/106.75}\right)^{1/3} \left(\frac{2}{g}\right) A_2 \xi. \quad (\text{VI.13})$$

In Fig. VI.3,  $\Delta N_{\text{eff}}$  bounds from BBN and CMB are compared for two different DM masses: the solid and dashed line represents BBN limits, i.e. we can use Eq. (VI.13) evaluated at  $T_1 = 1$  MeV, for  $m_{\text{DM}} = 10$  keV and  $m_{\text{DM}} = 100$  keV respectively, while the dotted and dashed-dotted line correspond to CMB limits for the same masses. The last two are derived by evaluating Eq. (VI.11) at  $T_1 = 0.24$  eV. As already pointed out, the limits from BBN are in general stronger than the respective  $\Delta N_{\text{eff}}$  results from CMB, especially for smaller  $\xi$  values. The largest possible temperature  $T_2$  for a 10 keV DM particle is  $\sim 240 T_1$ , assuming  $g = 1$ , i.e. a scalar DM species. For fermions or vector particles this bound has to be rescaled accordingly. Moreover, we observe that the limits from CMB scales differently compared to BBN bounds at smaller temperatures. In that regime, expanding the square root in Eq. (VI.11) leads to additional powers of  $T_1$  and hence a larger temperature sensitivity.

### VI.3.2 Limits from structure formation

Generally, a detailed study for a given “warm” DM or mixed “warm”/“hot” and CDM model (in the following we will generally refer to these as WDM) would require hydrodynamical  $N$ -body simulations to infer their impact on the formation of cosmological structures. However, the influence of a specific model on small scales can usually be understood by comparing its corresponding matter power spectrum with the associated power spectrum of  $\Lambda$ CDM. Based on this comparison, conclusions can be drawn whether a given WDM model features a too large suppression of structure formation at small scales. We

<sup>47</sup> The additional factor of two in the denominator takes into account that  $f(x, r)$  includes both particles and anti-particles, whereas  $N_{\text{eff}}$  is defined with regards to families of relativistic particle species.

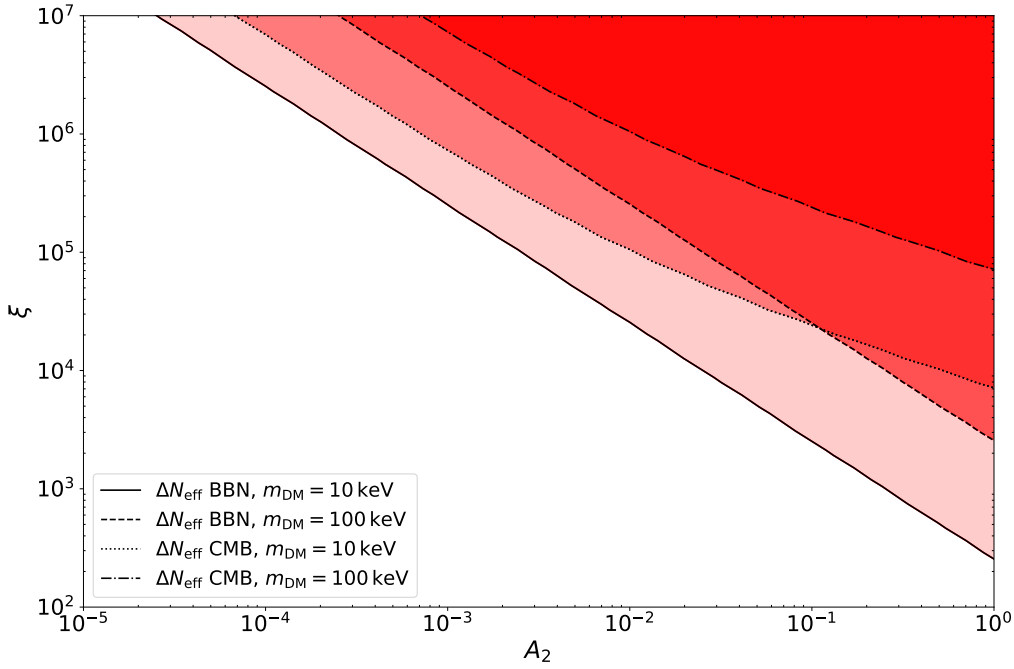


Figure VI.3:  $\Delta N_{\text{eff}}$  bounds derived from Eq. (VI.13) assuming  $m_P = 1 \text{ TeV}$ . The black solid line corresponds to  $m_{\text{DM}} = 10 \text{ keV}$  and the dashed line to  $m_{\text{DM}} = 100 \text{ keV}$  using the BBN bound  $\Delta N_{\text{eff}} < 0.344$ . The dotted and dashed-dotted line are the corresponding bounds for  $m_{\text{DM}} = 10 \text{ keV}$  and  $100 \text{ keV}$  from CMB measurements,  $\Delta N_{\text{eff}} < 0.28$ . For  $A_2 = 1$  temperature ratios  $\xi \gtrsim 240$  are excluded.

are using the public code CLASS [145, 146] to derive the matter power spectrum for the 2TDM model.

As explained in Section II.2.6, the suppression features of WDM models can be parameterized in terms of the transfer function  $T(k)$ ,

$$T(k)^2 = \frac{P_{\text{WDM}}}{P_{\Lambda\text{CDM}}}. \quad (\text{VI.14})$$

It can be used to employ a half-mode analysis (see Section II.2.6.1) to match limits from structure formation with specific WDM models.

On the contrary, this procedure is not suitable for the 2TDM model. Similar to mixed DM models we are dealing with a plateau in the transfer function [152, 311] and as such a simple half-mode analysis does not capture the whole picture of this model. Some examples are shown in Fig. VI.4 where transfer functions for three different parameter choices with  $m_{\text{DM}} = 30 \text{ keV}$  are compared to a thermal relic with mass  $m_{\text{TR}} = 2 \text{ keV}$ , which is shown in blue. The solid and dashed red curves correspond to  $A_2 = 0.2$  and  $\xi = 25$  or  $125$  respectively and the green curve has  $A_2 = 0.05$  and  $\xi = 25$ . While the transfer functions shown in red and green are generally smaller than the thermal reference below some wavenumber  $k$  due to the warmer DM subset, they still cross the blue line because the larger first DM subset features a milder suppression of galactic structures. Using a half-mode analysis would therefore exclude all three parameter choices and even a pretty small deviation for  $A_2 \ll 1$  would be disfavored by such analysis. However, the parameter choice shown in green is still allowed by limits on structure formation observables. Consequently, we are going to use the matter power spectrum directly to extract limits on the model parameter space. A similar conclusion for the ScM can be drawn from Fig. IV.4, where an adapted half-mode analysis gives rise to stronger constraints compared to a matter

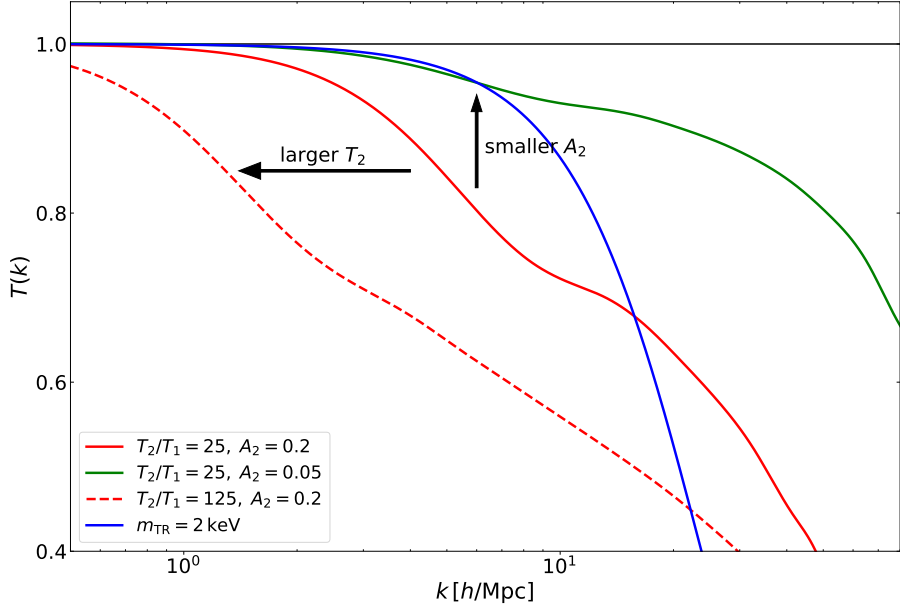


Figure VI.4: Transfer function  $T(k)$  for a 2TDM model where  $m_{\text{DM}} = 30 \text{ keV}$ ,  $A_2 = 0.2$  and  $\xi = 25, 125$  shown in red and dashed red respectively, while the blue line is derived from Eq. (II.45) for a thermal relic mass  $m_{\text{TR}} = 2 \text{ keV}$  indicating a potential limit from an analysis on structure formation. The green line correspond to  $\xi = 25$  and a smaller  $A_2 = 0.05$ . Applying a half-mode analysis, all three parameter choices would be excluded, but limits from observables on the matter power spectrum only exclude the two red lines, while the green line is not in conflict.

power spectrum analysis similar to the one discussed in the next subsection, but in that case these constraints were subdominant only. On the other hand, the half-mode analysis done in Section V.3 is reliable even though we considered two different DM production mechanisms. Note that for this case the corresponding averaged momenta are nearly identical and, further, for the photophilic ALP, one channel is clearly dominating.

### VI.3.2.1 Lyman- $\alpha$ forest data

The first tool we use to constrain the 2TDM framework is based on Section II.2.6.2. It uses a ratio  $\delta A$ , calculated from the momentum integrated  $P(k)$  of 2TDM parameter choices and compare it to  $\Lambda\text{CDM}$ , to approximate the amount of suppression by

$$\delta A \equiv \frac{A_{\Lambda\text{CDM}} - A}{A_{\Lambda\text{CDM}}}, \quad (\text{VI.15})$$

where  $A_{\Lambda\text{CDM}} = k_{\text{max}} - k_{\text{min}}$ . The results we are taken from an analysis examining the combination of the MIKE/HIRES and the XQ-100 datasets [56]. MIKE/HIRES observed quasars with redshifts  $z = 4.2\text{--}5.4$ , while XQ-100 measured between  $z = 3\text{--}4.2$ . Both sets combined span a range in  $k_\nu$ -space from  $0.003\text{--}0.08 \text{ s km}^{-1}$ . Hence, we will set  $k_{\text{min}} = 0.5 \text{ h/Mpc}$  and  $k_{\text{max}} = 10 \text{ h/Mpc}$  in the following.

To derive limits on the 2TDM, we have to define a reference WDM model with a corresponding  $\delta A_{\text{ref}}$  value first. The analysis in Ref. [56] yields a lower bound for thermal WDM given by  $m_{\text{WDM}} = 3.5 \text{ keV}$  (at 95% CL) considering a conservative thermal history of the universe. Under the assumption of a power-law evolution this bound strengthens to  $m_{\text{WDM}} = 5.3 \text{ keV}$ . Using these masses as input parameters for a thermal WDM model

we derive the following values:<sup>48</sup>

$$m_{\text{WDM}} = 3.5 \text{ keV} \quad \Rightarrow \quad \delta A_{\text{ref},1} = 0.30, \quad (\text{VI.16})$$

$$m_{\text{WDM}} = 5.3 \text{ keV} \quad \Rightarrow \quad \delta A_{\text{ref},2} = 0.20. \quad (\text{VI.17})$$

That means all parameter points in our scenario which have  $\delta A > \delta A_{\text{ref}}$  are excluded since their small scale suppression is too strong.

### VI.3.2.2 Number of Milky Way satellites

To predict the number of MW satellites or subhalos for the 2TDM we follow the procedure already explained in Sections II.2.6.3 and V.3. We calculate  $N_{\text{sub}}$  via the integral over the subhalo mass range (see Eqs. (II.58) and (II.59) for more details),

$$N_{\text{sub}} = \int_{M_{\text{min}}}^{M_{\text{MW}}} dM \frac{1}{34} \frac{1}{6\pi^2} \frac{M_0}{M} \frac{P(1/R)}{R^3 \sqrt{2\pi(S - S_0)}}, \quad (\text{VI.18})$$

which depends explicitly and implicitly via the variance  $S$  on the matter power spectrum  $P(k)$  of the underlying 2TDM. Here, the integration boundaries are given by,  $M_{\text{min}} = 10^8 M_{\odot}$  and the MW mass,  $M_{\text{MW}}$ .

Compared to Section V.3, we refine the limits on the MW mass. With the second data release of the GAIA mission, several works have calculated the MW mass using different analysis techniques (see Refs. [268, 269, 313–321] and [271]) and a compilation of these results is shown in Fig. VI.5. Combining every measurement and following Ref. [322] how to combine data points with asymmetric errors, we calculate for the MW mass,

$$M_{\text{MW}} = 1.18_{-0.15}^{0.16} \times 10^{12} M_{\odot} \text{ (95\% CL)}. \quad (\text{VI.19})$$

In the following we will set these limits as a lower (i.e. *light*) and upper (i.e. *heavy*) MW mass bound and reject parameter points if they have  $N_{\text{sub}} < 64$ .

As a side remark, we comment briefly on the MW mass dependence of this procedure. We matched it to the prediction of the *Aquarius* simulation [324], taking  $M_{\text{sub}} > 10^8 M_{\odot}$ , which is  $N_{\text{sub}} = 158$  by calculating  $P(k)$  for  $\Lambda$ CDM and a larger MW mass,  $M_{\text{MW}} \simeq 2 \times 10^{12} M_{\odot}$ . In contrast to the predicted number of this specific simulation, using the mass choices of Eq. (VI.19), we have found the number of subhalos to be only  $\simeq 100$  in the  $\Lambda$ CDM case.<sup>49</sup>

## VI.4 Detailed study of the parametrization

So far, we were assuming that the parent particles are thermalized when decaying, but in general this assumption does not hold for rather long-lived or weakly coupled particles. In the following, we show that a shifted MB distribution for  $f(x, r)$  can be used to describe the momentum distribution of DM produced from the decay of non-thermal parent particles, whose distribution function is set by a freeze-in or freeze-out mechanism. Further, we study the impact of a temperature dependent  $g_*^s(T)$  on the DM momentum distribution.

<sup>48</sup> As pointed out in Refs. [309, 312], these reference values are not clearly defined as they depend on the examined  $k$ -range and the wavenumber cutoff for the one-dimensional power spectrum. We use the cutoff  $k = 200 h/\text{Mpc}$  when evaluating Eq. (II.50) for our analysis.

<sup>49</sup> This observation was already pointed out in Ref. [325] as a possible explanation for the missing satellites problem.

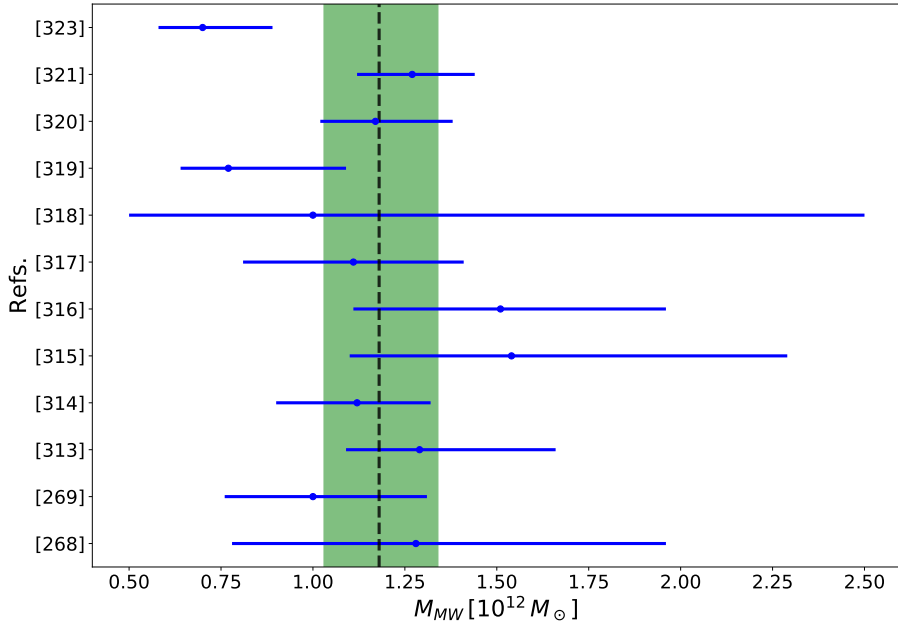


Figure VI.5: Compilation of different MW mass analyses using the second data release from the GAIA survey. Further information on the results can be found in Refs. [268, 269, 313–321, 323]. The black dotted line is the combination of all measurements and the green shaded region represents a  $2\sigma$  error range. On the contrary, blue errorbars correspond to 68% CL limits of the respective analyses.

#### VI.4.1 Non-thermalized parent particles

In Section VI.2.2 we suggested to use a shifted MB distribution to model late-time decays of parent particles. In the following, we are going to verify that this is a good approximation for the cases where  $f_P(x, r)$  is determined by a freeze-out, if the particle is sufficiently coupled or, if not, by a freeze-in.

To compare this approximation and the two late-time regimes we make use of Eq. (VI.10) to mock these decays, which are governed by  $C_\Gamma$ , with a shifted MB distribution and corresponding temperature ratio  $\xi$  (see Eq. (VI.5)). This will guarantee that DM is produced at approximately the same time. For the case of the frozen-in or frozen-out parent particle, we calculate  $f(x, r)$  numerically by inserting the corresponding  $f_P(x, r)$  into Eq. (VI.1). As an illustrative example we choose  $C_\Gamma \simeq 5.2 \times 10^{-4}$ , which corresponds to  $\xi \approx 40$  and set  $A_2 = 0.5$  for each production mechanism, to compare the results for the corresponding transfer functions for the case of a shifted MB distribution with the other two cases in Fig. VI.6. Shown in green is the result using a shifted MB distribution, while the transfer function for DM production by decays of parent particles after they are frozen-out or frozen-in are shown in blue and gray, respectively. We observe that the corresponding matter power spectra feature a similar scale where they deviate from  $\Lambda$ CDM. Only decays of frozen-in parent particles give rise to a slightly earlier drop in  $T(k)$ . Overall, the deviation between an appropriately shifted MB distribution and a freeze-in or freeze-out parent is only marginal; this allows us to model late-time decays using our simpler analytic expressions.

To highlight implications for structure formation even more, we calculate  $N_{\text{sub}}$  using the lighter MW mass and  $\delta A$  for fixed  $m_{\text{DM}} = 50 \text{ keV}$  and different choices of  $A_2$ . The respective results are shown in Table VI.1.

In summary, our findings indicate that we can model late-time decays to a good approximation by a temperature shifted momentum distribution assuming thermalized parents

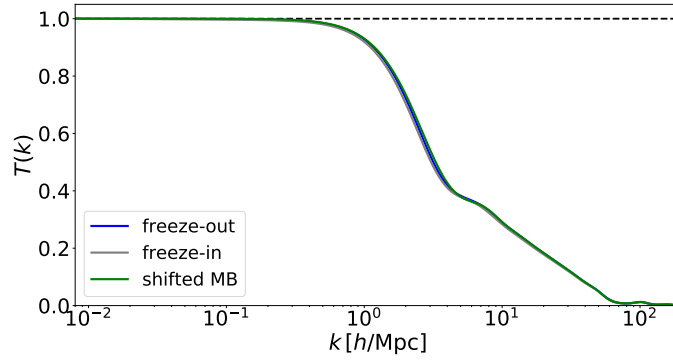


Figure VI.6: Comparison of the transfer function  $T(k)$  for a shifted MB distribution and a freeze-in/freeze-out scenario where the temperature ratio is set to  $\xi = 40$  and  $A_2 = 0.5$ , while  $m_{\text{DM}} = 10 \text{ keV}$ . We see that the analytical shifted MB distribution (red curve) is a good tool to approximate the numerical results for decays of frozen-out or frozen-in parents, shown in blue and gray, respectively. Hence we will use it in the following analysis to deduce constraints from structure formation. The horizontal black dashed line corresponds to a pure  $\Lambda$ CDM scenario.

	shifted MB		freeze-in		freeze-out	
$A_2$	$N_{\text{sub}}$	$\delta_A$	$N_{\text{sub}}$	$\delta_A$	$N_{\text{sub}}$	$\delta_A$
0.1	76	0.335	76	0.341	76	0.334
0.3	37	0.627	36	0.638	37	0.630
0.5	14	0.787	14	0.798	14	0.791

Table VI.1: Comparison of the corresponding structure formation observables using a shifted MB distribution for parent particles and the respective momentum distributions for non-thermal parent particles. The DM mass is set to  $50 \text{ keV}$  and only the abundance  $A_2$  is varied. The predictions for  $N_{\text{sub}}$  and  $\delta_A$  are nearly identical.

only.

As a final remark, we use above mentioned methods to place absolute lower mass bounds on the DM mass,  $m_{\text{DM}}^{\text{lim}}$ , by assuming  $\xi = 1$ . These values act as a guideline for the allowed parameter choices for the 2TDM and the respective limits from structure formation are summarized in Table VI.2.

	$N_{\text{sub}}$		Lyman- $\alpha$	
	light MW	heavy MW	$\delta A_{\text{ref},1}$	$\delta A_{\text{ref},2}$
$m_{\text{DM}}^{\text{lim}} [\text{keV}]$	12.8	9.0	12.7	7.7

Table VI.2: Lower DM mass limit  $m_{\text{DM}}^{\text{lim}}$  using constraints from structure formation assuming  $\xi = 1$ , i.e. all of DM has a common temperature  $T_2 = T_1$ .

#### VI.4.2 Impact of a variation in $g_*^s(T)$ during dark matter production

In the previous sections we have treated the number of entropic DOF  $g_*^s(T)$  as a fixed quantity. This assumption is only well justified for high decoupling temperatures,  $T_{\text{dec}} \gtrsim 160 \text{ GeV}$ , where  $g_*^s(T) = 106.75$  is constant (neglecting non-SM DOF). This simplification may be applicable for the first DM subset, but this simplifying assumption does not hold necessarily for the second warmer DM subset. Of course, the impact of a varying  $g_*^s(T)$

depends on the production time of the second DM subset, which is related to the mass of its respective parent particle.<sup>50</sup> We will use Eq. (II.30) to include the dynamics of  $g_*^s(T)$  in our analysis. Introducing a new variable  $z$  for the comoving momentum,

$$z = \left( \frac{g_*^s(m_P)}{g_*^s(m_P/r)} \right)^{1/3} x, \quad (\text{VI.20})$$

we rewrite Eq. (VI.1) to derive the more general DM momentum distribution function [111]

$$\begin{aligned} \frac{\partial f(z, r)}{\partial r} = & 2 \frac{C_\Gamma}{\sqrt{g_*^s(m_P/r)}} \left( 1 - \frac{r \partial_r g_*^s(m_P/r)}{3g_*^s(m_P/r)} \right) \frac{r^2}{z^2} \left( \frac{g_*^s(m_P)}{g_*^s(m_P/r)} \right)^{2/3} \\ & \times \int_{y_{\min}}^{\infty} dy \frac{r^2}{\sqrt{r^2 + y^2}} f_P(y, r), \end{aligned} \quad (\text{VI.21})$$

$$\text{where } y_{\min} = z \left( \frac{g_*^s(m_P/r)}{g_*^s(m_P)} \right)^{1/3} - \frac{r^2}{4z} \left( \frac{g_*^s(m_P)}{g_*^s(m_P/r)} \right)^{1/3}.$$

To outline the impact of a variation in  $g_*^s(T)$ , we insert the momentum distribution from Eq. (VI.3) into Eq. (VI.21) and vary  $m_P$ . Assuming  $\xi = 1$ , the results for  $z^2 f(z)$  are shown in Fig. VI.7. The mass scale  $m_P$  sets the time of the DM production, i.e. DM is produced earliest for  $m_P = 1 \text{ TeV}$ . For a better comparison we rescale the momentum distribution with a factor  $\sqrt{g_*^s(m_P)}$ , to compensate for the decrease in  $g_*^s(T)$  at late times. Besides from this overall change in magnitude, the shape of the distributions are going to change when DM is produced during periods of time where  $g_*^s(T)$  is rapidly changing: while the curves derived for  $m_P = 10^{-5} \text{ GeV}$ ,  $10 \text{ GeV}$  and  $1 \text{ TeV}$  are nearly identical, the other two curves, where  $m_P = 10^{-1} \text{ GeV}$  and  $1 \text{ GeV}$  clearly deviate, because the QCD phase transition leads to a rapid change in  $g_*^s(T)$  at  $T \approx 200 \text{ MeV}$ . In particular, the momentum distribution gets shifted to larger  $z$  values when DM is produced during this period of time, as can be seen from the blue curve, for which  $m_P = 1 \text{ GeV}$ .

To summarize, we have to be careful when defining a proper temperature ratio  $\xi$ , because

its definition is done by using  $\langle z \rangle = 2.5$  assuming constant  $g_*^s(T)$ .<sup>51</sup> That means we have to include a shift in the averaged momentum due to a change in  $g_*^s(T)$  when comparing against our results shown in the next section. For this purpose we compared the result for  $\langle z \rangle$  of Eq. (VI.21) to the reference case Eq. (VI.1) in Fig. VI.15 for  $m_P$  between  $1 \text{ MeV}$  and roughly  $1 \text{ TeV}$  and  $\xi$  up to  $\simeq 6000$ ; a maximum deviation of  $\approx 2.5$  can be observed at large  $\xi$  values and for  $m_P \simeq 1 \text{ MeV}$ . For a given parent particle mass, we extract a function  $h(\xi)$  from this contour plot and rescale the temperature ratio accordingly,  $\xi' = \xi/h(\xi)$ .

A change in the degrees of freedom also leads to a heating of the photon plasma compared to the decoupled DM temperature. This does not effect the ratio  $T_2/T_1$  but for the derivation of the matter power spectrum the DM temperature has to be defined with respect to the photon temperature  $T_\gamma$ . Compared to this reference temperature, the DM temperatures evolve as:

$$\frac{T_1}{T_\gamma} = \left( \frac{g_*^s(T_\gamma)}{g_*^s(T_{\text{prod},1})} \right)^{1/3}, \quad \frac{T_2}{T_\gamma} = \xi \left( \frac{g_*^s(T_\gamma)}{g_*^s(T_{\text{prod},2})} \right)^{1/3}. \quad (\text{VI.22})$$

Late times of production will come with a decrease in the number of entropic DOF,  $g_*^s(T_{\text{prod},2}) < g_*^s(T_{\text{prod},1})$  and compared to the photon temperature,  $T_2$  is increased and  $\xi$  is

<sup>50</sup> As discussed in Chapter IV, freeze-in is most dominant at temperatures  $r \approx 3$ , i.e.  $T \approx m_P/3$ .

<sup>51</sup> In the case  $g_*^s(T) = \text{const}$ , the dimensionless momentum variables are identical,  $z \equiv x$ .

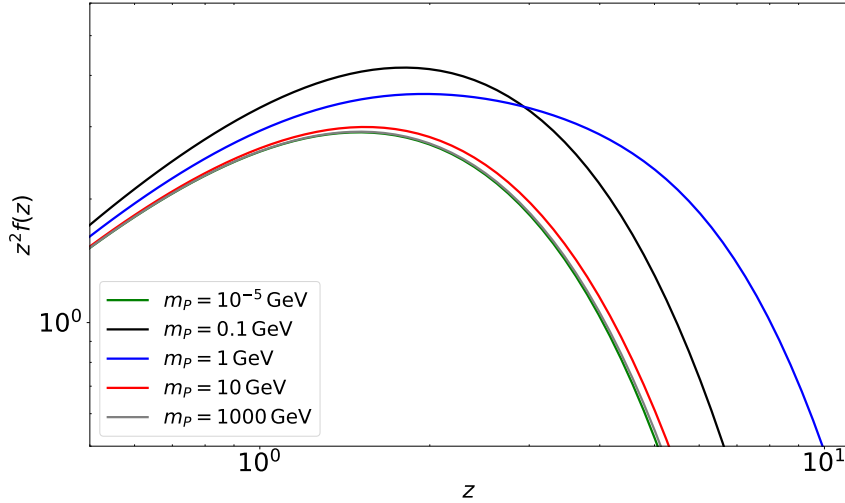


Figure VI.7: Numerical results for  $z^2 f(z)$  as defined in Eq. (VI.21) for different masses of the parent particle, ranging from  $m_P = 10^{-5}$  GeV to  $m_P = 1$  TeV and using Eq. (VI.3) for  $f(z)$  as an illustration. Masses of 0.1 and 1 GeV lead to the biggest impact on the shape of the spectrum, while the distributions of the other masses have similar shapes. All distributions are rescaled with a factor  $\sqrt{g_*^s(m_P)}$  for an easier comparison.

larger by a factor  $(g_*^s(T_{\text{prod},1})/g_*^s(T_{\text{prod},2}))^{1/3}$ . Again, as for a shift in  $\langle z \rangle$  this can be taken into account by defining a  $\xi' = \xi (g_*^s(T_{\text{prod},1})/g_*^s(T_{\text{prod},2}))^{-1/3}$  to include the reheating effect of the thermal plasma.

We will explain these rescaling procedures of  $\xi$  in more details in Section VI.6 where we apply it to specific models and extract limits on the allowed temperature ratio.

### VI.4.3 Three-body decays

Compared to two-body decays, decays involving three or more particles are more likely to feature small decay widths, because they can be suppressed by powers of small couplings, heavy off-shell intermediate particles or large mass ratios. In case of three-body decays we can have production of a DM particle  $X$  via the processes  $P \rightarrow S S X$ ,  $P \rightarrow S X X$  or  $P \rightarrow X X X$ . Similarly to the previously discussed two-body decays we can derive an analytic expression for the DM momentum distribution, assuming a thermalized parent particle [312],

$$f(x) \propto x^{-1.2} \exp(-1.11x). \quad (\text{VI.23})$$

The prefactor of this function is fixed by demanding  $A_2 = \int dx_1 (x_1)^2 f(x_2)$ . In contrast to two-body decays, the energy of the parent particle is distributed among three particles. This has two consequences for the interpretation of our results in the next section. First, the averaged momentum should be smaller by a factor of 2/3, in fact, we found that  $\langle x \rangle = 1.62$  using Eq. (VI.23). Further, the same factor has to be used when mapping the assumed decay width to the temperature ratio, in that case that relation is given by  $\xi \simeq 0.16/\sqrt{C_\Gamma g_*^s(T_{\text{prod}})}^{1/4}$  for the case of constant  $g_*^s(T)$  during DM production. We have checked that both, using the momentum distribution given in Eq. (VI.3) with a specific choice for  $\xi$  and Eq. (VI.23) with an appropriately rescaled ratio, give rise to nearly identical matter power spectra.

Although we do not present analytical results for three-body decays of frozen-out or frozen-in parent particles as for the two-body decays, we are confident that one can make use of



our procedure to extract limits for the case when the second subset is produced via late three-body decays with appropriately chosen values for the temperature ratio  $\xi$ . Since the deviations in the matter power spectrum are not very drastic, we expect that the results from Fig. VI.15 holds for three-body decays to a good degree and this allows to derive limits on production via three-body decays by applying our findings.

## VI.5 Analytical fitting of the exclusion limits

In the following we are using the tools discussed in Section VI.3 to answer the question how large and how hot the second DM subset can be. We are going to present our results in terms of the  $A_2$ - $\xi$  parameter space of the 2TDM. Results are derived for different choices of  $m_{\text{DM}}$  as higher DM masses give rise to weaker constraints.

As an example we show the constraints on the parameter plane in Fig. VI.8 where we set  $m_{\text{DM}} = 20 \text{ keV}$  and keep  $g_*^s(T) = 106.75$  fixed until all of the DM production has been completed. As can be seen, the limits from structure formation place strong constraints on the temperature ratio  $\xi$  in the range  $10^{-2} < A_2 < 1.0$  while the  $\Delta N_{\text{eff}}$  bound from the BBN epoch starts to become relevant at rather large temperature ratios,  $\xi > 10^4$ . Above this value, the bounds from structure formation become less reliable, because the hot DM subset starts to act like dark radiation instead of matter, an effect not captured in the calculation of  $P(k)$ . We already observed in Chapter IV that the  $\Delta N_{\text{eff}}$  bound exceeds structure formation limits for DM subsets with very high temperatures.

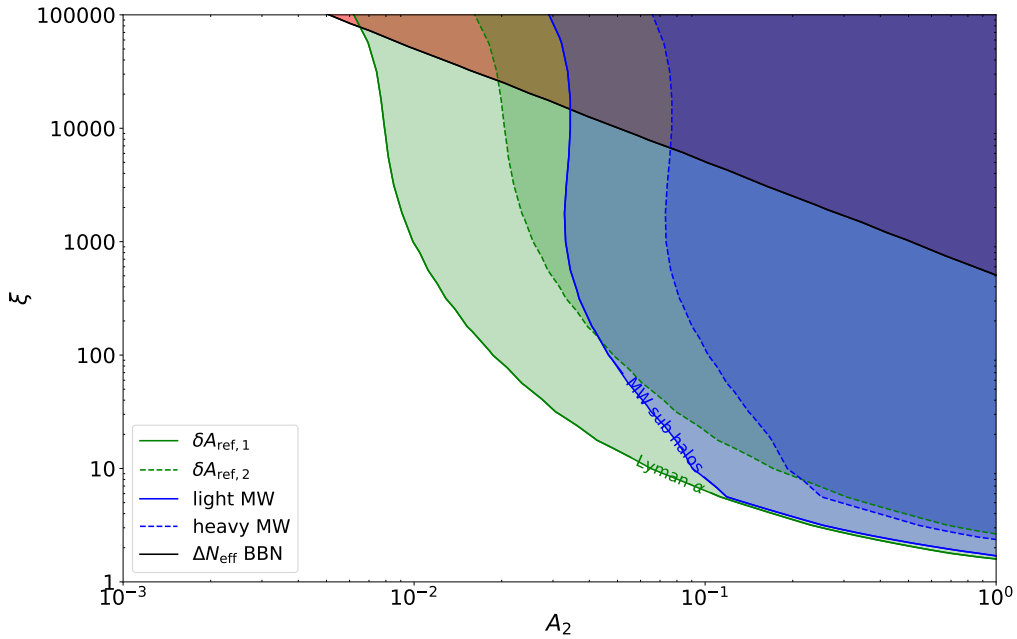


Figure VI.8: Limits from structure formation and the number of effective entropic DOF for  $m_{\text{DM}} = 20 \text{ keV}$  and fixed  $g_*^s(T) = 106.75$ . The blue shaded region is disfavored by the MW subhalo count and the green shaded region by limits from Lyman- $\alpha$  surveys, respectively. The solid lines are the corresponding stronger limits, whereas the weaker constraints are shown as dashed lines. The red shaded region in the upper right corner is disfavored by a too large  $\Delta N_{\text{eff}}$  value.

In the following, our aim is to provide our results in a model-independent way such that they can be applied to a variety of scenarios. For this reason we fit the respective exclusion limits with an exponential of the form  $\xi(A_2) = \exp(p_0 \cdot A_2^{-p_1} + p_2)$ , which we found to

be generally suitable. Furthermore, one parameter can be removed, because we know that the curve endpoint,  $\xi(A_2 = 1)$ , scales linearly with the DM mass starting from  $m_{\text{DM}}^{\text{lim}}$  as given in Table VI.2. By eliminating  $p_2$ , the exponential can be reduced to the expression

$$\xi(A_2) = \frac{m_{\text{DM}}}{m_{\text{DM}}^{\text{lim}}} \exp \left[ p_0 \left( A_2^{-p_1} - 1 \right) \right]. \quad (\text{VI.24})$$

This enables us to use either the abundance  $A_2$  or the temperature  $\xi$  as an input parameter and derive constraints on the other variable. The resulting fitting parameter for all four exclusion contours for  $m_{\text{DM}} = 20 \text{ keV}$  are shown in Table VI.3.

	Lyman- $\alpha$		$N_{\text{sub}}$	
	$\delta A_{\text{ref},1}$	$\delta A_{\text{ref},2}$	light MW	heavy MW
$p_0$	0.464	0.546	0.141	0.196
$p_1$	0.581	0.672	1.11	1.29

Table VI.3: Fit results for the respective exclusion limits based on Eq. (VI.24) using  $m_{\text{DM}} = 20 \text{ keV}$ .

Since only the limit endpoint scales linearly with DM mass, while the exclusion curve for  $A_2 < 1$  changes non-trivially with it, we extend this fitting procedure for other DM masses and simulate the exclusion limits for  $m_{\text{DM}}$  between 20 keV and 1000 keV. Then, the respective parameters  $p_i$  are extracted and fitted using the following polynomial:

$$p_i \left( \frac{m_{\text{DM}}}{\text{keV}} \right) = a_i + b_i \left( \frac{m_{\text{DM}}}{\text{keV}} \right)^{-1} + c_i \left( \frac{m_{\text{DM}}}{\text{keV}} \right) + d_i \left( \frac{m_{\text{DM}}}{\text{keV}} \right)^2, \quad (\text{VI.25})$$

to derive a final fit function which takes  $A_2$  and  $m_{\text{DM}}$  as input parameters to give the allowed temperature ratio  $\xi \equiv \xi(m_{\text{DM}}, A_2)$ . The results for all eight fit parameters can be found in Section VI.8.4 in the appendix. We explicitly compare this analytical fit against numerical simulations in the context of toy model examples in Section VI.6.1.

However, the assumption of constant  $g_*^s(T)$  obviously does not hold in general and we might have to drop at least some or all of above mentioned simplifying assumptions. We will explain in the following how to adapt our results beyond the simple picture.

The starting point is to collect the  $A_2$ - $\xi$  relation given in Eq. (VI.24), the expression for  $p_i(m_{\text{DM}})$  (see Eq. (VI.25)) and the corresponding fit parameters given in Table VI.5. As mentioned, this gives a first approximation of the exclusion limits, under the assumption  $g_*^s(T) = 106.75 = \text{const}$  during DM production. If this does not apply for the second subset, because its production happens at times  $T_{\text{prod},2}$  where  $g_*^s(T)$  is changing, it will lead in general to a warmer DM subset as compared to the case where  $g_*^s(T)$  is constant. Two corrections have to be done: first, the exclusion limit on  $\xi$  has to be divided by  $(g_*^s(T_{\text{prod},1})/g_*^s(T_{\text{prod},2}))^{1/3}$ . Second, we have to take the change in  $\langle x \rangle$  into account by extracting a correction function  $h(\xi)$  for the corresponding  $m_P$  from Fig. VI.15. This gives a rescaled version of the temperature ratio,  $\xi'$ ,

$$\xi' = \frac{\xi(m_{\text{DM}}, A_2)}{h(\xi(m_{\text{DM}}, A_2))} \left( \frac{g_*^s(T_{\text{prod},2})}{106.75} \right)^{1/3}. \quad (\text{VI.26})$$

Additionally, if the first subset features  $\langle x \rangle$  different from 2.5 or has  $g_*^s(T_{\text{prod},1}) < 106.75$ , which gives rise to a higher DM temperature  $T_1$  relative to the photon bath, one further step has to be done before the corresponding limits on  $\xi$ - $A_2$  can be extracted. This change of  $A_1$  can be quantified by multiplying  $\langle x \rangle$  with a factor  $\alpha$ , which is either given by the ratio

between the averaged momentum and our reference case,  $\alpha = \langle x \rangle / 2.5$ , or by the entropy dilution factor,  $\alpha = (106.75 / g_*^s(T_{\text{prod},1}))^{1/3}$ . Regarding its matter power spectrum, a DM with temperature  $\alpha T_1$  and mass  $m_{\text{DM}}$  has the same properties as a DM with temperature  $T_1$  and mass  $m_{\text{DM}}/\alpha$ . However, changing the mass by  $1/\alpha$  in Eq. (VI.25), we have to rescale the outcome for  $\xi'$  by multiplying it with  $\alpha$ , because the second DM subset is not affected. Taking all these corrections into account, the temperature limit is set by

$$\xi' = \alpha \frac{\xi(m_{\text{DM}}/\alpha, A_2)}{h(\xi(m_{\text{DM}}, A_2))} \left( \frac{g_*^s(T_{\text{prod},2})}{106.75} \right)^{1/3}. \quad (\text{VI.27})$$

In the next section we will explain in more detail how to incorporate these effects using several toy models as examples. A special emphasis will be put on the proper extraction of the limits on  $\xi$  when  $g_*^s(T)$  is not fixed.

## VI.6 Application to sample models

To explain the matching between our parametrization and “real” DM models we consider several example models where the DM is produced in different ways. Furthermore, we compare the limits obtained using our fit functions with those obtained from explicit simulations, where the matter power spectrum for particular choices of the momentum distribution function is calculated. Finally, we match our findings to the exemplar DM models, which we discussed in Chapters IV and V.

### VI.6.1 Model I: thermalized + out of equilibrium parents, constant $g_*^s(T)$

We start by discussing two thermalized parent particles,  $S$  and  $P$ , with masses  $m_S = m_P = 50 \text{ TeV}$  which are producing a DM species with mass  $m_{\text{DM}} = 50 \text{ keV}$  with their respective decays. Due to their large mass the number of entropic DOF can be treated as constant until all of them decayed into DM. Only afterwards, the dilution of  $g_*^s(T)$  has to be taken into account. We assume that  $S$  decays rapidly, while remaining in equilibrium with the thermal plasma. This is going to produce an amount  $A_1 < 1$  of DM particles with averaged momenta given by  $\langle x \rangle = 2.5$ . Additionally,  $P$  is going to decay at late times, after it is already frozen-out and produces an amount  $A_2$  of DM, such that  $A_1 + A_2 = 1$ . Now, because these decays are taking place at later times compared to production via  $S$  decays, we end up with DM which is highly energetic compared to the thermal plasma. The difference in the respective DM temperatures gives the ratio  $\xi$ .

The interesting question now is how hot the DM share  $A_2$  can be, without being in conflict with observations of structure formation. Following the procedure outlined in the previous section, we can neglect modifications stemming from a change in  $g_*^s(T)$  during DM production and extract the limits on  $\xi$  directly from Eq. (VI.24).

In Fig. VI.9 we compare our fitted exclusion limits for a DM mass of 50 keV against a numerical simulation. The left figure shows results from Lyman- $\alpha$  data (green shaded regions) and the right one from a MW subhalo count (blue shaded regions). In both figures, simulated results are shown as black lines and the stronger/weaker bounds are given by solid or dashed lines, respectively. As one can see, our fit gives a good approximation of the simulated results.

### VI.6.2 Model II: thermalized + out of equilibrium parents

In the previous example we illustrated how to interpret and extract the corresponding limits on  $A_2$  and  $\xi$  using our fit procedure under the assumption of constant  $g_*^s(T)$  during the production of DM. Based on this, we consider now a similar setup as before: again, we

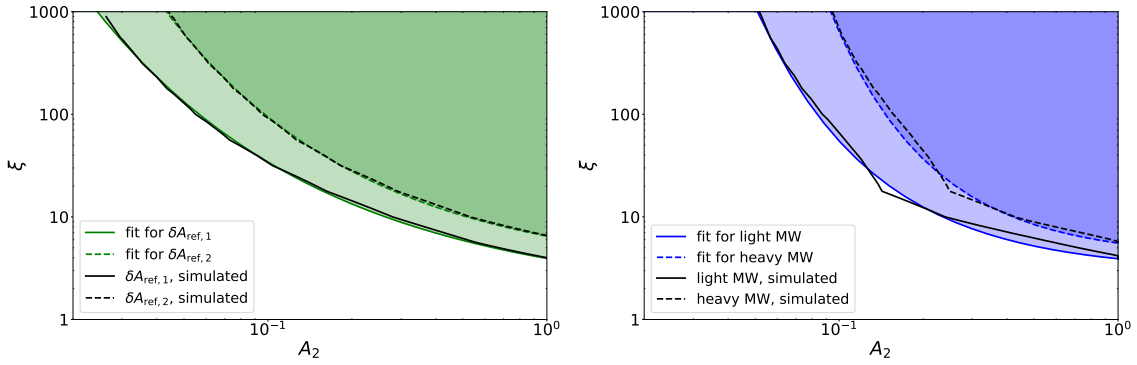


Figure VI.9: Structure formation limits given by shaded regions and derived from our analytic fit, Eqs. (VI.24) and (VI.25), using  $\delta A$  in the left and  $N_{\text{sub}}$  in the right figure. The DM mass is given by  $m_{\text{DM}} = 50 \text{ keV}$  and we assume  $g_*^s(T) = \text{const}$  during DM production. Shown as black lines are corresponding limits from a numerical simulation and solid/dashed lines correspond to stronger or weaker bounds, respectively.

have two thermalized parent particles,  $S$  and  $P$  whose decays will produce a DM species with mass  $m_{\text{DM}} = 35 \text{ keV}$ . However, now the parent masses are given by  $m_S = 1 \text{ TeV}$  and  $m_P = 10 \text{ GeV}$ . As before,  $S$  is producing a DM amount  $A_1$  while it remains in equilibrium with the thermal plasma, whereas an additional DM subset,  $A_2$ , is produced by late-time decays of  $P$  after it is frozen-out.

Since DM production now happens at times where  $g_*^s(T)$  is changing, we have to compensate for this effect by using Eq. (VI.26). Here we assume that the first subset is produced at early times where all SM particles are still part of the thermal bath, while the function  $h(\xi)$  can be read off Fig. VI.15 for the particle masses involved. Now we can take  $\xi'$  as the constraint on the temperature ratio for this toy model. Limits derived using  $\delta A_{\text{ref},1}$  and light MW masses are shown in the left and right figure of Fig. VI.10 as green and blue solid lines respectively, while the respective weaker bounds are shown as dashed lines. The black line and the red shaded region above it gives  $\Delta N_{\text{eff}} > 0.344$  during the BBN epoch; we note that this limit exceeds bounds from the MW subhalo count even for  $\xi < 1000$ , in particular the heavy MW mass choice. Compared to Fig. VI.9 we observe that the exclusion bands feature a kink around  $A_2 = 0.2$  and therefore smaller  $\xi'$  values are excluded in this region. The reason is that at this point,  $P$  particles decay around a temperature of  $T \simeq 1 \text{ GeV}$  where  $g_*^s(T)$  is rapidly changing and hence it gives rise to a larger averaged momentum  $\langle z \rangle$ , as illustrated in Fig. VI.7.

To demonstrate the usefulness of our approach, we simulate the combined matter power spectrum for this toy model with two different DM production channels for the benchmark points  $\xi = 10$  and  $40$ . We explicitly insert the out of equilibrium momentum distribution for  $S$  (see Eq. (VI.34)) taking changes in  $g_*^s(T)$  into account as well. The limits on  $A_2$  for these choices are indicated by a star and a diamond in both plots: here, the slightly grayed out symbols indicate the weaker limits. These benchmark points have to be matched onto  $\xi'$  as well, by multiplying them with a factor  $(106.75/g_*^s(T_{\text{prod},2}))^{1/3}$ , which evaluates roughly to  $0.5$  for  $\xi = 40$  and  $0.8$  for  $\xi = 10$ .

Further, it is noticeable that the benchmark points, indicated by dark blue stars or diamonds, seem to yield weaker constraints compared to our fit. For the scenario in mind, this can be explained by a DM fraction which is already produced while the parent particle is still in thermal equilibrium, giving rise to a peak at smaller momenta similar to the case of thermalized parent particle decays. Whereas in our parametrization we assume the second subset to be fully produced via late time decays. Consequently, at large  $\xi$  this fraction is only marginal, but becomes more dominant for smaller  $\xi$ . We calculated

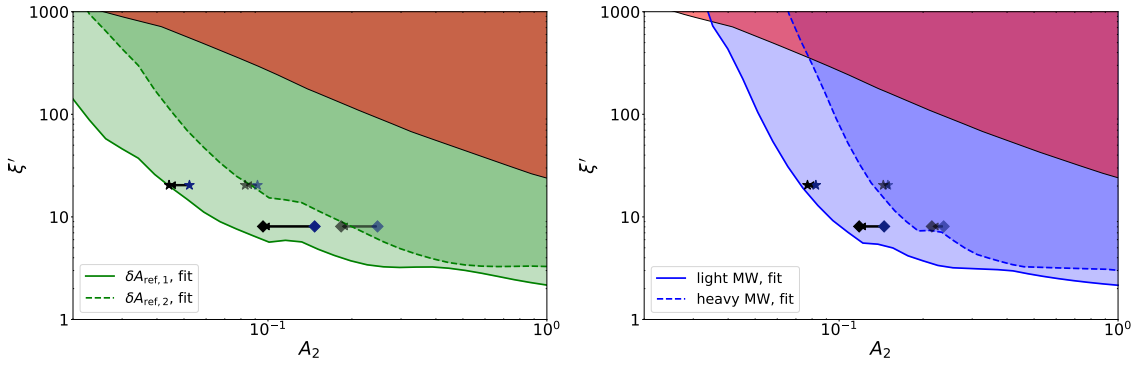


Figure VI.10: Structure formation limits using the  $\delta A_{\text{ref}}$  criterion in the left and a MW subhalo count in the right figure for the second toy model. Everything indicated by the green or blue shaded region is constrained by structure formation and solid lines correspond to strong and dashed lines to weak limits. For comparison, full numerical simulations to extract limits are run for  $\xi = 10$  and  $40$  and are indicated by the stars and diamonds in both plots. The difference between the dark blue and black symbols indicated by an arrow are due to specifics of this model choice and are further explained in the text. The red shaded region yields a too large  $\Delta N_{\text{eff}}$  stemming from the second subset.

this fraction explicitly and numerically extracted the updated bound on  $A_2$  shown as the black diamonds and stars in the plot. The difference between both is indicated by a black arrow and it is obvious, that the latter, more careful treatment fits better with our analytical result.

Furthermore, we show how the constraints on  $A_2$ – $\xi$  can be matched onto specific parameters for a concrete freeze-out model. The abundance  $A_2$ , produced by late-time decays, is fixed by the abundance of  $P$  which in turn is set by the time of its freeze-out,  $r_{\text{FO}}$ . Integrating Eq. (VI.34) over  $x$ , the yield  $Y_{\text{DM}} = n_{\text{DM}}/s$  is given by

$$A_2 = \frac{\Omega_{\text{DM}} h^2}{0.12} \simeq \left( \frac{m_{\text{DM}}}{10 \text{ keV}} \right) \left( \frac{106.75}{g_*^s(T_{\text{prod},2})} \right) \left( \frac{r_{\text{FO}}^2 K_2(r_{\text{FO}})}{49.5} \right) \left( \frac{m_{\text{DM}}}{20 \text{ keV}} \right). \quad (\text{VI.28})$$

The relation between the decay width of  $P$  and  $\xi$  is already discussed in Eq. (VI.10). Now we have all the ingredients to match between this specific model and our  $A_2$ – $\xi$  parametrization.

This toy model is similar to the ScM setup we discussed in Chapter IV, although we used a more conservative DM mass limit in Section IV.3.1 to extract limits from an adapted half-mode analysis. As we have shown, stronger bounds from Lyman- $\alpha$  and MW subhalo counts require  $m_{\text{DM}} \gtrsim 13 \text{ keV}$ , which would already exclude the scenario we considered in Chapter IV. Choosing as an example a fourth times larger mass for the lightest right-handed neutrino  $N_1$ ,  $m_{N_1} = 24 \text{ keV}$ , we use our result derived in this chapter to reevaluate the corresponding limits on the  $m_{\pm} - m_{N_{2,3}}$  parameter space. For this, we consider the parent particle  $N_2$  to have a mass  $m_{N_2} \simeq 300 \text{ GeV}$  and extract the corresponding  $h(\xi)$  function. Further, we take the three-body kinematics of  $N_2$  decays into account. We show the corresponding limits in the left plot of Fig. VI.11. As before, the green shaded region is excluded by  $\delta A_{\text{ref},1}$  and the blue shaded one by a subhalo count using the light MW mass.

These results have to be matched onto the ScM; this is shown in the right figure of Fig. VI.11, where we fix the mass of the charged  $\mathbf{Z}_2$  scalar to be  $m_{\pm} = 1200 \text{ GeV}$  and vary the mass of  $N_2$ . We can neglect the complication of the matching of  $A_2$  which we discussed above, because we are interested in the large  $\xi$  region where the second DM subset

is produced at sufficiently late-times. Compared to the 2TDM framework, there is less freedom to choose parameters; consequently, the black line indicates the temperature ratio  $\xi$  for the second DM subset, while the purple line shows the amount  $A_2$  of this subset. The green and blue lines are the corresponding lower limits on  $m_{N_2}$  using Eq. (VI.26). Using  $\delta A_{\text{ref},1}$  limits  $m_{N_2} \gtrsim 316$  GeV, thus excluding  $A_2 \gtrsim 0.5\%$  and  $\xi' \gtrsim 18000$ , while the subhalo count analysis yields a weaker limit,  $m_{N_2} \gtrsim 190$  GeV. Both limits clearly exceed the results shown in Fig. IV.4 assuming a conservative  $m_{\text{TR}} = 2$  keV limit. The bound on  $\Delta N_{\text{eff}}$  gives an even stronger constraint,  $m_{N_2} \gtrsim 435$  GeV, hence excluding  $\xi' \gtrsim 11000$  and  $A_2 \gtrsim 0.2\%$ , which is in accordance with the results we found in Section IV.3.2. In conclusion, we can quickly and reliably answer the question of *how much* DM, originating from a subdominant production mechanism, is possible, and *how hot* it is allowed to be in the process.

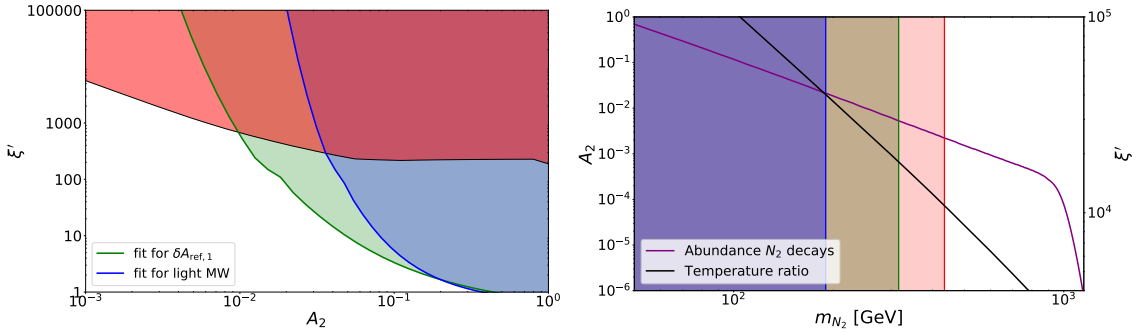


Figure VI.11: *Left figure:* Application of our fit results to the ScM with  $m_{\pm} = 1200$  GeV and  $m_{N_2} \simeq 300$  GeV. The green shaded region is the  $\delta A_{\text{ref},1}$  limit and the blue one the light MW subhalo count. Again, the red shaded region is excluded by the  $\Delta N_{\text{eff}}$  bound. *Right figure:* The corresponding abundance  $A_2$  (purple line) and DM temperature ratio  $\xi'$  (black line) for the same ScM setup, where Yukawa interactions are chosen as large as possible. The green/blue shaded regions are excluded by the respective structure formation limits and the red shaded regions by  $\Delta N_{\text{eff}}$ . For both plots, the mass of the DM candidate is  $m_{N_1} = 24$  keV.

Finally, we want to comment on the potential issue of late-time decays of heavy particles which may happen during the epoch of BBN and hence can spoil the abundance of light nuclei by injecting highly energetic particles into the thermal plasma [204, 326, 327]. However, this danger does not appear for our model setup, because we assume that the parent particle decays exclusively into DM via  $P \rightarrow X X$ . There is no heating of the SM plasma due to these decays, because the coupling between  $X$  and the SM plasma is assumed to be zero. On the contrary, for models which feature decays into SM particles besides DM,  $P \rightarrow X S$ , these decays tend to be dangerous when decaying at temperatures  $T \lesssim 1$  MeV. Using Eqs. (VI.9) and (VI.10) this can be translated into a bound on  $\xi$ ,

$$\frac{T}{\text{MeV}} = \frac{200}{\xi} \frac{m_P}{\text{GeV}}. \quad (\text{VI.29})$$

For our sample model this bound evaluates to  $\xi \leq 2000$  if  $P$  decays dominantly into hadrons. On the contrary, especially for mainly leptonic decays, the condition that  $T \gtrsim 1$  MeV can be relaxed substantially, if  $A_2 \ll 1$  as shown in Ref. [1].

### VI.6.3 Model III: thermalized + frozen-in parents

As a last toy model we assume that  $m_{\text{DM}} = 125 \text{ keV}$ , again an amount  $A_1$  of DM is produced via thermalized parent decays with  $m_S = 1 \text{ TeV}$ , but  $A_2$  stems from a frozen-in parent with mass  $m_P = 80 \text{ GeV}$ . Similarly to the previous toy model, we have to take a change in  $g_*^s(T)$  into account, although it will impact the limits on  $\xi$  at higher values, since  $m_P$  is larger in this case and DM is produced at earlier times compared to the previous case. The results of the fit are shown in Fig. VI.12 where we use the same color coding as before. Since the DM in this model is heavier than in the first toy model, the exclusion limits are shifted to larger  $\xi$  values. Further, the bound from  $\Delta N_{\text{eff}}$  is only marginally visible in this plot due to the rather large DM mass.

As before, we compare our analytical exclusion limits against some benchmark points using a full numerical simulation, but in this case we choose  $\xi = 40$  and  $300$ . Compared to the previous example, the benchmark points are closer to the fitted curve here. This is to be expected, as the momentum distribution function  $f(x, r)$  (see Eq. (VI.35)) arising from decays of frozen-in parents only features one distinct peak, because the parent particles are never thermalized and so no early decays are taking place. Hence, rescaling  $\xi$  by an appropriate factor, as explained around Eq. (VI.26), can be safely done even for  $A_2 \rightarrow 1$ . One can now match these limits onto model parameters describing frozen-in parent

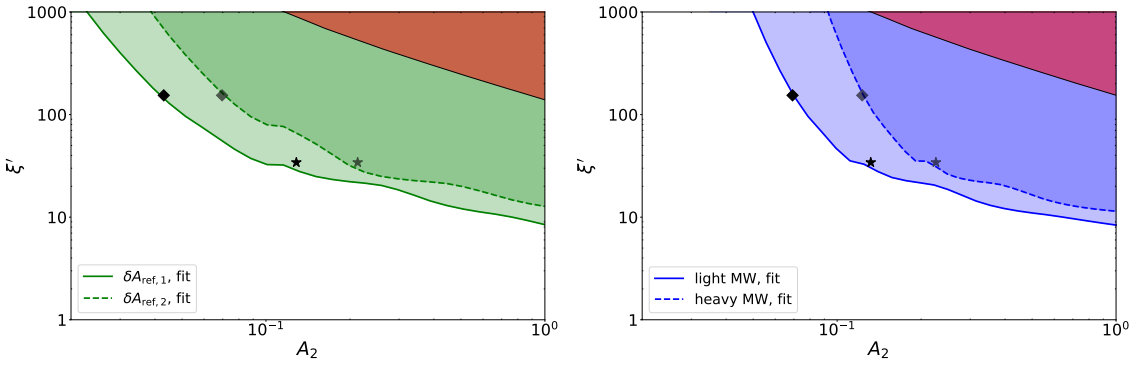


Figure VI.12: Structure formation limits using the  $\delta A_{\text{ref}}$  criterion in the left and a MW subhalo count in the right figure for the third toy model. Everything indicated by the green or blue shaded region is constrained by structure formation and solid lines correspond to strong and dashed lines to weak limits. For comparison a full numerical simulation to extract limits was run for  $\xi = 40$  and  $300$  and is indicated by the stars and diamonds in both plots. The  $\Delta N_{\text{eff}}$  bound is absent, because it is weaker compared to Fig. VI.10 due to the larger DM mass.

particles. Assuming that  $P$  itself is produced via an effective coupling  $C_P$ , the DM yield for this mechanism is given by

$$Y_{\text{DM}} = C_P \frac{135}{64\pi^2} \frac{1}{g_*^s(T_{\text{prod},2})}, \quad (\text{VI.30})$$

$$A_2 \simeq \left( \frac{m_{\text{DM}}}{125 \text{ keV}} \right) \left( \frac{106.75}{g_*^s(T_{\text{prod},2})} \right) \left( \frac{C_P}{1.7 \times 10^{-3}} \right). \quad (\text{VI.31})$$

When discussing freeze-in scenarios one might want to construct a model where all particles are decoupled from the thermal bath and therefore all of DM is produced by frozen-in parent particles. However, this situation requires some modifications, because the averaged momentum for the first subset generally differs from the case  $\langle z \rangle = 2.5$ . As pointed out in Section VI.5 this different setup can be handled by introducing a shift  $\langle z \rangle = 2.5 \alpha$ . If  $\alpha > 1$ , the DM carries a larger averaged momentum and hence stronger bounds are set

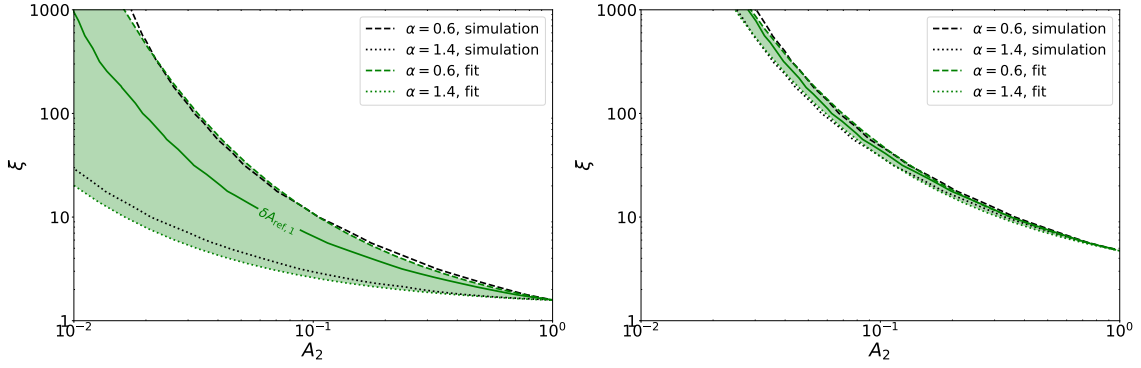


Figure VI.13: Effect of changing  $\langle z \rangle$  for the  $A_1$  set of the DM on the excluded region in the  $A_2$ - $\xi$  plane based on the  $\delta A_{\text{ref},1}$  criterion. The dashed lines correspond to  $\alpha = 0.6$ , while the dotted curves represents  $\alpha = 1.4$ . The black curves stem from a numerical analysis and the green ones from the adapted analytical fit as explained in Section VI.5. The left figure is derived for  $m_{\text{DM}} = 20$  keV and the right one for  $m_{\text{DM}} = 60$  keV.

on the parameter space. On the other hand,  $\alpha < 1$  corresponds to a DM with smaller averaged momenta and weaker structure formation constraints. It can be understood in terms of the temperature  $T_1$  as well: lower temperatures leads to a smaller value of  $\langle p/T \rangle$ , which gives rise to less stringent exclusion limits and vice versa for larger temperatures. This effect is shown in Fig. VI.13 where we choose  $\alpha = 0.6$  and  $1.4$  for two different DM mass choices and compare the corresponding  $\delta A_{\text{ref},1}$  exclusion bound to the reference case  $\alpha = 1$ , but do not change  $A_2$ . Further, these numerical results shown as the black curves are compared against limits we derived using our analytical fit prescription (green curves), adapted as explained at the end of Section VI.2. As can be seen both approaches agree to a good approximation. Only for rather small DM masses and  $\alpha > 1$  both curves differ from each other. However, this is not unexpected, as the structure formation observables are quickly changing in this region of parameter space, because for  $m_{\text{DM}} = 20$  keV and  $\alpha = 1.4$  the absolute mass limit given in Table VI.2 is reached. Finally, as expected, the impact on the bounds gets weaker if the DM mass is increasing and it becomes negligible for  $m_{\text{DM}} \gtrsim 100$  keV.

A similar effect appears when  $g_*^s(T_{\text{prod},1})$  is smaller compared to our assumption where all SM particles are still in the thermal bath. In that case, we would find a larger temperature  $T_1$  compared to the photon bath due to smaller reheating effects and accordingly the exclusion curves have to be corrected similar to the case of larger  $\langle z \rangle$  values shown in Fig. VI.13. For this case,  $\alpha$  is defined as the increase in  $T_1$ , which is given by the ratio  $\alpha = (106.75/g_*^s(T_{\text{prod},1}))^{1/3}$  and for sufficiently late production times the temperature can be twice as large as compared to early decays.

#### VI.6.4 Exploring the cold limit of the model parametrization

Motivated by our results in Section V.4 where we discussed that a warm freeze-in ALP DM may be accompanied by a fraction of “cold” ALP DM stemming from the misalignment mechanism, we briefly want to discuss in this section the case where the first DM subset can be considered CDM instead. Formally, this corresponds to the case  $T_1 \rightarrow 0$ , whereas the model parameter  $\xi$  has to be interpreted now in relation to our reference choice in the previous chapters,  $\xi = T_2/2.5$ .

As before, we are going to use Eq. (VI.24) to fit the corresponding exclusion limits based on our structure formation analysis. The parameters derived for  $m_{\text{DM}} = 20$  keV are shown in Table VI.4.



	Lyman- $\alpha$		$N_{\text{sub}}$	
	$\delta A_{\text{ref},1}$	$\delta A_{\text{ref},2}$	light MW	heavy MW
$p_0$	0.899	0.823	0.285	0.333
$p_1$	0.564	0.652	1.04	1.22

Table VI.4: Fit results for the respective exclusion limits based on Eq. (VI.24) using  $m_{\text{DM}} = 20 \text{ keV}$  and assuming that the first subset is composed of CDM.

Compared to the 2TDM, this scenario allows for a simple generalization for all  $m_{\text{DM}}$  choices. The effect of the CDM contribution  $A_1$  on structure formation is essentially independent of the DM mass; it only matters for  $A_2$ . For that reason, the fitted exclusion limits can be easily rescaled to accommodate heavier DM. To illustrate this procedure, we consider the photophilic ALP DM scenario discussed in Section V.5 consisting of “warm” ALP DM produced via scatterings with  $\langle p/T \rangle \approx 3.24$  and a potential subfraction of “cold” ALP DM produced via the misalignment mechanism. Using the values quoted in Table VI.4, correcting for the warmer averaged momentum by  $\alpha \sim 1.3$  and using  $m_{\text{DM}} = 17.4 \text{ keV}$  (stemming from the corresponding strong MW mass limit, i.e. the lighter mass), we are able to reproduce the limits as shown in Fig. VI.14 to a good extent. The blue shaded region is excluded by a subhalo count for this ALP DM setup, while the red curve gives the exclusion contour based on our fitting approach. It gives slightly weaker limits compared to the numerical study, because the lower MW mass limit employed in this chapter is marginally larger compared to Chapter V.

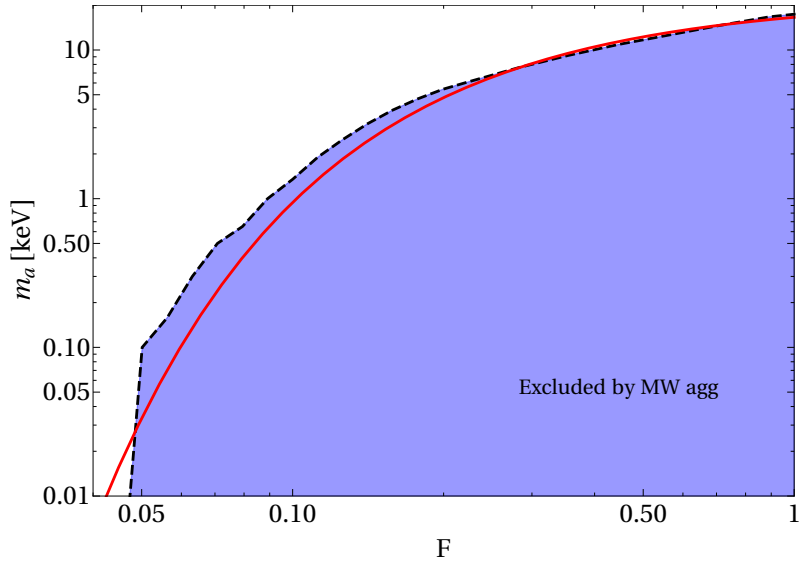


Figure VI.14: Similar to Fig. V.5, where limits for the photophilic ALP  $F - m_a$  parameter plane stemming from a MW subhalo count assuming the lighter MW mass choice are derived. Freeze-in contributes only a fraction  $F < 1$  of warm DM to the total ALP DM abundance, while the rest is made up by a CDM component. The blue shaded region is excluded because these parameters yield  $N_{\text{sub}} < 64$ . The red line is the limit derived using our analytic expressions for the light MW mass choice.

## VI.7 Summary of Chapter VI

Many extensions of the SM introduce entire dark sectors with several new particles and interactions among them. Therefore, it is natural to ask the question what happens if the DM is produced via different production channels, leading to DM composed of two subsets, each characterized by its own temperature. Depending on the size and the nature of the involved couplings and particles, these decays can easily take place at late times in the early Universe and give rise to an increased DM temperature. We examined such a scenario as model-independently as possible to allow for an easy comparison with specific WDM models. For this purpose, we assumed that the DM is produced by two different decay channels. One is due to decays of thermalized parents at rather early times, while the second contribution stems from decays happening at later times. Our setup (referred to as 2TDM) is parameterized by two key parameters: the abundance  $A_2$  of the second subset produced at later times and the temperature ratio between both DM subsets, denoted by  $\xi$ .

The impact of such a model setup on the formation of structures in the universe was evaluated. Specifically we derived predictions for the number of MW subhalos and the flux power spectrum and compared them against observations. Based on these, limits on the parameters  $\xi$  and  $A_2$  were derived for DM masses between 20–1000 keV. For  $\xi = 1$ , i.e. a single DM temperature setup, our limits on the DM mass are up to 11 keV using Lyman- $\alpha$  measurements and up to 13 keV counting the observed MW subhalos and using the MW mass derived from recent GAIA measurements. Typically, we could probe and constrain parameters for  $A_2$  between 1 and 0.01 for temperature ratios up to 1000 and in general, DM with a high temperature  $T_2$  can only make up a few percent of the total DM number density.

We presented an analytical fit for the respective exclusion limit and discussed further steps how to extract limits on specific model realizations. One focus was the incorporation of a change in the number of effective entropic DOF during the time of production of the DM species, as this impacted the interpretation of the fitted results. As an example we considered different examples and compared our analytical prediction against numerical results, where we made direct use of appropriate momentum distribution functions. Our procedure showed a good agreement between the analytical fit and actual results. Hence, it allows to predict limits on the temperature of a warmer DM fraction and its abundance without extensive simulations.

Further, we commented on the treatment of DM production via three-body decays inside our framework and how we calculated exclusion limits for these cases applying rescaled results. As an example we derived limits for a benchmark point of the ScM setup considered in Chapter IV. We also discussed the limit where  $T_1 \rightarrow 0$ , i.e. the first DM subset can be considered to be CDM instead; this particular case allowed us to present a simpler fitting method, since the corresponding results scale directly with  $m_{\text{DM}}$ . As an example, we matched this result to the corresponding numerical results for the photophilic ALP DM model with an admixture of misalignment DM, discussed in Section V.5 of Chapter V.

As a final remark, we want to point out that it is also possible to reinterpret our model in terms of a mixture of two DM species with different masses  $m_{\text{DM},1}$  and  $m_{\text{DM},2}$ , by adapting the model parameter  $\xi$  accordingly:  $\xi \equiv T_2/T_1 m_{\text{DM},1}/m_{\text{DM},2}$ .

## VI.8 Appendix of Chapter VI

### VI.8.1 Momentum distribution function of out of equilibrium parents

If the parent particle is sufficiently long-lived and has a sizeable coupling  $C_P$ , it thermalizes and its decay will happen after it drops out of the thermal bath. After the time of freeze-out,  $r_{\text{fo}}$ , the momentum distribution function of the parent is given by

$$f_P(x, r) = f_{\text{EQ}}(x, r), \quad r < r_{\text{FO}}, \quad (\text{VI.32})$$

$$f_P(x, r) = f_{\text{EQ}}(x, r_{\text{FO}}) \left( \frac{r + \sqrt{r^2 + x^2}}{r_{\text{FO}} + \sqrt{r_{\text{FO}}^2 + x^2}} \right)^{C_P x^2/2} \times \quad (\text{VI.33})$$

$$\times e^{-C_P(r\sqrt{r^2+x^2}-r_{\text{FO}}\sqrt{r_{\text{FO}}^2+x^2})/2}, \quad r > r_{\text{FO}}. \quad (\text{VI.34})$$

### VI.8.2 Momentum distribution function of never thermalized parents

Weakly coupled parent particles with  $C_P \ll 1$  never reach thermal equilibrium, but rather freeze-in before they start to decay. Their momentum distribution can be derived as

$$f_P(r, x) = C_P \int_0^r d\rho \rho K_1(\rho) \frac{\exp(-\sqrt{\rho^2 + x^2})}{\sqrt{\rho^2 + x^2}} \left( \frac{e^{\rho\sqrt{\rho^2+x^2}}}{e^{r\sqrt{r^2+x^2}}} \left( \frac{\rho + \sqrt{\rho^2 + x^2}}{r + \sqrt{r^2 + x^2}} \right)^{x^2/2} \right)^{C_P/2}. \quad (\text{VI.35})$$

### VI.8.3 Change in $\langle x \rangle$ due to $g_*^s(T)$

As explained in Section VI.4.2, the time-dependence of the number of effective entropic DOF,  $g_*^s(T)$ , generally shifts the DM momentum distribution function towards larger momenta. To examine this effect for the case of out of equilibrium decays, the average value  $\langle z \rangle$  is calculated, taking a change in  $g_*^s(T)$  into account, and compared against  $\langle x \rangle$ , where  $g_*^s(T)$  are kept fixed in the calculation. The result is shown in Fig. VI.15, where we varied the mass of the parent particle between 1 MeV and roughly 10 TeV for  $\xi$  between 1 and 6000. As can be seen, at rather small  $\xi$  the effect of a change in  $g_*^s(T)$  starts to be dominant at  $m_P < 10$  GeV; below this mass the averaged momentum can be even twice as large as compared to the case where  $g_*^s(T)$  are treated as constant. However, increasing  $\xi$  will give rise to a shift in  $\langle z \rangle$  even for rather large parent particle masses. This behavior is expected, because if DM is produced at sufficiently early times by decays of very heavy parent particles,  $g_*^s(T)$  stays approximately constant. However, demanding that this DM should have a large  $\xi$  as well, requires that it is produced at later times in the temperature and the effect of a change in  $g_*^s(T)$  becomes relevant.

### VI.8.4 Details on fitting procedure

As explained in Section VI.5, we fit the respective exclusion contours using Eq. (VI.24) and derive the fit parameters  $p_i$  for  $m_{\text{DM}}$  between 20–1000 keV. The mass-dependent  $p_i$  are than fitted using Eq. (VI.25). The results for all four structure formation limits are shown in Fig. VI.16 respectively. The numerical results of a MW subhalo count analysis using a light/heavy MW mass are shown as blue/dark blue crosses, whereas the  $\delta A_{\text{ref}}$  limits are shown in light and dark green. We compare these with the corresponding results of the aforementioned polynomial fit, which are presented in the same color scheme as a solid and dashed line, respectively. In summary, our fit describes the numerical results accurately, only for DM masses above 700 keV slightly larger deviations are visible, which is why we

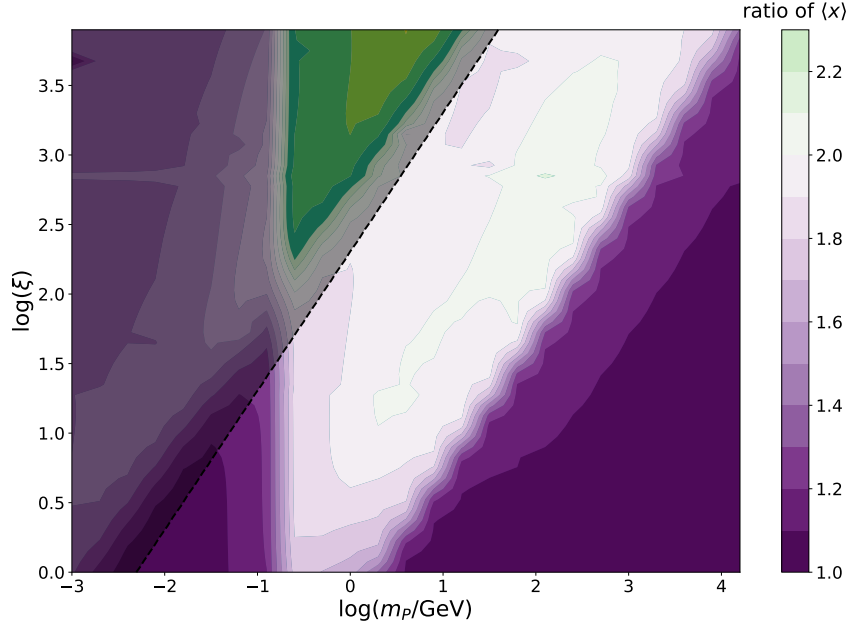


Figure VI.15: Ratio of  $\langle x \rangle$  derived comparing Eq. (VI.21) against Eq. (VI.1), i.e. comparing a time-dependent  $g_*^s(T)$  against constant case  $g_*^s(T) = 106.75$ . As can be seen, the averaged value is shifted to larger values, especially for  $m_P \sim 1 \text{ GeV}$  and large values of  $\xi$ , because in that region  $g_*^s(T)$  is changing rapidly. However, the effect becomes less prominent for heavier or lighter parent particles. It can also be seen that  $\langle x \rangle$  stays constant if both,  $m_P$  and  $\xi$  are increased. The black shaded region indicates decays which would take place after BBN.

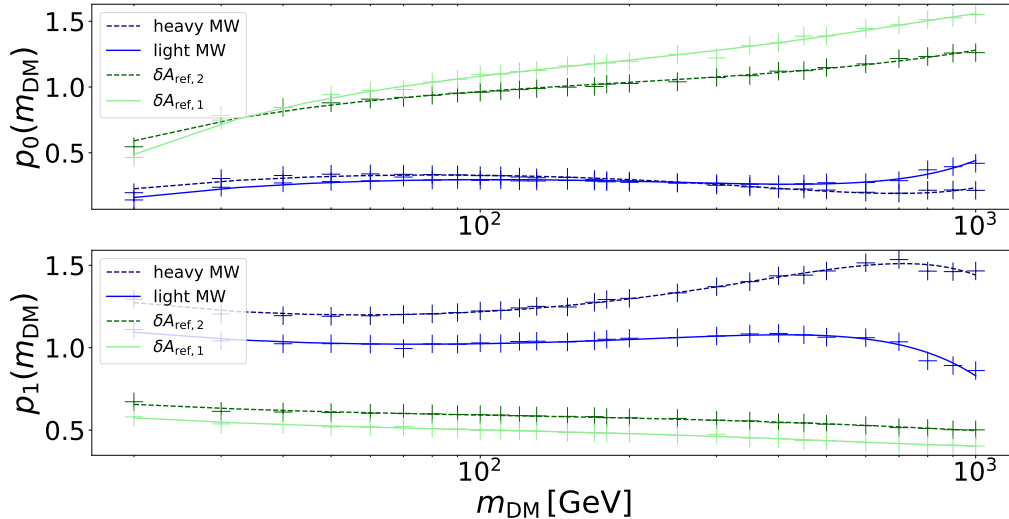


Figure VI.16: Comparison of the fit parameters  $p_i$  for different DM masses and structure formation limits shown as crosses, and the corresponding fourth-order polynomial fit (see Eq. (VI.24)). Stronger limits are shown as solid and weaker ones as dashed lines.

only examine DM masses up to 1000 keV. An even larger mass range would require an extended fit equation with more parameters. Therefore, we are using eight fit parameters in Eq. (VI.24) for our final fit in total and the results are summarized in Table VI.5. We

	$\delta A_{\text{ref},1}$	$\delta A_{\text{ref},2}$	light MW mass	heavy MW mass
$a_0$	1.16	1.03	0.383	0.428
$b_0$	-13.7	-8.83	-4.28	-3.77
$c_0$	$6.08 \times 10^{-4}$	$2.64 \times 10^{-4}$	$-5.07 \times 10^{-4}$	$-6.60 \times 10^{-4}$
$d_0$	$-1.95 \times 10^{-7}$	$-0.02 \times 10^{-7}$	$5.70 \times 10^{-7}$	$4.70 \times 10^{-7}$
$a_1$	0.504	0.589	0.942	1.07
$b_1$	1.47	1.39	2.80	3.63
$c_1$	$-1.82 \times 10^{-4}$	$-1.23 \times 10^{-4}$	$6.16 \times 10^{-4}$	$12.2 \times 10^{-4}$
$d_1$	$0.800 \times 10^{-7}$	$0.288 \times 10^{-7}$	$-7.32 \times 10^{-7}$	$-8.50 \times 10^{-7}$

Table VI.5: Final fit parameters for all four exclusion contours, according to Eq. (VI.25). The DM mass ranges between 20–1000 keV.

want to point out, that we do not assign an error on these results. Although we can estimate a statistical uncertainty stemming from a finite simulation grid size, systematical uncertainties of the fitted structure formation limits indicated by the strong/weak bound are clearly dominating.

### VI.8.5 Impact of $N_{\text{sub}}$ on the parameter limits

We already discussed the uncertainties involved when calculating  $N_{\text{sub}}$ . While we derived an upper and lower MW mass bound and presented our results for both mass choices, we kept the requirement that our 2TDM should fulfill  $N_{\text{sub}} \leq 64$  throughout this section. In the same way as done in Section V.7.3 we illustrate how the exclusion contours depend on the choice of the number of sub halos in Fig. VI.17 for the 2TDM with  $m_{\text{DM}} = 50$  keV. The left figure shows the result for the light MW mass and the right one for the heavy MW mass. Shown in blue is the exclusion limit for  $N_{\text{sub}} = 80$ , the red line is for  $N_{\text{sub}} = 50$  and the black line, finally corresponds to the standard choice. As in the case of ALP DM we observe that results derived for the light MW mass choice is more sensitive on the value of  $N_{\text{sub}}$ , although its impact is less compared to our results in Section V.7.3, because the lighter MW mass choice is slightly heavier.

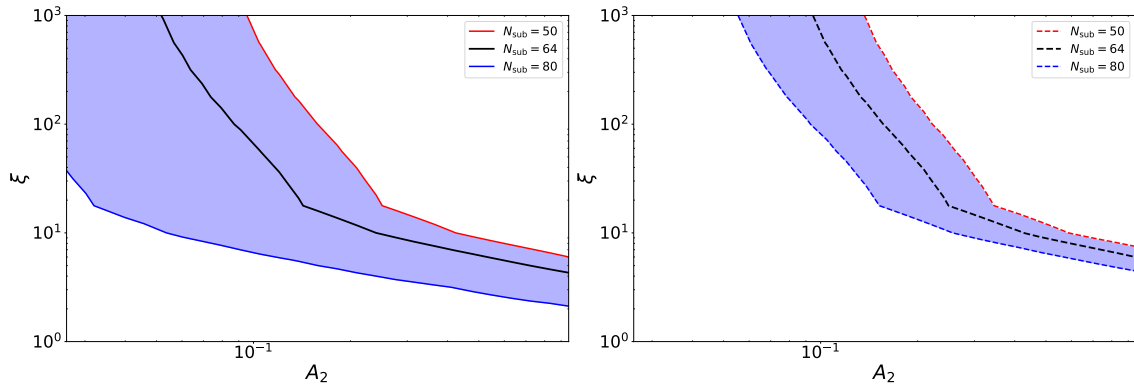


Figure VI.17: Comparison of mass limits for different choices of  $N_{\text{sub}}$  and MW masses for the 2TDM model with  $m_{\text{DM}} = 50$  keV. The left figure shows results for the light MW mass and the right one for the conservative choice. The blue lines are  $m_a$  limits for  $N_{\text{sub}} = 80$  and the red lines are using  $N_{\text{sub}} = 50$  while the black lines are results for  $N_{\text{sub}} = 64$ .

In addition we have evaluated the absolute mass limits  $m_{\text{DM}}^{\text{lim}}$  for the different cases similar to the procedure done to derive Table VI.2 and the results are shown in Table VI.6. This

MW \ $N_{\text{sub}}$	50	64	80
light mass	8.8 keV	12.8 keV	23.5 keV
heavy mass	7.2 keV	9.0 keV	11.4 keV

Table VI.6: Lower DM mass limit  $m_{\text{DM}}^{\text{lim}}$  for different choices of the observed amount of subhalos  $N_{\text{sub}}$  compared to the case  $N_{\text{sub}} = 64$  as used in this section. They were derived assuming  $\xi = 1$ , i.e. all of DM has a common temperature  $T_2 = T_1$ .

highlights again, that potentially new discoveries of subhalos offer the intriguing possibility of further constraining our framework.



# Aftermath







## Summary and conclusion

In this thesis, we studied the phenomenology of certain light dark matter (DM) models. In Chapter III we studied the prospects to discover light DM embedded in a dark sector at present and future particle colliders, whereas in Chapters IV to VI the impact on the early Universe and structure formation was studied in the context of these and further models.

Our first scenario consisted of the scotogenic model (ScM), which extends the standard model (SM) with three right-handed neutrinos (RHN) and a new scalar doublet, all charged under a discrete  $\mathbf{Z}_2$  symmetry. It features a rich phenomenology and allows for a simultaneous explanation of various open problems: the smallness of neutrino masses, DM and the observed baryon asymmetry of the Universe introducing TeV scale new physics. This motivated our search for this particular model setup at particle colliders which has been done in Chapter III.

For this purpose, we studied the pair production of the new charged scalar  $\sigma^\pm$  which decays into two different missing transverse energy ( $\cancel{E}_T$ ) signatures: first, we studied a two tau +  $\cancel{E}_T$  (di-tau) signature based on the ATLAS search on  $36.1 \text{ fb}^{-1}$  LHC data [214]. The other signature consists of two  $e$  or  $\mu$  and  $\cancel{E}_T$  (di-lepton) and was outlined again by ATLAS using  $36.1 \text{ fb}^{-1}$  of collected collision data [213]. We recasted these analyses and used the existing limits on the cross section to place bounds on our model. We found that the current limits do not constrain the model in consideration significantly and only a few parameter choices can be ruled out. Hence, we estimated the projected sensitivities for the high luminosity phase of the LHC (HL-LHC) based on the current analysis techniques, assuming a total luminosity of  $4000 \text{ fb}^{-1}$  collected at a center-of-mass energy of  $\sqrt{s} = 14 \text{ TeV}$ . We presented our results for the di-tau and di-lepton signatures for different branching ratios and masses of the scalar,  $m_\pm$  and heavy RHN,  $m_{N_2} = m_{N_3}$ . The corresponding couplings for the decays of  $\sigma^\pm$  are fixed by the Casas-Ibarra parametrization in order to satisfy the observed SM neutrino masses and mixings. Hence, we optimized these couplings to maximize the decays into  $e$  and  $\mu$  or tau leptons and compared them against the case where  $\sigma$  decays exclusively into one of the two final state signatures.

Our projected HL-LHC sensitivity curves allow to probe a significant part of the parameter space, ranging up to  $m_\pm \simeq 650 \text{ GeV}$  for the scalar mass and up to  $m_{N_2} \simeq 350 \text{ GeV}$  for the RHN in the case of a di-lepton signature. The projected results for the di-tau case are weaker since tau final states are not as clean as  $e$  or  $\mu$  tracks, because tau leptons decay hadronically as well.

Then, we presented results for future collider experiments, considering proton and electron colliders. For the former, we consider the FCC-hh with the luminosity goals of  $3 \text{ ab}^{-1}$  and  $30 \text{ ab}^{-1}$  at  $\sqrt{s} = 100 \text{ TeV}$ , and studied the electron linear collider CLIC at  $\sqrt{s} = 3 \text{ TeV}$  and a total luminosity of  $5 \text{ ab}^{-1}$ . Extending and adapting the analysis we

used for HL-LHC, we projected sensitivities for both experiments using the di-lepton signature. We found that they can probe a wide range of parameter space, extending up to  $m_{\pm} \simeq 2 \text{ TeV}$  and  $m_{N_2} \simeq 1.4 \text{ TeV}$  at FCC-hh. On the other hand, due to cleaner experimental signatures at lepton colliders, CLIC can probe the parameter region where  $m_{N_2} \lesssim m_{\pm}$ ; this is of particular interest when considering a resonant leptogenesis scenario to generate the observed baryon asymmetry.

Although it is possible to explore the heavy matter sector of the scotogenic model, we have seen that it is hard to detect its light DM component with  $m_{N_1} = 6 \text{ keV}$  at colliders. Therefore, we turned our attention in Chapter IV to study the light DM imprint on the cosmology of the early Universe and the formation of structures. In this framework, DM can be produced via prompt decays of thermalized  $\sigma^{\pm}$  scalars, or late-time decays of the next-to-lightest  $\mathbf{Z}_2$ -odd particle in the spectrum. Of particular interest is the second production mechanism, because it can give rise to highly energetic light DM which is relativistic for a significant time period. Thus, it contributes to the effective number of relativistic species,  $N_{\text{eff}}$ , with an amount  $\Delta N_{\text{eff}}$  and alters the formation of structures due to its non-vanishing free-streaming length. We employed the bound  $\Delta N_{\text{eff}} < 0.344$  during the time of big bang nucleosynthesis (BBN) and calculated the matter power spectrum  $P(k)$  of the DM to employ a half-mode analysis to put limits on the allowed model parameters; it turned out that the  $\Delta N_{\text{eff}}$  bound is superior. Further, all DM production has to happen before BBN takes place, or otherwise the abundance of light nuclei might be altered. Demanding that the production terminates before  $t = 1 \text{ s}$  restricts the parameter space further. In order to satisfy these bounds, the hot DM component can contribute only at the sub-percent level to the total DM abundance. Finally, we overlapped our findings with the projected sensitivities of the collider analysis and were able to show that cosmology already constrains parameter regions which cannot be accessed by current collider experiments. Further, we discussed how the bounds from cosmology will change when considering other coupling strengths and heavier DM  $N_1$ .

The model we studied in Chapter V extends the SM by an axion-light particle (ALP)  $a$  which can couple to photons and fermions. Assuming small couplings to these SM particles, the ALP DM can be produced via a freeze-in process by  $2 \rightarrow 2$  scatterings or annihilations. We have studied two different cases: either the ALP couples only to photons (photophilic) or fermions (photophobic). We calculated the ALP DM momentum distribution function  $f$  from the corresponding cross sections assuming Maxwell-Boltzmann distributions for the involved particles and derived the power spectrum  $P(k)$  for both cases. The photophilic scenario features an infrared (IR) singularity in the cross section due to a virtual gauge boson, which has to be regularized by an IR cutoff. As a result the momentum distribution function turns unphysical below a certain momentum. We redid the analysis using quantum statistics for the in- and out-going particles and regularized the IR singularity by the respective thermal gauge boson mass. Even in this case, we found the momentum distribution function to become negative below a certain momentum.

However, for structure formation the most relevant quantity is the averaged momentum  $\langle p/T \rangle \simeq 3$  and  $f$  turns only unphysical at rather low momenta. For this reason, we could still use it to extract limits on the parameter space. We found that besides an overall factor, the distribution function for both approaches are nearly identical and we used the analytic results assuming Maxwell-Boltzmann statistics for the analysis. Using a half-mode analysis assuming a weak and strong limit from Lyman- $\alpha$  forest observations, we can place limits on the ALP DM mass  $m_a \lesssim 19 \text{ keV}$ . Additionally, as a complementary probe, we calculated the predicted number of Milky Way (MW) subhalos for the

ALP DM and compared it against observations. Demanding that enough subhalos eventually form, the limit  $m_a \lesssim 17$  keV was derived, depending on the MW mass. Our limits do not depend on the coupling, as long as the ALP does not thermalize, but we considered gamma-ray searches to constrain these couplings due to  $a \rightarrow \gamma\gamma$  decays.

For the photophobic case there is no infrared-singularity because fermion masses act as a cutoff, and we found the limits  $m_a \lesssim 16$  keV from a half-mode analysis and  $m_a \lesssim 13$  keV based on a subhalo count. Compared to the photophilic case, at lowest order, the results do not depend on the assumed reheating temperature. If the ALP-fermion couplings are flavor-universal, additional bounds from XENON1T, red giant cooling and loop-induced photonic decays have to be taken into account. Finally, we considered the future Vera C. Rubin observatory which allows us to place strong mass limits up to  $m_a \lesssim 80$  keV in the photophilic case.

Inspired and motivated by these findings, we constructed a model-independent framework with two distinctive DM production mechanisms, each producing a subset of DM featuring its own temperature. We considered the first subset to be produced in decays of thermalized parent particles, while the second one stems from non-thermal and long-lived parents. The parameter space of this framework, which we referred to as the two temperature dark matter (2TDM) model, is spanned by the abundance  $A_2$  of the hotter subset to the total DM abundance, the temperature ratio  $\xi$  between both subsets, and the DM mass  $m_{\text{DM}}$ . We derived constraints on these parameters based on the number of MW subhalos, limits from the flux power spectrum of Lyman- $\alpha$  forest surveys and an additional contribution to  $N_{\text{eff}}$ . Further, we presented a fit equation which reproduces the corresponding exclusion limits for DM masses between 20 keV and 1 MeV to a very good approximation. We discussed how to adapt our result for the more general case when the relativistic degrees of freedom are not constant during DM production, employed our findings for exemplary toy models, and compared them against numerical simulations. Finally, we commented on the possible inclusion of three-body decays, a generalization of the first production method, and discussed the case where one subset can be considered “cold” DM instead. In particular, we matched these results to the aforementioned models.



# List of Figures

---

## Chapter II

- II.1 The trinity of DM detection: production of DM with highly energetic beams at colliders, direct detection of DM scattering events inside detectors and searches for decay products from DM annihilation processes. The circle in the middle represents an unspecified effective coupling between two DM particles  $\chi$  and SM particles. . . . . 13
- II.2 The matter power spectrum  $P(k)$  derived using CLASS [145, 146] and for cosmological parameters specified in Ref. [27]. At small wavenumbers it is increasing  $\propto k$ , whereas it drops  $\propto k^{-3}$  after it reaches a peak at  $k \approx 10^{-2} h/\text{Mpc}$ . The different colored horizontal lines indicate ranges of the spectrum which can be experimentally verified by observations and which are explained in more detail in the text. This figure is inspired by Fig. 1 in Ref. [147]. . . . . 24
- II.3 The corresponding matter power spectrum for a WDM with mass in range  $m_{\text{WDM}} = 0.5 \text{ keV} - 4 \text{ keV}$ . In general, a suppression of the power spectrum compared to  $\Lambda\text{CDM}$  can be observed and the scale at which it starts to deviate is related to the mass of the WDM candidate. . . . . 25

## Chapter III

- III.1 Allowed region in the  $\eta - m_{N_2}$  parameter space for a charged scalar mass  $m_{\pm} \simeq 590 \text{ GeV}$  (left) and  $m_{\pm} \simeq 795 \text{ GeV}$  (right). The BBN exclusion limits are shown in red, while the blue shaded region does not produce a sufficiently large baryon asymmetry. We observe that there is a region consistent with BBN limits in which the correct amounts of DM and baryon asymmetry can be obtained. . . . . 35
- III.2 Production channels for the  $\ell_i \ell_j + \cancel{E}_T$  process at the LHC. Pair produced charged scalars decay into heavy leptons  $N_{2,3}$  and charged SM leptons ( $e, \mu$  or  $\tau$ ). . . . . 39

III.3	Cross section $\sigma^{\text{prod}}$ for pair production of charged scalars $\sigma^\pm$ . The left panel shows the increase of $\sigma^{\text{prod}}$ for different center-of-mass energies and fixed scalar mass, $m_\pm = 400$ GeV. The black (blue) vertical lines indicate the energy range of the LHC (FCC-hh) and dashed lines indicate to the respective cross section of the experiment. In the right panel we show $\sigma^{\text{prod}}$ for different scalar masses and fixed energy. By increasing $m_\pm$ the cross section drops significantly. . . . .	39
III.4	Projected sensitivities for HL-LHC using $\mathcal{L} = 4000 \text{ fb}^{-1}$ and the same analysis techniques as in Ref. [214]. Given in blue are exclusion limits, $\mathcal{S} = 2$ , and shown in red are discovery limits, where $\mathcal{S} = 5$ . The dashed lines correspond to a 100% BR into tau leptons using the Casas-Ibarra parametrization, whereas the solid lines represent the case in which the maximized BR for NO (shown in Table III.3) is employed. . . . .	42
III.5	Projected sensitivities for HL-LHC using $\mathcal{L} = 4000 \text{ fb}^{-1}$ and the same analysis techniques as [213]. Given in blue are exclusion limits, $\mathcal{S} = 2$ , and shown in red are discovery limits, where $\mathcal{S} = 5$ . The dashed lines correspond to optimal BR into leptons, whereas to obtain the solid lines we used the value for NO given in Table III.5. . . . .	43
III.6	Sensitivity of FCC-hh with $\mathcal{L} = 3 \text{ ab}^{-1}$ ( $30 \text{ ab}^{-1}$ ) is shown with solid (dashed) lines. The analysis is based on a proposed search for a supersymmetric (SUSY) model presented in Ref. [225]. The red and blue curves correspond to the “best case” scenario with maximized couplings to $e$ , $\mu$ , indicating that a significant portion of the parameter space can be probed at FCC-hh. The situation further improves for larger luminosity. The thin black line corresponds to $m_{N_{2,3}} = m_\pm$ . . . . .	45
III.7	Production channels for the $\ell_i \ell_j + \cancel{E}_T$ process at CLIC. The left process is similar to hadron colliders, except for electrons in the initial state. Additionally, production via $e^+e^-$ collision can happen via a RHN mediated $t$ -channel diagram, although it is suppressed due to Yukawa couplings $y$ . . . . .	46
III.8	CLIC sensitivity for the di-lepton search. Using maximized couplings to $e$ , $\mu$ we obtained the red solid contour that corresponds to a $5\sigma$ discovery and the blue one that represents $2\sigma$ exclusion. The corresponding dashed contours are for the case where $\tau$ couplings are maximized. The thin black line indicates $m_{N_{2,3}} = m_\pm$ . . . . .	48

**Chapter IV**

IV.1	Production of the light DM $N_1$ either via two-body decays of heavy scalars (left figure) or three-body decays of heavy $N_{2,3}$ (right figure). Here, $\Sigma$ stands for all scalar particles: $\sigma^\pm$ and $\sigma^0$ . . . . .	56
IV.2	In the left (right) panel we show the DM momentum distribution function $f_{N_1}(x, r) x^2$ including both DM production mechanisms, taking $m_\pm = 600$ GeV and $m_{N_2} = 100$ GeV ( $m_{N_2} = 400$ GeV). The blue and red curve correspond to early $\Sigma$ decays and $N_2$ late-time decays, respectively. . . . .	58

IV.3	Transfer function $T^2(k)$ for the same benchmark points as in Fig. IV.2. The constraint from structure formation, using Eq. (II.45) with $m_{\text{TR}} = 2 \text{ keV}$ is shown in blue. RHN masses of around $100 \text{ GeV}$ clearly violate this constraint while the green line, corresponding to $m_{N_2} = 400 \text{ GeV}$ , is consistent with the data. The black dashed line represents $\Lambda\text{CDM}$ . . . . .	61
IV.4	<i>Left figure:</i> constraints from structure formation (red curves) confronted with $N_{\text{eff}}$ limits (blue curves) derived using Eq. (IV.23). The solid curves correspond to the ‘‘CMB weak’’ and dashed ones to the ‘‘CMB strong’’ choice of $\Delta N_{\text{eff}}$ . Note that our structure formation limits also indirectly depend on $\Delta N_{\text{eff}}$ as it is an input parameter for CLASS. Clearly, $N_{\text{eff}}$ yields much stronger limits in comparison to those arising from structure formation. Shown in black solid is the curve for $\Omega_{N_2 \rightarrow N_1} h^2 = 0.6 \times 10^{-3}$ . <i>Right figure:</i> same as left figure, whose contours are shown faded. The blue line indicates the new updated bound coming from the BBN limit on $\Delta N_{\text{eff}}$ while the red line stems from a $\delta A$ structure formation analysis as explained in Section IV.3.1. Additionally, the black dashed line indicates $\Omega_{N_2 \rightarrow N_1} h^2 = 0.36 \times 10^{-3}$ . . . . .	62
IV.5	BBN constraints for the case where $N_2$ dominantly decays into electrons and muons (left panel) and taus (right panel) are disfavoring parameter space below the black lines. The regions excluded by the BBN epoch limit on $\Delta N_{\text{eff}}$ are shown in red. The solid green curve indicates the parameter space for a limiting case in which all of the DM is produced by $N_2$ decays. The regions in blue represent constraints from LFV experiments. Finally, the region to the left of the vertical blue dashed line is favored by our collider analysis in the sense that the mass gap between $\sigma^\pm$ and $N_{2,3}$ is sufficiently large. The value of the charged scalar mass in both panels is fixed to $m_\pm = 600 \text{ GeV}$ . On the y-axis we show the average Yukawa coupling of $N_2$ and $N_3$ , defined as $\bar{y}_2 + \bar{y}_3 \equiv \sqrt{\sum_\alpha ( y_{2\alpha} ^2 +  y_{3\alpha} ^2)}/3$ . . . . .	63
IV.6	Same figures as shown in Figs. III.4 and III.5, but now overlapped with BBN constraints discussed in Section IV.3.3 and $N_{\text{eff}}$ limits discussed in Section IV.3.1. For the di-lepton scenario (right picture), cosmological constraints already exclude most of the potential exclusion region while the discovery region is completely covered for both cases. . . . .	65
IV.7	Summarized sensitivity curves for $\mathcal{S}_0 = 2$ as discussed in Sections III.4.2, III.5.1 and III.5.2 for the HL-LHC (red shaded region) with $4 \text{ ab}^{-1}$ (red shaded region), CLIC with $5 \text{ ab}^{-1}$ and (blue shaded region) and FCC-hh with $3 \text{ ab}^{-1}$ and $30 \text{ ab}^{-1}$ luminosity (orange and green shaded regions). Again, the thin black line indicates $m_{N_{2,3}} = m_\pm$ , whereas the thick black line shows BBN constraints and the gray solid curve represent $N_{\text{eff}}$ constraints for $m_{N_1} = 6 \text{ keV}$ . The corresponding dashed contours indicate BBN and $N_{\text{eff}}$ constraints for a DM particle with $m_{N_1} = 600 \text{ keV}$ . We assumed a maximal coupling to $e$ and $\mu$ in this case. . . . .	65
V.1	Tree level Feynman diagrams for the two processes of interest, $fV \rightarrow fa$ (top) and $\bar{f}f \rightarrow Va$ (bottom), in the photophilic (left) and photophobic (right) cases. <i>Image credits:</i> Enrico Morgante . . . . .	71

Chapter V

V.2	<p>The ALP momentum distribution function plotted as <math>x^2 f(x)</math>. <i>Left figure:</i> In blue we show the photophilic case for MB statistics; black lines represent the photophilic case with quantum statistics and in green we show the photophobic case for MB statistics. For each, the dashed (dot-dashed) line represents <math>\bar{f}f \rightarrow Va</math> (<math>fV \rightarrow fa</math>) and the solid line is their sum. The vertical dashed line marks <math>p = g'T</math>, left of which thermal corrections should be added [262]. <i>Right figure:</i> Photophilic scenario for MB and quantum statistics in QED, namely, including only a single fermion carrying unit charge. <i>Image credits:</i> Enrico Morgante (adapted by author)</p>	74
V.3	<p>Transfer function <math>T(k)</math> shown as blue lines for photophilic ALP DM with different masses compared to thermal relic limits presented as an analytic fit given in Eq. (II.45). Shaded in red is the weak limit whereas the light red shaded region is excluded by the strong limit. Hence, the weakest mass bound stemming from this analysis is <math>m_a \simeq 5</math> keV, as indicated by the dotted blue line.</p>	80
V.4	<p>The blue shaded regions are structure formation limits on the photophilic ALP parameter space derived using a half-mode analysis technique as well as a MW subhalo count. The former (latter) are denoted as Lyman-<math>\alpha</math> (MW). For both, weak and strong limits are shown (see Section V.3 for further analysis details). Additionally, gamma-ray limits from INTEGRAL (dark blue shaded) [275], NuSTAR (orange shaded) [276] and M31 [277] (red shaded) are shown. The diagonal dashed lines indicate specific values of <math>T_{RH}</math>, calculated by the requirement of producing the observed amount of DM. The dark gray line assumes only couplings between ALP and <math>B</math> bosons, whereas the light gray lines takes an additional coupling <math>c_{aWW}</math> into account. Finally, the red line at <math>m_a \sim 80</math> keV is the projected sensitivity from the forthcoming Vera C. Rubin observatory. <i>Image credits:</i> Vedran Brdar (adapted by author)</p>	86
V.5	<p>Limits for the photophilic ALP <math>F - m_a</math> parameter plane stemming from a MW subhalo count assuming the strong MW mass choice. We considered that freeze-in contributes only a fraction <math>F &lt; 1</math> to the total ALP DM abundance. The blue shaded region is excluded because these parameters yield <math>N_{\text{sub}} &lt; 64</math>. As the cold ALP DM contribution increases, the limit on <math>m_a</math> decreases correspondingly and effectively vanishes for <math>F \lesssim 0.05</math>.</p>	87
V.6	<p>As before, blue shaded regions are structure formation limits on the photophobic ALP parameter space derived using a half-mode analysis technique as well as a MW subhalo count. The former (latter) are denoted as Lyman-<math>\alpha</math> (MW). For both, weak and strong limits are shown (see Section V.3 for further analysis details). The green lines indicate the viable parameter space based on Eq. (V.41). If the ALP couples only to tau leptons, the ALP needs large couplings indicated by the uppermost line, whereas the other lines correspond to couplings to <math>c</math> or <math>b</math> quark and the sum over all three fermions. If the ALP has a flavor universal coupling, additional bounds from red giant cooling and limits from XENON1T has to be taken into account. Finally, the red line at <math>m_a \sim 60</math> keV is the projected sensitivity from the forthcoming Vera C. Rubin observatory. <i>Image credits:</i> Vedran Brdar (adapted by author)</p>	88



V.7	Impact of $T_{\text{RH}}$ on the viable parameter space of the photophobic ALP, assuming that it couples only to $b$ quarks. A larger ALP-fermion coupling is needed to get the correct DM abundance for lower reheating temperatures. The blue shaded regions are the same mass limits as in Fig. V.6, where $g_*^s(T_{\text{prod}}) = 106.75$ , while the black lines are computed taking a change in $g_*^s(T_{\text{prod}})$ into account. . . . .	89
V.8	Inverse production process of ALP DM via its coupling to photons (A1) and fermions (A21 and A22). An ALP particle $a$ is converted into a photon $\gamma$ by scattering off a fermion $f$ . . . . .	91
V.9	Inverse production process of ALP DM via its coupling to photons (B1) and fermions (B21 and B22). An ALP particle $a$ annihilates with a photon $\gamma$ into a fermion-antifermion pair. . . . .	92
V.10	Comparison of ALP DM mass limits for different choices of $N_{\text{sub}}$ and MW masses in the photophilic scenario. The upper part is the strong MW mass and the lower the weak mass choice. The blue lines are $m_a$ limits for $N_{\text{sub}} = 80$ and the red lines are using $N_{\text{sub}} = 50$ while the black lines are the results given in Tables V.1 and V.2. . . . .	97

**Chapter VI**

VI.1	Schematic representation of our setup: given in black is the background temperature $T_\gamma$ of the universe, while the blue and red curve represents the time evolution of the temperature of the first and second DM set, respectively. The first DM subset is produced at time $t_1$ with a temperature similar to $T_\gamma$ . After a while, the second DM subset is produced at $t_2$ but it has a higher temperature $T_2$ compared to $T_1$ . The bumps in the solid black line mimics entropy dilution due to particle freeze-out in the SM thermal bath. . . . .	101
VI.2	Example $x^2 f(x)$ spectrum for a specific 2TDM scenario with two observable peaks calculated for times when DM production is finished. The blue area corresponds to a dominant subset whereas the red area refers to a subdominant DM share but with higher temperature with respect to the first set. . . . .	102
VI.3	$\Delta N_{\text{eff}}$ bounds derived from Eq. (VI.13) assuming $m_P = 1$ TeV. The black solid line corresponds to $m_{\text{DM}} = 10$ keV and the dashed line to $m_{\text{DM}} = 100$ keV using the BBN bound $\Delta N_{\text{eff}} < 0.344$ . The dotted and dashed-dotted line are the corresponding bounds for $m_{\text{DM}} = 10$ keV and 100 keV from CMB measurements, $\Delta N_{\text{eff}} < 0.28$ . For $A_2 = 1$ temperature ratios $\xi \gtrsim 240$ are excluded. . . . .	106

VI.4	Transfer function $T(k)$ for a 2TDM model where $m_{\text{DM}} = 30 \text{ keV}$ , $A_2 = 0.2$ and $\xi = 25, 125$ shown in red and dashed red respectively, while the blue line is derived from Eq. (II.45) for a thermal relic mass $m_{\text{TR}} = 2 \text{ keV}$ indicating a potential limit from an analysis on structure formation. The green line correspond to $\xi = 25$ and a smaller $A_2 = 0.05$ . Applying a half-mode analysis, all three parameter choices would be excluded, but limits from observables on the matter power spectrum only exclude the two red lines, while the green line is not in conflict. . . . .	107
VI.5	Compilation of different MW mass analyses using the second data release from the GAIA survey. Further information on the results can be found in Refs. [268, 269, 313–321, 323]. The black dotted line is the combination of all measurements and the green shaded region represents a $2\sigma$ error range. On the contrary, blue errorbars correspond to 68% CL limits of the respective analyses. . . . .	109
VI.6	Comparison of the transfer function $T(k)$ for a shifted MB distribution and a freeze-in/freeze-out scenario where the temperature ratio is set to $\xi = 40$ and $A_2 = 0.5$ , while $m_{\text{DM}} = 10 \text{ keV}$ . We see that the analytical shifted MB distribution (red curve) is a good tool to approximate the numerical results for decays of frozen-out or frozen-in parents, shown in blue and gray, respectively. Hence we will use it in the following analysis to deduce constraints from structure formation. The horizontal black dashed line corresponds to a pure $\Lambda\text{CDM}$ scenario. . . . .	110
VI.7	Numerical results for $z^2 f(z)$ as defined in Eq. (VI.21) for different masses of the parent particle, ranging from $m_P = 10^{-5} \text{ GeV}$ to $m_P = 1 \text{ TeV}$ and using Eq. (VI.3) for $f(z)$ as an illustration. Masses of 0.1 and 1 GeV lead to the biggest impact on the shape of the spectrum, while the distributions of the other masses have similar shapes. All distributions are rescaled with a factor $\sqrt{g_*^s(m_P)}$ for an easier comparison. . . . .	112
VI.8	Limits from structure formation and the number of effective entropic DOF for $m_{\text{DM}} = 20 \text{ keV}$ and fixed $g_*^s(T) = 106.75$ . The blue shaded region is disfavored by the MW subhalo count and the green shaded region by limits from Lyman- $\alpha$ surveys, respectively. The solid lines are the corresponding stronger limits, whereas the weaker constraints are shown as dashed lines. The red shaded region in the upper right corner is disfavored by a too large $\Delta N_{\text{eff}}$ value. . . . .	113
VI.9	Structure formation limits given by shaded regions and derived from our analytic fit, Eqs. (VI.24) and (VI.25), using $\delta A$ in the left and $N_{\text{sub}}$ in the right figure. The DM mass is given by $m_{\text{DM}} = 50 \text{ keV}$ and we assume $g_*^s(T) = \text{const}$ during DM production. Shown as black lines are corresponding limits from a numerical simulation and solid/dashed lines correspond to stronger or weaker bounds, respectively. . . . .	116

- VI.10 Structure formation limits using the  $\delta A_{\text{ref}}$  criterion in the left and a MW subhalo count in the right figure for the second toy model. Everything indicated by the green or blue shaded region is constrained by structure formation and solid lines correspond to strong and dashed lines to weak limits. For comparison, full numerical simulations to extract limits are run for  $\xi = 10$  and 40 and are indicated by the stars and diamonds in both plots. The difference between the dark blue and black symbols indicated by an arrow are due to specifics of this model choice and are further explained in the text. The red shaded region yields a too large  $\Delta N_{\text{eff}}$  stemming from the second subset. . . . 117
- VI.11 *Left figure:* Application of our fit results to the ScM with  $m_{\pm} = 1200$  GeV and  $m_{N_2} \simeq 300$  GeV. The green shaded region is the  $\delta A_{\text{ref},1}$  limit and the blue one the light MW subhalo count. Again, the red shaded region is excluded by the  $\Delta N_{\text{eff}}$  bound. *Right figure:* The corresponding abundance  $A_2$  (purple line) and DM temperature ratio  $\xi'$  (black line) for the same ScM setup, where Yukawa interactions are chosen as large as possible. The green/blue shaded regions are excluded by the respective structure formation limits and the red shaded regions by  $\Delta N_{\text{eff}}$ . For both plots, the mass of the DM candidate is  $m_{N_1} = 24$  keV. . . . 118
- VI.12 Structure formation limits using the  $\delta A_{\text{ref}}$  criterion in the left and a MW subhalo count in the right figure for the third toy model. Everything indicated by the green or blue shaded region is constrained by structure formation and solid lines correspond to strong and dashed lines to weak limits. For comparison a full numerical simulation to extract limits was run for  $\xi = 40$  and 300 and is indicated by the stars and diamonds in both plots. The  $\Delta N_{\text{eff}}$  bound is absent, because it is weaker compared to Fig. VI.10 due to the larger DM mass. . . . 119
- VI.13 Effect of changing  $\langle z \rangle$  for the  $A_1$  set of the DM on the excluded region in the  $A_2$ - $\xi$  plane based on the  $\delta A_{\text{ref},1}$  criterion. The dashed lines correspond to  $\alpha = 0.6$ , while the dotted curves represents  $\alpha = 1.4$ . The black curves stem from a numerical analysis and the green ones from the adapted analytical fit as explained in Section VI.5. The left figure is derived for  $m_{\text{DM}} = 20$  keV and the right one for  $m_{\text{DM}} = 60$  keV. . . . 120
- VI.14 Similar to Fig. V.5, where limits for the photophilic ALP  $F - m_a$  parameter plane stemming from a MW subhalo count assuming the lighter MW mass choice are derived. Freeze-in contributes only a fraction  $F < 1$  of warm DM to the total ALP DM abundance, while the rest is made up by a CDM component. The blue shaded region is excluded because these parameters yield  $N_{\text{sub}} < 64$ . The red line is the limit derived using our analytic expressions for the light MW mass choice. . . . 121
- VI.15 Ratio of  $\langle x \rangle$  derived comparing Eq. (VI.21) against Eq. (VI.1), i.e. comparing a time-dependent  $g_*^s(T)$  against constant case  $g_*^s(T) = 106.75$ . As can be seen, the averaged value is shifted to larger values, especially for  $m_P \sim 1$  GeV and large values of  $\xi$ , because in that region  $g_*^s(T)$  is changing rapidly. However, the effect becomes less prominent for heavier or lighter parent particles. It can also be seen that  $\langle x \rangle$  stays constant if both,  $m_P$  and  $\xi$  are increased. The black shaded region indicates decays which would take place after BBN. . . . 124

VI.16 Comparison of the fit parameters  $p_i$  for different DM masses and structure formation limits shown as crosses, and the corresponding fourth-order polynomial fit (see Eq. (VI.24)). Stronger limits are shown as solid and weaker ones as dashed lines. . . . . 124

VI.17 Comparison of mass limits for different choices of  $N_{\text{sub}}$  and MW masses for the 2TDM model with  $m_{\text{DM}} = 50 \text{ keV}$ . The left figure shows results for the light MW mass and the right one for the conservative choice. The blue lines are  $m_a$  limits for  $N_{\text{sub}} = 80$  and the red lines are using  $N_{\text{sub}} = 50$  while the black lines are results for  $N_{\text{sub}} = 64$ . . . . . 125

# List of Tables

---

III.1	Signal regions with the corresponding cuts on final state momenta used in the di-tau analysis. The definition of the respective triggers are explained in the text. . . . .	40
III.2	95% CL limits on the non-SM cross section for the di-tau + $\cancel{E}_T$ analysis. . .	40
III.3	Largest possible BRs for the decay of $\sigma^\pm$ into $\tau$ and $N_{2,3}$ . Above the given value for $\eta_0$ , the BRs are to a good approximation independent of this parameter. As can be seen, the IO gives rise to smaller BRs compared to NO. . .	41
III.4	95% CL limits on the non-SM cross section for the di-lepton + $\cancel{E}_T$ analysis. .	43
III.5	Largest possible BRs for the decay of $\sigma^\pm$ into $e^\pm, u^\pm$ . Below the given value for $\eta_0$ , the BRs are to a good approximation independent of this parameter. Interestingly, the IO regime can feature a situation with a very small BR into tau's, implying approximate zeros in the third column of the Yukawa matrix. . .	43
III.6	Cuts made for distinguishing signal and background at FCC-hh with a luminosity of $3 \text{ ab}^{-1}$ . We show the number of signal and background events for $m_{N_{2,3}} = 500 \text{ GeV}$ and $m_\pm = 1 \text{ TeV}$ . In contrast to Eq. (III.13), $\lambda_3 = -0.27$ was used in this analysis. No systematic errors on the background were assumed for this analysis. . . . .	45
III.7	Signal regions used for an analysis at CLIC with a center of mass energy of $3 \text{ TeV}$ and a luminosity of $5 \text{ ab}^{-1}$ . We show the number of signal and background events together with the corresponding sensitivities for a benchmark point $m_{N_{2,3}} = 500 \text{ GeV}$ and $m_\pm = 1 \text{ TeV}$ . The results are shown both for "best" and "worst" case scenarios which correspond to maximizing couplings to $e, \mu$ and $\tau$ lepton, respectively. . . . .	47
V.1	Structure formation limits on the ALP mass $m_a$ in the <i>photophilic</i> scenario. . . . .	83
V.2	Structure formation limits on the ALP mass $m_a$ in the <i>photophobic</i> scenario under the assumption that $g_*^s(T_{\text{prod}}) = 106.75$ . . . . .	86
V.3	Limits on the ALP mass $m_a$ for different choices of the observed amount of subhalos $N_{\text{sub}}$ compared to the case $N_{\text{sub}} = 64$ as used in this section, assuming a photophilic scenario. . . . .	96

VI.1	Comparison of the corresponding structure formation observables using a shifted MB distribution for parent particles and the respective momentum distributions for non-thermal parent particles. The DM mass is set to 50 keV and only the abundance $A_2$ is varied. The predictions for $N_{\text{sub}}$ and $\delta_A$ are nearly identical. . . . .	110
VI.2	Lower DM mass limit $m_{\text{DM}}^{\text{lim}}$ using constraints from structure formation assuming $\xi = 1$ , i.e. all of DM has a common temperature $T_2 = T_1$ . . . . .	110
VI.3	Fit results for the respective exclusion limits based on Eq. (VI.24) using $m_{\text{DM}} = 20 \text{ keV}$ . . . . .	114
VI.4	Fit results for the respective exclusion limits based on Eq. (VI.24) using $m_{\text{DM}} = 20 \text{ keV}$ and assuming that the first subset is composed of CDM. . . . .	121
VI.5	Final fit parameters for all four exclusion contours, according to Eq. (VI.25). The DM mass ranges between 20–1000 keV. . . . .	125
VI.6	Lower DM mass limit $m_{\text{DM}}^{\text{lim}}$ for different choices of the observed amount of subhalos $N_{\text{sub}}$ compared to the case $N_{\text{sub}} = 64$ as used in this section. They were derived assuming $\xi = 1$ , i.e. all of DM has a common temperature $T_2 = T_1$ . . . . .	126

# List of abbreviations

---

<b><math>\nu</math>MSM</b> — neutrino minimal standard model	<b>lowE</b> — low-multipole CMB data
<b><math>\Lambda</math>CDM</b> — standard model of cosmology	<b>MACHO</b> — massive compact halo object
<b>ALP</b> — axion-like particle	<b>MB</b> — Maxwell-Boltzmann
<b>ARS</b> — Akhmedov-Rubakov-Smirnov mechanism	<b>MET</b> — missing transverse energy (also called $\cancel{E}_T$ )
<b>BAO</b> — baryonic acoustic oscillation	<b>MW</b> — Milky Way
<b>BAU</b> — baryon asymmetry of the Universe	<b>MSW</b> — Mikheyev-Smirnov-Wolfenstein
<b>BBN</b> — big bang nucleosynthesis	<b>NGB</b> — Nambu-Goldstone boson
<b>BR</b> — branching ratio	<b>NO</b> — normal ordering of neutrino masses
<b>BSM</b> — beyond the Standard Model	<b>PBH</b> — primordial black hole
<b>CDM</b> — cold dark matter	<b>PDP</b> — pseudo Dirac pair
<b>CKM</b> — Cabibbo-Kobayashi-Maskawa matrix	<b>PMNS</b> — Pontecorvo-Maki-Nakagawa-Sakata matrix
<b>CL</b> — confidence level	<b>PNGB</b> — pseudo Nambu-Goldstone boson
<b>CMB</b> — cosmic microwave background	<b>PQ</b> — Peccei-Quinn
<b>DM</b> — dark matter	<b>QCD</b> — quantum chromodynamics
<b>DOF</b> — degrees of freedom	<b>QED</b> — quantum electrodynamics
<b>EDM</b> — electric dipole moment	<b>RH</b> — right-handed
<b>EE</b> — CMB E mode polarization power spectrum	<b>RHN</b> — right-handed neutrino
<b>EM</b> — electromagnetism	<b>SM</b> — standard model
<b>EW</b> — electroweak	<b>ScM</b> — scotogenic model
<b>EWSB</b> — electroweak symmetry breaking	<b>SUSY</b> — supersymmetry
<b>FRW</b> — Friedmann-Robertson-Walker	<b>TT</b> — CMB temperature polarization power spectrum
<b>HB</b> — horizontal branch	<b>TE</b> — CMB temperature-E polarization cross-power spectrum
<b>IGM</b> — intergalactic medium	<b>TR</b> — thermal relic
<b>IO</b> — inverted ordering of neutrino masses	<b>VEV</b> — vacuum expectation value
<b>IR</b> — infrared	<b>WDM</b> — warm dark matter
<b>LFV</b> — lepton flavor violation	<b>WIMP</b> — weakly interacting massive particle
<b>LH</b> — left-handed	
<b>LNV</b> — lepton number violating	

# List of experiments and surveys

---

## Collider experiments and facilities

- **CLIC** — Compact Linear Collider
- **CEPC** — Circular Electron Positron Collider
- **FCC** — Future Circular Collider, as lepton (FCC-ee) or hadron (FCC-hh) collider
- **LHC** — Large Hadron Collider
  - **ALICE** — A Large Ion Collider Experiment
  - **ATLAS** — A Toroidal LHC ApparatuS
  - **CMS** — Compact Muon Solenoid
  - **LHCb** — LHC beauty
- **HE-LHC** — high-energy LHC
- **HL-LHC** — high-luminosity LHC
- **ILC** — International Linear Collider

## Neutrino experiments

- **DUNE** — Deep Underground Neutrino Experiment
- **KATRIN** — Karlsruhe Tritium Neutrino Experiment
- **IceCube** — IceCube Neutrino Observatory
- **MicroBooNE** — liquid argon detector for neutrino beamline

## Direct DM detection

- **CREST-III** — Third stage of Cryogenic Rare Event Search with Superconducting Thermometers
- **SENSEI** — Sub-Electron-Noise Skipper-CCD Experimental Instrument
- **SuperCDMS** — Super Cryogenic Dark Matter Search
- **XENON1T** — liquid xenon detector

## Gamma-ray spectra surveys and indirect DM detection

- **Fermi-LAT** — Fermi Large Area Telescope
- **H.E.S.S.** — High Energy Stereoscopic System
- **INTEGRAL** — International Gamma-Ray Astrophysics Laboratory
- **MAGIC** — Major Atmospheric Gamma Imaging Cherenkov Telescopes
- **M31** — reference to data taken by the Chandra X-ray Observatory
- **NUSTAR** — Nuclear Spectroscopic Telescope Array



- **Suzaku** — Suzaku satellite
- **THESEUS** — Transient High Energy Sky and Early Universe Surveyor
- **XMM-Newton** — X-ray Multi-Mirror Mission

**Cosmological and astrophysical surveys**

- **CMB-S4** — Stage-4 ground based cosmic microwave background experiment
- **GAIA** — Global Astrometric Interferometer for Astrophysics
- **HIRES** — Keck High Resolution Echelle Spectrometer
- **MIKE** — Magellan Inamori Kyocera Echelle spectrograph
- **PLANCK** — Planck satellite
- **R18** — reference to Supernova H0 for the Equation of State (SH0ES)
- **SDSS** — Sloan Digital Sky Survey
- **XQ-100** — dataset from the XSHOOTER spectrograph on the Very Large Telescope (VLT)

**Other terrestrial experiments**

- **ALPS** — Any Light Particle Search
- **CAST** — CERN Axion Solar Telescope
- **MEG II** — Mu to E Gamma II



## References

- [1] Sven Baumholzer et al. “Shining Light on the Scotogenic Model: Interplay of Colliders and Cosmology”. In: *JHEP* 09 (2020), p. 136. arXiv: [1912.08215 \[hep-ph\]](#).
- [2] Sven Baumholzer, Vedran Brdar, and Pedro Schwaller. “The New  $\nu$ MSM ( $\nu\nu$ MSM): Radiative Neutrino Masses, keV-Scale Dark Matter and Viable Leptogenesis with sub-TeV New Physics”. In: *JHEP* 08 (2018), p. 067. arXiv: [1806.06864 \[hep-ph\]](#).
- [3] Sven Baumholzer, Vedran Brdar, and Enrico Morgante. “Structure Formation Limits on Axion-Like Dark Matter”. In: *JCAP* 05 (2021), p. 004. arXiv: [2012.09181 \[hep-ph\]](#).
- [4] S. L. Glashow. “Partial Symmetries of Weak Interactions”. In: *Nucl. Phys.* 22 (1961), pp. 579–588.
- [5] Steven Weinberg. “A Model of Leptons”. In: *Phys. Rev. Lett.* 19 (21 Nov. 1967), pp. 1264–1266.
- [6] Abdus Salam. “Weak and Electromagnetic Interactions”. In: *Conf. Proc. C* 680519 (1968), pp. 367–377.
- [7] Gerard ’t Hooft and M. J. G. Veltman. “Regularization and Renormalization of Gauge Fields”. In: *Nucl. Phys. B* 44 (1972), pp. 189–213.
- [8] F. Englert and R. Brout. “Broken Symmetry and the Mass of Gauge Vector Mesons”. In: *Phys. Rev. Lett.* 13 (9 Aug. 1964), pp. 321–323.
- [9] Peter W. Higgs. “Broken Symmetries and the Masses of Gauge Bosons”. In: *Phys. Rev. Lett.* 13 (16 Oct. 1964), pp. 508–509.
- [10] G. S. Guralnik, C. R. Hagen, and T. W. B. Kibble. “Global Conservation Laws and Massless Particles”. In: *Phys. Rev. Lett.* 13 (20 Nov. 1964), pp. 585–587.
- [11] Peter W. Higgs. “Spontaneous Symmetry Breakdown without Massless Bosons”. In: *Phys. Rev.* 145 (4 May 1966), pp. 1156–1163.
- [12] T. W. B. Kibble. “Symmetry Breaking in Non-Abelian Gauge Theories”. In: *Phys. Rev.* 155 (5 Mar. 1967), pp. 1554–1561.
- [13] Georges Aad et al. “Observation of a new particle in the search for the Standard Model Higgs boson with the ATLAS detector at the LHC”. In: *Phys. Lett. B* 716 (2012), pp. 1–29. arXiv: [1207.7214 \[hep-ex\]](#).
- [14] Serguei Chatrchyan et al. “Observation of a New Boson at a Mass of 125 GeV with the CMS Experiment at the LHC”. In: *Phys. Lett. B* 716 (2012), pp. 30–61. arXiv: [1207.7235 \[hep-ex\]](#).
- [15] Michael E. Peskin and Daniel V. Schroeder. *An Introduction to quantum field theory*. Reading, USA: Addison-Wesley, 1995.

- 
- [16] Matthew D. Schwartz. *Quantum Field Theory and the Standard Model*. Cambridge University Press, Mar. 2014.
- [17] Steven Weinberg. *The Quantum theory of fields. Vol. 1: Foundations*. Cambridge University Press, June 2005.
- [18] Steven Weinberg. *The quantum theory of fields. Vol. 2: Modern applications*. Cambridge University Press, Aug. 2013.
- [19] Nicola Cabibbo. “Unitary Symmetry and Leptonic Decays”. In: *Phys. Rev. Lett.* 10 (12 June 1963), pp. 531–533.
- [20] Makoto Kobayashi and Toshihide Maskawa. “CP Violation in the Renormalizable Theory of Weak Interaction”. In: *Prog. Theor. Phys.* 49 (1973), pp. 652–657.
- [21] B. Pontecorvo. “Mesonium and anti-mesonium”. In: *Sov. Phys. JETP* 6 (1957), p. 429.
- [22] B. Pontecorvo. “Inverse beta processes and nonconservation of lepton charge”. In: *Zh. Eksp. Teor. Fiz.* 34 (1957), p. 247.
- [23] Ziro Maki, Masami Nakagawa, and Shoichi Sakata. “Remarks on the unified model of elementary particles”. In: *Prog. Theor. Phys.* 28 (1962), pp. 870–880.
- [24] Raymond Davis, Don S. Harmer, and Kenneth C. Hoffman. “Search for Neutrinos from the Sun”. In: *Phys. Rev. Lett.* 20 (21 May 1968), pp. 1205–1209.
- [25] Y. Fukuda et al. “Evidence for oscillation of atmospheric neutrinos”. In: *Phys. Rev. Lett.* 81 (1998), pp. 1562–1567. arXiv: [hep-ex/9807003](#).
- [26] M. Aker et al. “Improved Upper Limit on the Neutrino Mass from a Direct Kinematic Method by KATRIN”. In: *Phys. Rev. Lett.* 123.22 (2019), p. 221802. arXiv: [1909.06048 \[hep-ex\]](#).
- [27] N. Aghanim et al. “Planck 2018 results. VI. Cosmological parameters”. In: *Astron. Astrophys.* 641 (2020). [Erratum: *Astron. Astrophys.* 652, C4 (2021)], A6. arXiv: [1807.06209 \[astro-ph.CO\]](#).
- [28] Michelle J. Dolinski, Alan W. P. Poon, and Werner Rodejohann. “Neutrinoless Double-Beta Decay: Status and Prospects”. In: *Ann. Rev. Nucl. Part. Sci.* 69 (2019), pp. 219–251. arXiv: [1902.04097 \[nucl-ex\]](#).
- [29] Ivan Esteban et al. “The fate of hints: updated global analysis of three-flavor neutrino oscillations”. In: *JHEP* 09 (2020), p. 178. arXiv: [2007.14792 \[hep-ph\]](#).
- [30] B. Abi et al. *The DUNE Far Detector Interim Design Report Volume 1: Physics, Technology and Strategies*. arXiv: [1807.10334 \[physics.ins-det\]](#).
- [31] Stefano Dell’Oro et al. “Neutrinoless double beta decay: 2015 review”. In: *Adv. High Energy Phys.* 2016 (2016), p. 2162659. arXiv: [1601.07512 \[hep-ph\]](#).
- [32] Steven Weinberg. “Baryon and Lepton Nonconserving Processes”. In: *Phys. Rev. Lett.* 43 (1979), pp. 1566–1570.
- [33] Peter Minkowski. “ $\mu \rightarrow e\gamma$  at a Rate of One Out of  $10^9$  Muon Decays?” In: *Phys. Lett. B* 67 (1977), pp. 421–428.
- [34] Rabindra N. Mohapatra and Goran Senjanović. “Neutrino Mass and Spontaneous Parity Nonconservation”. In: *Phys. Rev. Lett.* 44 (14 Apr. 1980), pp. 912–915.
- [35] Tsutomu Yanagida. “Horizontal Symmetry and Masses of Neutrinos”. In: *Conf. Proc.* C7902131 (1979), pp. 95–99.
- [36] M. Fukugita and T. Yanagida. “Baryogenesis Without Grand Unification”. In: *Phys. Lett. B* 174 (1986), pp. 45–47.

- 
- [37] Sacha Davidson, Enrico Nardi, and Yosef Nir. “Leptogenesis”. In: *Phys. Rept.* 466 (2008), pp. 105–177. arXiv: [0802.2962 \[hep-ph\]](#).
- [38] J. Schechter and J. W. F. Valle. “Neutrino Masses in SU(2) x U(1) Theories”. In: *Phys. Rev. D* 22 (1980), p. 2227.
- [39] George Lazarides, Q. Shafi, and C. Wetterich. “Proton Lifetime and Fermion Masses in an SO(10) Model”. In: *Nucl. Phys. B* 181 (1981), pp. 287–300.
- [40] Robert Foot et al. “Seesaw Neutrino Masses Induced by a Triplet of Leptons”. In: *Z. Phys. C* 44 (1989), p. 441.
- [41] Ernest Ma. “Pathways to naturally small neutrino masses”. In: *Phys. Rev. Lett.* 81 (1998), pp. 1171–1174. arXiv: [hep-ph/9805219](#).
- [42] Yi Cai et al. “From the trees to the forest: a review of radiative neutrino mass models”. In: *Front. in Phys.* 5 (2017), p. 63. arXiv: [1706.08524 \[hep-ph\]](#).
- [43] Gianfranco Bertone and Dan Hooper. “History of dark matter”. In: *Rev. Mod. Phys.* 90.4 (2018), p. 045002. arXiv: [1605.04909 \[astro-ph.CO\]](#).
- [44] Gianfranco Bertone, Dan Hooper, and Joseph Silk. “Particle dark matter: Evidence, candidates and constraints”. In: *Phys. Rept.* 405 (2005), pp. 279–390. arXiv: [hep-ph/0404175](#).
- [45] C. Alcock et al. “The MACHO project: Microlensing results from 5.7 years of LMC observations”. In: *Astrophys. J.* 542 (2000), pp. 281–307. arXiv: [astro-ph/0001272](#).
- [46] L. Wyrzykowski et al. “The OGLE view of microlensing towards the Magellanic Clouds - IV. OGLE-III SMC data and final conclusions on MACHOs”. In: *Monthly Notices of the Royal Astronomical Society* 416.4 (Aug. 2011), pp. 2949–2961.
- [47] Bernard Carr and Florian Kuhnel. “Primordial Black Holes as Dark Matter Candidates”. In: *Les Houches summer school on Dark Matter*. Oct. 2021. arXiv: [2110.02821 \[astro-ph.CO\]](#).
- [48] F. Zwicky. “Die Rotverschiebung von extragalaktischen Nebeln”. In: *Helv. Phys. Acta* 6 (1933), pp. 110–127.
- [49] Vera C. Rubin and W. Kent Ford Jr. “Rotation of the Andromeda Nebula from a Spectroscopic Survey of Emission Regions”. In: *Astrophys. J.* 159 (1970), pp. 379–403.
- [50] Maxim Markevitch et al. “Direct constraints on the dark matter self-interaction cross-section from the merging galaxy cluster 1E0657-56”. In: *Astrophys. J.* 606 (2004), pp. 819–824. arXiv: [astro-ph/0309303](#).
- [51] Douglas Clowe, Anthony Gonzalez, and Maxim Markevitch. “Weak lensing mass reconstruction of the interacting cluster 1E0657-558: Direct evidence for the existence of dark matter”. In: *Astrophys. J.* 604 (2004), pp. 596–603. arXiv: [astro-ph/0312273](#).
- [52] N. Aghanim et al. “Planck 2018 results. VI. Cosmological parameters”. In: *Astron. Astrophys.* 641 (2020), A6. arXiv: [1807.06209 \[astro-ph.CO\]](#).
- [53] Matteo Nori et al. “Lyman  $\alpha$  forest and non-linear structure characterization in Fuzzy Dark Matter cosmologies”. In: *Mon. Not. Roy. Astron. Soc.* 482.3 (2019), pp. 3227–3243. arXiv: [1809.09619 \[astro-ph.CO\]](#).
- [54] Scott Tremaine and James E. Gunn. “Dynamical Role of Light Neutral Leptons in Cosmology”. In: *Phys. Rev. Lett.* 42 (6 Feb. 1979), pp. 407–410.

- [55] Lisa Randall, Jakub Scholtz, and James Unwin. “Cores in Dwarf Galaxies from Fermi Repulsion”. In: *Mon. Not. Roy. Astron. Soc.* 467.2 (2017), pp. 1515–1525. arXiv: [1611.04590 \[astro-ph.GA\]](#).
- [56] Vid Iršič et al. “New Constraints on the free-streaming of warm dark matter from intermediate and small scale Lyman- $\alpha$  forest data”. In: *Phys. Rev. D* 96.2 (2017), p. 023522. arXiv: [1702.01764 \[astro-ph.CO\]](#).
- [57] Paolo Gondolo and Graciela Gelmini. “Cosmic abundances of stable particles: Improved analysis”. In: *Nucl. Phys. B* 360 (1991), pp. 145–179.
- [58] Edward W. Kolb and Michael S. Turner. *The Early Universe*. Vol. 69. 1990.
- [59] V. Mukhanov. *Physical Foundations of Cosmology*. Oxford: Cambridge University Press, 2005.
- [60] P. Cushman et al. “Working Group Report: WIMP Dark Matter Direct Detection”. In: *Community Summer Study 2013: Snowmass on the Mississippi*. Oct. 2013. arXiv: [1310.8327 \[hep-ex\]](#).
- [61] Mark W. Goodman and Edward Witten. “Detectability of Certain Dark Matter Candidates”. In: *Phys. Rev. D* 31 (1985). Ed. by M. A. Srednicki, p. 3059.
- [62] E. Aprile et al. “Dark Matter Search Results from a One Ton-Year Exposure of XENON1T”. In: *Phys. Rev. Lett.* 121.11 (2018), p. 111302. arXiv: [1805.12562 \[astro-ph.CO\]](#).
- [63] E. Aprile et al. “Light Dark Matter Search with Ionization Signals in XENON1T”. In: *Phys. Rev. Lett.* 123.25 (2019), p. 251801. arXiv: [1907.11485 \[hep-ex\]](#).
- [64] A. H. Abdelhameed et al. “First results from the CRESST-III low-mass dark matter program”. In: *Phys. Rev. D* 100.10 (2019), p. 102002. arXiv: [1904.00498 \[astro-ph.CO\]](#).
- [65] R. Agnese et al. “First Dark Matter Constraints from a SuperCDMS Single-Charge Sensitive Detector”. In: *Phys. Rev. Lett.* 121.5 (2018). [Erratum: *Phys.Rev.Lett.* 122, 069901 (2019)], p. 051301. arXiv: [1804.10697 \[hep-ex\]](#).
- [66] Orr Abramoff et al. “SENSEI: Direct-Detection Constraints on Sub-GeV Dark Matter from a Shallow Underground Run Using a Prototype Skipper-CCD”. In: *Phys. Rev. Lett.* 122.16 (2019), p. 161801. arXiv: [1901.10478 \[hep-ex\]](#).
- [67] M. G. Aartsen et al. “Search for annihilating dark matter in the Sun with 3 years of IceCube data”. In: *Eur. Phys. J. C* 77.3 (2017). [Erratum: *Eur.Phys.J.C* 79, 214 (2019)], p. 146. arXiv: [1612.05949 \[astro-ph.HE\]](#).
- [68] M. G. Aartsen et al. “Search for Neutrinos from Dark Matter Self-Annihilations in the center of the Milky Way with 3 years of IceCube/DeepCore”. In: *Eur. Phys. J. C* 77.9 (2017), p. 627. arXiv: [1705.08103 \[hep-ex\]](#).
- [69] M. L. Ahnen et al. “Limits to Dark Matter Annihilation Cross-Section from a Combined Analysis of MAGIC and Fermi-LAT Observations of Dwarf Satellite Galaxies”. In: *JCAP* 02 (2016), p. 039. arXiv: [1601.06590 \[astro-ph.HE\]](#).
- [70] Sebastian Hoof, Alex Geringer-Sameth, and Roberto Trotta. “A Global Analysis of Dark Matter Signals from 27 Dwarf Spheroidal Galaxies using 11 Years of Fermi-LAT Observations”. In: *JCAP* 02 (2020), p. 012. arXiv: [1812.06986 \[astro-ph.CO\]](#).
- [71] H. Abdallah et al. “Search for dark matter annihilations towards the inner Galactic halo from 10 years of observations with H.E.S.S.”. In: *Phys. Rev. Lett.* 117.11 (2016), p. 111301. arXiv: [1607.08142 \[astro-ph.HE\]](#).

- 
- [72] Albert M Sirunyan et al. “Search for new physics in final states with a single photon and missing transverse momentum in proton-proton collisions at  $\sqrt{s} = 13$  TeV”. In: *JHEP* 02 (2019), p. 074. arXiv: [1810.00196 \[hep-ex\]](#).
- [73] Georges Aad et al. “Search for dark matter in association with an energetic photon in  $pp$  collisions at  $\sqrt{s} = 13$  TeV with the ATLAS detector”. In: *JHEP* 02 (2021), p. 226. arXiv: [2011.05259 \[hep-ex\]](#).
- [74] G. Aad et al. “Search for new phenomena in events with an energetic jet and missing transverse momentum in  $pp$  collisions at  $\sqrt{s} = 13$  TeV with the ATLAS detector”. In: *Phys. Rev. D* 103 (11 June 2021), p. 112006.
- [75] Armen Tumasyan et al. “Search for new particles in events with energetic jets and large missing transverse momentum in proton-proton collisions at  $\sqrt{s} = 13$  TeV”. In: *JHEP* 11 (2021), p. 153. arXiv: [2107.13021 \[hep-ex\]](#).
- [76] Lawrence J. Hall et al. “Freeze-In Production of FIMP Dark Matter”. In: *JHEP* 03 (2010), p. 080. arXiv: [0911.1120 \[hep-ph\]](#).
- [77] Mark Hindmarsh, Russell Kirk, and Stephen M. West. “Dark Matter from Decaying Topological Defects”. In: *JCAP* 03 (2014), p. 037. arXiv: [1311.1637 \[hep-ph\]](#).
- [78] Yonit Hochberg et al. “Mechanism for Thermal Relic Dark Matter of Strongly Interacting Massive Particles”. In: *Phys. Rev. Lett.* 113 (2014), p. 171301. arXiv: [1402.5143 \[hep-ph\]](#).
- [79] Duccio Pappadopulo, Joshua T. Ruderman, and Gabriele Trevisan. “Dark matter freeze-out in a nonrelativistic sector”. In: *Phys. Rev. D* 94.3 (2016), p. 035005. arXiv: [1602.04219 \[hep-ph\]](#).
- [80] Scott Dodelson and Lawrence M. Widrow. “Sterile-neutrinos as dark matter”. In: *Phys. Rev. Lett.* 72 (1994), pp. 17–20. arXiv: [hep-ph/9303287 \[hep-ph\]](#).
- [81] M. Drewes et al. “A White Paper on keV Sterile Neutrino Dark Matter”. In: *JCAP* 1701.01 (2017), p. 025. arXiv: [1602.04816 \[hep-ph\]](#).
- [82] A. Boyarsky et al. “Sterile neutrino Dark Matter”. In: *Prog. Part. Nucl. Phys.* 104 (2019), pp. 1–45. arXiv: [1807.07938 \[hep-ph\]](#).
- [83] Kevork Abazajian, George M. Fuller, and Mitesh Patel. “Sterile neutrino hot, warm, and cold dark matter”. In: *Phys. Rev. D* 64 (2001), p. 023501. arXiv: [astro-ph/0101524 \[astro-ph\]](#).
- [84] Mona Dentler et al. “Updated Global Analysis of Neutrino Oscillations in the Presence of eV-Scale Sterile Neutrinos”. In: *JHEP* 08 (2018), p. 010. arXiv: [1803.10661 \[hep-ph\]](#).
- [85] P. Abratenko et al. *Search for an anomalous excess of charged-current  $\nu_e$  interactions without pions in the final state with the MicroBooNE experiment.* arXiv: [2110.14065 \[hep-ex\]](#).
- [86] R. Shrock. “Decay  $L^0 \rightarrow \nu_l \gamma$  in gauge theories of weak and electromagnetic interactions”. In: *Phys. Rev. D* 9 (1974), pp. 743–748.
- [87] Palash B. Pal and Lincoln Wolfenstein. “Radiative Decays of Massive Neutrinos”. In: *Phys. Rev. D* 25 (1982), p. 766.
- [88] Kerstin Perez et al. “Almost closing the  $\nu$ MSM sterile neutrino dark matter window with NuSTAR”. In: *Phys. Rev. D* 95.12 (2017), p. 123002. arXiv: [1609.00667 \[astro-ph.HE\]](#).

- [89] Kevork Abazajian, George M. Fuller, and Wallace H. Tucker. “Direct detection of warm dark matter in the X-ray”. In: *Astrophys. J.* 562 (2001), pp. 593–604. arXiv: [astro-ph/0106002](#).
- [90] Alexey Boyarsky et al. “Constraints on sterile neutrino as a dark matter candidate from the diffuse x-ray background”. In: *Mon. Not. Roy. Astron. Soc.* 370 (2006), pp. 213–218. arXiv: [astro-ph/0512509](#).
- [91] O. Urban et al. “A Suzaku Search for Dark Matter Emission Lines in the X-ray Brightest Galaxy Clusters”. In: *Mon. Not. Roy. Astron. Soc.* 451.3 (2015), pp. 2447–2461. arXiv: [1411.0050 \[astro-ph.CO\]](#).
- [92] Kenny C. Y. Ng et al. “Improved Limits on Sterile Neutrino Dark Matter using Full-Sky Fermi Gamma-Ray Burst Monitor Data”. In: *Phys. Rev. D* 92.4 (2015), p. 043503. arXiv: [1504.04027 \[astro-ph.CO\]](#).
- [93] Esra Bulbul et al. “Detection of An Unidentified Emission Line in the Stacked X-ray spectrum of Galaxy Clusters”. In: *Astrophys. J.* 789 (2014), p. 13. arXiv: [1402.2301 \[astro-ph.CO\]](#).
- [94] Alexey Boyarsky et al. “Unidentified Line in X-Ray Spectra of the Andromeda Galaxy and Perseus Galaxy Cluster”. In: *Phys. Rev. Lett.* 113 (2014), p. 251301. arXiv: [1402.4119 \[astro-ph.CO\]](#).
- [95] Alexey Boyarsky et al. “Checking the Dark Matter Origin of a 3.53 keV Line with the Milky Way Center”. In: *Phys. Rev. Lett.* 115 (2015), p. 161301. arXiv: [1408.2503 \[astro-ph.CO\]](#).
- [96] Tesla E. Jeltema and Stefano Profumo. “Discovery of a 3.5 keV line in the Galactic Centre and a critical look at the origin of the line across astronomical targets”. In: *Mon. Not. Roy. Astron. Soc.* 450.2 (2015), pp. 2143–2152. arXiv: [1408.1699 \[astro-ph.HE\]](#).
- [97] A. Boyarsky et al. *Comment on the paper “Dark matter searches going bananas: the contribution of Potassium (and Chlorine) to the 3.5 keV line” by T. Jeltema and S. Profumo*. arXiv: [1408.4388 \[astro-ph.CO\]](#).
- [98] Esra Bulbul et al. *Comment on “Dark matter searches going bananas: the contribution of Potassium (and Chlorine) to the 3.5 keV line”*. arXiv: [1409.4143 \[astro-ph.HE\]](#).
- [99] Aurel Schneider. “Astrophysical constraints on resonantly produced sterile neutrino dark matter”. In: *JCAP* 04 (2016), p. 059. arXiv: [1601.07553 \[astro-ph.CO\]](#).
- [100] Xiang-Dong Shi and George M. Fuller. “A New dark matter candidate: Nonthermal sterile neutrinos”. In: *Phys. Rev. Lett.* 82 (1999), pp. 2832–2835. arXiv: [astro-ph/9810076 \[astro-ph\]](#).
- [101] L. Wolfenstein. “Neutrino Oscillations in Matter”. In: *Phys. Rev. D* 17 (1978), pp. 2369–2374.
- [102] S. P. Mikheyev and A. Yu. Smirnov. “Resonance Amplification of Oscillations in Matter and Spectroscopy of Solar Neutrinos”. In: *Sov. J. Nucl. Phys.* 42 (1985), pp. 913–917.
- [103] Ernest Ma. “Verifiable radiative seesaw mechanism of neutrino mass and dark matter”. In: *Phys. Rev. D* 73 (2006), p. 077301. arXiv: [hep-ph/0601225 \[hep-ph\]](#).
- [104] Takehiko Asaka, Steve Blanchet, and Mikhail Shaposhnikov. “The nuMSM, dark matter and neutrino masses”. In: *Phys. Lett.* B631 (2005), pp. 151–156. arXiv: [hep-ph/0503065 \[hep-ph\]](#).



- 
- [105] Takehiko Asaka and Mikhail Shaposhnikov. “The nuMSM, dark matter and baryon asymmetry of the universe”. In: *Phys. Lett. B* 620 (2005), pp. 17–26. arXiv: [hep-ph/0505013](#) [[hep-ph](#)].
- [106] Louis Lello and Daniel Boyanovsky. “Cosmological Implications of Light Sterile Neutrinos produced after the QCD Phase Transition”. In: *Phys. Rev. D* 91 (2015), p. 063502. arXiv: [1411.2690](#) [[astro-ph.CO](#)].
- [107] F. Bezrukov, D. Gorbunov, and M. Shaposhnikov. “On initial conditions for the Hot Big Bang”. In: *JCAP* 06 (2009), p. 029. arXiv: [0812.3622](#) [[hep-ph](#)].
- [108] Louis Lello, Daniel Boyanovsky, and Robert D. Pisarski. “Production of heavy sterile neutrinos from vector boson decay at electroweak temperatures”. In: *Phys. Rev. D* 95.4 (2017), p. 043524. arXiv: [1609.07647](#) [[hep-ph](#)].
- [109] Kalliopi Petraki and Alexander Kusenko. “Dark-matter sterile neutrinos in models with a gauge singlet in the Higgs sector”. In: *Phys. Rev. D* 77 (2008), p. 065014. arXiv: [0711.4646](#) [[hep-ph](#)].
- [110] Bibhushan Shakya. “Sterile Neutrino Dark Matter from Freeze-In”. In: *Mod. Phys. Lett. A* 31.06 (2016), p. 1630005. arXiv: [1512.02751](#) [[hep-ph](#)].
- [111] Johannes König, Alexander Merle, and Maximilian Tetzlauer. “keV Sterile Neutrino Dark Matter from Singlet Scalar Decays: The Most General Case”. In: *JCAP* 1611 (2016), p. 038. arXiv: [1609.01289](#) [[hep-ph](#)].
- [112] Adisorn Adulpravitchai and Michael A. Schmidt. “Sterile Neutrino Dark Matter Production in the Neutrino-phillic Two Higgs Doublet Model”. In: *JHEP* 12 (2015), p. 023. arXiv: [1507.05694](#) [[hep-ph](#)].
- [113] Marco Drewes and Jin U Kang. “Sterile neutrino Dark Matter production from scalar decay in a thermal bath”. In: *JHEP* 05 (2016), p. 051. arXiv: [1510.05646](#) [[hep-ph](#)].
- [114] A. D. Dolgov and S. H. Hansen. “Massive sterile neutrinos as warm dark matter”. In: *Astropart. Phys.* 16 (2002), pp. 339–344. arXiv: [hep-ph/0009083](#).
- [115] J. R. Bond, G. Efstathiou, and J. Silk. “Massive Neutrinos and the Large Scale Structure of the Universe”. In: *Phys. Rev. Lett.* 45 (1980). Ed. by M. A. Srednicki, pp. 1980–1984.
- [116] R. J. Crewther et al. “Chiral Estimate of the Electric Dipole Moment of the Neutron in Quantum Chromodynamics”. In: *Phys. Lett. B* 88 (1979). [Erratum: *Phys.Lett.B* 91, 487 (1980)], p. 123.
- [117] Maxim Pospelov and Adam Ritz. “Electric dipole moments as probes of new physics”. In: *Annals Phys.* 318 (2005), pp. 119–169. arXiv: [hep-ph/0504231](#).
- [118] C. Abel et al. “Measurement of the permanent electric dipole moment of the neutron”. In: *Phys. Rev. Lett.* 124.8 (2020), p. 081803. arXiv: [2001.11966](#) [[hep-ex](#)].
- [119] R. D. Peccei and Helen R. Quinn. “CP Conservation in the Presence of Instantons”. In: *Phys. Rev. Lett.* 38 (1977), pp. 1440–1443.
- [120] R. D. Peccei and Helen R. Quinn. “Constraints Imposed by CP Conservation in the Presence of Instantons”. In: *Phys. Rev. D* 16 (1977), pp. 1791–1797.
- [121] R. D. Peccei. “The Strong CP problem and axions”. In: *Lect. Notes Phys.* 741 (2008). Ed. by Markus Kuster, Georg Raffelt, and Berta Beltran, pp. 3–17. arXiv: [hep-ph/0607268](#).
- [122] Frank Wilczek. “Problem of Strong  $P$  and  $T$  Invariance in the Presence of Instantons”. In: *Phys. Rev. Lett.* 40 (1978), pp. 279–282.

- [123] Steven Weinberg. “A New Light Boson?” In: *Phys. Rev. Lett.* 40 (1978), pp. 223–226.
- [124] David J. E. Marsh. “Axion Cosmology”. In: *Phys. Rept.* 643 (2016), pp. 1–79. arXiv: [1510.07633 \[astro-ph.CO\]](#).
- [125] Martin Bauer, Matthias Neubert, and Andrea Thamm. “Collider Probes of Axion-Like Particles”. In: *JHEP* 12 (2017), p. 044. arXiv: [1708.00443 \[hep-ph\]](#).
- [126] Klaus Ehret et al. “New ALPS Results on Hidden-Sector Lightweights”. In: *Phys. Lett. B* 689 (2010), pp. 149–155. arXiv: [1004.1313 \[hep-ex\]](#).
- [127] S. Andriamonje et al. “An Improved limit on the axion-photon coupling from the CAST experiment”. In: *JCAP* 04 (2007), p. 010. arXiv: [hep-ex/0702006](#).
- [128] E. Aprile et al. “Excess electronic recoil events in XENON1T”. In: *Phys. Rev. D* 102.7 (2020), p. 072004. arXiv: [2006.09721 \[hep-ex\]](#).
- [129] Christina Gao et al. “Reexamining the Solar Axion Explanation for the XENON1T Excess”. In: *Phys. Rev. Lett.* 125.13 (2020), p. 131806. arXiv: [2006.14598 \[hep-ph\]](#).
- [130] Luca Di Luzio et al. “Solar axions cannot explain the XENON1T excess”. In: *Phys. Rev. Lett.* 125.13 (2020), p. 131804. arXiv: [2006.12487 \[hep-ph\]](#).
- [131] Pierluca Carenza et al. “Constraints on the coupling with photons of heavy axion-like-particles from Globular Clusters”. In: *Phys. Lett. B* 809 (2020), p. 135709. arXiv: [2004.08399 \[hep-ph\]](#).
- [132] P. Sikivie. “Experimental Tests of the Invisible Axion”. In: *Phys. Rev. Lett.* 51 (1983). Ed. by M. A. Srednicki. [Erratum: *Phys.Rev.Lett.* 52, 695 (1984)], pp. 1415–1417.
- [133] Renée Hlozek et al. “A search for ultralight axions using precision cosmological data”. In: *Phys. Rev. D* 91.10 (2015), p. 103512. arXiv: [1410.2896 \[astro-ph.CO\]](#).
- [134] Vivian Poulin et al. “Cosmological implications of ultralight axionlike fields”. In: *Phys. Rev. D* 98.8 (2018), p. 083525. arXiv: [1806.10608 \[astro-ph.CO\]](#).
- [135] Olivier Wantz and E.P.S. Shellard. “Axion Cosmology Revisited”. In: *Phys. Rev. D* 82 (2010), p. 123508. arXiv: [0910.1066 \[astro-ph.CO\]](#).
- [136] Paola Arias et al. “WISPy Cold Dark Matter”. In: *JCAP* 06 (2012), p. 013. arXiv: [1201.5902 \[hep-ph\]](#).
- [137] Steven Weinberg. *Gravitation and Cosmology: Principles and Applications of the General Theory of Relativity*. New York: John Wiley and Sons, 1972.
- [138] P.A. Zyla et al. “Review of Particle Physics”. In: *PTEP* 2020.8 (2020), p. 083C01.
- [139] Edward R. Harrison. “Fluctuations at the threshold of classical cosmology”. In: *Phys. Rev. D* 1 (1970), pp. 2726–2730.
- [140] Ya. B. Zeldovich. “A Hypothesis, unifying the structure and the entropy of the universe”. In: *Mon. Not. Roy. Astron. Soc.* 160 (1972), 1P–3P.
- [141] Max Tegmark et al. “The 3-D power spectrum of galaxies from the SDSS”. In: *Astrophys. J.* 606 (2004), pp. 702–740. arXiv: [astro-ph/0310725](#).
- [142] Héctor Gil-Marrin et al. “The clustering of galaxies in the SDSS-III Baryon Oscillation Spectroscopic Survey: RSD measurement from the power spectrum and bispectrum of the DR12 BOSS galaxies”. In: *Mon. Not. Roy. Astron. Soc.* 465.2 (2017), pp. 1757–1788. arXiv: [1606.00439 \[astro-ph.CO\]](#).

- 
- [143] Chiaki Hikage et al. “Cosmology from cosmic shear power spectra with Subaru Hyper Suprime-Cam first-year data”. In: *Publ. Astron. Soc. Jap.* 71.2 (2019), p. 43. arXiv: [1809.09148 \[astro-ph.CO\]](#).
- [144] M. Gatti et al. “Dark energy survey year 3 results: weak lensing shape catalogue”. In: *Mon. Not. Roy. Astron. Soc.* 504.3 (2021), pp. 4312–4336. arXiv: [2011.03408 \[astro-ph.CO\]](#).
- [145] Julien Lesgourgues and Thomas Tram. “The Cosmic Linear Anisotropy Solving System (CLASS) IV: efficient implementation of non-cold relics”. In: *JCAP* 1109 (2011), p. 032. arXiv: [1104.2935 \[astro-ph.CO\]](#).
- [146] Julien Lesgourgues. *The Cosmic Linear Anisotropy Solving System (CLASS) I: Overview*. arXiv: [1104.2932 \[astro-ph.IM\]](#).
- [147] Max Tegmark and Matias Zaldarriaga. “Separating the early universe from the late universe: Cosmological parameter estimation beyond the black box”. In: *Phys. Rev. D* 66 (2002), p. 103508. arXiv: [astro-ph/0207047](#).
- [148] Matteo Viel et al. “Constraining warm dark matter candidates including sterile neutrinos and light gravitinos with WMAP and the Lyman-alpha forest”. In: *Phys. Rev. D* 71 (2005), p. 063534. arXiv: [astro-ph/0501562 \[astro-ph\]](#).
- [149] Stephane Colombi, Scott Dodelson, and Lawrence M. Widrow. “Large scale structure tests of warm dark matter”. In: *Astrophys. J.* 458 (1996), p. 1. arXiv: [astro-ph/9505029](#).
- [150] Takeshi Kobayashi et al. “Lyman- $\alpha$  constraints on ultralight scalar dark matter: Implications for the early and late universe”. In: *Phys. Rev. D* 96.12 (2017), p. 123514. arXiv: [1708.00015 \[astro-ph.CO\]](#).
- [151] Riccardo Murgia et al. ““Non-cold” dark matter at small scales: a general approach”. In: *JCAP* 11 (2017), p. 046. arXiv: [1704.07838 \[astro-ph.CO\]](#).
- [152] Alexey Boyarsky et al. “Lyman-alpha constraints on warm and on warm-plus-cold dark matter models”. In: *JCAP* 0905 (2009), p. 012. arXiv: [0812.0010 \[astro-ph\]](#).
- [153] Andrew J. Benson et al. “Dark matter halo merger histories beyond cold dark matter – I. Methods and application to warm dark matter”. In: *Monthly Notices of the Royal Astronomical Society* 428.2 (Nov. 2012), pp. 1774–1789.
- [154] Aurel Schneider. “Structure formation with suppressed small-scale perturbations”. In: *Mon. Not. Roy. Astron. Soc.* 451.3 (2015), pp. 3117–3130. arXiv: [1412.2133 \[astro-ph.CO\]](#).
- [155] Aurel Schneider, Robert E. Smith, and Darren Reed. “Halo Mass Function and the Free Streaming Scale”. In: *Mon. Not. Roy. Astron. Soc.* 433 (2013), p. 1573. arXiv: [1303.0839 \[astro-ph.CO\]](#).
- [156] Anatoly A. Klypin et al. “Where are the missing Galactic satellites?” In: *Astrophys. J.* 522 (1999), pp. 82–92. arXiv: [astro-ph/9901240](#).
- [157] Ben Moore et al. “Cold collapse and the core catastrophe”. In: *Mon. Not. Roy. Astron. Soc.* 310 (1999), pp. 1147–1152. arXiv: [astro-ph/9903164](#).
- [158] A.M. Nierenberg et al. “The Cosmic Evolution of Faint Satellite Galaxies as a Test of Galaxy Formation and the Nature of Dark Matter”. In: *Astrophys. J.* 772 (2013), p. 146. arXiv: [1302.3243 \[astro-ph.CO\]](#).
- [159] Daisuke Homma et al. “Searches for New Milky Way Satellites from the First Two Years of Data of the Subaru/Hyper Suprime-Cam Survey: Discovery of Cetus~III”. In: *Publ. Astron. Soc. Jap.* 70 (2018), p. 18. arXiv: [1704.05977 \[astro-ph.GA\]](#).

- [160] Daisuke Homma et al. “Boötes. IV. A new Milky Way satellite discovered in the Subaru Hyper Suprime-Cam Survey and implications for the missing satellite problem”. In: *Publ. Astron. Soc. Jap.* 71.5 (2019). arXiv: [1906.07332 \[astro-ph.GA\]](#).
- [161] Stacy Y. Kim, Annika H. G. Peter, and Jonathan R. Hargis. “Missing Satellites Problem: Completeness Corrections to the Number of Satellite Galaxies in the Milky Way are Consistent with Cold Dark Matter Predictions”. In: *Phys. Rev. Lett.* 121.21 (2018), p. 211302. arXiv: [1711.06267 \[astro-ph.CO\]](#).
- [162] William H. Press and Paul Schechter. “Formation of galaxies and clusters of galaxies by selfsimilar gravitational condensation”. In: *Astrophys. J.* 187 (1974), pp. 425–438.
- [163] Cedric G. Lacey and Shaun Cole. “Merger rates in hierarchical models of galaxy formation”. In: *Mon. Not. Roy. Astron. Soc.* 262 (1993), pp. 627–649.
- [164] Emil Polisensky and Massimo Ricotti. “Constraints on the Dark Matter Particle Mass from the Number of Milky Way Satellites”. In: *Phys. Rev. D* 83 (2011), p. 043506. arXiv: [1004.1459 \[astro-ph.CO\]](#).
- [165] Christopher P. Ahn et al. “The Tenth Data Release of the Sloan Digital Sky Survey: First Spectroscopic Data from the SDSS-III Apache Point Observatory Galactic Evolution Experiment”. In: *Astrophys. J. Suppl.* 211 (2014), p. 17. arXiv: [1307.7735 \[astro-ph.IM\]](#).
- [166] Noam I. Libeskind et al. “The Distribution of satellite galaxies: The Great pancake”. In: *Mon. Not. Roy. Astron. Soc.* 363 (2005), pp. 146–152. arXiv: [astro-ph/0503400](#).
- [167] A. Drlica-Wagner et al. “Milky Way Satellite Census. I. The Observational Selection Function for Milky Way Satellites in DES Y3 and Pan-STARRS DR1”. In: *Astrophys. J.* 893 (2020), p. 1. arXiv: [1912.03302 \[astro-ph.GA\]](#).
- [168] Oliver Newton et al. “Constraints on the properties of warm dark matter using the satellite galaxies of the Milky Way”. In: *JCAP* 08 (2021), p. 062. arXiv: [2011.08865 \[astro-ph.CO\]](#).
- [169] Oliver Newton et al. “The total satellite population of the Milky Way”. In: *Monthly Notices of the Royal Astronomical Society* 479.3 (May 2018), pp. 2853–2870. eprint: <https://academic.oup.com/mnras/article-pdf/479/3/2853/25149561/sty1085.pdf>.
- [170] Inc. Wolfram Research. *Mathematica, Version 11+12*. Champaign, IL, 2021.
- [171] Guido Van Rossum and Fred L Drake Jr. *Python reference manual*. Centrum voor Wiskunde en Informatica Amsterdam, 1995.
- [172] Guido Van Rossum and Fred L. Drake. *Python 3 Reference Manual*. Scotts Valley, CA: CreateSpace, 2009.
- [173] Charles R. Harris et al. “Array programming with NumPy”. In: *Nature* 585.7825 (2020), pp. 357–362. arXiv: [2006.10256 \[cs.MS\]](#).
- [174] John D. Hunter. “Matplotlib: A 2D Graphics Environment”. In: *Comput. Sci. Eng.* 9.3 (2007), pp. 90–95.
- [175] Aaron Meurer et al. “SymPy: symbolic computing in Python”. In: *PeerJ Comput. Sci.* 3 (2017), e103.
- [176] Pauli Virtanen et al. “SciPy 1.0—Fundamental Algorithms for Scientific Computing in Python”. In: *Nature Meth.* 17 (2020), p. 261. arXiv: [1907.10121 \[cs.MS\]](#).

- 
- [177] Fernando Perez and Brian E. Granger. “IPython: A System for Interactive Scientific Computing”. In: *Comput. Sci. Eng.* 9.3 (2007), pp. 21–29.
- [178] Joshua Ellis. “TikZ-Feynman: Feynman diagrams with TikZ”. In: *Comput. Phys. Commun.* 210 (2017), pp. 103–123. arXiv: [1601.05437 \[hep-ph\]](#).
- [179] Wes McKinney. “Data Structures for Statistical Computing in Python”. In: *Proceedings of the 9th Python in Science Conference*. Ed. by Stéfan van der Walt and Jarrod Millman. 2010, pp. 56–61.
- [180] Rabindra N. Mohapatra and Goran Senjanovi ć. “Neutrino Mass and Spontaneous Parity Nonconservation”. In: *Phys. Rev. Lett.* 44 (14 Apr. 1980), pp. 912–915.
- [181] Murray Gell-Mann, Pierre Ramond, and Richard Slansky. “Complex Spinors and Unified Theories”. In: *Conf. Proc.* C790927 (1979), pp. 315–321. arXiv: [1306.4669 \[hep-th\]](#).
- [182] Emiliano Molinaro, Carlos E. Yaguna, and Oscar Zapata. “FIMP realization of the scotogenic model”. In: *JCAP* 1407 (2014), p. 015. arXiv: [1405.1259 \[hep-ph\]](#).
- [183] Manfred Lindner et al. “Fermionic WIMPs and vacuum stability in the scotogenic model”. In: *Phys. Rev.* D94.11 (2016), p. 115027. arXiv: [1608.00577 \[hep-ph\]](#).
- [184] Kresimir Kumericki, Ivica Picek, and Branimir Radovic. “TeV-scale Seesaw with Quintuplet Fermions”. In: *Phys. Rev.* D86 (2012), p. 013006. arXiv: [1204.6599 \[hep-ph\]](#).
- [185] Vedran Brdar, Ivica Picek, and Branimir Radovic. “Radiative Neutrino Mass with Scotogenic Scalar Triplet”. In: *Phys. Lett.* B728 (2014), pp. 198–201. arXiv: [1310.3183 \[hep-ph\]](#).
- [186] Ivania M. Ávila et al. “Phenomenology of scotogenic scalar dark matter”. In: *Eur. Phys. J. C* 80.10 (2020), p. 908. arXiv: [1910.08422 \[hep-ph\]](#).
- [187] Shoichi Kashiwase and Daijiro Suematsu. “Baryon number asymmetry and dark matter in the neutrino mass model with an inert doublet”. In: *Phys. Rev.* D86 (2012), p. 053001. arXiv: [1207.2594 \[hep-ph\]](#).
- [188] Daijiro Suematsu. “Thermal Leptogenesis in a TeV Scale Model for Neutrino Masses”. In: *Eur. Phys. J.* C72 (2012), p. 1951. arXiv: [1103.0857 \[hep-ph\]](#).
- [189] Thomas Hugle, Moritz Platscher, and Kai Schmitz. “Low-Scale Leptogenesis in the Scotogenic Neutrino Mass Model”. In: *Phys. Rev. D* 98.2 (2018), p. 023020. arXiv: [1804.09660 \[hep-ph\]](#).
- [190] J. Racker. “Mass bounds for baryogenesis from particle decays and the inert doublet model”. In: *JCAP* 1403 (2014), p. 025. arXiv: [1308.1840 \[hep-ph\]](#).
- [191] Devabrat Mahanta and Debasish Borah. “Fermion Dark Matter with  $N_2$  Leptogenesis in Minimal Scotogenic Model”. In: *JCAP* 1911.11 (2019), p. 021. arXiv: [1906.03577 \[hep-ph\]](#).
- [192] Debasish Borah, P. S. Bhupal Dev, and Abhass Kumar. “TeV scale leptogenesis, inflaton dark matter and neutrino mass in a scotogenic model”. In: *Phys. Rev.* D99.5 (2019), p. 055012. arXiv: [1810.03645 \[hep-ph\]](#).
- [193] Devabrat Mahanta and Debasish Borah. “TeV Scale Leptogenesis with Dark Matter in Non-standard Cosmology”. In: *JCAP* 04.04 (2020), p. 032. arXiv: [1912.09726 \[hep-ph\]](#).
- [194] Evgeny K. Akhmedov, V. A. Rubakov, and A. Yu. Smirnov. “Baryogenesis via neutrino oscillations”. In: *Phys. Rev. Lett.* 81 (1998), pp. 1359–1362. arXiv: [hep-ph/9803255 \[hep-ph\]](#).

- [195] Thomas Hambye and Daniele Teresi. “Higgs doublet decay as the origin of the baryon asymmetry”. In: *Phys. Rev. Lett.* 117.9 (2016), p. 091801. arXiv: [1606.00017 \[hep-ph\]](#).
- [196] Admir Greljo and Ben A. Stefanek. “Third family quark–lepton unification at the TeV scale”. In: *Phys. Lett. B* 782 (2018), pp. 131–138. arXiv: [1802.04274 \[hep-ph\]](#).
- [197] Dario Buttazzo et al. “B-physics anomalies: a guide to combined explanations”. In: *JHEP* 11 (2017), p. 044. arXiv: [1706.07808 \[hep-ph\]](#).
- [198] Roel Aaij et al. “Search for lepton-universality violation in  $B^+ \rightarrow K^+ \ell^+ \ell^-$  decays”. In: *Phys. Rev. Lett.* 122.19 (2019), p. 191801. arXiv: [1903.09252 \[hep-ex\]](#).
- [199] A. Abdesselam et al. “Test of Lepton-Flavor Universality in  $B \rightarrow K^* \ell^+ \ell^-$  Decays at Belle”. In: *Phys. Rev. Lett.* 126.16 (2021), p. 161801. arXiv: [1904.02440 \[hep-ex\]](#).
- [200] A. Abdesselam et al. *Measurement of  $\mathcal{R}(D)$  and  $\mathcal{R}(D^*)$  with a semileptonic tagging method*. arXiv: [1904.08794 \[hep-ex\]](#).
- [201] R. N. Mohapatra and J. W. F. Valle. “Neutrino mass and baryon-number nonconservation in superstring models”. In: *Phys. Rev. D* 34 (5 Sept. 1986), p. 1642.
- [202] Rabindra N. Mohapatra. “Mechanism for understanding small neutrino mass in superstring theories”. In: *Phys. Rev. Lett.* 56 (6 Feb. 1986), p. 561.
- [203] Asmaa Abada et al. “Neutrino masses, leptogenesis and dark matter from small lepton number violation?” In: *JCAP* 12 (2017), p. 024. arXiv: [1709.00415 \[hep-ph\]](#).
- [204] Masahiro Kawasaki et al. “Revisiting Big-Bang Nucleosynthesis Constraints on Long-Lived Decaying Particles”. In: *Phys. Rev.* D97.2 (2018), p. 023502. arXiv: [1709.01211 \[hep-ph\]](#).
- [205] G. C. Branco et al. “Theory and phenomenology of two-Higgs-doublet models”. In: *Phys. Rept.* 516 (2012), pp. 1–102. arXiv: [1106.0034 \[hep-ph\]](#).
- [206] Takashi Toma and Avelino Vicente. “Lepton Flavor Violation in the Scotogenic Model”. In: *JHEP* 01 (2014), p. 160. arXiv: [1312.2840](#).
- [207] Alexander Merle and Moritz Platscher. “Running of radiative neutrino masses: the scotogenic model — revisited”. In: *JHEP* 11 (2015), p. 148. arXiv: [1507.06314 \[hep-ph\]](#).
- [208] J. A. Casas and A. Ibarra. “Oscillating neutrinos and muon  $\rightarrow e, \gamma$ ”. In: *Nucl. Phys.* B618 (2001), pp. 171–204. arXiv: [hep-ph/0103065 \[hep-ph\]](#).
- [209] C. Patrignani et al. “Review of Particle Physics”. In: *Chin. Phys.* C40.10 (2016), p. 100001.
- [210] Ivan Esteban et al. “Global analysis of three-flavour neutrino oscillations: synergies and tensions in the determination of  $\theta_{23}$ ,  $\delta_{CP}$ , and the mass ordering”. In: *JHEP* 01 (2019), p. 106. arXiv: [1811.05487 \[hep-ph\]](#).
- [211] Amine Ahriche, Adil Jueid, and Salah Nasri. “Radiative neutrino mass and Majorana dark matter within an inert Higgs doublet model”. In: *Phys. Rev.* D97.9 (2018), p. 095012. arXiv: [1710.03824 \[hep-ph\]](#).
- [212] Andre G. Hessler et al. “Probing the scotogenic FIMP at the LHC”. In: *JHEP* 01 (2017), p. 100. arXiv: [1611.09540 \[hep-ph\]](#).
- [213] M. Aaboud et al. “Search for electroweak production of supersymmetric particles in final states with two or three leptons at  $\sqrt{s} = 13$  TeV with the ATLAS detector”. In: *Eur. Phys. J.* C78.12 (2018), p. 995. arXiv: [1803.02762 \[hep-ex\]](#).

- [214] Morad Aaboud et al. “Search for the direct production of charginos and neutralinos in final states with tau leptons in  $\sqrt{s} = 13$  TeV  $pp$  collisions with the ATLAS detector”. In: *Eur. Phys. J. C* 78.2 (2018), p. 154. arXiv: [1708.07875 \[hep-ex\]](#).
- [215] Georges Aad et al. “Search for electroweak production of charginos and sleptons decaying into final states with two leptons and missing transverse momentum in  $\sqrt{s} = 13$  TeV  $pp$  collisions using the ATLAS detector”. In: *Eur. Phys. J. C* 80.2 (2020), p. 123. arXiv: [1908.08215 \[hep-ex\]](#).
- [216] Adam Alloul et al. “FeynRules 2.0 - A complete toolbox for tree-level phenomenology”. In: *Comput. Phys. Commun.* 185 (2014), pp. 2250–2300. arXiv: [1310.1921 \[hep-ph\]](#).
- [217] J. Alwall et al. “The automated computation of tree-level and next-to-leading order differential cross sections, and their matching to parton shower simulations”. In: *JHEP* 07 (2014), p. 079. arXiv: [1405.0301 \[hep-ph\]](#).
- [218] Torbjorn Sjostrand, Stephen Mrenna, and Peter Z. Skands. “A Brief Introduction to PYTHIA 8.1”. In: *Comput. Phys. Commun.* 178 (2008), pp. 852–867. arXiv: [0710.3820 \[hep-ph\]](#).
- [219] J. de Favereau et al. “DELPHES 3, A modular framework for fast simulation of a generic collider experiment”. In: *JHEP* 02 (2014), p. 057. arXiv: [1307.6346 \[hep-ex\]](#).
- [220] C. G. Lester and D. J. Summers. “Measuring masses of semiinvisibly decaying particles pair produced at hadron colliders”. In: *Phys. Lett. B* 463 (1999), pp. 99–103. arXiv: [hep-ph/9906349](#).
- [221] Alan Barr, Christopher Lester, and P. Stephens. “m(T2): The Truth behind the glamour”. In: *J. Phys.* G29 (2003), pp. 2343–2363. arXiv: [hep-ph/0304226 \[hep-ph\]](#).
- [222] G. Apollinari et al. “High Luminosity Large Hadron Collider HL-LHC”. In: *CERN Yellow Rep.* 5 (2015), pp. 1–19. arXiv: [1705.08830 \[physics.acc-ph\]](#).
- [223] Glen Cowan et al. “Asymptotic formulae for likelihood-based tests of new physics”. In: *Eur. Phys. J. C* 71 (2011). [Erratum: *Eur. Phys. J.*C73,2501(2013)], p. 1554. arXiv: [1007.1727 \[physics.data-an\]](#).
- [224] A. Abada et al. “FCC-hh: The Hadron Collider”. In: *Eur. Phys. J. ST* 228.4 (2019), pp. 755–1107.
- [225] Stefania Gori et al. “Prospects for Electroweakino Discovery at a 100 TeV Hadron Collider”. In: *JHEP* 12 (2014), p. 108. arXiv: [1410.6287 \[hep-ph\]](#).
- [226] J. de Blas et al. *The CLIC Potential for New Physics*. arXiv: [1812.02093 \[hep-ph\]](#).
- [227] M J Boland et al. *Updated baseline for a staged Compact Linear Collider*. Ed. by P Lebrun et al. arXiv: [1608.07537 \[physics.acc-ph\]](#).
- [228] Dominik Arominski et al. *A detector for CLIC: main parameters and performance*. arXiv: [1812.07337 \[physics.ins-det\]](#).
- [229] Alexander Kusenko. “Sterile neutrinos, dark matter, and the pulsar velocities in models with a Higgs singlet”. In: *Phys. Rev. Lett.* 97 (2006), p. 241301. arXiv: [hep-ph/0609081](#).
- [230] D. Barducci et al. “Collider limits on new physics within micrOMEGAs\_4.3”. In: *Comput. Phys. Commun.* 222 (2018), pp. 327–338. arXiv: [1606.03834 \[hep-ph\]](#).

- [231] Christophe Yèche et al. “Constraints on neutrino masses from Lyman-alpha forest power spectrum with BOSS and XQ-100”. In: *JCAP* 1706.06 (2017), p. 047. arXiv: [1702.03314 \[astro-ph.CO\]](#).
- [232] Girish Kulkarni et al. “Characterizing the Pressure Smoothing Scale of the Intergalactic Medium”. In: *Astrophys. J.* 812 (2015), p. 30. arXiv: [1504.00366 \[astro-ph.CO\]](#).
- [233] Alexander Merle, Aurel Schneider, and Maximilian Totzauer. “Dodelson-Widrow Production of Sterile Neutrino Dark Matter with Non-Trivial Initial Abundance”. In: *JCAP* 1604.04 (2016), p. 003. arXiv: [1512.05369 \[hep-ph\]](#).
- [234] Julian Heeck and Daniele Teresi. “Cold keV dark matter from decays and scatterings”. In: *Phys. Rev. D* 96.3 (2017), p. 035018. arXiv: [1706.09909 \[hep-ph\]](#).
- [235] Alexander Merle and Maximilian Totzauer. “keV Sterile Neutrino Dark Matter from Singlet Scalar Decays: Basic Concepts and Subtle Features”. In: *JCAP* 1506 (2015), p. 011. arXiv: [1502.01011 \[hep-ph\]](#).
- [236] Pablo F. de Salas and Sergio Pastor. “Relic neutrino decoupling with flavour oscillations revisited”. In: *JCAP* 07 (2016), p. 051. arXiv: [1606.06986 \[hep-ph\]](#).
- [237] Cyril Pitrou et al. “Precision big bang nucleosynthesis with improved Helium-4 predictions”. In: *Phys. Rept.* 754 (2018), pp. 1–66. arXiv: [1801.08023 \[astro-ph.CO\]](#).
- [238] A. M. Baldini et al. “The design of the MEG II experiment”. In: *Eur. Phys. J. C* 78.5 (2018), p. 380. arXiv: [1801.04688 \[physics.ins-det\]](#).
- [239] Kevork Abazajian et al. *CMB-S4 Science Case, Reference Design, and Project Plan*. arXiv: [1907.04473 \[astro-ph.IM\]](#).
- [240] Giorgio Arcadi et al. “The waning of the WIMP? A review of models, searches, and constraints”. In: *Eur. Phys. J. C* 78.3 (2018), p. 203. arXiv: [1703.07364 \[hep-ph\]](#).
- [241] Alexander Merle, Viviana Niro, and Daniel Schmidt. “New Production Mechanism for keV Sterile Neutrino Dark Matter by Decays of Frozen-In Scalars”. In: *JCAP* 03 (2014), p. 028. arXiv: [1306.3996 \[hep-ph\]](#).
- [242] Vedran Brdar et al. “X-Ray Lines from Dark Matter Annihilation at the keV Scale”. In: *Phys. Rev. Lett.* 120.6 (2018), p. 061301. arXiv: [1710.02146 \[hep-ph\]](#).
- [243] André De Gouvêa et al. “Dodelson-Widrow Mechanism in the Presence of Self-Interacting Neutrinos”. In: *Phys. Rev. Lett.* 124.8 (2020), p. 081802. arXiv: [1910.04901 \[hep-ph\]](#).
- [244] Jae-Weon Lee. “Brief History of Ultra-light Scalar Dark Matter Models”. In: *EPJ Web Conf.* 168 (2018). Ed. by B. Gwak et al., p. 06005. arXiv: [1704.05057 \[astro-ph.CO\]](#).
- [245] Lam Hui et al. “Ultralight scalars as cosmological dark matter”. In: *Phys. Rev. D* 95.4 (2017), p. 043541. arXiv: [1610.08297 \[astro-ph.CO\]](#).
- [246] Javier Redondo and Marieke Postma. “Massive hidden photons as lukewarm dark matter”. In: *JCAP* 02 (2009), p. 005. arXiv: [0811.0326 \[hep-ph\]](#).
- [247] Thomas Hambye et al. “Dark matter from dark photons: a taxonomy of dark matter production”. In: *Phys. Rev. D* 100.9 (2019), p. 095018. arXiv: [1908.09864 \[hep-ph\]](#).
- [248] Joerg Jaeckel, Javier Redondo, and Andreas Ringwald. “3.55 keV hint for decaying axionlike particle dark matter”. In: *Phys. Rev. D* 89 (2014), p. 103511. arXiv: [1402.7335 \[hep-ph\]](#).



- 
- [249] Sang Hui Im and Kwang Sik Jeong. “Freeze-in Axion-like Dark Matter”. In: *Phys. Lett. B* 799 (2019), p. 135044. arXiv: [1907.07383 \[hep-ph\]](#).
- [250] Jonathan L. Ouellet et al. “First Results from ABRACADABRA-10 cm: A Search for Sub- $\mu\text{eV}$  Axion Dark Matter”. In: *Phys. Rev. Lett.* 122.12 (2019), p. 121802. arXiv: [1810.12257 \[hep-ex\]](#).
- [251] David J. E. Marsh and Joe Silk. “A Model For Halo Formation With Axion Mixed Dark Matter”. In: *Mon. Not. Roy. Astron. Soc.* 437.3 (2014), pp. 2652–2663. arXiv: [1307.1705 \[astro-ph.CO\]](#).
- [252] Nayara Fonseca and Enrico Morgante. “Relaxion Dark Matter”. In: *Phys. Rev. D* 100.5 (2019), p. 055010. arXiv: [1809.04534 \[hep-ph\]](#).
- [253] Nayara Fonseca and Enrico Morgante. “Probing photophobic axion and relaxion dark matter”. In: *Phys. Rev. D* 103.1 (2021), p. 015011. arXiv: [2009.10974 \[hep-ph\]](#).
- [254] Abhishek Banerjee, Hyungjin Kim, and Gilad Perez. “Coherent relaxion dark matter”. In: *Phys. Rev. D* 100.11 (2019), p. 115026. arXiv: [1810.01889 \[hep-ph\]](#).
- [255] Jonathan L. Feng et al. “Axionlike particles at FASER: The LHC as a photon beam dump”. In: *Phys. Rev. D* 98.5 (2018), p. 055021. arXiv: [1806.02348 \[hep-ph\]](#).
- [256] Matthew J. Dolan et al. “Revised constraints and Belle II sensitivity for visible and invisible axion-like particles”. In: *JHEP* 12 (2017), p. 094. arXiv: [1709.00009 \[hep-ph\]](#).
- [257] Sergey Alekhin et al. “A facility to Search for Hidden Particles at the CERN SPS: the SHiP physics case”. In: *Rept. Prog. Phys.* 79.12 (2016), p. 124201. arXiv: [1504.04855 \[hep-ph\]](#).
- [258] Vedran Brdar et al. “Axionlike Particles at Future Neutrino Experiments: Closing the Cosmological Triangle”. In: *Phys. Rev. Lett.* 126.20 (2021), p. 201801. arXiv: [2011.07054 \[hep-ph\]](#).
- [259] Alberto Salvio, Alessandro Strumia, and Wei Xue. “Thermal axion production”. In: *JCAP* 01 (2014), p. 011. arXiv: [1310.6982 \[hep-ph\]](#).
- [260] Davide Cadamuro and Javier Redondo. “Cosmological bounds on pseudo Nambu-Goldstone bosons”. In: *JCAP* 02 (2012), p. 032. arXiv: [1110.2895 \[hep-ph\]](#).
- [261] P. A. Zyla et al. “Review of Particle Physics”. In: *PTEP* 2020.8 (2020), p. 083C01.
- [262] Eric Braaten and Tzu Chiang Yuan. “Calculation of screening in a hot plasma”. In: *Phys. Rev. Lett.* 66 (1991), pp. 2183–2186.
- [263] M. Bolz, A. Brandenburg, and W. Buchmuller. “Thermal production of gravitinos”. In: *Nucl. Phys. B* 606 (2001). [Erratum: *Nucl.Phys.B* 790, 336–337 (2008)], pp. 518–544. arXiv: [hep-ph/0012052](#).
- [264] Kyu Jung Bae et al. “Light axinos from freeze-in: production processes, phase space distributions, and Ly- $\alpha$  forest constraints”. In: *JCAP* 01 (2018), p. 054. arXiv: [1707.06418 \[hep-ph\]](#).
- [265] A. Garzilli et al. *How warm is too warm? Towards robust Lyman- $\alpha$  forest bounds on warm dark matter*. arXiv: [1912.09397 \[astro-ph.CO\]](#).
- [266] Jen-Wei Hsueh et al. “SHARP – VII. New constraints on the dark matter free-streaming properties and substructure abundance from gravitationally lensed quasars”. In: *Mon. Not. Roy. Astron. Soc.* 492.2 (2020), pp. 3047–3059. arXiv: [1905.04182 \[astro-ph.CO\]](#).

- [267] Wenting Wang et al. “Estimating the dark matter halo mass of our Milky Way using dynamical tracers”. In: *Mon. Not. Roy. Astron. Soc.* 453.1 (2015), pp. 377–400. arXiv: [1502.03477 \[astro-ph.GA\]](#).
- [268] Thomas Callingham et al. *The mass of the Milky Way from satellite dynamics*. arXiv: [1808.10456 \[astro-ph.GA\]](#).
- [269] Marius Cautun et al. “The Milky Way total mass profile as inferred from Gaia DR2”. In: *Mon. Not. Roy. Astron. Soc.* 494.3 (2020), pp. 4291–4313. arXiv: [1911.04557 \[astro-ph.GA\]](#).
- [270] E.V. Karukes et al. “A robust estimate of the Milky Way mass from rotation curve data”. In: *JCAP* 05 (2020), p. 033. arXiv: [1912.04296 \[astro-ph.GA\]](#).
- [271] Wenting Wang et al. “The mass of our Milky Way”. In: *Sci. China Phys. Mech. Astron.* 63.10 (2020), p. 109801. arXiv: [1912.02599 \[astro-ph.GA\]](#).
- [272] G.R. Dvali. *Removing the cosmological bound on the axion scale*. arXiv: [hep-ph/9505253](#).
- [273] Raymond T. Co, Eric Gonzalez, and Keisuke Harigaya. “Axion Misalignment Driven to the Bottom”. In: *JHEP* 05 (2019), p. 162. arXiv: [1812.11186 \[hep-ph\]](#).
- [274] Maxim Pospelov, Adam Ritz, and Mikhail B. Voloshin. “Bosonic super-WIMPs as keV-scale dark matter”. In: *Phys. Rev. D* 78 (2008), p. 115012. arXiv: [0807.3279 \[hep-ph\]](#).
- [275] Alexey Boyarsky et al. “Constraining DM properties with SPI”. In: *Mon. Not. Roy. Astron. Soc.* 387 (2008), p. 1345. arXiv: [0710.4922 \[astro-ph\]](#).
- [276] Brandon M. Roach et al. “NuSTAR Tests of Sterile-Neutrino Dark Matter: New Galactic Bulge Observations and Combined Impact”. In: *Phys. Rev. D* 101.10 (2020), p. 103011. arXiv: [1908.09037 \[astro-ph.HE\]](#).
- [277] Shunsaku Horiuchi et al. “Sterile neutrino dark matter bounds from galaxies of the Local Group”. In: *Phys. Rev. D* 89.2 (2014), p. 025017. arXiv: [1311.0282 \[astro-ph.CO\]](#).
- [278] Y. Akrami et al. “Planck 2018 results. X. Constraints on inflation”. In: *Astron. Astrophys.* 641 (2020), A10. arXiv: [1807.06211 \[astro-ph.CO\]](#).
- [279] L. Amati et al. “The THESEUS space mission concept: science case, design and expected performances”. In: *Adv. Space Res.* 62 (2018), pp. 191–244. arXiv: [1710.04638 \[astro-ph.IM\]](#).
- [280] E. O. Nadler et al. “Milky Way Satellite Census. III. Constraints on Dark Matter Properties from Observations of Milky Way Satellite Galaxies”. In: *Phys. Rev. Lett.* 126 (2021), p. 091101. arXiv: [2008.00022 \[astro-ph.CO\]](#).
- [281] Francesco Capozzi and Georg Raffelt. “Axion and neutrino bounds improved with new calibrations of the tip of the red-giant branch using geometric distance determinations”. In: *Phys. Rev. D* 102.8 (2020), p. 083007. arXiv: [2007.03694 \[astro-ph.SR\]](#).
- [282] Nicolás Viaux et al. “Neutrino and axion bounds from the globular cluster M5 (NGC 5904)”. In: *Phys. Rev. Lett.* 111 (2013), p. 231301. arXiv: [1311.1669 \[astro-ph.SR\]](#).
- [283] Cristina Benso et al. “Prospects for Finding Sterile Neutrino Dark Matter at KATRIN”. In: *Phys. Rev. D* 100.11 (2019), p. 115035. arXiv: [1911.00328 \[hep-ph\]](#).
- [284] Alex Drlica-Wagner et al. *Probing the Fundamental Nature of Dark Matter with the Large Synoptic Survey Telescope*. arXiv: [1902.01055 \[astro-ph.CO\]](#).

- 
- [285] Cora Dvorkin, Tongyan Lin, and Katelin Schutz. “Cosmology of Sub-MeV Dark Matter Freeze-In”. In: *Phys. Rev. Lett.* 127.11 (2021), p. 111301. arXiv: [2011.08186 \[astro-ph.CO\]](#).
- [286] M. A. Luty. “Baryogenesis via leptogenesis”. In: *Phys. Rev. D* 45 (1992), pp. 455–465.
- [287] Simon Knapen, Tongyan Lin, and Kathryn M. Zurek. “Light Dark Matter: Models and Constraints”. In: *Phys. Rev. D* 96.11 (2017), p. 115021. arXiv: [1709.07882 \[hep-ph\]](#).
- [288] Paul Bode, Jeremiah P. Ostriker, and Neil Turok. “Halo formation in warm dark matter models”. In: *Astrophys. J.* 556 (2001), pp. 93–107. arXiv: [astro-ph/0010389](#).
- [289] James S. Bullock and Michael Boylan-Kolchin. “Small-Scale Challenges to the  $\Lambda$ CDM Paradigm”. In: *Ann. Rev. Astron. Astrophys.* 55 (2017), pp. 343–387. arXiv: [1707.04256 \[astro-ph.CO\]](#).
- [290] B. Moore et al. “Dark matter substructure within galactic halos”. In: *Astrophys. J. Lett.* 524 (1999), pp. L19–L22. arXiv: [astro-ph/9907411](#).
- [291] W. J. G. de Blok. “The Core-Cusp Problem”. In: *Advances in Astronomy* 2010 (2010), pp. 1–14.
- [292] Michael Boylan-Kolchin, James S. Bullock, and Manoj Kaplinghat. “Too big to fail? The puzzling darkness of massive Milky Way subhaloes”. In: *Monthly Notices of the Royal Astronomical Society: Letters* 415.1 (June 2011), pp. L40–L44.
- [293] Michael Boylan-Kolchin, James S. Bullock, and Manoj Kaplinghat. “The Milky Way’s bright satellites as an apparent failure of  $\Lambda$ CDM”. In: *Monthly Notices of the Royal Astronomical Society* 422.2 (Mar. 2012), pp. 1203–1218.
- [294] Adi Zolotov et al. “BARYONS MATTER: WHY LUMINOUS SATELLITE GALAXIES HAVE REDUCED CENTRAL MASSES”. In: *The Astrophysical Journal* 761.1 (Nov. 2012), p. 71.
- [295] Aaron A. Dutton et al. “NIHAO V: too big does not fail – reconciling the conflict between  $\Lambda$ CDM predictions and the circular velocities of nearby field galaxies”. In: *Mon. Not. Roy. Astron. Soc.* 457.1 (2016), pp. L74–L78. arXiv: [1512.00453 \[astro-ph.GA\]](#).
- [296] Mark R. Lovell et al. “Addressing the too big to fail problem with baryon physics and sterile neutrino dark matter”. In: *Mon. Not. Roy. Astron. Soc.* 468.3 (2017), pp. 2836–2849. arXiv: [1611.00005 \[astro-ph.GA\]](#).
- [297] Wayne Hu, Rennan Barkana, and Andrei Gruzinov. “Cold and fuzzy dark matter”. In: *Phys. Rev. Lett.* 85 (2000), pp. 1158–1161. arXiv: [astro-ph/0003365](#).
- [298] Bodo Schwabe et al. “Simulating mixed fuzzy and cold dark matter”. In: *Phys. Rev. D* 102.8 (2020), p. 083518. arXiv: [2007.08256 \[astro-ph.CO\]](#).
- [299] Roberta Diamanti et al. “Cold dark matter plus not-so-clumpy dark relics”. In: *JCAP* 06 (2017), p. 008. arXiv: [1701.03128 \[astro-ph.CO\]](#).
- [300] D Anderhalden et al. “The galactic halo in mixed dark matter cosmologies”. In: *Journal of Cosmology and Astroparticle Physics* 2012.10 (Oct. 2012), pp. 047–047.
- [301] Marc Davis, F.J. Summers, and David Schlegel. “Large scale structure in a universe with mixed hot and cold dark matter”. In: *Nature* 359 (1992), pp. 393–396.
- [302] Anatoly Klypin et al. “Structure formation with cold plus hot dark matter”. In: *Astrophys. J.* 416 (1993), pp. 1–16. arXiv: [astro-ph/9305011](#).

- [303] Anatoly Klypin et al. “Damped Lyman alpha systems versus Cold + Hot Dark Matter”. In: *Astrophys. J.* 444 (1995), p. 1. arXiv: [astro-ph/9405003](#).
- [304] Chung-Pei Ma and Edmund Bertschinger. “Do galactic systems form too late in cold + hot dark matter models?”. In: *Astrophys. J. Lett.* 434 (1994), p. L5. arXiv: [astro-ph/9407085](#).
- [305] Scott Dodelson, Evalyn Gates, and Albert Stebbins. “Cold + hot dark matter and the cosmic microwave background”. In: *Astrophys. J.* 467 (1996), pp. 10–18. arXiv: [astro-ph/9509147](#).
- [306] Dan Hooper, Farinaldo S. Queiroz, and Nickolay Y. Gnedin. “Non-Thermal Dark Matter Mimicking An Additional Neutrino Species In The Early Universe”. In: *Phys. Rev. D* 85 (2012), p. 063513. arXiv: [1111.6599 \[astro-ph.CO\]](#).
- [307] Mathias Garny and Jan Heisig. “Interplay of super-WIMP and freeze-in production of dark matter”. In: *Phys. Rev. D* 98.9 (2018), p. 095031. arXiv: [1809.10135 \[hep-ph\]](#).
- [308] Jonathan L. Feng, Arvind Rajaraman, and Fumihiro Takayama. “SuperWIMP dark matter signals from the early universe”. In: *Phys. Rev. D* 68 (2003), p. 063504. arXiv: [hep-ph/0306024](#).
- [309] Quentin Decant et al. *Lyman- $\alpha$  constraints on freeze-in and superWIMPs*. arXiv: [2111.09321 \[astro-ph.CO\]](#).
- [310] G. Parimbelli et al. *Mixed dark matter: matter power spectrum and halo mass function*. arXiv: [2106.04588 \[astro-ph.CO\]](#).
- [311] Wayne Hu, Daniel J. Eisenstein, and Max Tegmark. “Weighing neutrinos with galaxy surveys”. In: *Phys. Rev. Lett.* 80 (1998), pp. 5255–5258. arXiv: [astro-ph/9712057](#).
- [312] Francesco D’Eramo and Alessandro Lenoci. *Lower Mass Bounds on FIMPs*. arXiv: [2012.01446 \[hep-ph\]](#).
- [313] G. Monari et al. “The escape speed curve of the Galaxy obtained from Gaia DR2 implies a heavy Milky Way”. In: *Astronomy & Astrophysics* 616 (Aug. 2018), p. L9.
- [314] Alis J Deason et al. “The local high-velocity tail and the Galactic escape speed”. In: *Monthly Notices of the Royal Astronomical Society* 485.3 (Mar. 2019), pp. 3514–3526.
- [315] Robert J J Grand et al. “The effects of dynamical substructure on Milky Way mass estimates from the high-velocity tail of the local stellar halo”. In: *Monthly Notices of the Royal Astronomical Society: Letters* 487.1 (June 2019), pp. L72–L76.
- [316] Laura L. Watkins et al. “Evidence for an Intermediate-mass Milky Way from Gaia DR2 Halo Globular Cluster Motions”. In: *The Astrophysical Journal* 873.2 (Mar. 2019), p. 118.
- [317] T K Fritz et al. “The mass of our Galaxy from satellite proper motions in the Gaia era”. In: *Monthly Notices of the Royal Astronomical Society* 494.4 (Apr. 2020), pp. 5178–5193.
- [318] Lorenzo Posti and Amina Helmi. “Mass and shape of the Milky Way’s dark matter halo with globular clusters from Gaia and Hubble”. In: *Astronomy & Astrophysics* 621 (Jan. 2019), A56.
- [319] Eugene Vasiliev. “Proper motions and dynamics of the Milky Way globular cluster system from Gaia DR2”. In: *Monthly Notices of the Royal Astronomical Society* 484.2 (Jan. 2019), pp. 2832–2850.

- 
- [320] Gwendolyn Eadie and Mario Jurić. “The Cumulative Mass Profile of the Milky Way as Determined by Globular Cluster Kinematics from Gaia DR2”. In: *The Astrophysical Journal* 875.2 (Apr. 2019), p. 159.
- [321] Zhao-Zhou Li et al. “Constraining the Milky Way Mass Profile with Phase-space Distribution of Satellite Galaxies”. In: *The Astrophysical Journal* 894.1 (Apr. 2020), p. 10.
- [322] Roger Barlow. “Asymmetric statistical errors”. In: *Statistical Problems in Particle Physics, Astrophysics and Cosmology*. June 2004, pp. 56–59. arXiv: [physics/0406120](#).
- [323] Lina Necib and Tongyan Lin. *Substructure at High Speed II: The Local Escape Velocity and Milky Way Mass with Gaia DR2*. arXiv: [2102.02211 \[astro-ph.GA\]](#).
- [324] Mark R. Lovell et al. “The properties of warm dark matter haloes”. In: *Mon. Not. Roy. Astron. Soc.* 439 (2014), pp. 300–317. arXiv: [1308.1399 \[astro-ph.CO\]](#).
- [325] Jie Wang et al. “The missing massive satellites of the Milky Way”. In: *Monthly Notices of the Royal Astronomical Society* 424.4 (July 2012), pp. 2715–2721.
- [326] Marco Hufnagel, Kai Schmidt-Hoberg, and Sebastian Wild. “BBN constraints on MeV-scale dark sectors. Part I. Sterile decays”. In: *JCAP* 02 (2018), p. 044. arXiv: [1712.03972 \[hep-ph\]](#).
- [327] Paul Frederik Depta, Marco Hufnagel, and Kai Schmidt-Hoberg. “Updated BBN constraints on electromagnetic decays of MeV-scale particles”. In: *JCAP* 04 (2021), p. 011. arXiv: [2011.06519 \[hep-ph\]](#).

*Lebenslauf*  
**Sven Baumholzer**

Geburtsdatum: 28. Juni 1993  
Anschrift: Westring 257, 55120 Mainz  
Telefon (privat): 0170/3303763  
E-Mail: svenbaumholzer@gmx.net  
Staatsangehörigkeit: deutsch

## Ausbildung

---

- 06/18 - heute    Forschender Doktorand, Fachrichtung Physik  
**Johannes Gutenberg-Universität, Mainz**  
Titel: "Searching for warm dark matter down on Earth and among the stars"  
Betreuer: Prof. Dr. Pedro Schwaller, Bewertung: magna cum laude (1.0)  
Abgabe: 30.11.2021  
Prüfung: 18.03.2022
- 04/16 - 04/18    Master of Science, Fachrichtung Physik  
**Johannes Gutenberg-Universität, Mainz**  
Masterarbeit: "New production mechanism for sterile Neutrinos",  
Betreuer: Prof. Dr. Pedro Schwaller, Gesamtnote: 1.0
- 10/12 - 12/15    Bachelor of Science, Fachrichtung Physik  
**Johannes Gutenberg-Universität, Mainz**  
Bachelorarbeit: "Strahlungskorrekturen zum Quark-Formfaktor in  
masseloser QCD",  
Betreuer: apl. Prof. Dr. Hubert Spiesberger, Gesamtnote: 1.3
- 08/09 - 04/12    Allgemeine Hochschulreife  
**Gymnasium am Römerkastell, Alzey**  
Gesamtnote: 1.2 *Bestes Abiturzeugnis*

## Publikationen

---

- 2021 S. Baumholzer, P. Schwaller  
*Probing non-thermal light DM with structure formation and  $N_{\text{eff}}$* , prepared for submission, E-Print: 2112.03993
- 2020 S. Baumholzer, V. Brdar, E. Morgante  
*Structure Formation Limits on Axion-Like Dark Matter*, *JCAP* **05** (2021) 004, E-Print: 2012.09181
- 2019 S. Baumholzer, V. Brdar, P. Schwaller, A. Segner  
*Shining Light on the Scotogenic Model: Interplay of Colliders and Cosmology*, *JHEP* **09** (2020) 134, E-Print: 1912.08215
- 2018 S. Baumholzer, V. Brdar, P. Schwaller,  
*The New  $\nu$ MSM ( $\nu\nu$ MSM): Radiative Neutrino Masses, keV-Scale Dark Matter and Viable Leptogenesis with sub-TeV New Physics*, *JHEP* **08** (2018) 067, E-Print: 1806.06864

Mainz, 5. April 2022

